SPIE.

ROBUST SPECKLE METROLOGY: TECHNIQUES FOR STRESS ANALYSIS AND NDT

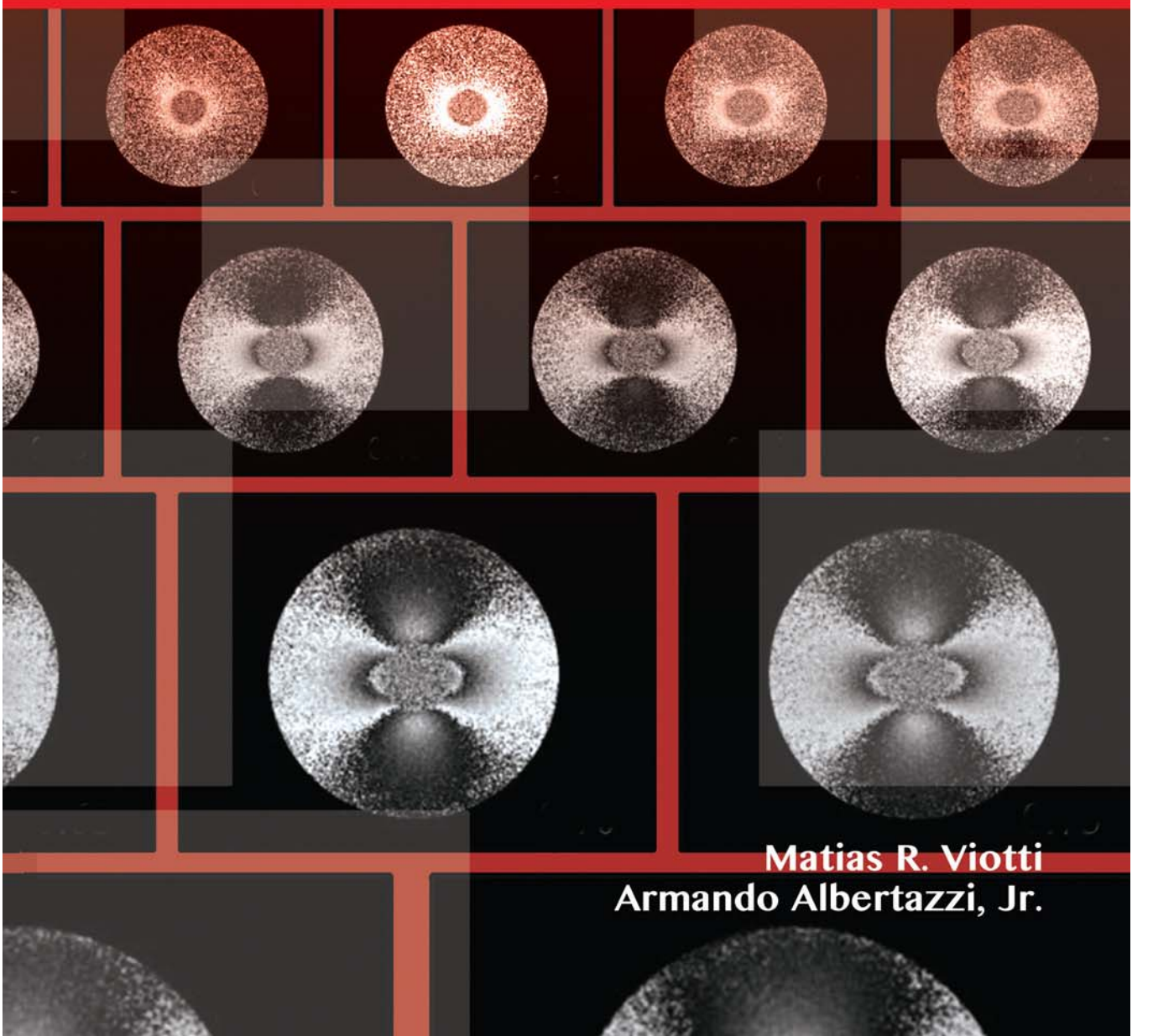

Matias R. Viotti
Armando Albertazzi, Jr.

ROBUST SPECKLE METROLOGY

Techniques for Stress Analysis and NDT

ROBUST SPECKLE METROLOGY

Techniques for Stress Analysis and NDT

Matias R. Viotti
Armando Albertazzi, Jr.

SPIE PRESS
Bellingham, Washington USA

Library of Congress Cataloging-in-Publication Data

Viotti, Matias R., author.
Robust speckle metrology techniques for stress analysis and NDT / Matias R. Viotti and Armando Albertazzi, Jr.
pages cm.
Includes bibliographical references and index.
1. Speckle metrology. 2. Strains and stresses. 3. Nondestructive testing. I. Albertazzi, Armando, Jr., author. II. Title.
TA418.7.V56 2014
620.1'1230287–dc23

2014021899

Published by

SPIE
P.O. Box 10
Bellingham, Washington 98227-0010 USA
Phone: 360.676.3290
Fax: 360.647.1445
Email: Books@spie.org
www.spie.org

Printed in the United States of America.
First printing.

SPIE.

Table of Contents

Preface

The invention of the laser in the early 1960s allowed for light sources with a high coherence degree, which generated many novel research lines in order to make use of them. People working with these light sources noticed that a high-contrast and fine-scale granular pattern was produced when a rough surface was illuminated with laser light. This effect was called a "speckle effect," characterized by a random distribution of scattered light. After recognizing that each speckle has a definite phase, several techniques were developed to measure deformations, displacements, stresses, vibrations, and inner defects.

Several multiauthor books have been published beyond the first one published in 1978 (*Speckle Metrology*, edited by R. K. Erf)—including *Digital Speckle Pattern Interferometry and Related Techniques*, edited by P. K. Rastogi, and *Advances in Speckle Metrology and Related Techniques*, edited by G. H. Kaufmann—show new branches in speckle metrology, new proposed schemes and improvements in processing techniques, and optical approaches that have occurred over the last 20 years.

The main goal of nondestructive testing (NDT) is to detect and characterize anomalies that can adversely affect the performance of the component under test without impairing its intended service.

Optical techniques can be considered as alternative approaches to traditional NDT methods. They are very attractive for NDT due to their noncontacting nature and their high relative speed of inspection. The application of digital techniques allows for automatic processing. Consequently, a fast inspection procedure enables the evaluation of large areas (e.g., aircraft wings and ship structures) or a large number of parts (e.g., automotive components). Speckle techniques have the advantages cited for optical methods. Additionally, they are appropriate for the evaluation of real components without further preparation of the surface or time-intensive analysis.

This book provides tips, ideas, and examples for the successful application of optical techniques (more specifically based on the speckle phenomenon) outside the laboratory room. Readers can see that the topics presented in the following nine chapters have been selected to benefit graduate students, engineers, and scientists who are interested in the in-field application of

speckle techniques to solve specific problems related to optical metrology, experimental mechanics, and NDT.

Chapter 1 discusses aspects to consider when designing mechanical parts and structures for safe and reliable products because several applications are usually related with human life and ecology. This chapter also shows that the working conditions influence the performance and mechanical integrity of the part. This influence can sometimes cause an accident due to a lack of corrective actions. For this reason, the chapter highlights the use of NDT to foresee possible accidents and focuses on optical techniques, especially speckle methods.

Chapter 2 addresses the theoretical aspects of the origin and formation of the speckle phenomenon. The most important principles for speckle interferometry are then developed, showing how the phase of the speckle distribution carries essential information for measuring displacements fields, object shapes, etc. For this reason, several tools to quantify the phase of the speckle distribution are presented, as well as the phase-unwrapping principles that are used to deal with 2π jumps obtained after the use of phase-shifting techniques.

Chapter 3 presents traditional digital-speckle-pattern-interferometry (DSPI) optical configurations used to measure displacement fields and their derivatives. Measurements are divided into (a) out-of-plane and (b) in-plane displacements. For the former, the working principle is presented, as well as a possible laboratory optical setup. For the latter, traditional interferometers with in-plane sensitivity are presented; radial, in-plane interferometer setups capable of measuring polar coordinates are also presented. Finally, principles for shearography are shown.

Chapter 4 gives a more-detailed description of the requirements for robust optical setups. The chapter offers tools, tips, and reference parameters to guide the development and design of interferometers based on the speckle phenomenon for use outside of the laboratory. Additionally, various environment agents are described, showing the effect that they have on the measuring performance of the optical system.

Chapter 5 discusses the application of DSPI to measure mechanical stresses as an auxiliary tool for structural integrity assessment. After a short introduction, the principles for traditional strain-gage sensors are presented. Some interferometric solutions are shown in order to measure 3D displacements (along three sensitivity directions) and displacements in polar coordinates. For the latter, several tips are listed for the measurement of large strain fields without loss of correlation. Finally, an application example shows the effectiveness of the proposed solution.

Many service failures of structural or mechanical components are caused by a combination of residual stress fields in the material and mechanical stresses produced by applied loads. For this reason, Chapter 6 provides experimental solutions to compute residual stresses. The traditional method

combines strain gages with the hole-drilling technique. In this case, a small hole is introduced into the material, allowing for local stress relief that enables stress measurements. The chapter also explores a combination of the hole-drilling technique and DSPI. A practical application outside the laboratory is described, showing the high potential of the technique as an integrity-evaluation tool.

Chapter 7 begins with a list of the traditional nondestructive techniques used in defect detection. The chapter highlights shearography as a NDT tool with important applications in the automotive, aeronautical, and petroleum and gas industries. Several optical configurations suitable for in-field applications are presented. One of the most important components in a shearographic device is the loading/excitation setup. For this reason, several possible methods are described. Finally, applications in some industries, mechanical parts, and structures are shown. Available commercial systems highlight the fast growth of shearography as a NDT technique. Some significant commercial devices are illustrated in this chapter.

Previous chapters address principles, optical setups, and application examples for interferometric techniques based on the speckle phenomenon. Another optical speckle technique that has grown quickly over the last two decades is digital image correlation (DIC), which is considered a noninterferometric technique. A short review of the available literature about this technique is presented in Chapter 8, which is oriented to NDT applications.

Finally, Chapter 9 briefly discusses all of the presented techniques to help readers select the best optical setup for their needs, or, beyond that, develop new solutions (for those cases where there are none) to measure a specific measurand.

We would like to thank the following people: Prof. Guillermo Kaufmann and SPIE Press Manager Tim Lamkins for their encouragement before writing this book; Prof. Gary Schajer for his kind help and valuable collaboration with some figures obtained by residual stress measurements with the hole-drilling techniques; Prof. Gustavo Galizzi for his help during the elaboration of some simulated figures used in the phase-unwrapping section; Dr. Gordon Craggs for several fruitful discussions about Chapters 2 and 3 and for his help with some phrasing; the peer reviewers for their important comments and corrections; and Scott McNeill and the SPIE editorial department for their help and support.

Last, but not least, we are grateful to our families for their support and patience during our time "inside the book." In particular, we would like to give thanks to God for the opportunity to write this book.

Florianópolis, Brazil *Matias R. Viotti*
August 2014 *Armando Albertazzi, Jr.*

List of Symbols and Notation

A	Cross-sectional area of a uniform conductor
$\mathbf{A}_i$	Camera calibration matrix
$\overline{a}_{ij}$, $\overline{b}_{ij}$	Matrices of calibration coefficients
AFM	Atomic force microscopy
AOM	Acousto-optical modulator
AOV	Angle of view of the camera
ASTM	American Society for Testing and Materials
atan2	Full four-quadrant arctangent function
b	Diameter of the aperture
BS	Beamsplitter
$\mathbf{c}$	Matrix operator that acts over the curvature of the solution for nonuniform residual stresses
CASI	Computer-aided speckle interferometry
C_{Ax}	External axial load
CCD	Charge-coupled device
CFRP	Carbon-fiber-reinforced polymer
CMOS	Complementary metal–oxide semiconductor
CT	Computed tomography
$\mathbf{d}$	Displacement vector
$\mathbf{d} = [u, v, w]$	Displacement vector at point P
d_f	Diameter of the conductor after application of the strain
DIC	Digital image correlation
d_o	Diameter of the conductor before the application of the strain
DOE	Diffractive optical element
$\mathbf{d}_{opt}$	Optimal displacement vector
$\mathbf{d}(\mathrm{P}')$	Displacement vector at point P′
DPSS	Diode-pumped solid state
DSCM	Digital speckle correlation method
d_{sp}	Averaged speckle size
DSPI	Digital speckle pattern interferometry
$(d_{sp})_{obj}$	Size of the speckle on the illuminated object
dx, dy	Distances between adjacent pixel in the x and y directions

$d\tau$	Time interval between successive registrations
E	Modulus of elasticity
ESPI	Electronic speckle pattern interferometry
f	Focal length of the optical system
F	Reference image
$\overline{F}$	Medium value for the subset
F_b	Numerical aperture of the optical system
$F_1 \ldots F_n$	Set of external loads
G	Image after displacement
$\overline{G}$	Medium value for the subset
G_e	Geometric factor associated with the directions of illumination and observation
GLARE	Glass-reinforced aluminum laminate
GPGPU	General-purpose computing on graphics processing unit
G_r	Modulus of elasticity in shear (also known as the modulus of rigidity)
$H_0(r_s)$	Zero-order Fourier coefficient
$H_1(r_s)$	First-order Fourier series coefficient
$H_2(r_s)$	Second-order Fourier coefficient
$H_{nS}(r_s)$	Total magnitude of the n^{th} harmonic
$H_{nS}(r_s)$, $H_{nC}(r_s)$	Sine and cosine components, respectively, of the n^{th} Fourier series coefficient
$\hat{\mathbf{i}}$, $\hat{\mathbf{k}}$	Unitary vectors for the x and z directions, respectively
I_0	Averaged (or background) intensity
I_{0f}	Averaged correlation intensity
I_1, I_2	Intensities of the interfering beams
I_{12}	Subtraction of the intensities of the interfering beams
I_c	Cosine intensity obtained from the wrapped difference phase map $\Delta\phi_w(m, n, t_1, t_2)$
IEEE	Institute of Electrical and Electronics Engineers
Im	Imaginary part
I_M	Modulation intensity
I_{ner}	Moment of inertia of the section
IR	Infrared
I_s	Sine intensity obtained from the wrapped-difference phase map $\Delta\phi_w(m, n, t_1, t_2)$
$\mathbf{k}$	Sensitivity vector
K_0, K_x, K_y K_{0R}, K_{1C}, K_{1S},	Constant fitting values of the bending plane
K_{2C}, K_{2S}, K_0	Least-square fitting coefficients
K_{11} to K_{66}	Coefficients of elasticity of the material
k_c	Multiplicative constant for a speckle distribution
$\mathbf{k}_i$	Wave-propagation vectors corresponding to the illumination direction

$\mathbf{k}_o$	Wave-propagation vectors corresponding to the observation direction
L	Length of a uniform conductor
$l_0 \times l_0$	Cross-section of the illuminated area
l_f	Final length of the bar
l_o	Initial length of the bar
LUS	Laser ultrasound
M	Bending moment applied to the beam
M_1	45-deg mirror in the radial interferometer
M_2	Mobile mirror in the radial interferometer
M_3	Fixed mirror in the radial interferometer
M_g	Magnification of the optical system
M(T)	Middle-crack tension
(n, m, t)	Nondimensional coordinates of the discrete image
$\mathbf{n}_A$, $\mathbf{n}_B$	Illumination unitary vectors
NDT	Nondestructive testing
NINT	Rounding to the nearest integer
$N_n \times N_m$	Sensor pixel number (horizontal and vertical)
$\hat{\mathbf{n}}_o$, $\hat{\mathbf{n}}_i$	Unitary vectors
NSSD	Normalized sum of square difference
N_t	Number of successive acquired images
OMS	Optical measurement system
OPA	Operational amplifier
OPD	Optical path difference
$\mathbf{p}$	Parameter vector of the shape function
p, q, t	Combination variables between the strains ε_1, ε_2, and ε_3
P	Equal-biaxial stress
P_1, P_2	Points at the illuminated surface
P_1, P_2	Unwrapping paths
p_r	Period of the grating structure
PZT	Piezoelectric translator
Q	45-deg shear stress
$Q(x, y)$	Points at the imaging plane
q_{mult}	Multiplying factor
$\mathbf{r}$	Position vector
r, θ	Polar coordinates
R	Resistance of a uniform conductor
r_0	Radius of the hole
R_e	Real part
r_{ex}, r_{in}	External and internal radius, respectively, of the pipe
$\mathbf{r}_i$	Curvature center of the incident wavefront
$\mathbf{R}_i$	Rotation matrix
$\mathbf{r}_o$	Position vector of the observation point
ROI	Region of interest

r_s	Sampling radius
s	Scale factor
S	Scattering surface
S_A	Sensitivity of the metallic alloy used as a conductor
SAE	Society of Automotive Engineers
SAW	Submerged arc welding
SEM	Scanning electron microscopy
SG	Strain gage
sgn I	sign[$I(1) - I(2)$] for the Carré algorithm
sig	Sign function
SLM	Spatial light modulator
SNR	Signal-to-noise ratio
s_{OPD}	Optical path difference
SSD	Sum of squared deviations
T	Shear stress
t_1, t_2	Time for the first and second interferogram acquisition
$\mathbf{T}_i$	Translation vector
u	Component of the displacement field along the x direction
$(u_1, v_1, 1)$, $(u_2, v_2, 1)$	Image coordinates for both cameras
UOE	U-shape, O-shape, and expansion (pipe-fabrication process)
u_r	Radial component of the in-plane displacement
USB	Universal serial bus
u_t	Amount of uniform rigid-body translation
V	Fringe visibility or contrast
VDIC	Volumetric digital image correlation
V_f	Correlation fringe visibility or contrast
V_r	Radial phase variation around a pixel
w	Component of the displacement of the object surface along the z direction
$w(\mathbf{x})$	Weighting function
$\mathbf{x}(x, y)$	Coordinates on the observation plane
(x, y, z)	Cartesian coordinates
$(x_{c1}, y_{c1}, z_{c1}, 1)$, $(x_{c2}, y_{c2}, z_{c2}, 1)$	Homogenous coordinates corresponding to point Q in camera 1 and camera 2, respectively
$(x_w, y_w, z_w, 1)$	Homogeneous coordinates in the world coordinate system
y	Distance from the neutral line
z	Distance between the screen where the scattered light is gathered and the object
z_i	Distance between the aperture and the imaging plane
ZNSSD	Zero-normalized sum of squared differences
z_o	Distance from the object to the aperture
ZSSD	Zero-mean sum of squared differences

α	Angle that defines the translation direction
α_P, α_Q, α_T	Factors to control of the amount of regularization
α_t	Relative phase shift between acquired interferograms
γ	Illumination angle
Υ	Wrapping operator
γ_1, γ_2	Illumination angles for an in-plane interferometer
γ_{ij}	Shear strains being $i = x$, y, or z and $j = x$, y, or z
Δ	Change in the parameter
$\Delta\mathbf{d}$	Displacement difference
Δl	Change of the length
δ_{NL}	Angle of the neutral line
ΔOPC	Optical path change generated by the PZT displacement
ΔPZT	Displacement of the piezoelectric transducer
$\Delta\mathbf{r}$	Displacements of the scattering surface
Δs_{OPD}	Optical path difference
δx	Lateral shift in shearography
$\delta_{\sigma max}$	Angular position of the maximum stress axis
$\Delta\varphi$	Variation of the phase of the speckle in the object beam produced by the displacements of the diffuser
$\Delta\phi$	Variation in the phase difference
$\Delta\phi(m,n)$	Wrapped phase to be determined
$\Delta\phi_w(n,m)$	Measured wrapped phase
ε_1, ε_2	Principal strains
ε_1, ε_2, ε_3	Measured strains by gages 1, 2, and 3 (see Fig. 6.2)
ε_i	Normal strains, being $i = x$, y, or z
$\zeta(\mathbf{x},\mathbf{p})$	Subset function
η	Principal angle (for mechanical stresses)
λ	Wavelength of the illumination source
ν	Poisson ratio
ξ	Diffraction angle for the m-order
$\xi(x,y)$	Surface height at (x, y)
ρ	Specific resistance of a uniform conductor
σ	Normal stress
σ_1, σ_2	Principal stresses
σ_B	Bending stress
σ_C	Stress along the circumferential direction
σ_L	Stress along the longitudinal direction
$\sigma_L(x,y)$	Longitudinal stress component measured in each angular point
τ	Shearing stress
τ	Time on the observation plane
φ	Phase of the speckle
ϕ	Relative phase between the interfering beams
φ_1, φ_2	Phases of the interfering wavefronts

ϕ_i^E	Phase value for the i^{th} pixel on the external circle
ϕ_i^I	Phase of i^{th} pixel on the internal circle
φ_s	Random component of the phase of the speckle
ϕ_w	Wrapped phase
χ	Angle of the conical mirror
$\chi(\mathbf{p})$	Cost function
ψ	Deterministic component of the phase of the speckle
ψ_i	Initial optical phase
ψ_o	Object phase
$\Omega(\mathbf{r})$	Complex amplitude at each point in a speckle pattern
ω_i	Complex amplitude of the incident light in (x, y)

Chapter 1
NDT Applications in Engineering

1.1 Mechanical Design of Structures and Mechanical Parts

Civil structures (e.g., bridges and buildings) exist to address people's needs and simplify life. In the same way, mechanical parts and components (e.g., shafts, fasteners, springs, weldments, etc.) for cars, motorbikes, planes, and various machines are currently used to solve practical problems and to increase comfort.

In all cases, structures and mechanical components were designed after considering their primary function and the particular problem that they are intended to solve. These structures and components are the consequence of a designing process performed by multidisciplinary teams composed of engineers, designers, researchers, technicians, etc. In addition, the resulting product must be functional, safe, reliable, competitive, usable, manufacturable, and marketable.[1]

This chapter addresses some aspects to be considered during the design of a mechanical part in order to meet requirements—primarily safety and reliability because many applications are related to human and environmental safety (ecology). For this reason, the following sections show readers how work conditions could influence the performance and mechanical integrity of a part, thus causing an accident due to lack of corrective actions. Finally, the chapter presents the standard techniques used to perform nondestructive testing (NDT), emphasizing optical techniques (especially in speckle methods).

1.1.1 Mechanical-design procedure

A product is usually the result of a design process that began when a need was identified. Figure 1.1 shows the complete design process. It starts with the identification of a need and continues with the decision to develop a potential solution. Several iterations between the members of the team will finish with the production of a plan to satisfy the need. In some cases, these steps are

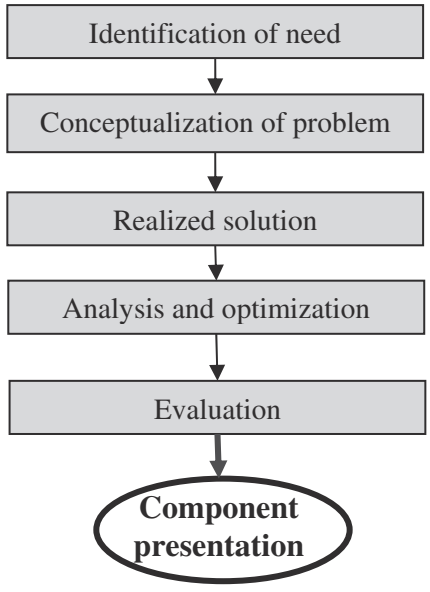

Figure 1.1 Phases of the design process.

developed until the product is manufactured; in others, they are repeated throughout the whole life of the component.

The first step is the identification of the need. Depending on the application, the recognition of the need is a straightforward process because it is clear to the designer team, e.g., the development of a new material able to resist high temperatures in a corrosive atmosphere is an evident need. However, the need for some applications is not always so obvious. Budynas and Nisbett[1] describe a good example involving a food-packaging machine, and they explain that the need to do something can be indicated by the noise level, by a variation in the package weight, and by slightly perceptible variations in the quality of the packaging or wrap.

At first glance, conceptualizing the problem and identifying the need could be seen as the same activity. However, they are different: conceptualization is a more specific task and involves defining all of the specifications of the component or structure to be designed. A correct group of specifications will define the exact cost of the component, its expected life, its physical limitations (e.g., temperature and pressure), its dimensional limitations (e.g., weight or length dimensions), and its reliability. For many engineering applications, reliability is the most important feature and is usually associated with structural integrity. In other words, the component or structure will withstand service loads effectively and efficiently during its functional life.

The steps "realized solution" and "analysis and optimization" are reciprocal parts of an iterative process that will lead to the conceptualization of the final prototype. After the definition of the specifications, the designer

team will propose and investigate several probable solutions. These solutions will also be quantified in terms of very well-defined metrics in order to compare them. As solutions are proposed, analysis must be performed to assess whether the solution performance is satisfactory or not, and if satisfactory, to what degree. Unsatisfactory solutions should be revised, improved, or discarded.

A component usually belongs to a mechanical system that comprises several interrelated mechanical components. For this reason, its design should not be considered as an isolated process; the design team will separately synthesize and optimize each component. They will then assemble each component in order to identify possible interferences or inconsistencies. Consequently, a potential revision of some components will be necessary, e.g., the design of an optical system for imaging an object with a camera and a set of lenses first requires attention to the design and selection of the individual components, such as the lenses, pupils, camera sensor, etc. However, these components are not independent. In order to choose a set of lenses for a determined magnification, it is necessary to know the object size as well as the camera sensor dimensions. Information about the camera sensor can be obtained from the camera specifications. Designers can adjust the relative position between lenses and define special focal lengths to improve image aberrations. Nevertheless, commercial lenses are available with certain values of focal lengths that limit the number of solutions. It is clear that a rough estimation is the starting point for a realized solution. An iterative process is performed until a satisfactory proposal is obtained for each component and for the overall design specifications.

During the step "analysis and optimization," mathematical models are built in order to quantify the performance of each proposed solution. A real model (prototype) is tested in the laboratory during the "evaluation" step. As a result, the designer team will determine if the designed component will satisfy the needs.

A presentation is then created to start production of the component. Budynas and Nisbett[1] note that "presentation is a selling job" because the team presents the solution to the administrative, managerial, or supervisory board in an attempt to prove that the solution is better than the existing alternatives.

1.1.2 The influence of working conditions on the mechanical performance of the structure

As stated earlier, the design of a component is primarily performed to satisfy a need. Several parameters are evaluated and collected when defining the problem to find the best possible solutions. One of the most important features under consideration in practical applications is the structural-integrity reliability of the component during its service life—in other words, its ability to withstand service loads effectively and efficiently without failure.[2]

For these reasons, several parameters associated with structural integrity (such as service loads, working temperature and pressure, safety coefficients, etc.) as well as mathematical models should be adequately considered in order to develop a solution closer to reality. Among them, the correct definition of service loads and the suitable selection of the mathematical model can be highlighted when the mechanical performance of the structure is taken into account.

Service loads are those loads, specified or unspecified, that designers should consider as the more probable set of loads to be applied on the component during its service life. When service loads are unknown, they should be estimated before the design step begins. At this point, the informed judgment of the design team is the most important tool for the real estimation of loads. For example, in the case of critical applications (such as airframes), service test data are used to enable an appropriate service-load estimation.[2] The estimation process sometimes involves field testing prototypes.

After establishing the service loads, the mechanical analysis of the component will be conducted by using a mathematical model of the structure. Throughout this model, service loads are translated into stresses or deflections, allowing for the evaluation of the component's structural performance. It is clear that the closer the model is to reality, the more accurately deflections and stresses will be identified. Samuel and Weir[2] state that designers must be absolutely aware that the analysis of results reflects only the behavior of the model, not the behavior of the real component.

As an example of the influence working conditions have on the mechanical performance of a component, consider the design of a pipeline used to transport petroleum or gas. Three loads should be calculated in order to perform the most accurate dimensioning of the pipeline: (a) pressure, (b) pipe weight, and (c) temperature.[3,4]

- The main external load for designing and sizing a pipeline is the internal pressure that enables a safe estimation of the wall thickness of the pipe.
- The pipe weight is usually considered as a distributed load. For above-ground pipes that are placed on supports, this load is used to compute the deformation of the pipe between two consecutive supports due to bending and to size the supports in order to resist the pipe weight. For buried pipelines, the pipe weight influences the friction between the pipe and the ground around it.
- The other load to be considered is the temperature of the fluid being transported; its effect will vary for above-ground and below-ground (buried) pipelines. For the former, variations in the temperature will generate displacements of the structure produced by torsion and bending of the pipe. The correct sizing of the pipe and the definition of the limits of the operation temperature will only depend on the flexibility of the configuration (pipe and supports). Furthermore, the selected wall thickness, capable of resisting the internal pressure of the

Figure 1.2 Pipeline with local buckling created by soil movement (figure courtesy of Pacheco et al.[5]).

fluid being transported, will resist deformations generated by temperature changes. For buried pipes (Fig. 1.2), changes in the fluid temperature are transformed in axial loading. The selected wall thickness for the working internal pressure will sometimes not be sufficient to also resist this kind of loading.

1.2 The Importance of Inspection: Avoiding Accidents

As explained in the previous section, designed components are exposed to specified and unspecified loads. The main task of the design team is to design the component to mechanically withstand these loads during its service life. Nevertheless, the effects of unpredictable loads (as shown in Fig. 1.2), external agents (that generate corrosion), and known service loads (that produce fatigue or wear situations) necessitate inspection to ensure the integrity and safe functioning of the component.

Engineering applications, such as transportation via trains or aircraft, work under regulations and codes that require an operator to maintain and inspect several mechanical parts in accordance with appropriate standards. Other examples includes pipe transmission lines and nuclear plants.

In all cases, standards define maintenance programs with inspection and safety rules intended to keep the mechanical component safely functioning and to anticipate failures and accidents. In addition, the maintenance program should define a maintenance schedule that should be completed promptly and in time for operation of the component. In other words, inspection should be done in a short amount time, avoiding long stops and identifying all possible damages. Inspection techniques should be capable of

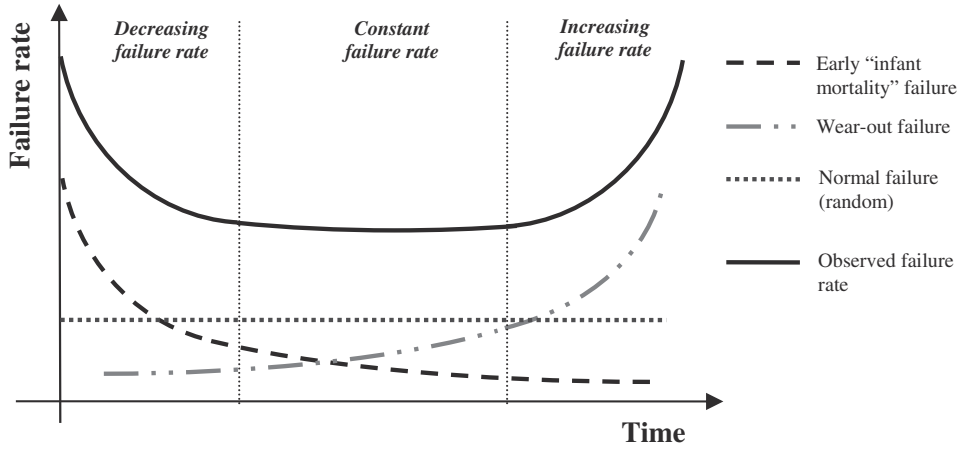

Figure 1.3 "Bathtub" failure-probability curve.

evaluating the whole component and quickly providing the inspector with an assessment of its mechanical integrity.

It is generally accepted that most things follow a "bathtub" failure-probability curve. This curve shows that components have a higher probability of failing early in their service life (when they are new) or later in life as they wear (when they are old). Figure 1.3 shows a generic bathtub curve with identified intervals for the failure rate. This curve does not depict the failure rate of a single item but rather the relative failure rate of an entire population of products over time. "Infant mortality" failures are highly undesirable and always related to defects and blunders: material defects, design blunders, assembly errors, etc. Normal failures are random cases of stresses exceeding strength. Wear-out is related to fatigue, corrosion, etc. (in other words, mechanical, physical, and chemical phenomena produced during the life of the component).

Figure 1.4 shows the effect of inspection and maintenance actions over the bathtub curve. According to this figure, the failure rate can be kept low if correct examination and working control of the component are employed.

In conclusion, the availability of inspection tools allows for the evaluation of the mechanical integrity of a determined component or structure. In addition, the results of the inspection procedures provide tools for selecting corrective actions and avoiding possible accidents.

1.3 Application of Nondestructive Techniques

The primary aim of NDT is to detect and characterize anomalies that can adversely affect the performance of the component under test without impairing its intended service.[6] NDT is indispensable for quality assurance in the industrial production chain as well as for maintenance purposes.[7,8]

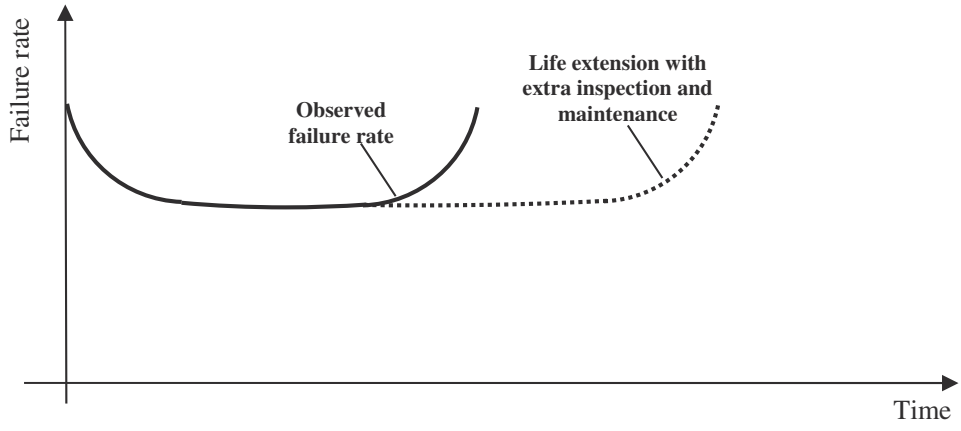

Figure 1.4 Improvement in the performance of a mechanical component.

It is assumed that several anomalies are present in a component from the start of its service life. These anomalies usually deviate component performance from a nominal or desired condition. When this deviation exceeds a tolerated margin, the anomaly is called a defect, and the object is discarded. There are a wide range of defects that can be related to the shape, internal structure, or composition of the material. Some examples of defects found in metallic materials are cracks, inclusions, pores, incomplete regions of welds, and macro- or microstructural degradation. In composite materials, delaminated or deboned regions and fiber fractures are typical examples.

In short, defects can be present in the raw material, or they can be introduced by machining, heat treatment, welding, or incorrect assembly; thus, they exist from the beginning of the service life of the component. It was noted earlier that they can be introduced by specified or unspecified loads that can produce creep, fatigue, stress, corrosion, etc. Examination of the component using quantitative techniques to characterize anomalies, such as defects, stresses, and microstructural degradation, can help avoid damage and loss of structural integrity. In this regard, NDT plays an important role in assessing anomalies by performing the inspection at various stages.

There are several nondestructive techniques based on various physical principles. The iteration between anomalies is usually introduced into the material under study, and the detecting medium (e.g., sound waves, electromagnetic radiation) is used to compare a nondestructively measured or derived physical parameter with quantitative information generated by an anomaly. For example, eddy-current NDT involves measuring the change of the material impedance, which is affected by anomalies such as changes in the microstructure or cracks.

NDT can be used to perform dynamic evaluation for online monitoring. Acoustic emission and infrared thermography belong to this category. The rest of the techniques are used in static evaluations for offline

monitoring: liquid penetrant testing, leak testing, magnetic particle inspection, ultrasonic testing, eddy-current testing, gamma- and x-ray radiography, and, of course, acoustic emission and infrared thermography.

Most NDT techniques have a wide range of applications and capabilities. Selecting the right one for a specific application depends on several factors, such as the minimum size of the defect to be detected, the confidence level of detection, etc. It will also depend on applicability, accessibility, and suitability. Sometimes, only one technique is adequate for a specific application; other times, a combination of two or more techniques, in a complementary way, will provide a more reliable and complete inspection procedure. The available information about the material composition, properties, microstructure, etc., enables the identification of probable defects. This information helps the user select the correct combination or individual application of NDT.

1.4 The Importance of Optical Techniques as Nondestructive Evaluation Tools

Visual inspection was perhaps the first way to "see" the integrity evaluation of a mechanical or civil structure. Even today, it remains an important, widely used nondestructive method, primarily for assessing discontinuities open to the surface of the material. Advances in optics and in digital-image storage and processing have expanded the applications of visual inspection. Optical methods can be considered as an extension of visual inspection because they are used to "observe" the surface of a material under test and to identify possible anomalies not only on the surface but also below it.

Optical techniques are very attractive for NDT due to the lack of contact and relatively high inspection speed. The application of digital techniques allows automatic processing. Consequently, a fast inspection procedure was developed for the evaluation of large areas (e.g., aircraft wings, ship sides, etc.) or a large number of parts, such as automotive components.

Thermography, reflectometry, laser ultrasound (LUS), computed tomography (CT), and speckle techniques are examples of optical techniques applied to NDT of materials. Bergmann and Huke[8] discuss at length the application and measurement of these techniques (except CT) and give examples of their application for NDT. On the other hand, Bauer et al.[9] describe the application of CT as a nondestructive technique; they discuss the accuracy limits for the measurement of volumetric data and the classification of material defects. Moreover, Bergmann and Huke[8] describe the application of shearography.

Shearography belongs to a group of interferometric techniques related to the speckle effect. This effect is a consequence of the iteration between the coherent light of a laser source and the microgeometry of rough surfaces. By using interferometric or noninterferometric approaches, speckle properties can be deterministically related to displacement fields produced on the surface of the specimen under investigation.

Speckle techniques have the advantages cited for optical methods, such as high inspection velocity, digital processing, automation of the data-analysis process, and noncontacting nature. Furthermore, they are adequate for the evaluation of real components without further preparation of the surface to be analyzed. Consequently, speckle techniques are suitable for NDT in industrial applications. Several possibilities and application approaches are discussed in later chapters.

On the other hand, speckle techniques are usually used in laboratories due to interferometric limitations—namely, sensitivity to environmental disturbances and usage of stabilized light sources—and, as a consequence, speckle methods are not completely established for industrial applications. Fortunately, these optical methods can be used in industrial environments when a set of design requirements is fulfilled. These prerequisites are introduced in the next section and further discussed in Chapter 4. Speckle techniques can be used in a robust way not only for NDT assessment of components but also for stress analysis used to evaluate the integrity of mechanical structures.

1.5 Requirements for Field Applications of Optical Techniques

Interferometers using a laser as a light source are frequently encountered in research laboratories. They are usually operated on mechanically isolated optical tables on which the part to be measured is placed. Temperature, humidity, and voltage are frequently well controlled or at least much more stable than in outdoor environments. The laser source usually has high wavelength stability.

In industrial applications, on the other hand, it is notable (in some cases, it is essential) that speckle interferometers are taken to the piece to be measured. Measurements could thus be conducted on a factory's shop floor or in a tropical jungle. The availability of a portable interferometer capable of addressing industrial prerequisites is currently a pressing need; thus, a set of requirements (summarized in Fig. 1.5) can be identified that should be fulfilled in order to perform a successful measurement in an industrial environment:

- **Robust:** The interferometer must be able to successfully work in places with environmental disturbances. It must be tightly clamped to the specimen surface and stiff enough to negate internal and external relative motions produced by mechanical vibrations. It must be able to handle environmental temperature variations as well as voltage oscillations, or it should be battery-operated. It must also have some protection against dust, moisture, and daylight.
- **Flexible:** The interferometer must be adjustable and attachable to a variety of specimen geometries and materials. Relative positioning and alignment requirements show that the device should be handled in a very flexible way. Furthermore, it should be possible to place the

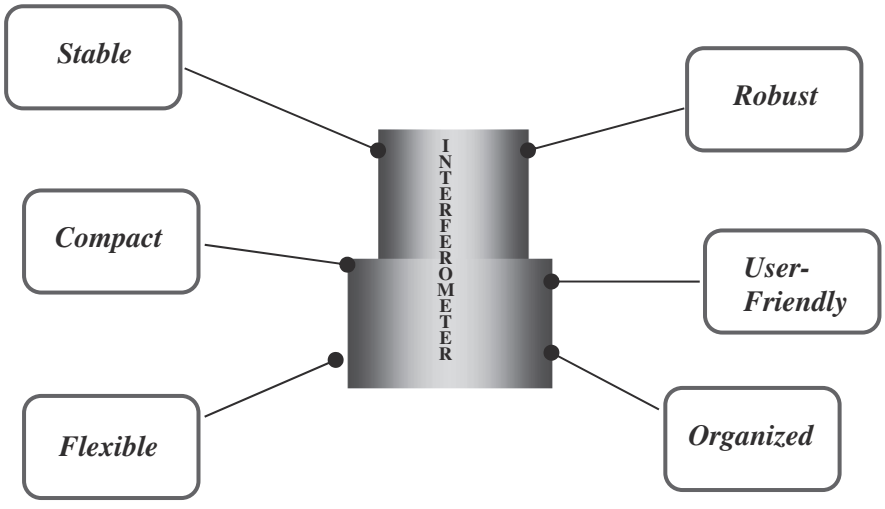

Figure 1.5 Main requirements for a portable interferometer.

measuring device quickly and precisely on a given point of interest on the specimen's surface as well as in several positions.

- **Compact:** The device must be as small as possible. This feature makes the interferometer easier to transport and to fit in small spaces. Compactness is an important factor that guarantees stiffness and robustness against mechanical vibrations and relative motions.
- **Stable:** The interferometer must remain stable during its metrological performance. No temperature or time dependence on the calibration is highly desirable. It must be reliable everywhere and every time.
- **User-Friendly:** Time and comfortable working conditions are often limited for complicated adjustments involving out-of-laboratory applications. Therefore, the interferometer must be easy to install, adjust, and operate. Additionally, it is important to present clear results on-demand for the cases where decisions must be made as soon as possible and close to the part being measured.
- **Organized:** A good system should provide structure for the experimental work. There are two components: guidance and documentation. The former relates to detailing the steps that must be followed; this reduces the risk of a technician forgetting to do something important. The latter component involves organizing the information of all steps, partial data, and notes involved in the experimental work. Ideally, the system should be able to automatically produce a technical report of the measurements.

Diode lasers are natural candidates for use as the light source of portable interferometers. They are compact, cheap, robust, and easy to operate. However, it is well known that their wavelength is not completely stable: it easily varies with temperature and current. On the other hand, wavelength-stabilized He-Ne lasers

are established light sources in laboratories, but they are perhaps too large and fragile to be used in portable systems. Diode lasers with stabilized wavelengths are currently available on the market and appear to be a good choice; however, they are not compact, and they are significantly more expensive than alternative light sources, which would considerably increase the cost and size of a portable interferometer. There is no ideal solution. Rather, several optical solutions can be introduced in order to manage instabilities of the diode-laser wavelength, allowing for the construction of compact devices.

References

1. R. G. Budynas and J. K. Nisbett, *Shigley's Mechanical Engineering Design*, 10th Ed., Mcgraw-Hill, New York (2014).
2. A. Samuel and J. Weir, *Introduction to Engineering Design*, Elsevier, Oxford, UK (1999).
3. M. W. Kellogg Company, *Design of Piping Systems*, 2nd Ed. (1956).
4. S. Crocker, *Piping Handbook*, 7th Ed., McGraw-Hill, New York (2007).
5. A. Pacheco, L. A. dos Santos, M. Moya, M. R. Viotti, and A. Albertazzi, Jr., "Geotechnical and metallurgical aspects of the analysis of buried pipeline stresses due to ground movement," Rio Pipeline Conference & Exposition 2013 (2013).
6. R. Baldev, T. Jayakumar, and B. P. C. Rao, "Non-destructive testing and evaluation for structural integrity," *Sadhana* **20**, 5–38 (1995).
7. *Nondestructive Testing Handbook*, 3rd Ed., Vols. 1–10, P. O. Moore, ed., The American Society for Nondestructive Testing (ASNT), Columbus, OH (1998–2010).
8. R. B. Bergmann and P. Huke, "Advanced methods for optical nondestructive testing," *Optical Imaging and Metrology*, W. Osten and N. Reingand, eds., Wiley-VCH Verlag, Weinheim, Germany (2012).
9. W. Bauer, F. T. Bessler, E. Zabler, and R. B. Bergmann, "Computer tomography for nondestructive testing in the automotive industry," *Proc. SPIE* **5535**, 464–472 (2004) [doi: 10.1117/12.555578].

Chapter 2
Principles of Digital Speckle Pattern Interferometry

2.1 Introduction

The invention of the laser in 1960 allowed for the availability, as never before, of light sources with a high degree of coherence. Researchers working with this kind of light source noticed that a strange phenomenon was produced: when a rough surface is illuminated with laser light, a high-contrast and fine-scale granular pattern is observable.[1] This effect was called the "speckle effect,"[2,3] characterized by the random distribution of scattered light.

Although the random distribution of the optical field can be deterministically modified by displacement or rotation of the diffuser where the light is reflected or transmitted,[1] this effect was considered as a mere nuisance, especially for the first holography techniques developed at that time. In addition to this property, the distribution is also modified by changes in the illumination and observation geometry, in the wavelength of the laser light, and in the refractive index of the medium through which the laser travels. Thus, speckle distribution can be used to measure features of the surface under investigation, such as (a) out-of-plane and in-plane components of the surface deformation of a rough object, (b) 3D surface shapes (by generating contours of the constant depth of an object), and (c) derivatives of the surface displacements.

For these reasons, important research efforts began in the late '60s and early '70s focusing on the development of new methods for high-sensitivity measurements on diffusely reflecting surfaces; these methods can be categorized as speckle interferometry.

Photographic films were initially used to produce images, and the information was processed by optical methods. The need for an optical table to process and reveal negative films was the main drawback to overcome for measurements in industrial environments. Consequently, research was directed to substitute holographic film with TV cameras and to electronically process the video signal. The new method was called electronic speckle pattern

interferometry (ESPI). The first results were discouraging because of the low detector resolution, low sensitivity, and high SNR.

Advances in technology, particularly for high-speed and high-resolution data-acquisition systems, made it possible for engineers to connect a TV camera (later, a CCD or CMOS camera) to a host computer in order to acquire a digital image of the surface illuminated by the laser light. Advances in data transmission enabled a direct link from the cameras to the computer (IEEE-1394 or USB interfaces) to transmit digital images without needing additional elements to digitize the acquired image (such as frame grabbers). At this point, ESPI was renamed DSPI (the word "electronic" was changed to "digital") due to the use of digital images as well as digital processing techniques.

Over the years, the technique has been thoroughly investigated, theoretically as well as experimentally, and it has been improved. For this reason, speckle methods can now be considered as well-established experimental techniques and important tools for performing measurements in laboratory and industrial environments.

2.2 Speckle Principle

Huygens' principle states that "every point on a propagating wavefront serves as the source of spherical secondary wavelets, such that the wavefront at some later time is the envelope of these wavelets."[4] When a surface is illuminated by coherent light from a laser, each point on the surface can be considered as a small source that follows Huygens' principle (shown in Fig. 2.1). In addition, the magnitude of the optical field in each point of the space will be determined by the complex coherent addition of all wavelets coming from each scattering point on the surface.

Additionally, if the laser light is incident on an optically rough surface with height variations greater than the wavelength λ of the light or transmitted through an "optically rough" diffuser having thickness variations

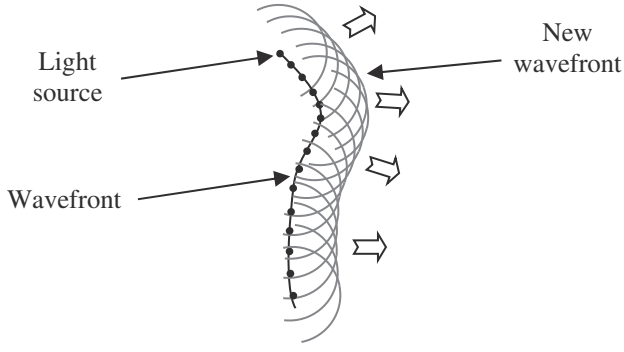

Figure 2.1 Huygens' principle: each point is considered as a light source of the propagating wavelet.

greater than λ, and because the lateral scale of the surface roughness is smaller than the illuminated spot, the incident laser light will be scattered in all directions. The scattered waves will interfere and form an interference pattern consisting of dark and bright spots that are randomly distributed in the space. This light distribution, called speckle distribution, can be seen in Fig. 2.2.

Consider a surface located in a plane xy that is illuminated by a coherent source light with a wavelength λ (see Fig. 2.3). The light field at a specific point $Q(\mathbf{r})$ in a speckle pattern is the sum of a large number of components that represent the light coming from all points located on the scattering

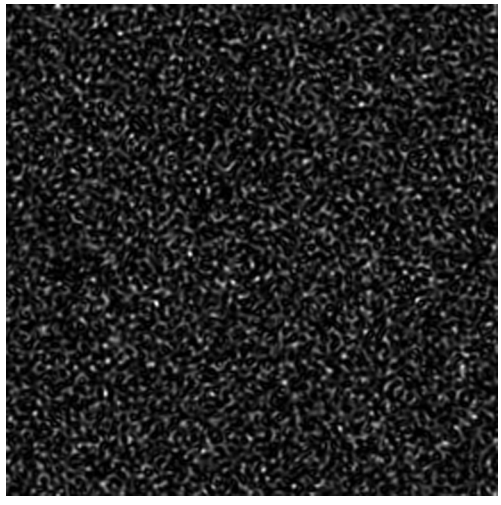

Figure 2.2 Typical simulated speckle distribution.

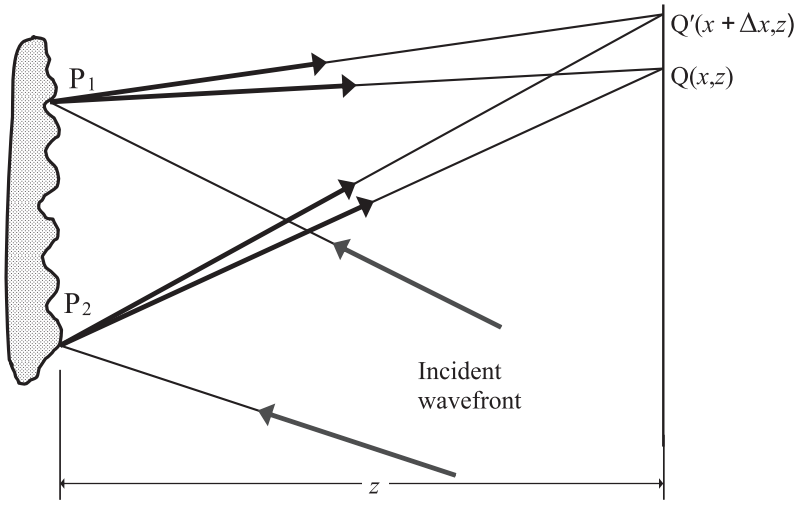

Figure 2.3 Objective speckle.

surface. Therefore, the complex amplitude at each point in a speckle pattern can be written as[2]

$$Q(\mathbf{r}) = k_c \iint_S \omega_i(x,y)\exp\left[\frac{2\pi i}{\lambda} G_e \xi(x,y)\right] dxdy, \tag{2.1}$$

where **r** is the position vector of the point Q, S is the scattering surface, k_c is a constant, ω_i is the complex amplitude of the incident light in (x, y), $\xi(x, y)$ is the surface height at that point, and G_e is a geometric factor associated with the directions of illumination and observation (this factor can be considered as a constant value when the point Q is far away from the scattering surface). Because the height of the roughness of the scattering surface varies randomly with a magnitude equal to or larger than the wavelength of the incident light, the phase terms $G_e\xi(x, y)$ will also change randomly with the same magnitude. For this reason, the random amplitude value of the point Q is described by a set of vectors with random phase (which are added), thus generating a resulting vector with random amplitude. This problem is known as "random walk." The amplitude has a value with ranges from zero and the maximum value, which is determined by the magnitude and the phase of the individual amplitudes. As the observation point moves, the resulting amplitude and intensity will have different values.

Figure 2.4 shows two random walks that produce (a) a large resultant and (b) a small resultant. In both cases, phasor directions and lengths are random, and no single contribution dominates the sum. The vector with the thicker arrow represents the resultant of the complex sum.

In addition to the book written by Goodman,[1] there are other books that readers can consult for further information about speckle statistics and the complex addition of phasors;[5–8] among them, the book edited by J. C. Dainty et al.[5] is the most widely cited, and the treatment found in the chapter written by M. H. Lehmann is an excellent reference for speckle properties applied to DSPI.

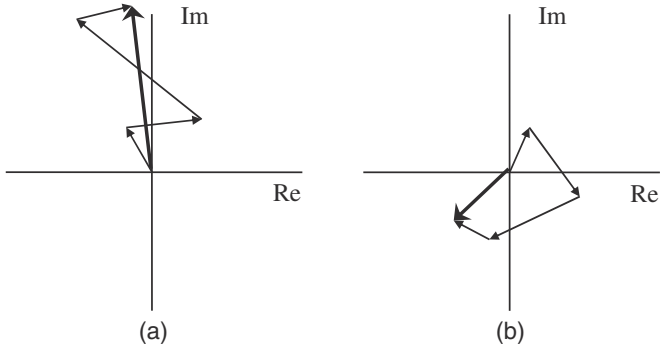

Figure 2.4 Random walks: (a) constructive addition and (b) destructive addition.

2.3 Objective and Subjective Speckle

When an optically rough object is illuminated by a laser, there are two primary geometries where speckles are observed. The first is called an "objective speckle" and corresponds to speckles in a freely propagating field that fills the 3D space in front of the object surface. Conversely, if an image is captured by using an image device, such as a camera or the human eye, speckles will be present in the image plane, and they will be called "subjective speckles."

2.3.1 Objective speckle

In order to find a representative value of the speckle size, a geometric computation can be performed with the help of Fig. 2.3. This figure shows a rough surface illuminated by laser light over an area with a cross-section $l_0 \times l_0$. Points P_1 and P_2 belong to the boundaries of this surface. The optical path difference s_{OPD} from points P_1 and P_2 to $Q(x, y)$ can be expressed by

$$s_{OPD} = P_1Q - P_2Q \approx \frac{xl_0}{z} + \left(\frac{1}{2}\right)\frac{l_0^2}{z}. \tag{2.2}$$

In the same way, the OPD for an adjacent point $Q'(x + \Delta x, y)$ will be described by

$$P_1Q' - P_2Q' \approx \frac{xl_0}{z} + \left(\frac{1}{2}\right)\frac{l_0^2}{z} + \frac{\Delta x l_0}{z}. \tag{2.3}$$

Thus, the relative OPD between Q and Q′ is expressed as

$$\Delta s_{OPD} = \frac{\Delta x l_0}{z}. \tag{2.4}$$

For those points where $\Delta s_{OPD} < \lambda$, the relative phases of the components will have approximately the same value. On the other hand, if

$$\Delta s_{OPD} = \frac{\Delta x l_0}{z} \approx \lambda, \tag{2.5}$$

then the relative phases will be completely different, and the intensity at point Q′ will not be correlated with the intensity at point Q. Consequently, the averaged speckle size d_{sp} will be expressed as

$$d_{sp} = \lambda z / l_0. \tag{2.6}$$

According to Eq. (2.6), it can be seen that the speckle size depends on the size of the illuminated area as well as on the distance between the screen where the scattered light is gathered and the object. In addition, the speckle size does not depend on the optical system used to observe it, which is why this kind of speckle is referred to as objective.

2.3.2 Subjective speckle

Figure 2.5 shows the same conditions observed in Fig. 2.3, but in this case, the scattering surface is imaged by an optical system comprising a lens and a circular aperture.

In accordance with this figure, a point P_1 that belongs to the illuminated surface is imagined on the imaging plane as an intensity distribution centered at point Q (Airy disc). As shown for objective speckle, the light coming from point P_1 has a random phase related to the roughness of the scattering surface. The point Q receives light contributions from other points placed in the neighborhoods of the point P_1. Thus, a set of Airy distributions with random phase will be superposed in Q. In the same way, a new point P_2 can then be considered (see Fig. 2.5) whose diffraction pattern is centered at point Q′. For this particular point, the first minimum intensity value of the Airy distribution will be coincident with point Q, and thus point P_2 will not illuminate point Q. Additionally, points placed farther from point P_1 will also not contribute to illumination at point Q because the secondary maximum intensity values are quite lower than the central maximum, which has a weak contribution.

As a result, the light intensity at point Q is provided by contributions from a circular area of the illuminated object centered at point P_1 whose radius is the distance between points P_1 and P_2. The averaged speckle size d_{sp} corresponds to the radius of the Airy disc:

$$d_{sp} = 1.22\frac{\lambda z_i}{b}, \tag{2.7}$$

where z_i is the distance between the aperture and the imaging plane, and b is the diameter of the aperture. The distance P_1P_2, which is the radius of the

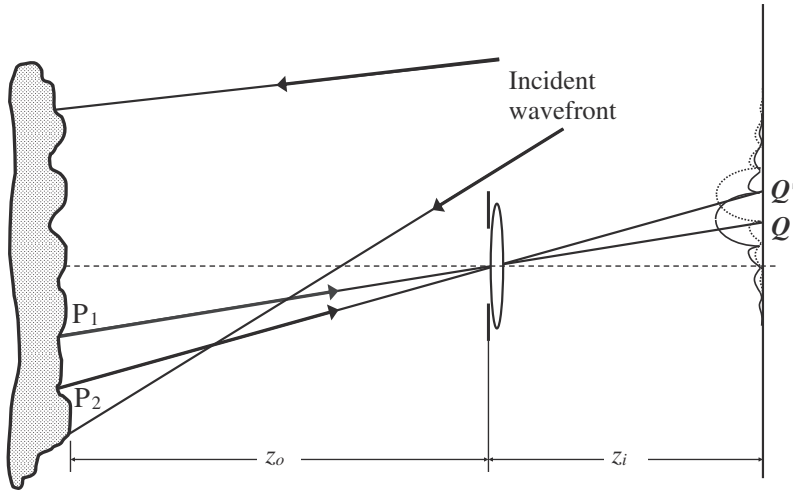

Figure 2.5 Subjective speckle.

scattering element placed on the illuminated surface that scatters the light at point Q, is given by

$$(d_{sp})_{obj} = 1.22\frac{\lambda z_o}{b}, \tag{2.8}$$

where z_o is the distance from the object to the aperture. This area is known as the resolution cell of the optical system, and it corresponds to the speckle grain on the illuminated object.

If M_g is the magnification of the optical system and f is its focal length, the following relations can be deduced:

$$z_i = (1 + M_g)f, \tag{2.9}$$

$$z_o = \frac{z_i}{M_g} = \frac{1 + M_g}{M_g}f. \tag{2.10}$$

By considering $F_b = f/b$ as the numerical aperture of the optical system, the speckle size can be written as

$$d_{sp} = 1.22\lambda F_b(1 + M_g). \tag{2.11}$$

Finally, the size of the speckle on the illuminated object can be expressed as

$$(d_{sp})_{obj} = 1.22\frac{\lambda F_b(1 + M_g)}{M_g}. \tag{2.12}$$

Thus, small subjective speckles are related to large lens apertures. In other words, as the lens aperture increases, smaller subjective speckles are obtained. This can be easily verified by stopping down the eye aperture when looking at a speckle pattern.

A deep analysis of the first-order statistics obtains expressions of probability distributions for the complex amplitude, the phase, and the intensity of the scattered wavefront, as well as for the speckle contrast. Goodman[1] and Kreis[9] provide expressions for these probability distributions. Additionally, second-order statistics describe the variations of the intensity between a point and its neighboring points, thus estimating the averaged speckle size as well as its distribution along the space with a correlation function.[1,8] As a result, Eq. (2.7) is obtained by the use of second-order statistics.

2.4 Speckle Interferometry

As previously indicated, speckle distributions are deterministically modified by displacements of the scattering surface, changes in the illumination and observation geometry, and changes in the wavelength of the light source or in the refractive index of the medium through which light travels.[1]

The approximation of paraxial rays can be used by considering that the area on the diffuser surface, which contributes to the speckle distribution on

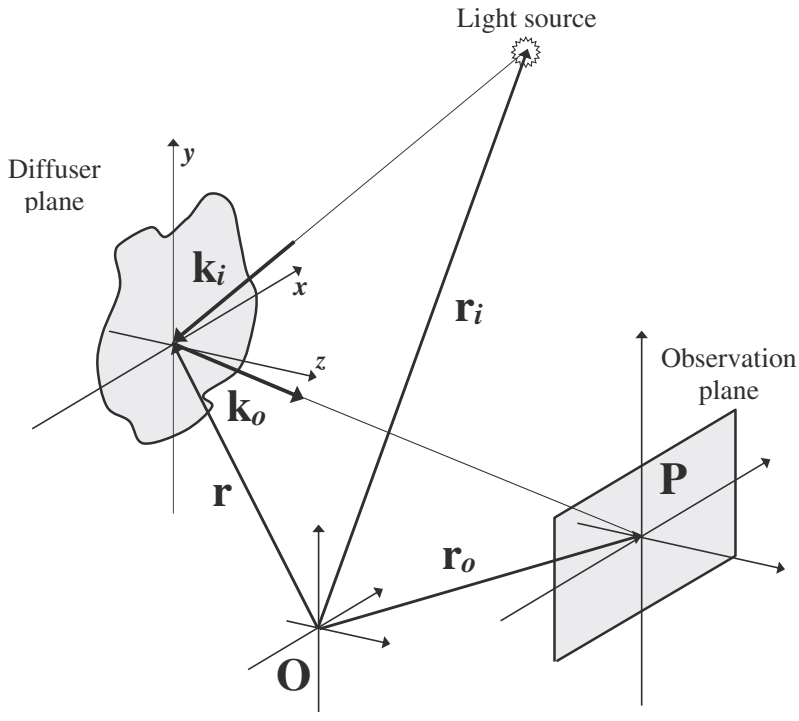

Figure 2.6 Sensitivity of the phase of the speckle.

the observation plane, tends toward a small angle with the observation point or with the axis of the optical system. In this case, the optical phase of the speckle distribution in each point P of the observation plane can be expressed as a function of the optical path traveled by the light from the light source in the following way (see Fig. 2.6):

$$\varphi = \varphi_s + \psi = \varphi_s + \psi_i + \mathbf{k}_i \cdot (\mathbf{r} - \mathbf{r}_i) + \mathbf{k}_o \cdot (\mathbf{r}_o - \mathbf{r}). \tag{2.13}$$

The phase φ of the speckle is formed by a random component φ_s and a deterministic component ψ. The magnitude of φ_s for each point of the speckle distribution depends on the roughness of the scattering surface along the area that contributes to the speckle in that point.

The deterministic part consists of (a) the initial optical phase ψ_i (at the output of the light source), (b) the phase changes produced along the path between the light source and the scattering surface $[\mathbf{k}_i \cdot (\mathbf{r} - \mathbf{r}_i)]$, and (c) the phase changes that occurred along the path between the diffuser and the observation point $[\mathbf{k}_o \cdot (\mathbf{r}_o - \mathbf{r})]$. For simplicity, the refractive index was omitted in the equations, but it is important to note that variations in this index will affect the phase changes. The vector $\mathbf{r}$ is the position vector, which is constant for all of the points on the diffuser due to the paraxial assumption. Additionally, $\mathbf{r}_i$ indicates the curvature center of the incident wavefront, $\mathbf{r}_o$ is the position vector of the observation point, and $\mathbf{k}_i$ and $\mathbf{k}_o$

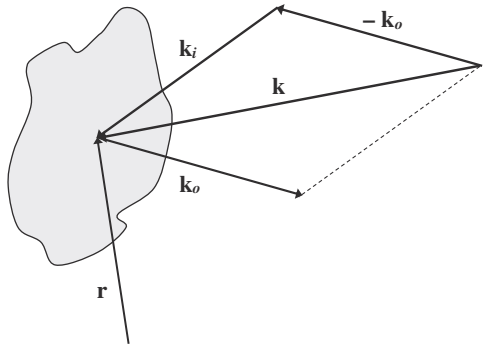

Figure 2.7 Sensitivity vector.

are the wave-propagation vectors corresponding to the illumination and observation directions, respectively:

$$\begin{aligned}\mathbf{k}_i &= \frac{2\pi}{\lambda}\hat{\mathbf{n}}_i,\\ \mathbf{k}_o &= \frac{2\pi}{\lambda}\hat{\mathbf{n}}_o,\end{aligned} \tag{2.14}$$

where $\hat{\mathbf{n}}_o$ and $\hat{\mathbf{n}}_i$ are the unitary vectors.

The sensitivity vector (see Fig. 2.7) is defined as

$$\mathbf{k} = \mathbf{k}_i - \mathbf{k}_o. \tag{2.15}$$

This vector indicates the direction of the diffuser that produces the maximum variation of phase at the point P of the observation plane.

Equation (2.13) can be rewritten as

$$\varphi = \varphi_s + \psi_i + \mathbf{k}_o \cdot \mathbf{r}_o - \mathbf{k}_i \cdot \mathbf{r}_i + (\mathbf{k}_i - \mathbf{k}_o) \cdot \mathbf{r}, \tag{2.16}$$

$$\varphi = \varphi_s + \psi' + \mathbf{k} \cdot \mathbf{r}, \tag{2.17}$$

with

$$\psi' = \psi_i + \mathbf{k}_o \cdot \mathbf{r}_o - \mathbf{k}_i \cdot \mathbf{r}_i. \tag{2.18}$$

When the diffuser is displaced, or when the illumination and observation direction are changed, the phase of the speckle experiences a variation that can be expressed as

$$\Delta\varphi = \Delta\varphi_s + \Delta\psi' + \Delta(\mathbf{k} \cdot \mathbf{r}), \tag{2.19}$$

where

$$\Delta(\mathbf{k} \cdot \mathbf{r}) = [(\mathbf{k} + \Delta\mathbf{k}) \cdot (\mathbf{r} + \Delta\mathbf{r})] - (\mathbf{k} \cdot \mathbf{r}) = \Delta\mathbf{k} \cdot \mathbf{r} + \mathbf{k} \cdot \Delta\mathbf{r} + \Delta\mathbf{k} \cdot \Delta\mathbf{r}. \tag{2.20}$$

In this way,

$$\Delta\varphi = \Delta\varphi_s + \Delta\psi' + \Delta\mathbf{k} \cdot \mathbf{r} + \mathbf{k} \cdot \Delta\mathbf{r} + \Delta\mathbf{k} \cdot \Delta\mathbf{r}, \tag{2.21}$$

where

$$\Delta\psi' = \Delta\psi_i + \Delta(\mathbf{k}_o \cdot \mathbf{r}_o) - \Delta(\mathbf{k}_i \cdot \mathbf{r}_i). \tag{2.22}$$

The term $\mathbf{k} \cdot \Delta\mathbf{r}$ represents the increment in the optical phase generated by the diffuser movement. On the other hand, $\Delta\psi' + \Delta\mathbf{k} \cdot \mathbf{r}$ is produced by changes in the geometry of the illumination and observation directions in the wavelength, in the refractive index, and in the initial phase of the source. Finally, $\Delta\mathbf{k} \cdot \Delta\mathbf{r}$ denotes the combining effect and the variation of both parameters. If the microstructure related to the roughness of the scattering surface is kept relatively invariable, the random component φ_s will be constant, leading to $\Delta\varphi_s = 0$. All changes in the phase distribution will only be produced by the deterministic component; moreover, the diffuser usually moves without any changes in the sensitivity vector. Thus, changes in $\Delta\mathbf{k} \cdot \Delta\mathbf{r}$ are negligible, having the following simplification:

$$\Delta\varphi \approx \Delta\psi = \Delta\psi' + \Delta\mathbf{k} \cdot \mathbf{r} + \mathbf{k} \cdot \Delta\mathbf{r}. \tag{2.23}$$

This expression can be used to describe all geometries and working conditions, and it can model all interferometric techniques based on speckle distributions. For example, to measure displacements, the experiment will be designed to cancel all terms of Eq. (2.23), except for the term with $\Delta\mathbf{r}$. This is achieved when the illumination and observation directions are kept constant, as well as the refractive index. Consequently, changes in the phase of the speckle will only be reflected in the diffuser displacements along the direction of the sensitivity vector:

$$\Delta\varphi \approx \Delta\psi = \mathbf{k} \cdot \Delta\mathbf{r}. \tag{2.24}$$

The intensity distribution of the speckle does not change when small displacements are introduced in the diffuser. However, the phase distribution of the speckle experiments changes, which can be evoked by interfering the original speckle distribution with a reference beam from the same light source and with the same polarization direction. The reference beam can be either uniform or speckled.

Hecht[4] shows that the intensity of the resultant beam after interfering two beams with intensities I_1 and I_2 can be written as

$$I = I_1 + I_2 + 2\sqrt{I_1 I_2}\cos(\varphi_1 - \varphi_2), \tag{2.25}$$

where φ_1 and φ_2 are the phases of the interfering wavefronts. Note that I, I_1, I_2, φ_1, and φ_2 are functions of the position $\mathbf{r}(x, y, z)$ and the time τ. Equation (2.25) can be expressed as[10]

$$I = I_0(1 + V\cos\phi), \tag{2.26}$$

with the averaged intensity (background intensity)

$$I_0 = I_1 + I_2 \tag{2.27}$$

and the fringe visibility or contrast

$$V = \frac{2\sqrt{I_1 I_2}}{I_1 + I_2}. \tag{2.28}$$

The relative phase between the interfering beams is computed as

$$\phi = \varphi_1 - \varphi_2. \tag{2.29}$$

The previous equations are valid for classic interferometry as well as for interferometry with speckle distributions. For the latter, Eq. (2.26) is a random distribution sensitive to changes in the optical phase and is called a speckled interferogram, or specklegram.

When the interfering optical fields are speckle distributions, the statistical properties of the interferogram are similar to the original distributions. A scale factor should be added due to the increase of the intensity generated by the superposition of two wavefronts.[1,11,12] On the other hand, when the speckle distribution interferes with a uniform optical field, the statistical properties are different from the original distribution—the contrast decreases, and the averaged speckle size increases.[1]

The phase in Eq. (2.26) carries information relative to the configuration of the interferometer. Regardless of the displacement of the diffuser, any variation in the sensitivity vectors of each beam, change in the wavelength of the light, or variation in the refractive index will produce changes in the relative phase ϕ.

In order to generalize techniques that use two speckle distributions of one distribution and a uniform wavefront as reference beam, the relative phase of the speckle can be expressed by using Eqs. (2.17) and (2.26):

$$\phi = \varphi_s - \psi_r + \psi_o, \tag{2.30}$$

where

$$\varphi_s = (\varphi_{s1} - \varphi_{s2}), \tag{2.31}$$

$$\psi_r = (\psi'_1 - \psi'_2), \tag{2.32}$$

and

$$\psi_o = (\mathbf{k}_1 \cdot \mathbf{r}_1 - \mathbf{k}_2 \cdot \mathbf{r}_2). \tag{2.33}$$

The phase labeled φ_s belongs to the random components of the interfering phases and contributes to the speckle noise. For surfaces whose roughness exceeds the wavelength of the light, φ_s has a spatial distribution in the interval $(-\pi, \pi)$.[1] This noise confers the granular aspect to the interferogram. The phase ψ_r is deliberately introduced by changing the initial phase of both beams or by changing the travel distances or direction of the illumination and observation paths [see Eq. (2.18)]. The object phase ψ_o depends on the sensitivity vectors of the interfering beams and on the instantaneous configuration of the scattering surface (position at the space). This is the term with the information that is used to compute the deformation of the diffuser.

The terms in Eq. (2.30) are usually functions of the coordinates $\mathbf{x}(x, y)$ on the observation plane and of the time τ. However, experimental

interferometers are designed to consider two simplifying hypotheses. The first one considers that the speckle distribution is neither decorrelated during the acquisition nor significantly displaced along a transversal direction during the measurement. Thus, φ_s, I_0, and V can be considered independent of the time. The second assumption takes into account that the illumination and observation directions are the same for the whole interferogram. In this way, $\mathbf{k}_1$, $\mathbf{k}_2$, and ψ_r are only dependent on the time; in other words, beams incident on the diffuser as well as the observation beam are collimated.[9] In practice, collimated beams imply the use of large optical elements, which is very expensive. For this reason, diverging beams are used with expander lenses, placed far from the object, that have as large a curvature radius as possible. Accounting for these considerations,

$$\phi(\mathbf{x},\tau) = \varphi_s(\mathbf{x}) + \psi_r(\tau) + \psi_o(\mathbf{x},\tau), \tag{2.34}$$

where

$$\psi_o(\mathbf{x},\tau) = \mathbf{k}_1(\tau)\cdot\mathbf{r}_1(\mathbf{x},\tau) - \mathbf{k}_2(\tau)\cdot\mathbf{r}_2(\mathbf{x},\tau). \tag{2.35}$$

The intensity of the speckle interferogram corresponding to a determined state of the object can thus be written from Eq. (2.26) as follows:

$$I(\mathbf{x},\tau) = I_0(\mathbf{x})\{1 + V(\mathbf{x})\cos[\varphi_s(\mathbf{x}) - \psi_r(\tau) + \psi_o(\mathbf{x},\tau)]\}. \tag{2.36}$$

For speckle interferometry (or any other interferometry technique), variations in the phase difference between the beams allow for the measurement of the displacements that occurred in the diffuser. The change in the phase difference is

$$\Delta\phi = \Delta\varphi_s + \Delta\psi_r + \Delta\psi_o. \tag{2.37}$$

If the speckle is not decorrelated between both acquisitions ($\Delta\varphi_s = 0$), and if the phase difference of the reference $\Delta\psi_r$ is known and introduced deliberately, then the variation of the intensity in Eq. (2.36) will reveal only changes in the object phase $\Delta\psi_o$. From Eq. (2.23), it is possible to see that changes in the phase are related to displacements $\Delta\mathbf{r}$ of the scattering surface only if the sensitivity vectors are constant. The direction of the sensitivity vector will determine the sensitivity direction of the interferometer, but these principles are discussed in Chapter 3.

To separate the object phase ψ_o from the phase difference ϕ, two different states of the object should be compared. Note that a displacement field was introduced in the diffuser between both states without speckle decorrelation; consequently, $\Delta\varphi_s$ is zeroed.

The following paragraphs demonstrate the different methods used to codify the variation of the OPD $\Delta\psi_o$ between two object stages. Equation (2.36) describes the intensity distribution of a speckle distribution for a particular state of the observed object. By considering

$$I_1(\mathbf{x},\tau_1) = I_0\{1 + V(\mathbf{x})\cos[\phi(\mathbf{x},\tau_1)]\} \tag{2.38}$$

and

$$I_2(\mathbf{x},\tau_2) = I_0\{1 + V(\mathbf{x})\cos[\phi(\mathbf{x},\tau_2)]\} \tag{2.39}$$

as the intensity distributions corresponding to the observed states before and after the deformation of the object, respectively, where

$$\phi(\mathbf{x},\tau_1) = \varphi_1 - \varphi_2, \quad \phi(\mathbf{x},\tau_2) = \varphi_1 + \Delta\varphi - \varphi_2\,; \tag{2.40}$$

then $\Delta\varphi$ is the variation of the phase of the speckle in the object beam produced by the displacements of the diffuser.

If $I_{12} = [I_1 - I_2]^2$ is evaluated and the following trigonometric identities are accounted for:

$$\cos(a) - \cos(b) = 2\sin\left(\frac{a+b}{2}\right)\sin\left(\frac{b-a}{2}\right), \tag{2.41}$$

$$\sin^2(a) = \left(\frac{1}{2}\right) - \left(\frac{1}{2}\right)\cos(2a), \tag{2.42}$$

then

$$I_{12} = I_{0f}[1 + V_f\cos(\Delta\phi)], \tag{2.43}$$

where

$$\Delta\phi = \phi(\mathbf{x},\tau_1) - \phi(\mathbf{x},\tau_2), \tag{2.44}$$

and

$$I_{0f} = {I_0}^2 V^2\{1 - \cos[\phi(\mathbf{x},t_1) + \phi(\mathbf{x},t_2)]\}, V_f = -1, \tag{2.45}$$

where $\Delta\phi$ is the variation in the phase difference produced by the change in the phase of the speckle of the object beam.

By considering Eq. (2.28), Eq. (2.43) can be expressed as

$$I_{12} = I_{0f}[1 + V_f\cos(\Delta\psi_o - \Delta\psi_r)], \tag{2.46}$$

where the random phase φ_s presented in the I_{0f} term causes the granular aspect of I_{12} and has components with high spatial frequencies. The cosine term produces modulation fringes with low frequency and codifies phase differences between t_1 and t_2. If the phase of the reference beam is known, then this term will only depend on the changes of the object beam generated by the deformation. Thus, the subtraction of the specklegrams permits codifying the intensity variations in the object phase. This modulation in the intensity is referred to as "correlation fringes," depicted in Fig. 2.8. It is important to note the similarity between Eqs. (2.26) and (2.43), which describe the intensity distribution of a specklegram and of correlation fringes, respectively. In the former, the visibility and intensity are related to the speckle, whereas in the latter, they are related to correlation fringes.

Correlation fringes can be interpreted as links between points with equal displacements along the sensitivity direction. The points where $\Delta\psi_o = 2n\pi$ ($n = 0, 1, 2, \ldots$) have identical speckle distributions, and the intensity I_{12} is

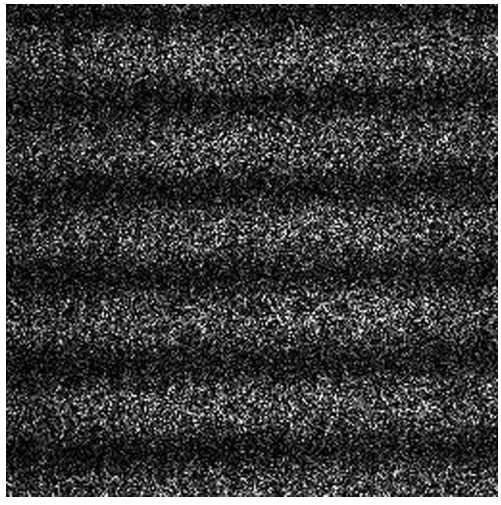

Figure 2.8 Correlation fringes.

null, producing dark fringes (horizontal black fringes in Fig. 2.8). Conversely, the points where $\Delta\psi_o = (2n + 1)\pi$ have bright fringes (horizontal white fringes in Fig. 2.8). Note how the figure also illustrates the granularity conferred by the I_{0f} term. Table 2.1 compares the nomenclatures used in Eqs. (2.26) and (2.43).

In practice, it is easier to compute $|I_1 - I_2|$ than $[I_1 - I_2]^2$, and a distribution with a slightly different form than that represented by Eq. (2.46) is obtained, but principally in high-order harmonics. Because the evaluation of the phase from the correlation fringes involves a noise-reduction step that eliminates these terms, the phase $\Delta\psi_o$ is equivalent.

In closing, the direct visualization of correlation fringes is adequate for the qualitative analysis of several problems. However, it is frequently desirable to obtain a quantitative value of $\Delta\phi$, which is discussed in the following section.

Table 2.1 Comparison of nomenclatures used in Eqs. (2.26) and (2.43).

$I = I_0(1 + V\cos\phi)$		$I_{12} = I_{0f}[1 + V_f\cos(\Delta\phi)]$	
Symbol	**Description**	**Symbol**	**Description**
I	The intensity of the resultant beam after interfering two beams.	I_{12}	The intensity of the correlation function.
I_0	A medium value of the resultant intensity.	I_{0f}	A medium value of the correlation intensity.
V	A quantity that modulates the medium intensity I_0.	V_f	The visibility (modulation) of the correlation fringes.
ϕ	The phase variation between both interfering beams.	$\Delta\phi$	The phase variation in the phase of the object beam.

2.5 Phase Shifting as a Quantitative Tool

Two components can be separated in a system that uses DSPI: (a) the optical part composed by the interferometer, and (b) the electronic part that acquires the interferogram and generates the correlation fringes. In order to quantitatively evaluate the phase distribution, these fringes are numerically processed, as shown in Fig. 2.9. The figure shows two steps involved in the formation and analysis of the interferogram. The first step is called the acquisition stage, where interferograms are acquired before and after the introduction of the perturbation into the object. Consequently, speckle distributions $I_1(\mathbf{x}, \tau_1)$ and $I_2(\mathbf{x}, \tau_2)$ are available at this stage, and they should be processed to obtain the variation in the phase difference generated by the perturbation.

The next step is called the processing step, and it enables the analysis and processing of the acquired interferograms. This stage can be split in two parts: (a) evaluation of the phase difference $\Delta\phi$ and (b) conversion of the phase values to physical parameters that describe the perturbation (e.g., stresses, strains, etc.).

The previous section showed that correlation fringes have the following intensity distribution:

$$\begin{aligned} I_{12}(\mathbf{x},\tau) &= I_{0f}(\mathbf{x},\tau)\{1 + V_f(\mathbf{x},\tau)\cos[\Delta\phi(\mathbf{x},\tau)]\} \\ &= I_{0f}(\mathbf{x},\tau) + I_M(\mathbf{x},\tau)\cos[\Delta\phi(\mathbf{x},\tau)], \end{aligned} \tag{2.47}$$

where I_{0f} is the averaged intensity, V_f is the fringe visibility, I_M is the modulation intensity, and $\Delta\phi$ is the variation in the phase difference.

To extract the value of $\Delta\phi$ from Eq. (2.47), it must be inverted. Because the cosine function is odd and has a period of 2π,

$$\cos\Delta\phi = \cos(\mathrm{sig}\Delta\phi + 2\pi Q_{mult}) \quad \mathrm{sig} \in \{-1, 1\} \quad Q_{mult} \in \mathbf{Z}, \tag{2.48}$$

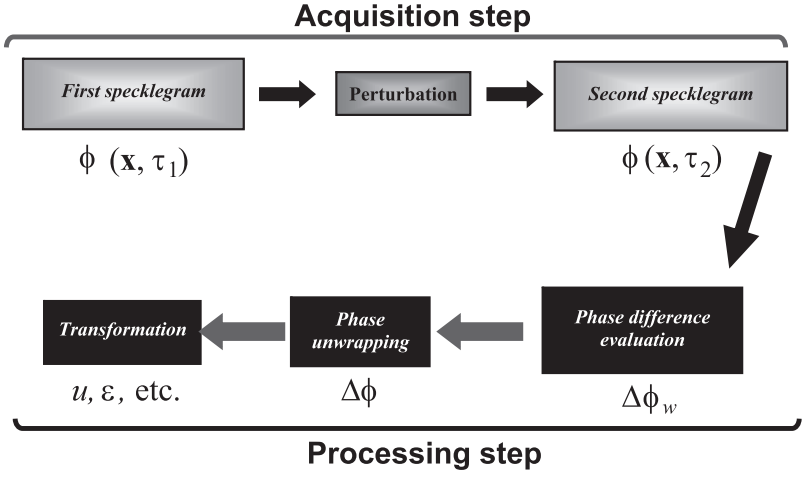

Figure 2.9 Steps to analyze DSPI interferograms.

where the phase computed from only one I_{12} distribution will have an undetermined sign (sig) and a multiple factor Q_{mult} of 2π.

There are several methods for avoiding sign ambiguity without previous assumptions. The most prevalent method involves the addition of a known phase function, called a phase ramp, which is linear in time and position. When this function is used, intensity distributions are acquired in discrete time intervals in a method known as "temporal phase shifting."[13] When a linear carrier function is used in the space, only one distribution is acquired because continuous changes in the phase between adjacent points are introduced. In this case, all data for the evaluation of the phase are acquired in one unique interferogram in a method known as "spatial phase shifting."[9,14] This method is a good alternative to temporal phase shifting when dynamic events are being investigated or when vibration is a problem. Kujawinska[14] and Takeda[15] provide useful reviews of this subject area. Most examples and solutions in this book use temporal phase shifting to quantify the phase. For this reason, a more detailed explanation will be performed for temporal algorithms.

Interferograms are currently acquired by digital cameras that usually produce 8-bit images (256 gray levels, where 0 is the black level, and 255 is the white level). There are also cameras with 10 or 12 bits to work with low-modulation signals. The digitization of N_t successive images with a sensor of $N_n \times N_m$ pixels gives a discrete 3D intensity distribution $I(n, m, t)$, where $n = 0, 1, 2, \ldots, N_n - 1$, $m = 0, 1, 2, \ldots, N_m - 1$, and $t = 0, 1, 2, \ldots, N_t - 1$. Thus, Eq. (2.25) can be written as

$$I(n,m,t) = I_0(n,m,t)[1 + V(n,m,t)\cos\phi(n,m,t)]. \tag{2.49}$$

The nondimensional coordinates of the discrete image (n, m, t) are related to the dimensional and continuous coordinates $(\mathbf{x}, \tau)$ of the image plane, where $\mathbf{x} = (x, y)$ using the following relations:

$$x = ndx, \quad y = mdy, \quad \tau = td\tau, \tag{2.50}$$

where dx and dy are the distances between adjacent pixels in the x and y directions, respectively, and $d\tau$ is the time interval between successive registrations.

For a speckle interferometer, terms $I(n, m, t)$, $V(n, m, t)$, and $\phi(n, m, t)$ are functions with fast variations in n and m due to the spatial structure of the speckle, but they slowly vary with the time t. This condition implies that fractional changes $(\delta I_o)/I_o$, $(\delta V)/V$, and $(\delta\phi)/2\pi$ are less than the unit during the interval time between successive interferograms. If these conditions are satisfied, temporal phase shifting can be used, and it is usually introduced in the object beam. In this way, a certain number of interferograms N_t are acquired with a relative phase shift α_t; thus, Eq. (2.49) can be rewritten as

$$I(n,m,t) = I_0(n,m)\{1 + V(n,m)\cos[\phi(n,m) + \alpha_t]\}. \tag{2.51}$$

This method involves independent data analysis for each pixel. For this reason, the dependence on pixel coordinates (n, m) will be omitted from Eq. (2.52).

There are currently a wide variety of algorithms that use three or more images and a phase shift α_t. For all cases, the phase value in a determined point is obtained by using the intensity at that point of the N_t interferograms; consequently, these methods are also considered as local methods.

The more common types of these algorithms use known values of α_t that are equal for all points in each interferogram.[13,16] In accordance with Eq. (2.51), there are three unknowns (I_0, V, ϕ), and at least three measurements are required to determine the phase values.

One of the simplest cases, called the "four-frame algorithm," is obtained by considering the case of four images shifted by $\alpha_t = \pi/2$. By substituting $t = 0$, 1, 2, and 3 into Eq. (2.51), the following set of equations is obtained:[10,17]

$$\begin{aligned} I(0) &= I_0 + I_M \cos\phi; \\ I(1) &= I_0 + I_M \cos\left(\phi + \pi/2\right) = I_0 - I_M \sin\phi; \\ I(2) &= I_0 + I_M \cos(\phi + \pi) = I_0 - I_M \cos\phi; \\ I(3) &= I_0 + I_M \cos\left(\phi + 3\pi/2\right) = I_0 + I_M \sin\phi. \end{aligned} \tag{2.52}$$

By rearranging this set of equations, the value of I_M and ϕ_w can be obtained:

$$\phi_w = \tan^{-1}\left[\frac{I(3) - I(1)}{I(0) - I(2)}\right], \tag{2.53}$$

$$I_M = \frac{\sqrt{[I(3) - I(1)]^2 + [I(0) - I(2)]^2}}{2}. \tag{2.54}$$

The phase value calculated by Eq. (2.53) lies in the range $(-\pi, \pi)$, provided that a full four-quadrant arctangent function is used. (In some programing languages, it is called *atan2*). In practice, the main drawback of this algorithm is its susceptibility to errors due to miscalibration of the phase-shifting device. A more detailed explanation about errors can be found elsewhere.[10,13,14]

The five-frame algorithm was proposed by Schwider et al.[18] as a development of the four-frame algorithm.[10] In this case, five interferograms of $\alpha_t = \pi/2$ are acquired, and the phase and modulation can be computed as follows:[10]

$$\phi_w = \tan^{-1}\left\{\frac{2[I(3) - I(1)]}{I(4) + I(0) - 2I(2)}\right\}, \tag{2.55}$$

$$I_M = \frac{\sqrt{4[I(3) - I(1)]^2 + [I(4) + I(0) - 2I(2)]^2}}{4}. \tag{2.56}$$

Huntley[10] shows that this algorithm is less susceptible to miscalibration errors of the phase shifter than the four-frame algorithm.

An alternative method to avoid miscalibration errors of the phase shifter was introduced by Carré.[19] This method considers α_t as a further unknown. If the phase shifts between successive images are all equal, Eq. (2.51) will have four unknowns. The following phase shifts are traditionally selected:

$$\alpha_t = \frac{2t-3}{2}\alpha, \quad t = 0,\ 1,\ 2,\ 3\,. \tag{2.57}$$

The following four intensities are thus acquired:

$$\begin{aligned} I(0) &= I_0 + I_M \cos\left(\phi - \frac{3\alpha}{2}\right), \\ I(1) &= I_0 + I_M \cos\left(\phi - \frac{\alpha}{2}\right), \\ I(2) &= I_0 + I_M \cos\left(\phi + \frac{\alpha}{2}\right), \\ I(3) &= I_0 + I_M \cos\left(\phi + \frac{3\alpha}{2}\right). \end{aligned} \tag{2.58}$$

From this set of equations, the phase difference can be computed as[10,19]

$$\phi_w + \frac{3\alpha}{2} = \tan^{-1}\left[\frac{\mathrm{sgn}\sqrt{[I(0)-I(3)+I(1)-I(2)]\{3[I(1)-I(2)]-I(0)+I(3)\}}}{I(1)+I(2)-I(0)-I(3)}\right], \tag{2.59}$$

where ϕ_w is the wrapped phase, and sgn = sign$[I(1) - I(2)]$. The sign function introduces the correct sign of the phase values for the four quadrants. The term $(3\alpha)/2$ on the left side is due to the choice of the carrier origin. It disappears after the phase difference values are calculated.

The phase shifter most often used in speckle interferometers is a piezoelectric translator (PZT) because of its low cost and drive requirements. A PZT is moved a specified fraction of microns by a low voltage, and it can be controlled by an analog-to-digital converter (ADC) plugged into a computer used to produce the interferograms. The PZT is usually joined to the mirror reflecting the object beam (reference) before its expansion. In some applications, PZT-driven glass wedges are used as an alternative to mirrors in order to avoid unwanted lateral translation tilting of the beam.[20] Optical fibers wrapped around PZT cylinders can be used to construct compact, fiber-based phase-shifting interferometers.[21,22] For dynamic problems, Pockels cells can be used as phase modulators because they have a response time in nanoseconds.[23,24] Other possible solutions to introduce phase shifts involve rotating a half-wave plate, moving a diffraction grating, or tilting a glass plate.[25] Figure 2.10 illustrates these solutions.

The wrapped phase computed by Eqs. (2.53), (2.55), and (2.59) has the initial random phase $\phi(n, m, 0) = \varphi_s(n, m, 0) - \psi_r(n, m, 0) + \psi_o(n, m, 0)$.

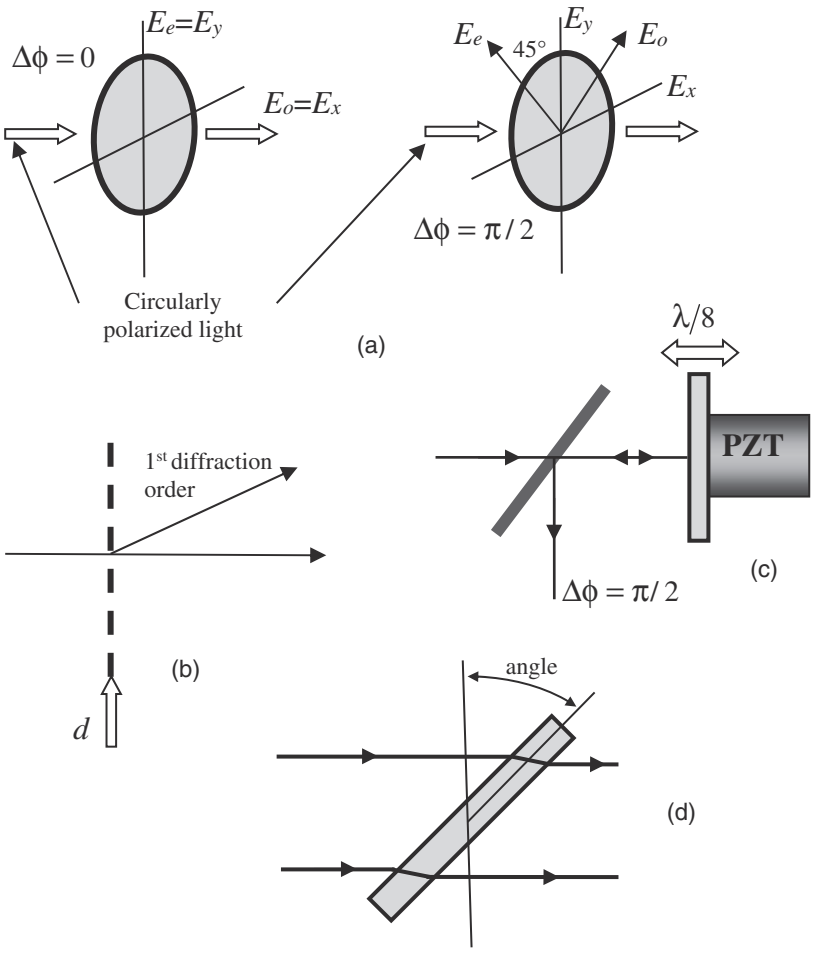

Figure 2.10 Phase shifting by (a) rotating a half-wave plate, (b) moving a diffraction grating, (c) moving a mirror with a PZT, and (d) tilting a glass plate.

The difference between the phase distributions registered at t_1 and t_2 can eliminate φ_s and ψ_r. This condition is true if there is neither speckle decorrelation [$\varphi_s(n, m, t_1) = \varphi_s(n, m, t_2)$] nor changes in the setup of the interferometer [$\psi_r(n, m, t_1) = \psi_r(n, m, t_2)$]. Thus, the phase distribution generated by the deformation of the diffuser can be expressed as

$$\Delta\phi_{ww}(n, m, t_1, t_2) = \phi_w(n, m, t_2) - \phi_w(n, m, t_1). \tag{2.60}$$

Because values of ϕ_w range between $-\pi$ and π, the phase $\Delta\phi_{ww}$ lies in the interval $[-2\pi, 2\pi]$. To display the phase, it is wrapped back on the range $[-\pi, \pi]$ by using the wrapping operator Υ:

$$\Upsilon(\phi) = \phi - 2\pi\mathrm{NINT}(\phi/2\pi), \tag{2.61}$$

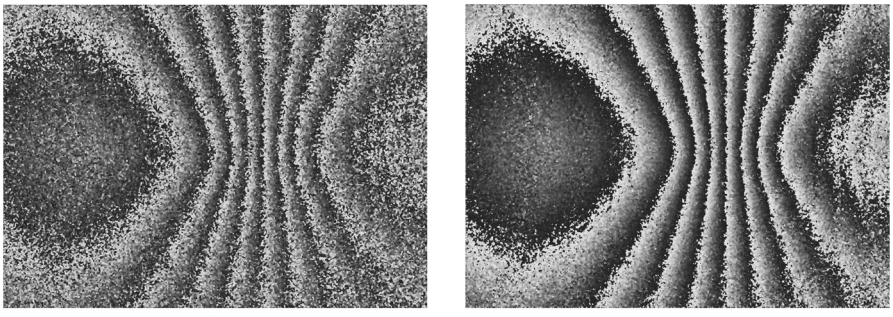

Figure 2.11 Phase maps: (a) phase-of-difference approach and (b) difference-of-phases approach. Images reprinted from Gundlach et al.[26] with permission.

where NINT denotes rounding to the nearest integer. The phase difference in the 2π module results in

$$\Delta\phi_w(n, m, t_1, t_2) = \Upsilon[\Delta\phi_{ww}(n, m, t_1, t_2)]. \tag{2.62}$$

This method is called "difference of phases." There is another alternative method, called "phase of differences," which is based on the formation of correlation fringes. In this method, one image is acquired before the deformation, and N_t images are acquired after (or vice versa). The initial image is subtracted from the N_t images, and a set of N_t phase-shifted correlation fringes is obtained. After this, they are filtered and can be analyzed by a standard phase-shifting algorithm. This technique is advantageous for dynamic applications because the unique image can be acquired during the transient event, and the set of N_t images can be acquired with the object at rest. The main disadvantage of this method is the reduction in the quality of the computed phase maps. For example, Figs. 2.11(a) and (b) show wrapped-phase maps obtained with a speckle-shearing interferometer and presented by Huntley[10] and Gundlach et al.[26] Figure 2.11(a) was obtained by using the phase-of-differences approach, and Fig. 2.11(b) was obtained by the difference of phases. Both cases used the same input datasets. A comparison of these figures shows that the difference of phases produces a better SNR, which is why this method is more suitable for static applications.

2.6 Phase-Unwrapping Processing

The arctangent function used in Eqs. (2.53), (2.55), and (2.59) is multivalued and produces phase values in the interval $[-\pi, \pi]$ with 2π jumps. For this reason, additional processing is necessary to add the correct integral multiple of 2π to each pixel value, as shown in Fig. 2.12. This further image processing is known as "phase unwrapping." (More-detailed treatments of this topic can be found elsewhere.[27,28])

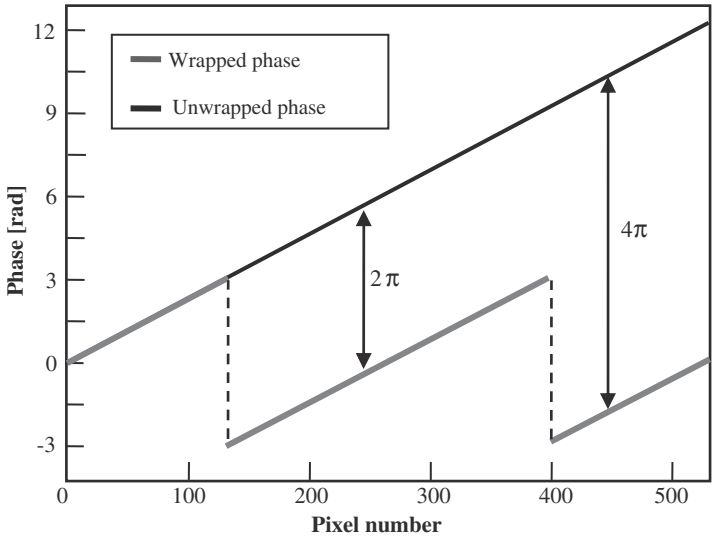

Figure 2.12 Plots showing the unwrapped and wrapped phase.

In order to correctly unwrap a given phase distribution, the original phase maps must have been properly sampled in accordance with Shannon's sampling theorem.[10] If this requirement is satisfied for successive samples along the time axis, the phase at each pixel can be unwrapped as a function of time by adding multiples of 2π, as shown in Fig. 2.12. This procedure is known as temporal phase unwrapping. It is clear that, for this case, the sampling theorem will also be satisfied for adjacent pixels in each image, thus allowing the spatial phase unwrapping.

It is not necessary to satisfy the sampling theorem simultaneously in time and spatial dimensions.[10] For example, for a phase difference $\Delta\phi_w(n, m, t_1, t_2)$, the sampling theorem will be violated for the time axis because changes occurred at times t_1 and t_2. However, this phase difference will satisfy the theorem for the spatial case, thus allowing spatial phase unwrapping. Most of the techniques shown in this book usually use spatial phase unwrapping. For this reason, the following paragraphs only describe spatial methods rather than temporal ones. Several papers published by Huntley's group[10,24] are the best reference to obtain further information about temporal phase unwrapping.

Before discussing the principal algorithms used for spatial phase unwrapping, it is important to note that there is only one case where phase unwrapping can be avoided in general. This is the case for strain measurements in which users are more interested in spatial gradients of phase rather than phase values. One approach involves obtaining the images I_c and I_s from the wrapped difference phase map $\Delta\phi_w(m, n, t_1, t_2)$:[10]

$$\begin{aligned} I_s(n,m) &= \sin[\Delta\phi_w(n,m)], \\ I_c(n,m) &= \cos[\Delta\phi_w(n,m)], \end{aligned} \tag{2.63}$$

where the t_1 and t_2 dependence are hidden for clarity.

Numerical differentiation can be carried out using numerical methods shown in Huntley[10] (Section 2.5.6), and the phase gradient data can be calculated, for example, along the n direction, as follows:[10]

$$\frac{\partial}{\partial n}\Delta\phi_w(n,m) = I_c(n,m)\frac{\partial I_s(n,m)}{\partial n} - I_s(n,m)\frac{\partial I_c(n,m)}{\partial n}. \qquad (2.64)$$

This method has the limitation that the size of the subimage over which the differentiation is performed must be much smaller than one fringe period. An alternative approach is obtained by carrying out the differentiation in the Fourier domain.[29]

Several techniques for phase unwrapping have been described elsewhere.[27,29,31] The simplest method follows the principle shown in Fig. 2.12, which integrates the phase by adding multiples of 2π following a path that scans the whole image.[32] For a noise-free and correctly sampled phase, the unwrapped optical phase is independent of the integration path [see Fig. 2.13(b)]. By using Green's theorem, it can be demonstrated that this path independence is valid if and only if the integral of the gradient of the phase (in a 2π module) along each and every closed loop in the whole image is null.[28] Figure 2.13(a) shows a set of points (indicated as circles) that represent the position of four adjacent pixels. The sum of the gradients between each pixel is zero.

On the other hand, phase maps measured in practical applications usually have localized parts of the image with phase discontinuities [see Fig. 2.14(a)]. These discontinuities are produced by local noise speckle, local decorrelation of speckle, under-sampling of global features (e.g., the edges of the specimen or holes), or cracks. In the case of Fig. 2.14(a), the sum of gradients along a close loop is zero at all pixels except for the two loops L_1 and L_2 around points 1 and 2; here, the phase unwrapping procedure produces different phase

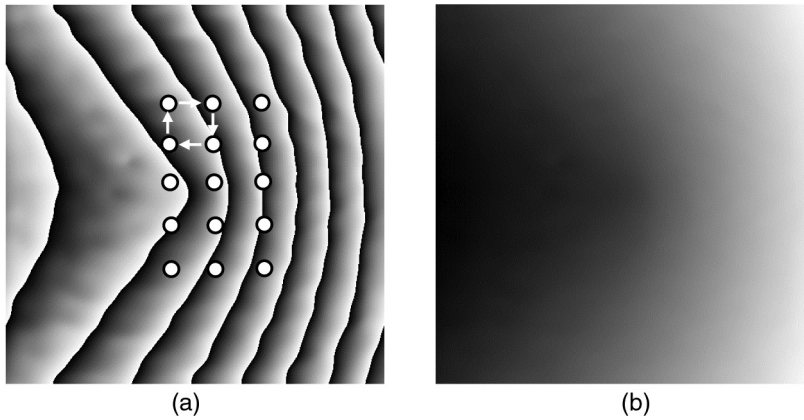

Figure 2.13 (a) Wrapped and (b) unwrapped phase. The wrapped phase shows close loops. Figures reprinted with permission from G. E. Galizzi.

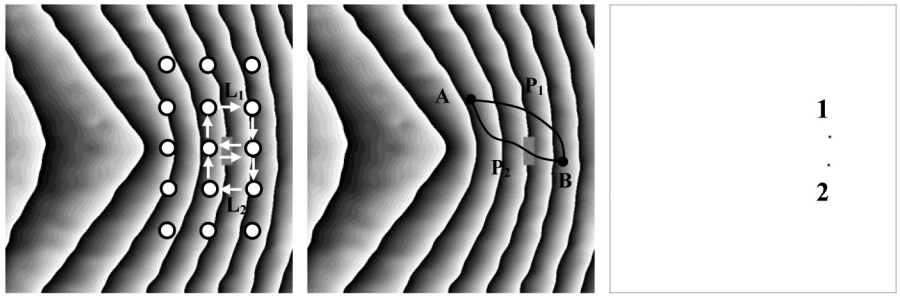

Figure 2.14 (a) Wrapped phase showing a close loop around a phase fault, (b) unwrapping using two different paths, and (c) inconsistencies found in the wrapped phase shown in (a). Figures reprinted with permission from G. E. Galizzi.

values if different paths are followed. The unwrapped-phase value will thus be different if the algorithm goes from point A to B by the P_1 or P_2 paths [see Fig. 2.14(b)]. In other words, the unwrapping problem has path dependence. Points 1 and 2 [Fig. 2.14(c)] are isolated points presented in the image, and they are called inconsistencies,[28] residues,[33] or discontinuity sources.[34,35] Inconsistencies have positive and negative values, and they also appear together in a configuration called "dipoles." Huntley[10] gives a more detailed explanation about dipoles and procedures to identify discontinuities.

Nearly all of phase unwrapping algorithms developed up to now can be grouped in one of two categories: (a) those that select a single unwrapping path and (b) those that choose the computed unwrapped phase by means of global optimization.[10] Algorithms based on placing branch cuts to act as unwrapping barriers belong to the former group. For the latter group, the least-squares unwrapping is a very known and good approach.

An interesting and peculiar fact about branch-cut algorithms is that they were independently developed by researchers in satellite-radar-interferometry[33], experimental mechanics,[34] and optical astronomy[36] communities. In all cases, the methods place barriers (called branch cuts) between residues, thus avoiding the unwrapping process across these points. A judicious choice of branch cuts makes it possible to produce phase maps with a single value.[10] Huntley and Buckland[35] present a statistical argument that shows that the most likely cut distribution is the one that minimizes the sum of the squares of the cut lengths.

One of the simplest approaches is called the nearest-neighbor method. The idea is to join the two opposite residues (or one residue and the boundary of the image) that are separated by the shortest distance. In order to overcome some cases where the nearest-neighbor method fails, several improved optimization methods have been proposed[37,39] to minimize the total cut length. Among these, an algorithm[39] based on a graphic theory approach, called the Hungarian algorithm, is guaranteed to find the

minimum global cut length. Further explanations and mathematical theory can be found elsewhere.[28]

A family of global methods based on L^P norm minimization was developed by Ghiglia and Romero.[40] For this approach, authors formulated the phase unwrapping problem in a generalized minimum-norm sense. Thus, the algorithm seeks the unwrapped solution phase whose local derivatives match the derivatives of the measured wrapped phase as closely as possible. This is obtained by minimizing the differences between gradients of the wrapped phase and the solution phase. The general case of these algorithms is known as the L^P norm-minimization algorithm, where the exponent is selected in accordance with user needs.

By supposing that $\Delta\phi_w(n, m)$ are the wrapped-phase values and $\Delta\phi(n, m)$ are the wrapped-phase values to be determined, the L^P norm solution will minimize the following error term:

$$:^p = \sum_{n=0}^{N_n-2}\sum_{m=0}^{N_m-1} |\Delta\phi(n+1,m) - \Delta\phi(n,m) - \Upsilon[\Delta\phi_w(n+1,m) - \Delta\phi_w(n,m)]|^p + \sum_{n=0}^{N_n-1}\sum_{m=0}^{N_m-2} |\Delta\phi(n,m+1) - \Delta\phi(n,m) - \Upsilon[\Delta\phi_w(n,m+1) - \Delta\phi_w(n,m)]|^p, \tag{2.65}$$

where Υ is the wrapping operator defined in Eq. (2.61). Least-squares unwrapping is a special case for $p = 2$. In this case, the idea is to choose the $N_n \times N_m$ values of $\Delta\phi(n, m)$ so that the difference between neighboring pixels matches (in accordance with the least-squares approach) the corresponding phase difference computed from the measured wrapped phase. Ghiglia and Romero[40] describe an efficient algorithm for computing this solution with a forward and inverse discrete cosine transform.

The introduction of weighting factors to account for regions with poor data considerably improves this algorithm.[40] However, the computational effort is significantly increased because this algorithm is now iterative.

An interesting variation occurs when $p = 0$. This solution physically corresponds to the requirement that the solution phase gradients equal the input phase gradients as much as possible. Therefore, an equivalent method is to unwrap with a set of branch cuts chosen to minimize the total branch cut length.[10] The relationship between L^0 and branch-cut algorithms are discussed in detail by Robinson[28] and Ghiglia and Romero.[41]

References

1. J. W. Goodman, *Speckle Phenomena in Optics: Theory and Applications*, Roberts and Company, Englewood, CO (2006).
2. R. Jones and K. Wykes, *Holographic and Speckle Interferometry*, 2nd Ed., Cambridge University Press, Cambridge, UK (1989).

3. M. Françon, *La Granularité Laser (Speckle)*, 2nd Ed., Masson, Paris (1978).
4. E. Hecht, *Optics*, 4th Ed., Addison-Wesley, Reading, MA (2002).
5. J. C. Dainty et al., *Laser Speckle and Related Phenomena*, 2nd Ed., Springer-Verlag, Berlin (1984).
6. M. Françon, *Laser Speckle and Applications in Optics*, H. H. Arsenault, trans. (English), Academic Press, San Diego (1979).
7. B. Y. Zel'dovich, A. V. Mamaev, and V. V. Shkunov, *Speckle-Wave Interaction in Application to Holography and Nonlinear Optics*, CRC Press, Boca Raton, FL (1995).
8. M. Lehmann, "Speckle statistics in the context of digital speckle interferometry," *Digital Speckle Pattern Interferometry and Related Techniques*, P. K. Rastogi, ed., pp. 60–139, John Wiley and Sons, New York (2001).
9. T. Kreis, *Holographic Interferometry: Principles and Methods*, Wiley-VCH, Berlin (1996).
10. J. M. Huntley, "Automated analysis of speckle interferograms." *Digital speckle pattern interferometry and related techniques*, P. K. Rastogi, ed., pp. 1–58, John Wiley and Sons, New York (2001).
11. O. J. Løkberg and G. A. Slettemoen. "Basic Electronic Speckle Pattern Interferometry." *Applied Optics and Optical Engineering*, R. Shannon and J. C. Wyant, eds., pp. 455–504, Academic Press, San Diego, CA (1987).
12. R. S. Sirohi, *Speckle Metrology*, Marcel Dekker, New York (1993).
13. K. Creath, "Temporal Phase Measurement Methods." *Interferogram Analysis: digital fringe pattern measurement techniques*, D. W. Robinson and G. T. Reid, Eds., pp. 94–140, Institute of Physics Publishing, Bristol, UK (1993).
14. M. Kujawinska, "Spatial Phase Measurement Methods," *Interferogram Analysis: Digital Fringe Pattern Measurement Techniques*, D. W. Robinson and G. T. Reid, eds., pp. 141–193, Institute of Physics Publishing, Bristol, UK (1993).
15. M. Takeda, "Spatial-carrier fringe-pattern analysis and its applications to precision interferometry and profilometry: an overview," *Ind. Metrol.* **1**, 79–99 (1990).
16. J. C. Wyant, "Interferometric optical metrology: basic principles and new systems," *Laser Focus* **18**(5), 65–71 (1982).
17. T. Kreis, *Handbook of Holographic Interferometry: Optical and Digital Methods*, Wiley-VCH, Berlin (2005).
18. J. Schwider, P. Burow, K. E. Elssner, J. Grzanna, R. Spolaczyk, and K. Merkel, "Digital wavefront measuring interferometry – some systematic error sources," *Appl. Opt.* **22**, 3421–3432 (1983).

19. P. Carré, "Installation et utilisation du comparateur photoélectrique et interférentiel du Bureau International des Poids et Mesures," *Metrologia* **2**, 13–23 (1966).
20. J. M. Huntley, S. J. P Palmer, H. T. Goldrein, and L. G. Melin, "Microstructural strain analysis by high magnification moiré interferometry," *Proc. SPIE* **2545**, 86–95 (1995) [doi: 10.1117/12.212633].
21. D. A. Jackson, R. Priest, A. Dandrige, and A. B. Tveten, "Elimination of drift in a single-mode optical fiber interferometer using a piezoelectrically stretched coiled fiber," *Appl. Opt.* **19**, 2926–2929 (1980).
22. J. D. Valera, D. Harvey, and J. D. C. Jones, "Automatic heterodyning in fiber optic speckle pattern interferometry using laser velocimetry," *Opt. Eng.* **31**(8), 1646–1653 (1992) [doi: 10.1117/12.58843].
23. L. Crescentini and G. Renzella, "A wide-band high-sensitivity laser strainmeter," *Rev. Sci. Instrum*. **62**, 1206–1209 (1991).
24. J. M. Huntley, G. H. Kaufmann, and D. Kerr, "Phase-shifted dynamic speckle pattern interferometry at 1 kHz," *Appl. Opt.* **38**, 6556–6563 (1999).
25. S. De Nicola, P. Ferraro, A. Finizio, and G. Pierattini, "Compensation of aberrations in Fresnel off-axis digital holography," *Fringe 2001*, W. Osten and W. Jüptner, eds., pp 407–412 (2001).
26. A. Gundlach, J. M. Huntley, B. Manske, and J. Schwider, "Speckle shearing interferometry using a diffractive optical beamsplitter," *Opt. Eng.* **36**(5), 1488–1493 (1997) [doi: 10.1117/1.601351].
27. D. W. Robinson, "Phase unwrapping methods," *Interferogram Analysis: Digital Fringe Pattern Measurement Techniques*, D. W. Robinson and G. T. Reid, eds., Institute of Physics Publishing, Bristol, UK (1993).
28. D. C. Ghiglia and M. D. Pritt, *Two-Dimensional Phase Unwrapping: Theory, Algorithms, and Software*, John Wiley and Sons, New York (1998).
29. G. K. Bhat, "A Fourier-transform technique to obtain phase derivatives in interferometry," *Opt. Commun*. **110**, 279–286 (1994).
30. R. T. Judge and P. J. Bryanston-Cross, "A review of phase unwrapping techniques in fringe analysis," *Opt. Lasers Eng.* **21**, 199–239 (1994).
31. J. M. Huntley, "New methods for unwrapping noisy phase maps," *Proc. SPIE* **2340**, 110–123 (1994) [doi: 10.1117/12.195900].
32. K. Itoh, "Analysis of the phase unwrapping problem," *Appl. Opt.* **21**, 2470–2476 (1982).
33. R. M. Goldstein, H. A. Zebker, and C. L. Werner, "Satellite radar interferometry: Two-dimensional phase unwrapping," *Radio Sci.* **23**, 713–720 (1988).

34. J. M. Huntley, "Noise-immune phase unwrapping algorithm," *Appl. Opt.* **28**, 3268–3270 (1989).
35. J. M. Huntley and J. R. Buckland, "Characterization of sources of 2π phase discontinuity in speckle interferograms," *J. Opt. Soc. Am.* **12**, 1990–1996 (1995).
36. L. D. Barr, V. Coudé du Foresto, J. Fox, G. A. Poczulp, J. Richardson, C. Roddier, and F. Roddier, "Large-mirror testing facility at the national-optical-astronomy-observatories," *Opt. Eng.* **30**(9), 1405–1414 (1991) [doi: 10.1117/12.55939].
37. R. Cusack, J. M. Huntley, and H. T. Goldrein, "Improved noise-immune phase-unwrapping algorithm," *Appl. Opt.* **34**, 781–789 (1995).
38. J. A. Quiroga, A. González-Cano, and E. Bernabeu, "Stable-marriage algorithm for preprocessing phase maps with discontinuity sources," *Appl. Opt.* **34**, 5029–5038 (1995).
39. J. R. Buckland, J. M. Huntley, and S. R. E. Turner, "Unwrapping noisy phase maps by use of a minimum-cost-matching algorithm," *Appl. Opt.* **34**, 5100–5108 (1995).
40. D. C. Ghiglia and L. A. Romero, "Robust two-dimensional weighted and unweighted phase unwrapping that uses fast transforms and iterative methods," *J. Opt. Soc. Am. A* **11**, 107–117 (1994).
41. D. C. Ghiglia and L. A. Romero, "Minimum L^p-norm two-dimensional phase unwrapping," *J. Opt. Soc. Am. A* **13**, 1999–2013 (1996).

Chapter 3
Optical Configurations for Measurements Using DSPI

3.1 Displacement Measurements

Chapter 2 showed that the variation in optical phase of a speckle distribution can be deterministically related to (a) displacements of the scattering surface, (b) changes in the illumination and observation geometry, and (c) changes in the wavelength of the light source or in the refractive index of the medium through which it travels.[1] In cases where the geometry remains constant during the measurement process, as well as the wavelength of the laser light and refractive index, the interferometric configuration is capable of measuring displacement fields produced in the surface of the investigated specimen. Several optical arrangements can be found in the literature that can be categorized as interferometers with sensitivity to either out-of-plane or in-plane displacements. Additionally, there are optical arrangements that are also sensitive to the derivative of displacements; they are known as shearography interferometers.

3.1.1 Out-of-plane sensitivity

Figure 3.1 shows a possible experimental setup of a speckle interferometer with out-of plane sensitivity. Note that the sensitivity direction is close to the normal vector of the surface of the object. In practical applications, this direction should be adjusted parallel to the observation direction.[2,3] Consequently, the light source is placed far from the object surface, and the illumination angle is kept close to zero.

By analyzing Fig. 3.1, it can be seen that the scattering surface is laterally illuminated with a collimated beam that makes a small angle γ with the direction of observation. The speckle distribution scattered by the object interferes with either a smooth reference beam ($\varphi_{s2} = 0$) or with a reference speckle distribution ($\varphi_{s2} \neq 0$). The interferogram intensity is registered in the sensor of the camera located in the imaging plane.

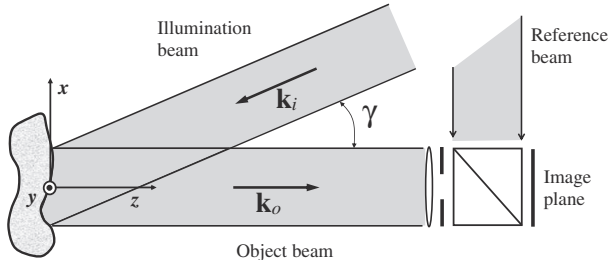

Figure 3.1 Interferometer optical setup with out-of-plane sensitivity.

The phase of the object beam is

$$\varphi_1 = \varphi_{s1} + \psi_1{}' + \mathbf{k} \cdot \mathbf{r}. \tag{3.1}$$

Because the phase of the reference beam is independent of the roughness of the surface object, it can be expressed as

$$\varphi_2 = \varphi_{s2} + \psi_2{}', \tag{3.2}$$

where φ_{s2} is null because the reference beam is smooth.

By taking into account Fig. 3.1, the sensitivity vector is

$$\mathbf{k} = \mathbf{k}_i - \mathbf{k}_o = \frac{-2\pi}{\lambda}\left[\sin\gamma\hat{\mathbf{i}} + (1+\cos\gamma)\hat{\mathbf{k}}\right], \tag{3.3}$$

where $\hat{\mathbf{i}}$ and $\hat{\mathbf{k}}$ are the unitary vectors for the x and z directions, respectively, and λ is the wavelength of the light source.

By using Eq. (2.35), the object phase will be expressed as

$$\psi_o(\mathbf{x},\tau) = \mathbf{k} \cdot \mathbf{r}(\mathbf{x},\tau) = \left\{\frac{-2\pi}{\lambda}\left[\sin\gamma\hat{\mathbf{i}} + (1+\cos\gamma)\hat{\mathbf{k}}\right]\right\} \cdot \mathbf{r}(\mathbf{x},\tau), \tag{3.4}$$

and its variation as

$$\Delta\psi_o(\mathbf{x},\tau) = \mathbf{k} \cdot \Delta\mathbf{r}(\mathbf{x},\tau) = \left\{\frac{-2\pi}{\lambda}\left[\sin\gamma\hat{\mathbf{i}} + (1+\cos\gamma)\hat{\mathbf{k}}\right]\right\} \cdot \Delta\mathbf{r}(\mathbf{x},\tau). \tag{3.5}$$

For small values of γ, the variation of the phase is highly sensitive to displacements generated along the direction of observation and slightly sensitive to displacements that occur in the xy plane (see Fig. 3.1).

When the directions of illumination and observation are parallel (see Fig. 3.2, where $\gamma = 0$), Eqs. (3.4) and (3.5) can be rewritten as

$$\mathbf{k} = \frac{-4\pi}{\lambda}\hat{\mathbf{k}} \Rightarrow \quad \Delta\psi_o(\mathbf{x},\tau) = \frac{-4\pi w}{\lambda}, \tag{3.6}$$

where w is the component of the displacement of the object surface along the z direction. The negative sign results from the selection of the reference system on the object.

For this type of interferometer, the maximum visibility of the correlation fringes will be reached when the optical aperture of the imaging system

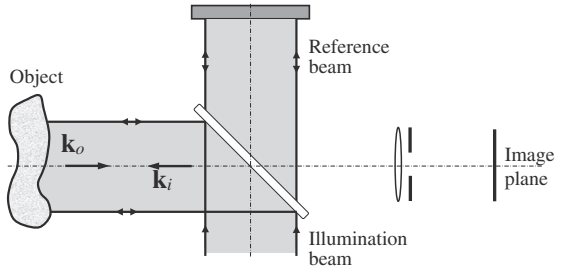

Figure 3.2 Alternative optical setup for out-of-plane sensitivity.

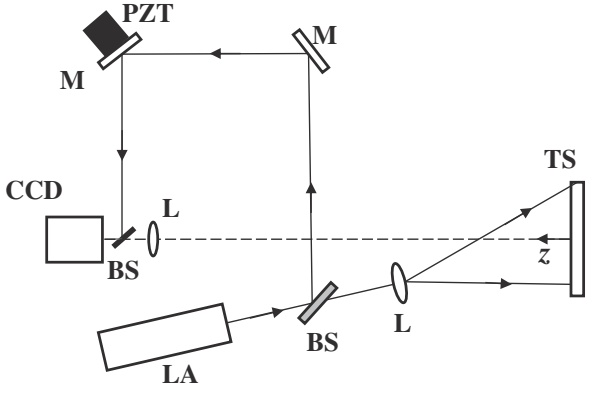

Figure 3.3 Out-of-plane interferometer: laser source (LA), beamsplitters (BS), mirrors (M), piezoelectric-driven mirror (PZT), lens (L), camera (CCD), and test specimen (TS).

generates a subjective speckle distribution with a spatial frequency in accordance with the maximum frequency resolved by the camera sensor. Additionally, the ratio between the intensity of the object beam and that of the reference beam must be 1.7.[2]

Figure 3.3 shows a practical configuration for a traditional DSPI interferometer with out-of-plane sensitivity. The laser light is divided by the beamsplitter BS. One of the beams is expanded by the lens L in order to illuminate the surface of the test specimen. The scattered light is captured by the lens used before the camera as an imaging system. The second beam is guided by the set of mirrors M going into the camera by means of the beamsplitter located between the CCD and the lens. Mirrors are placed on the optical table in order to have the same length between both interferometer arms. A piezoelectric actuator should be joined to one of the mirrors to introduce a shift in the reference beam and to compute the phase by using phase-shifting techniques.

3.1.2 In-plane sensitivity

Optical configurations for measuring in-plane displacements are usually based on the two-beam illumination arrangement first described by Leendertz in 1970.[4] These interferometers are generally capable of measuring the displacement component that is coincident with the in-plane direction.

3.1.2.1 Measuring with only one sensitivity direction

Figure 3.4 shows the basic setup for this kind of interferometer. Two expanded and eventually collimated beams illuminate the object surface, forming two angles with the direction of illumination: γ_1 and γ_2. Thus, two speckle distributions coming from the object surface, with their respective sensitivity vectors $\mathbf{k}_{i1}$ and $\mathbf{k}_{i2}$, interfere in the imaging plane of the camera. The optical phase of these speckle distributions can be expressed as

$$\varphi_1 = \varphi_{s1} + \psi'_1 + \mathbf{k}_1 \cdot \mathbf{r}_1, \tag{3.7}$$

$$\varphi_2 = \varphi_{s2} + \psi'_2 + \mathbf{k}_2 \cdot \mathbf{r}_2. \tag{3.8}$$

By taking into account Eq. (2.35) and $\mathbf{r}_1 = \mathbf{r}_2 = \mathbf{r}$, the object phase difference will be

$$\psi_o(\mathbf{x}, \tau) = (\mathbf{k}_1 - \mathbf{k}_2) \cdot \mathbf{r}(\mathbf{x}, \tau) = \mathbf{k} \cdot \mathbf{r}(\mathbf{x}, \tau), \tag{3.9}$$

where $\mathbf{k}$ represents the net sensitivity vector obtained from subtracting the sensitivity vector from each beam; it becomes perpendicular to the z direction of observation when $\gamma_1 = \gamma_2 = \gamma$. In this case, if the illumination vectors are in the xz plane, the net sensitivity will be

$$k_x \frac{-4\pi}{\lambda} \sin\gamma, \tag{3.10}$$

where k_x is the component of the sensitivity vector along the x direction. Analyzing this equation shows that the magnitude of the angle γ can adjust

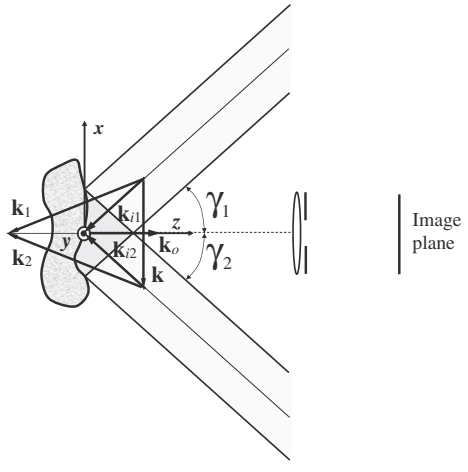

Figure 3.4 Optical setup for in-plane sensitivity.

the sensitivity of the interferometer from a null value (as with illumination perpendicular to the object surface) to a maximum limit value of $-4\pi/\lambda$ (as with illumination parallel to the object surface).

In order to obtain the phase difference for two object states, Eq. (3.10) should be substituted into Eq. (3.9):

$$\Delta\psi_o(\mathbf{x},\tau) = \mathbf{k}\cdot\Delta\mathbf{r}(\mathbf{x},\tau) = k_x u(\mathbf{x},\tau) = \frac{-4\pi}{\lambda}u(\mathbf{x},\tau)\sin\gamma, \qquad (3.11)$$

where u is the component of the displacement field along the x direction.

For this kind of interferometer, the maximum visibility of the subtraction fringes will be obtained when the optical system correctly resolves every speckle produced by the scattering surface and when the ratio between both illumination beam intensities is equal to 1.[2]

Figure 3.5 illustrates conventional in-plane DSPI with symmetrical dual-beam illumination. According to this figure, two expanders are used to illuminate the object. Because the distance between the object and the expander lens is a hundred times larger than the measurement region, the variation of the sensitivity vector across the field of view can be considered negligible.

3.1.2.2 Measuring along two sensitivity directions

In practical situations, 3D displacement fields are frequently separated into one component normal to the surface to be measured and two components along the tangential direction. For a plane or smooth surface, the former is known as the out-of-plane displacement component, and latter are called in-plane components. In-plane displacements are generally more interesting for engineering applications where the main task is determining strain and stress fields applied to mechanical parts in evaluating their integrity. Currently, electrical strain gages are the most widely used devices by industrial and academic laboratories in order to monitor strain and stress fields.[5] Even though portability, robustness, accuracy, and range of measurement of strain gages have been firmly established, their installation is time-consuming and requires a well-trained technician.

The interferometer shown in Fig. 3.5 presents sensitivity in only one direction (1D sensitivity). An important requirement in many engineering measurements is the simultaneous computation of both in-plane components,[6] which requires measuring in two determined (usually perpendicular) directions (2D sensitivity). These systems consist of two interferometers sensitive to two orthogonal displacement directions and are based on polarization discrimination methods that use a polarizing beamsplitter that splits the laser beam into two orthogonal, linearly polarized beams.[7,8] Other possibilities apply high-speed-switching methods by using a LCD that changes the polarization of the laser light. Bowe et al.[9] and Facchini and Zanetta[10] discuss possible solutions for switching methods.

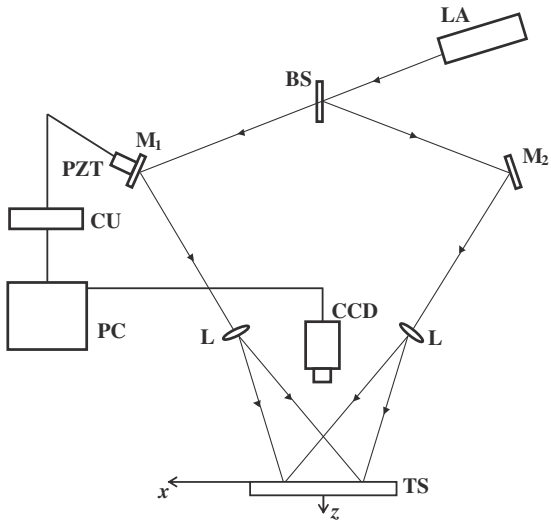

Figure 3.5 Dual-beam illumination interferometer: laser source (LA), beamsplitter (BS), mirrors (M_1 and M_2), piezoelectric-driven mirror (PZT), lens (L), camera (CCD), control unit (CU), personal computer (PC), and test specimen (TS).

Both displacement components are thus measured simultaneously. Two drawbacks affect this approach: (a) the test surface can appreciably depolarize the two orthogonally polarized dual-beam illumination sets, causing cross-interference, and (b) the optical setup becomes more bulky and complex. Albertazzi et al.[11] and Viotti et al.[12] have managed to deal with these limitations by developing a novel double-illumination DSPI system. This interferometer presents an optical arrangement that provides radial in-plane sensitivity, and its first version is described in depth in the following section.

3.1.2.3 Measuring along radial sensitivity directions

Figure 3.6 shows a cross-section of a conical mirror used to obtain radial in-plane sensitivity when used in a digital speckle pattern interferometer.[11–13] This mirror is positioned near the specimen surface, allowing for its double illumination.

Figure 3.6 also displays two particular light rays chosen from a collimated illumination source. Each light ray is reflected by the conical mirror surface toward a point P over the specimen surface, reaching it with the same incidence angle. The illumination directions are indicated by the unitary vectors $\mathbf{n_A}$ and $\mathbf{n_B}$, and the sensitivity direction is given by the vector $\mathbf{k}$, which is obtained from the subtraction of both unitary vectors. Because the angle is the same for both light rays, in-plane sensitivity is reached at point P. Over the same cross-section and for any other point over the specimen surface, it can be verified that there is only one pair of light rays that merge at that point. Moreover, in the cross-section shown in Fig. 3.6, the incidence angle is always

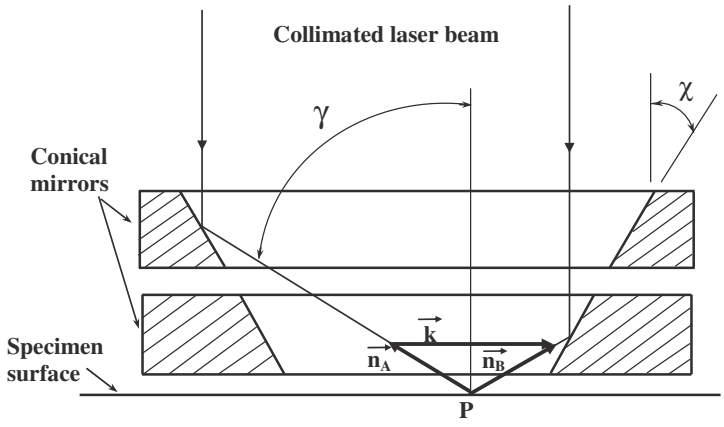

Figure 3.6 Cross-section of the upper and lower parts of the conical mirror, showing the radial in-plane sensitivity of the interferometer.

the same for every point over the specimen surface and symmetric with respect to the mirror axis. By accounting for the unitary vectors and comparing Figs. 3.6 and 3.4, readers can note similarities in both configurations. Consequently, if the normal of the specimen surface and the axis of the conical mirror are parallel, then $\mathbf{n_A}$ and $\mathbf{n_B}$ will have the same angle; therefore, the sensitivity vector $\mathbf{k}$ will be parallel to the specimen surface, and in-plane sensitivity will be obtained.

The previous description, presented for this particular cross-section, can be extended to any other cross-section of the conical mirror. If the central point is kept out of this analysis, it can be demonstrated that each point of the specimen surface is illuminated by only one pair of light rays. Because both rays are coplanar with the mirror axis and symmetrically oriented to it, the full 360-deg radial in-plane sensitivity is therefore obtained for a circular region over the specimen.

A practical configuration of the radial in-plane interferometer is shown in Fig. 3.7. The light from a diode laser is expanded and collimated via two convergent lenses, reflected toward the conical mirror by a mirror that forms a 45-deg angle with the axis of the conical mirror. The central hole placed at this mirror prevents the laser light from directly reaching the sample surface, which has triple illumination and provides a viewing window for the CCD camera.

The intensity of the light is not constant over the whole circular illuminated area on the specimen surface, and it is particularly higher at the central point because this point receives light contributions from all cross-sections. As a result, a very bright spot will be visible at the central part of the circular measurement region, and thus the fringe quality will be reduced. To avoid this effect, the conical mirror is formed by two parts with a small gap between them. The width of this gap is selected in such a way that the light

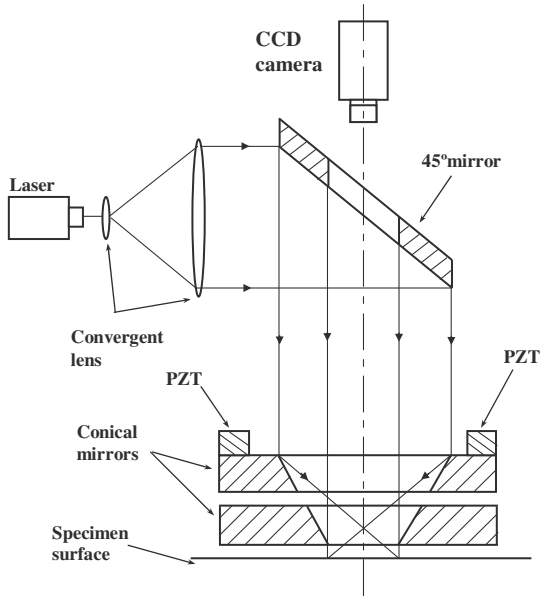

Figure 3.7 Optical arrangement of the radial in-plane interferometer.

rays reflected to the center are blocked. A small circular shadow is therefore created in the center of the illuminated area, and fringe blurring is avoided.

Each point over the specimen is shown to be illuminated for two rays of the double illumination coming from the upper and lower part of the conical mirror. A piezoelectric transducer (PZT) was joined with the upper part of the conical mirror. Consequently, the lower part is fixed while the upper part is mobile. The PZT moves the upper part of the conical mirror along its axial direction, and the gap between both parts is increased; a small optical path change between both light rays that interfere on each point is then produced, and the PZT allows the introduction of a phase shift to evaluate the optical phase distribution by means of any phase-shifting algorithm.[14]

Due to the use of collimated light, it can be verified that the optical path change is exactly the same for each point of the illuminated surface. The relation between the displacement ΔPZT of the piezoelectric transducer and the optical path change ΔOPC is given by the following equation:[13,15]

$$\Delta\mathrm{OPC} = [1 - \cos(2\chi)]\ \Delta\mathrm{PZT}, \tag{3.12}$$

where χ is the angle of the conical mirror.

Finally, the radial in-plane displacement field $u_r(r, \theta)$ can be calculated from the optical phase distribution:[6]

$$u_r(r,\theta) = \frac{\Delta\phi(r,\theta)\ \lambda}{4\pi\ \sin\gamma}. \tag{3.13}$$

As before, λ is the wavelength of the laser, and γ is the angle between the illumination direction and the normal direction of the specimen surface.

Two main drawbacks can be identified in the setup shown in Fig. 3.7: (a) it uses a high-quality, aluminum conical mirror that can be quite expensive, and (b) it requires wavelength stabilization of the laser used as the light source, which cannot easily be achieved for a compact and cheap diode laser. Consequently, applications outside the laboratory can be difficult or even unfeasible.

Diffractive structures are known to separate white light into a spectrum of colors. However, if the incident light is monochromatic, the grating will generate an array of regularly spaced beams in order to split and shape the wavefront beam.[16] The diffraction angle ξ of the spaced beams is given by the following well-known grating equation:[16,17]

$$p_r \sin\xi = m\lambda \Rightarrow \sin\xi = \frac{m\lambda}{p_r}, \tag{3.14}$$

where p_r is the period of the grating structure, and ξ is the diffraction angle for the m-order. From this equation, it is clear that the -1 and $+1$ orders have symmetrical angles with the incident rays.

Recent developments in microlithography manufacturing allowed the production of diffractive optical elements (DOEs). The ability to manufacture diffraction gratings with a large variety of geometries and configurations made it possible to develop a new and flexible family of optical elements with several optical functions, such as diffractive lenses, beamsplitters, and diffractive shaping optics. A special diffractive optical element can be designed to achieve radial in-plane sensitivity with DSPI. It consists of a circular diffraction grating with a binary profile and a constant period p_r, as shown in Fig. 3.8.

If an axis-symmetric circular binary DOE is used instead of conical mirrors, as in the figure, a double-illuminated circular area with radial in-plane sensitivity is achieved.[18,19] The symmetry of the -1 and $+1$ orders will produce double illumination with symmetrical angles, which generates radial in-plane sensitivity.

Some advantages can be found by comparing DOEs and conical mirror usage: (a) due to advances in microlithography techniques, DOE manufacturing has reached a certain maturity that makes it less expensive than specially fabricated conical mirrors, and (b) because of the dual-beam illumination setup, interferometer sensitivity is independent of the wavelength of the laser used as the light source.

By considering Eq. (3.13), the corresponding fringe equation is

$$u_r(r,\theta) = \frac{\lambda}{2\sin\gamma}. \tag{3.15}$$

According to Eq. (3.15), the sensitivity of the method would change if the angle γ or the wavelength of the light source were modified. For example, if the angle γ were increased, the sensitivity of the interferometer would also increase.

Figure 3.8 shows that the diffraction angle ξ and the angle between the direction of illumination and the normal to the specimen surface γ are the

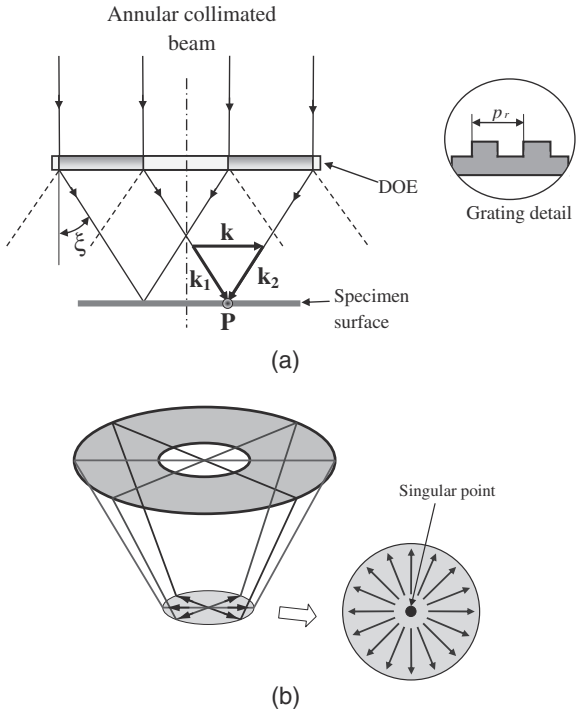

Figure 3.8 (a) Cross-section of the diffractive optical element, showing radial in-plane sensitivity. (b) Illumination principle.

same, and thus $\sin\xi = \sin\gamma$. By replacing Eq. (3.14) with Eq. (3.13) and by only considering the first-order diffraction ($m = 1$),

$$u_r(r,\theta) = \frac{\Delta\phi(r,\theta)\lambda}{4\pi\frac{\lambda}{p_r}} = \frac{\Delta\phi(r,\theta)p_r}{4\pi}. \tag{3.16}$$

In the same way, the corresponding fringe equation will be

$$u_r(r,\theta) = \frac{p_r}{2}. \tag{3.17}$$

Equations (3.16) and (3.17) show that the displacement field and the optical phase distribution are related by using the period of the grating of the DOE and not by the wavelength of the laser. This particular and curious effect can be understood through the following explanation: when the wavelength of the illumination source increases or decreases, the sine function of the diffraction angle decreases or increases by the same amount [Eq. (3.15)]. Because λ is divided by $\sin\gamma$ in Eq. (3.13), the ratio between them will be constant.

An optical arrangement similar to the layout of Fig. 3.7 can be built in order to integrate the DOE. This new practical configuration of the radial in-plane interferometer is shown in Fig. 3.9. The light from a diode laser L is expanded by

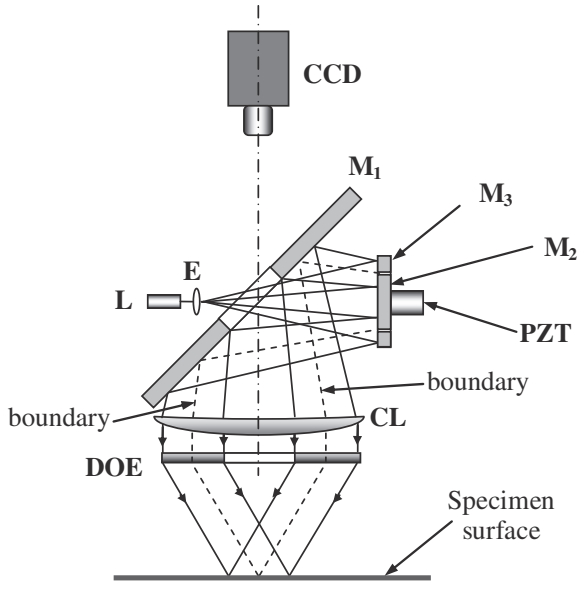

Figure 3.9 Optical arrangement of the radial in-plane interferometer with a DOE.

a plane concave lens E; it then passes through the elliptical hole of the mirror M_1, which forms a 45-deg angle with the axis of the DOE, illuminates mirrors M_2 and M_3, and reflects back to the mirror M_1. Thus, the central hole placed at M_1 allows the light coming from the laser source to reach mirrors M_2 and M_3. As before, this hole has other functions: (a) preventing the laser light from directly reaching the specimen surface with triple illumination and (b) providing a viewing window for the CCD camera. Mirror M_1 directs the expanded laser light to the lens CL in order to obtain an annular collimated beam. Finally, the light is diffracted by the DOE, primarily in the first diffraction order, toward the specimen surface. Residual nondiffracted light or light from higher diffraction orders is not considered to be a problem because it is not directed to the central measuring area on the specimen surface.

M_2 and M_3 are two special circular mirrors: The former is joined to a piezoelectric actuator PZT, and the latter has a circular hole with a diameter slightly larger than the diameter of M_2. Mirror M_3 is fixed, whereas M_2 is mobile. The PZT actuator moves the mirror M_2 along its axial direction, generating a relative phase difference between the beam reflected by M_2 (central beam) and the one reflected by M_3 (external beam). The boundary between both beams is indicated in Fig. 3.9 with dashed lines. The figure shows that every point over the illuminated area receives only one ray from M_2 and only another one from M_3. Thus, the PZT enables the introduction of a phase shift to calculate the optical phase distribution by means of phase-shifting algorithms.

As before, the intensity of the light is not constant over the whole circular illuminated area on the specimen surface, and it is particularly higher at the

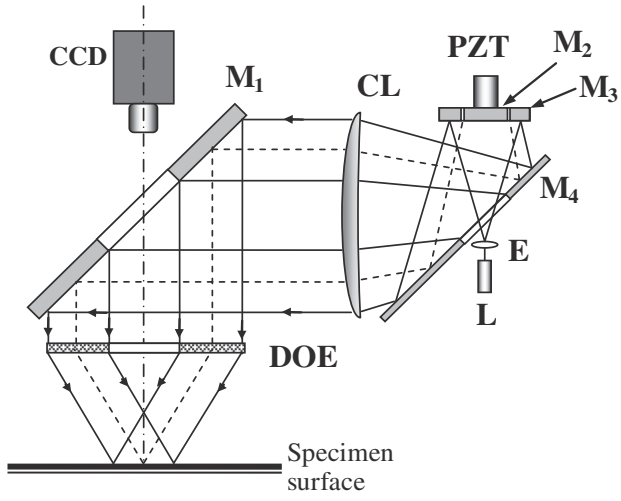

Figure 3.10 Alternative setup for a radial in-plane interferometer.

central point because this point receives a light contribution from all cross-sections. For this reason, the outlier diameter of mirror M_2 and the diameter of central hole at M_3 are computed by obtaining a gap of about 1.0 mm in order to block the light rays reflected to the center of the measurement area.

The optical layout shown in Fig. 3.9 allows for a measurement area of approximately 10 mm in diameter. For some applications, smaller areas of illumination are more interesting and efficient for the measurement; consequently, the DOE should be as small as possible, and the hole of mirror M_1 should also be small. For this reason, manufacturing this mirror becomes a complex task because its diameter decreases considerably, and an extra hole in a perpendicular axis (along the direction of observation) should be made. To overcome this practical problem, an off-axis configuration in accordance with Fig. 3.10 can be developed.[20]

3.2 Derivative Measurements

Digital speckle shearing interferometry (more widely known as shearography) has been used as a tool to measure derivatives of surface displacements generated in an object under deformation. A shearing device is introduced in the imaging system in order to produce two superimposed images of the object on the CCD of the camera. In other words, the object is duplicated or a point of the object is displaced a determined lateral shift, which is called shear.

The shearing effect can be produced in different ways. Figure 3.11 shows the possibility of using a wedge with very small angle. Light rays coming from point P, indicated as continuous lines in the figure, are focused by the lower part of the lens at the point P′ located on the image plane. On the other hand, the wedge slightly tilts the light rays coming from P (plotted in dashed lines), focused on the

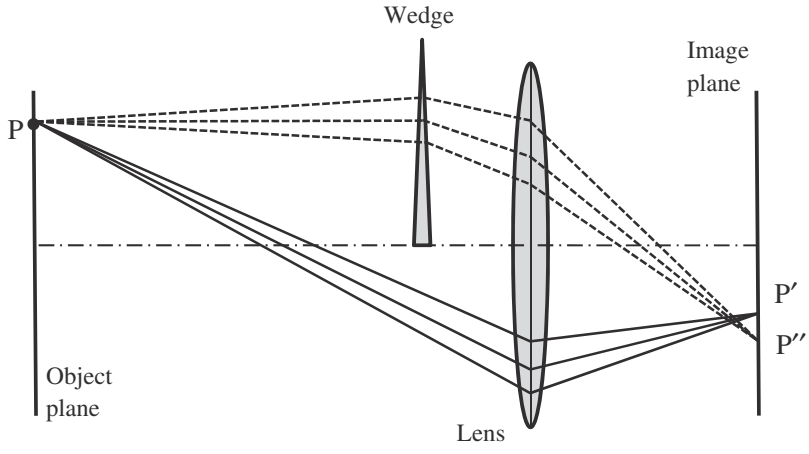

Figure 3.11 Production of the shearing effect by a wedge.

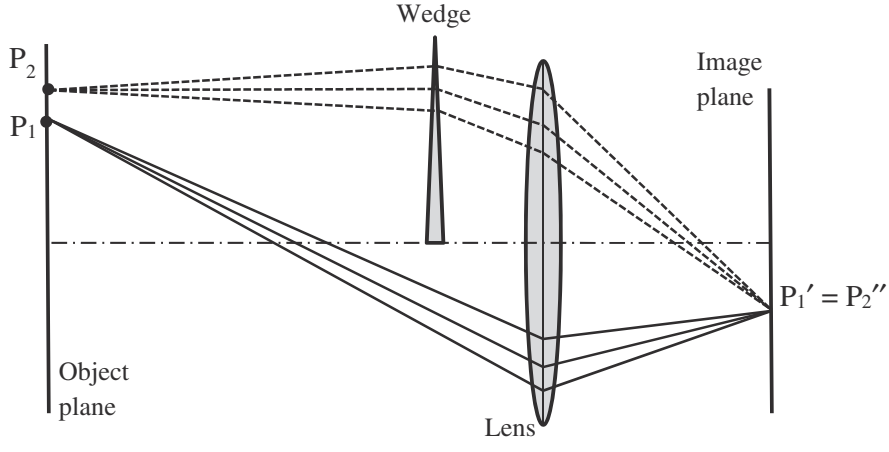

Figure 3.12 Interference between light coming from two points P_1 and P_2.

image plane in a shifted position P″ from P′. Therefore, a double image of point P is visible on the image plane with a constant vertical shift.

On the other hand, each point on the image plane receives light scattered from two different points located on the object surface. Figure 3.12 shows this effect, where light coming from P_1 and P_2 merge to the same point $P' = P''$ on the image plane. If the rough surface of the object is illuminated by coherent light, speckles will be visible on the image plane. The superposition of two laterally shifted speckle patterns will produce an interference speckle pattern on the image plane whose phase difference will remain stable as long as the phase difference between P_1 and P_2 remains stable.

The configuration shown in Figs. 3.11 and 3.12 is very compact and robust because it involves immobile and adjustable parts. However, it produces a fixed shear amount in only one direction because the vertical shift is directly related to the angle of the wedge. A more flexible and functional configuration is shown in Figs. 3.13 and 3.14. It comprises two mirrors and a beamsplitter cube in a Michelson configuration.[21–23] The object is illuminated by collimated light with an incidence angle γ. The scattered light is partially deflected by the beamsplitter, illuminating a flat mirror M_1 (rays are represented by solid lines). The rays are then reflected by this mirror to the imaging system and focused on the CCD sensor at point P. On the other hand, rays of light passing through the beamsplitter (represented with dotted lines) illuminate the flat mirror M_2. These rays are reflected back from this mirror and, after being deflected into the beamsplitter, are imaged on the CCD sensor at point P″. By tilting mirror M_2, point P′ is laterally shifted from P′ in δx. The amount of tilt to mirror M_2 controls the magnitude of lateral shear of the image as well as the distance between points P′ and P″. The tilt shown in Fig. 3.13 produces a vertical shear. A horizontal shift of these points is achieved by rotating mirror M_2 around a vertical axis.

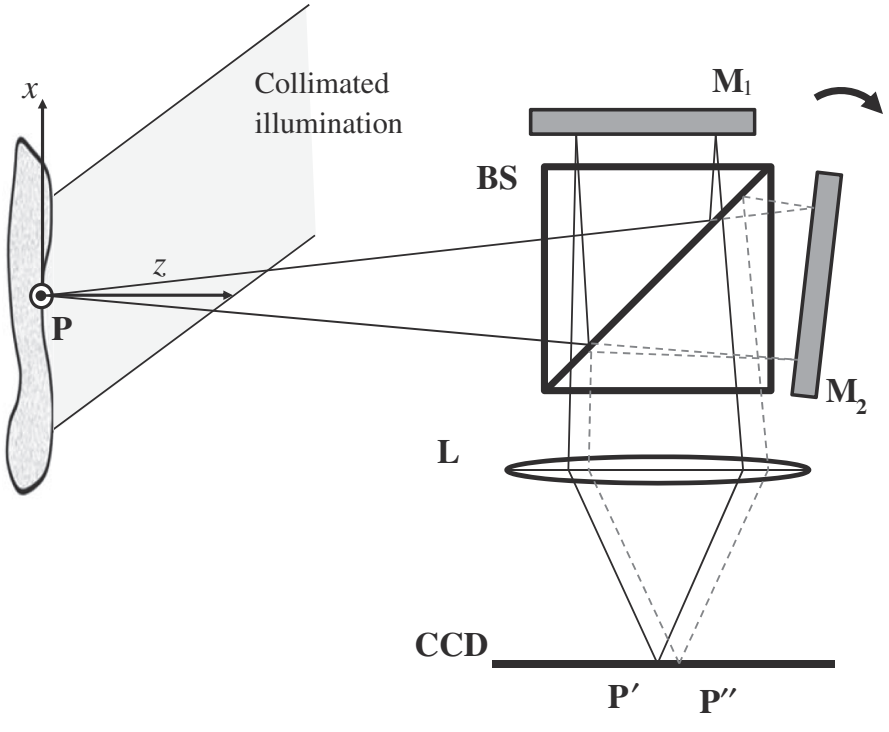

Figure 3.13 Production of a variable shearing effect by tilting a flat mirror: formation of a laterally shifted image.

The configuration shown in Fig. 3.13 is very convenient for generating the phase shift between both interfering specklegrams. Mirror M_1 can be slightly moved up and down in a parallel motion, changing by a small amount the relative phase difference between the interfering light rays. This adjustment can be easily performed by attaching the upper flat mirror to a microtranslator, such as a piezoelectric translator. Phase shifting is also very important in shearography for increasing the image quality and for quantitative purposes.

By considering that points P′ and P″ merge at the same point P on the CCD (see Fig. 3.14) for the effect of the shear, the optical path lengths traveled from the light source to the image plane will be different for each point. For the reference state, the object phase difference due to these travelled optical path lengths will be [see Fig. 3.15(a)]

$$\psi_o(\mathbf{x},\tau) = \delta\mathbf{x}(\mathbf{x},\tau)\cdot\mathbf{k}_i - \delta\mathbf{x}(\mathbf{x},\tau)\cdot\mathbf{k}_o = \delta\mathbf{x}(\mathbf{x},\tau)\cdot(\mathbf{k}_i - \mathbf{k}_o) = \delta\mathbf{x}(\mathbf{x},\tau)\cdot\mathbf{k}, \quad (3.18)$$

where the shear vector is $\delta\mathbf{x} = \mathbf{r}' - \mathbf{r}''$, and the sensitivity vector is $\mathbf{k} = \mathbf{k}_i - \mathbf{k}_o$. This vector can be expressed in components as $\mathbf{k} = [k_x, k_y, k_z]$.

Due to the deformation of the object, point P′ displaces to P_d' [having a displacement vector $\mathbf{d}(P')$] and P″ to P_d'' [with a displacement vector $\mathbf{d}(P'')$], as shown in Fig. 3.15(b). The new shear vector will thus be

$$\delta\mathbf{x}' = \delta\mathbf{x} + \mathbf{d}(P'') - \mathbf{d}(P'). \quad (3.19)$$

The object phase difference computed for the deformed state will be

$$\begin{aligned}
\psi_o(\mathbf{x},\tau) &= \delta\mathbf{x}'(\mathbf{x},\tau)\cdot\mathbf{k}_i - \delta\mathbf{x}'(\mathbf{x},\tau)\cdot\mathbf{k}_o = \delta\mathbf{x}'(\mathbf{x},\tau)\cdot(\mathbf{k}_i - \mathbf{k}_o),\\
\psi_o(\mathbf{x},\tau) &= \{\delta\mathbf{x}(\mathbf{x},\tau) + \mathbf{d}(P'') - \mathbf{d}(P')\}\cdot(\mathbf{k}_i - \mathbf{k}_o),\\
\psi_o(\mathbf{x},\tau) &= \delta\mathbf{x}(\mathbf{x},\tau)\cdot(\mathbf{k}_i - \mathbf{k}_o) + [\mathbf{d}(P'') - \mathbf{d}(P')]\cdot(\mathbf{k}_i - \mathbf{k}_o). \quad (3.20)
\end{aligned}$$

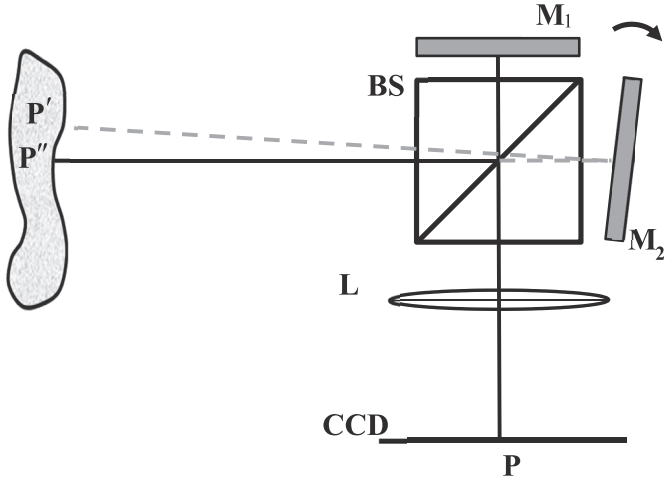

Figure 3.14 Production of a variable shearing effect by tilting a flat mirror: light from P′ and P″ merges to point P.

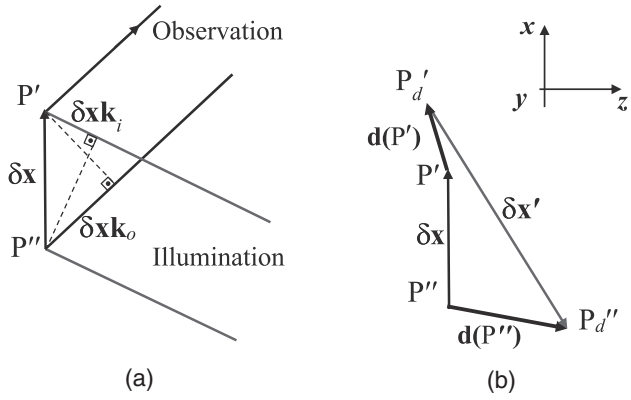

Figure 3.15 Geometry for: (a) the reference state and (b) the deformed state.

The phase difference is obtained by subtracting Eq. (3.18) from Eq. (3.20):

$$\Delta\varphi = [\mathbf{d}(\mathrm{P}'') - \mathbf{d}(\mathrm{P}')] \cdot (\mathbf{k}_i - \mathbf{k}_o). \tag{3.21}$$

The displacement difference $\Delta\mathbf{d} = \mathbf{d}(\mathrm{P}'') - \mathbf{d}(\mathrm{P}')$ can be expressed as a Taylor series along the shear direction $\delta x = |\delta\mathbf{x}|$ as[24]

$$\Delta\mathbf{d} = \frac{\partial\mathbf{d}}{\partial x}\delta x + \left(\frac{1}{2}\right)\frac{\partial^2\mathbf{d}}{\partial x^2}\delta x^2 + \left(\frac{1}{6}\right)\frac{\partial^3\mathbf{d}}{\partial x^3}\delta x^3 + \ldots \tag{3.22}$$

By considering only the first order of the series,[24] the phase difference will assume the following form:[24,25]

$$\Delta\varphi = \mathbf{k} \cdot \frac{\partial\mathbf{d}}{\partial x}\delta x = \left(k_x\frac{\partial u}{\partial x} + k_y\frac{\partial v}{\partial x} + k_z\frac{\partial w}{\partial x}\right)\delta x, \tag{3.23}$$

where $\mathbf{d} = [u, v, w]$ is the displacement vector at point P.

Equation (3.23) shows that the phase difference measured by shearography is composed of three parts: (a) the deformation of the object, which appears to derivate in the shear direction; (b) the directions of observation and illumination, as well as the wavelength of the laser, which define the sensitivity vector; and (c) the shear δx, which also defines the sensitivity vector as a variable value, allowing for wide adjustment of the sensitivity. Thus, when shearography is compared with the DSPI interferometers discussed earlier, the influence of the shear on the net sensitivity of the interferometer is shown to confer flexibility to measurements without important changes in the geometry of the interferometer. For example, with an in-plane interferometer, only changes in the laser source (wavelength) or in the geometry will change the sensitivity; conversely, only a small change in the angle of mirror M_2 (see Fig. 3.13) will quickly and easily change the sensitivity of the shearing interferometer, providing more versatility for industrial measurements.

Shearography is a technique that is usually used for NDT for defect detection in composite materials. Previous knowledge of possible size defects

will orient the user to select the best shear value in order to identify unwanted defects inside the material structure. If a large shear value is selected, the interferometer might not "see" defects with inadequate sizes for the integrity of the composite structure. (Of course, a smaller shear value will identify smaller defects.) Further details about shearography are explained in Chapter 7.

3.3 Concluding Remarks

Although the measurement of dynamic events is not the principal objective of this book, it is important to note that optical layouts similar to those previously shown can be used for transient measurements. In this case, the main objective is the characterization of vibration, e.g., the measurement of the vibration modes of a mechanical component, in order to validate its design.

When dynamics events are evaluated, two kind of motions can be found:[26] (a) periodic, harmonic deformations and (b) transient or aperiodic motions. Time-averaged techniques are usually used for periodic motions; consequently, data is acquired for traditional cameras with exposure times longer than the period of the motion. For transient deformations, interferometer components should be considered in order to allow short exposure times (high-power pulsed lasers, high-speed cameras, etc.).

Moore et al.[26] provide an extensive discussion about DSPI applications for dynamic measurements as well as the mathematical recovery of the vibration amplitude from the Bessel functions obtained in the correlation fringes and fringe maps.

The following list compares all of the interferometric layouts explained in the chapter, and pros and cons are mentioned to help readers with future applications.

Out-of-plane

- These interferometers usually allow the measurement of displacements along directions perpendicular (or close to this) of the surface of the specimen being measured.
- They feature easy implementation for transient measurements.
- They are sensitive to external vibration sources because the reference beam travels a long path from the beamsplitter to the CCD sensor in order to have the same length of the object beam.
- It is difficult to apply these interferometers beyond the optical table.

In-plane

- These interferometers are used to measure displacements that occur in the surface of the material (in-plane motions).
- The displacement fields should be oriented along the sensitivity direction. For most practical applications, the main direction of displacement is not usually known beforehand.

- Interfering beams travel long paths with difficulty in applications outside the laboratory.

In-plane polarization

- These interferometers are usually used to measure orthogonal in-plane displacements.
- They are adequate for applications in which the maximum displacement field is not known.
- They are bulky.
- The surface of the object can depolarize beams, producing cross-interference and decreasing the image quality.

Radial in-plane

- These interferometers allow the measurement of radial in-plane displacements that occur in a small circular area of the surface of the specimen under investigation.
- They enable the design and building of a compact optical setup.
- They can be used outside the laboratory.
- The use of conical mirrors introduces dependence on the laser source.
  - The use of DOEs overcomes the conical-mirror disadvantage, and thus the interferometer becomes independent of the wavelength of the laser source.
- They allow the measurement of small areas.
- Large areas involve the application of excessively large optical elements.

Shearographic

- These interferometers allow the measurement of derivatives of displacement fields that occur on the surface of the specimen.
- They allow for easy and fast changes to the sensitivity, which is suitable for NDT (see Chapter 7).
- Both beams travel a short path after splitting, which is highly recommended for outside measurements.
- They are robust to vibration and environmental agents.
- They can only achieve qualitative measurements and results. This feature may be beneficial, depending on the application, e.g., nondestructive measurements.

References

1. J. W. Goodman, *Speckle Phenomena in Optics: Theory and Applications*, Roberts and Company, Englewood, CO (2006).
2. R. Jones and K. Wykes. *Holographic and Speckle Interferometry*, 2nd Ed., Cambridge University Press, Cambridge, UK (1989).
3. D. Malacara, M. Servín, and Z. Malacara, *Interferogram Analysis for Optical Testing*: *Optical Engineering*, Marcel Dekker, New York (1998).

4. J. A. Leendertz, "Interferometric displacement measurement on scattering surfaces utilizing speckle effect," *J. Phys. E. Sci. Instrum.* **3**, 214–218 (1970).
5. J. W. Dally and W. F. Riley, *Experimental Stress Analysis*, 4th Ed., McGraw-Hill, New York (2005).
6. P. K. Rastogi, "Measurement of Static Surface Displacements, Derivatives of Displacements, and Three-Dimensional Surface Shapes - Examples of Applications to Non-destructive Testing," *Digital Speckle Pattern Interferometry And Related Techniques*, P. K. Rastogi, ed., John Wiley and Sons, New York (2001).
7. A. J. Moore and J. R. Tyrer, "An electronic speckle pattern interferometer for complete in-plane measurement," *Meas. Sci. Tech.* **1**, 1024–1030 (1990).
8. A. J. Moore and J. R. Tyrer, "Two-dimensional strain measurement with ESPI," *Opt. Laser Eng.* **24**, 381–402 (1996).
9. B. Bowe, S. Martin, V. Toal, A. Langhoff, and M. Whelan, "Dual in-plane electronic speckle pattern interferometry system with electro-optical switching and phase shifting," *Appl. Opt.* **38**, 666–673 (1999).
10. M. Facchini and P. Zanetta, "An electronic speckle interferometry in-plane system applied to the evaluation of mechanical characteristics of masonry," *Meas. Sci. Technol.* **6**, 1260–1269 (1995).
11. A. Albertazzi, Jr., M. R. Borges, and C. Kanda, "A radial in-plane interferometer for residual stresses measurement using ESPI," *Proc. SEM IX International Congress on Experimental Mechanics*, 108–111 (2000).
12. M. R. Viotti, A. Albertazzi, Jr., and G. H. Kaufmann, "Measurement of residual stresses using local heating and a radial in-plane speckle interferometer," *Opt. Eng.* **44,** 093606 (2005) [doi: 10.1117/1.2050307].
13. M. R. Viotti, R. Sutério, A. Albertazzi, Jr., and G. H. Kaufmann, "Residual stress measurement using a radial in-plane speckle interferometer and laser annealing: preliminary results," *Opt. Laser Eng.* **42**, 71–84 (2004).
14. J. M. Huntley, "Automated analysis of speckle interferograms," *Digital speckle Pattern Interferometry and Related Techniques*, P. K. Rastogi, ed., John Wiley and Sons, New York (2001).
15. J. Boettger, "Development of a portable field residual stresses measurement device using ESPI and hole drilling method [Portuguese]," Master's Thesis, Federal University of Santa Catarina, Brazil (1998).
16. D. C. O'Shea, T. J. Suleski, A. D. Kathman, and D. W. Prather, *Diffractive Optics: Design, Fabrication and Test*, SPIE Press, Bellingham, WA (2003) [doi: 10.1117/3.527861].
17. E. Hecht, *Optics*, 4th Ed., Addison-Wesley, Reading, MA (1974).

18. M. R. Viotti, A. Albertazzi, Jr., and W. Kapp, "Experimental comparison between a portable DSPI device with diffractive optical element and a hole drilling strain gage combined system," *Opt. Laser Eng.* **46**, 835–841 (2008).
19. M. R. Viotti, W. Kapp, and A. Albertazzi, Jr., "Achromatic digital speckle pattern interferometer with constant radial in-plane sensitivity by using a diffractive optical element," *App. Opt.* **48**, 2275–2281 (2009).
20. M. R. Viotti, A. Albertazzi, Jr., and W. Kapp, "Mechanical stress measurement by an achromatic optical digital speckle pattern interferometry strain sensor with radial in-plane sensitivity: experimental comparison with electrical strain gages," *App. Opt.* **50**, 1014–1022 (2011).
21. J. A. Leendertz, and J. N. Butters, "An image-shearing speckle pattern interferometer for measuring bending moments," *J. Phys. E. Sci. Instrum.* **6**, 1107–1110 (1973).
22. Y. Y. Hung and C. E. Taylor, "Speckle-shearing interferometric camera – a tool for measurement of derivatives of surface displacements," *Proc. SPIE* **41**, 169–175 (1973) [doi: 10.1117/12.953850].
23. Y. Y. Hung, "Shearography: a novel and practical approach to nondestructive testing," *J. Nondestruct. Eval.* **8**, 55–68 (1989).
24. S. Waldner, "Quantitative Strain Measurement with Image-Shearing Speckle Pattern Interferometry (Shearography)," Doctoral Thesis, ETH Zurich, No. 13469 (2000).
25. S. Waldner and S. Brem, "Compact shearography system for the measurement of 3D deformation," *Proc. SPIE* **3745**, 141–148 (1999) [doi: 10.1117/12.357771].
26. A. J. Moore, J. D. C. Jones, and J. D. R. Valera, "Dynamic measurements," *Digital Speckle Pattern Interferometry and Related Techniques*, P. K. Rastogi, ed., John Wiley and Sons, New York (2001).

Chapter 4
Robust Optical Systems

4.1 Introduction

There are many applications of interferometry where the specimen cannot be transported to the laboratory, i.e., where an appropriate interferometer cannot be installed in a quiet and isolated environment. In these cases, the interferometer should be brought to the specimen. The specimen is sometimes located in a harsh environment where the interferometer must operate correctly. This chapter analyzes the primary harsh agents and the requirements that make it possible for an interferometer to successfully and consistently work in a harsh environment.

A basic definition of a harsh environment is anywhere not "indoors." However, this definition is not complete. It can be extended to a place where any condition of extremes relative to the human condition applies: temperature, humidity, environment (including pressure), radiation, shock and vibration, erosive flows, and corrosive media, whether indoors or not.[1]

Figure 4.1 shows two examples of harsh environments that fulfill the above definition because users are exposed to temperature, atmospheric variations, humidity, sun radiation, vibration, wind, and dust. The right part of this figure is a photograph of a measurement performed with a DSPI interferometer in a very aggressive environment with conditions far from temperature and humidity laboratory settings. In this case, residual stresses are being measured in a buried pipeline by using a portable digital speckle pattern interferometer combined with the incremental hole-drilling method.[2] The device is firmly attached to the pipeline surface by using strong rare-earth magnets and an appropriate isotactic clamping system. It is evident from the figure that the interferometer should "survive" in the harsh environment, but it is also important to note that it must also give reliable results.

Several other examples of harsh environments can be found in agricultural plants, farms, industrial plants (food, oil, pharmaceutical, chemical and manufacturing), explosion areas, transport industry, and oceanography.

Figure 4.1 Examples of harsh environments.

4.2 Negative Environmental Agents for Optical Methods

Atmospheric conditions (such as temperature, humidity, and pressure), as well as shock, vibration, and radiation, are among the primary harsh agents that negatively affect interferometric measurements, as shown in Fig. 4.2. Their principal effects on the mesurand or on the performance of the measurement system are presented and discussed in the following subsections. (Although corrosion and erosion are usually critically harsh agents for interferometric measurements, they are not discussed here.)

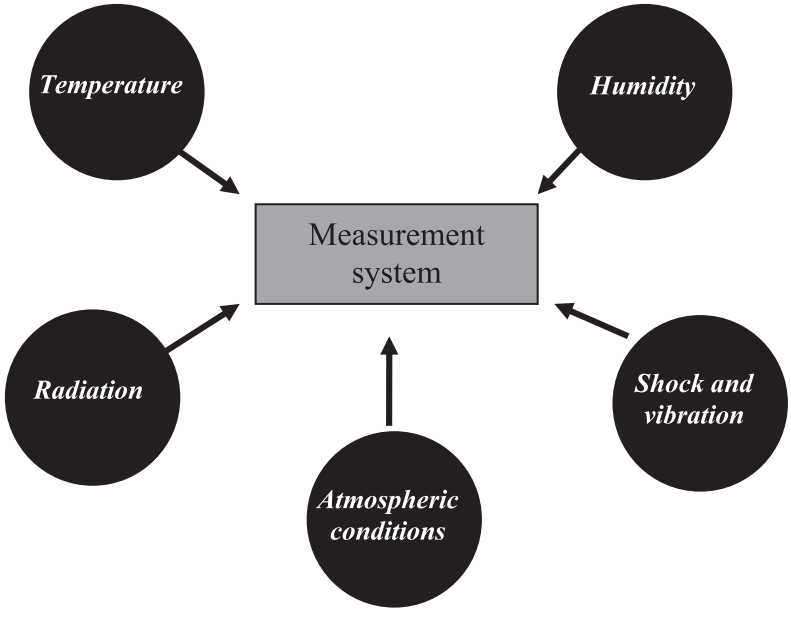

Figure 4.2 Primary harsh agents acting on a measurement system.

4.2.1 Temperature

Temperature usually has a strong influence on any physical measurement. Because the mechanical, chemical, optical, or electrical properties of most materials are dependent on temperature, the performance of a measurement system, made of components with different materials, will also depend on temperature. If the temperature varies while a measurement is in progress, it can sometimes be very difficult to determine whether the measurement indication has changed due to either temperature variations or changes in the mesurand. On the other hand, the mesurand itself can also be modified by temperature, as seen in the thermal deformation of mechanical components. Temperature can also influence the life and mechanical resistance of components. All of those effects are also present in optical measurement systems. Figure 4.3 synthesizes the principal effects of temperature on interferometric measurements.

The influence of temperature on the measurement performance of an interferometer can be affected by at least four effects: wavelength changes, sensitivity changes, signal drift, and electronic noise. The wavelength of some light sources can be directly affected by temperature, e.g., nonstabilized diode lasers. Wavelength changes in interferometric systems can result in sensitivity changes, thus affecting the ratio between the fringe order and the physical quantity variation. A signal drift can also be associated with a wavelength change as well as with thermal expansion of the interferometer parts. High temperature can affect the amount of electronic noise of camera sensors; it also has a strong influence on the life of electronic components.

Temperature can produce some changes in the mesurand. Thermal deformation of the specimen will affect its dimensions. Nonuniform

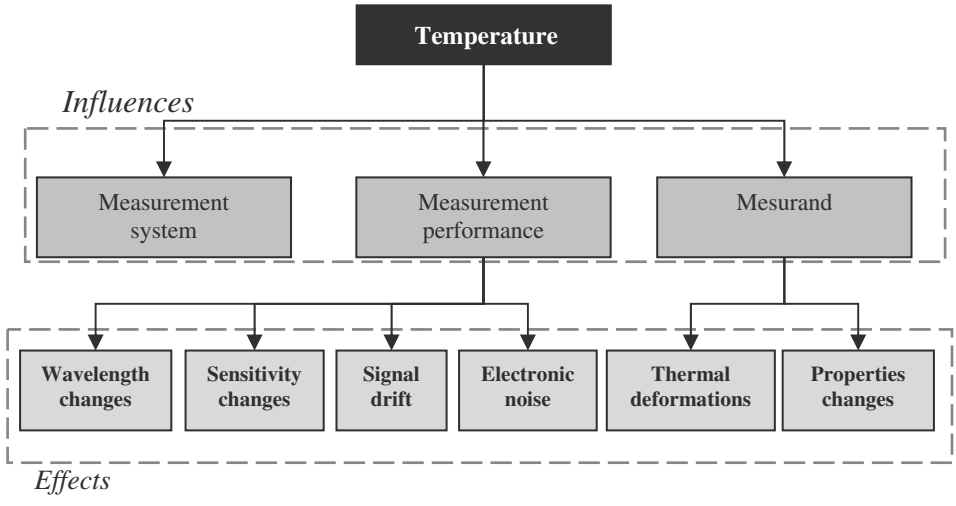

Figure 4.3 Effects of temperature on interferometric measurements.

temperature fields, or the combination of materials with different thermal expansion coefficients, can produce distortions in the specimen, generating changes in the original geometrical shape of the mesurand. Other optical, electrical, or chemical properties can also be affected.

4.2.2 Humidity

High humidity levels are sources of problems for optical measurements, especially when there is moisture condensation. Figure 4.4 shows the primary effects of humidity on interferometric measurements. These effects were divided according to the influence on the structure of the measurement system, the measurement performance, and the mesurand. High humidity levels can cause the malfunction of a component. It can also change the effective wavelength of the light source, generating measurement errors. Moisture condensation on optical components can blur the imaging acquisition and change the reflectivity of the specimen's surface.

4.2.3 Atmospheric conditions

Atmospheric conditions, including variables such as temperature, moisture, wind velocity, and barometric pressure, become disturbances that can influence an interferometric measurement. The main causes and effects are shown in Fig. 4.5. Dust, droplets, and suspended particles absorb light and make the air less translucent, thus reducing the image quality. However, the most drastic effect of dust and droplets is the contamination of optical components.

Pressure variation produces changes of the refractive index of the media, which, in turn, change the effective wavelength of the light source. Thermal currents produced by natural convection can produce severe instability in the

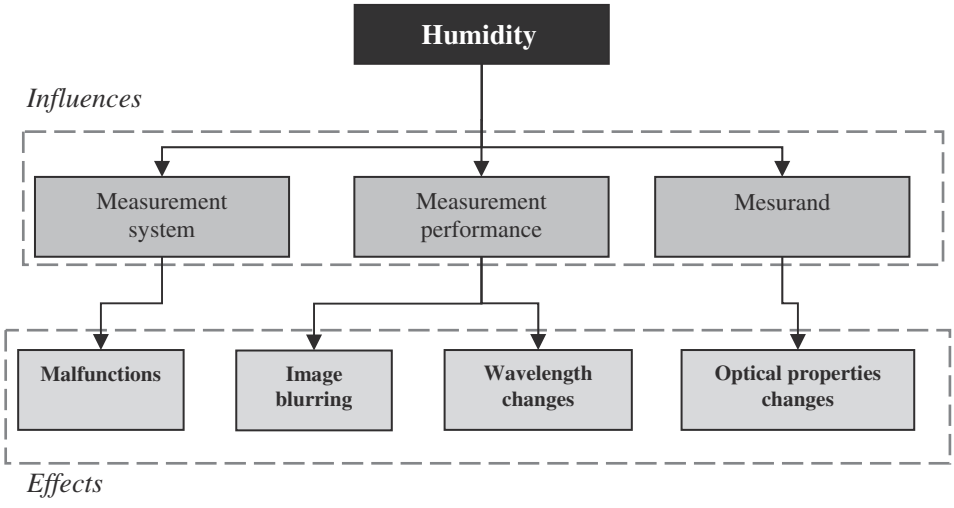

Figure 4.4 Effects of humidity (moisture condensation) on interferometric measurements.

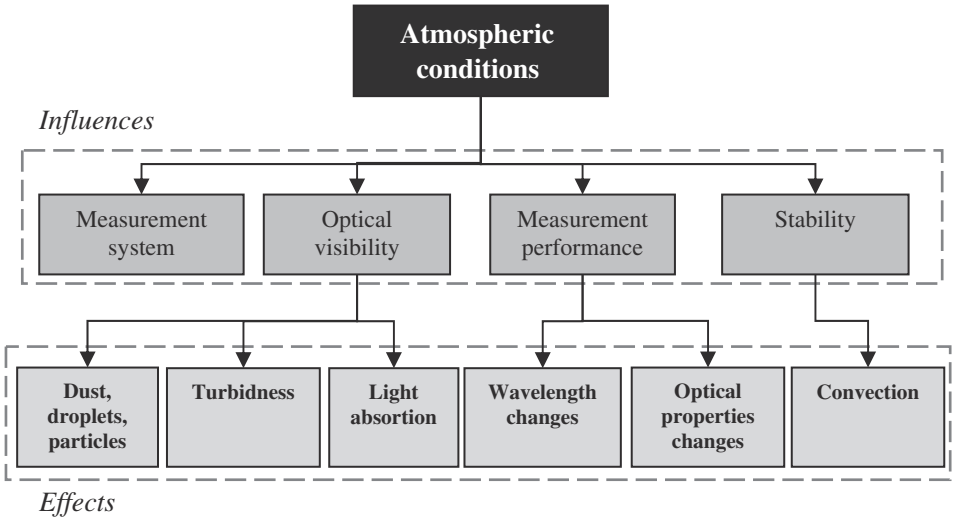

Figure 4.5 Effects of atmosphere and pressure on interferometric measurements.

interferometric measurement because they produce local and rapid variations of the refractive index of the surrounding media. The effects of such instability on interferometric measurement results are uncontrolled phase shifts and motions in the fringe patterns that disturb the fringe processing and deteriorate the measurement uncertainty.

4.2.4 Shock and vibration

Mechanical vibrations and shocks are usually associated with relative motion between the parts of an interferometer or between the interferometer and the mesurand. Several effects of shock and vibration are listed in Fig. 4.6. Severe shock levels can compromise the mechanical integrity of components and, of course, the interferometer itself. The relative motions produced by moderate shocks or mechanical vibration can influence the measurement performance by blurring the interferogram, increasing the level of random errors, and reducing the resolution of the measurement system. Vibrations can also affect the relative alignment of the interferometer parts and the alignment between the interferometer and the specimen.

4.2.5 Radiation and background illumination

Interferometers are usually affected by two kinds of radiation: electromagnetic fields and background illumination, as listed in Fig. 4.7. Strong electromagnetic fields can compromise the life of electronic components, e.g., camera sensors. Moderate electromagnetic fields can degrade the SNR of some electronic components.

On the other hand, background illumination can affect the interferometer performance by reducing the quality of the measurement signal (i.e., fringe

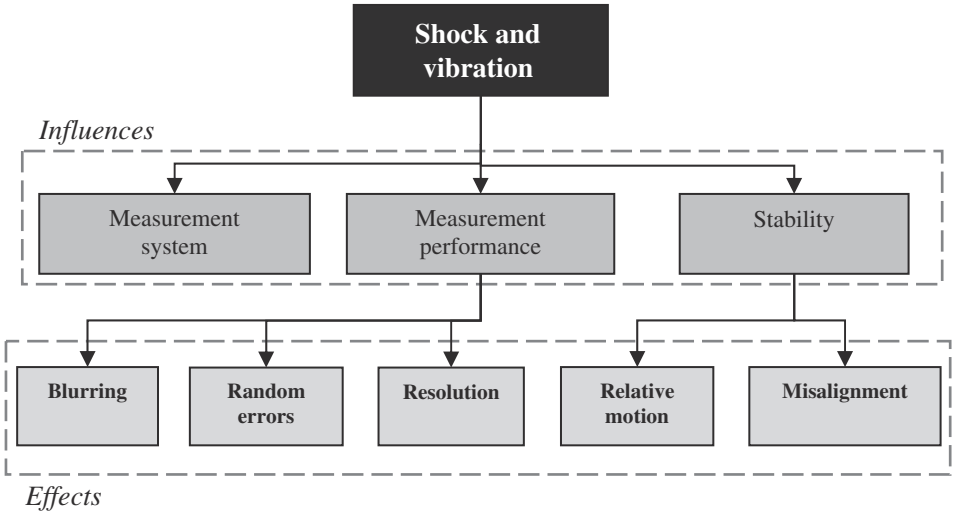

Figure 4.6 Effects of shock and vibration on interferometric measurements.

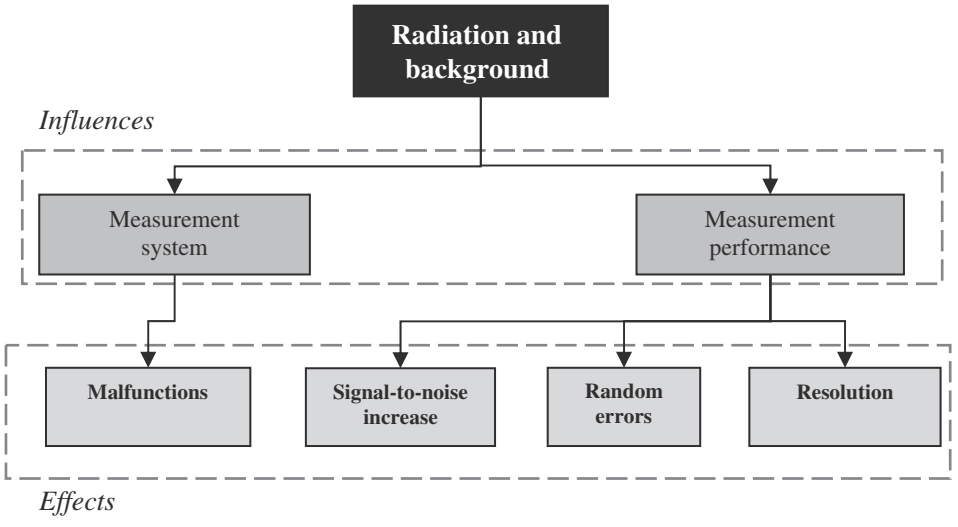

Figure 4.7 Effects of radiation and background illumination on interferometric measurements.

contrast), decreasing the SNR, generating a higher level of random errors, and worsening the resolution.

4.3 Requirements for Robust Measurements

In order to successfully operate outside the laboratory environment with a portable interferometer, some requirements (previously listed in Chapter 1)

should be fulfilled by the interferometer. It must be robust, flexible, compact, stable, user-friendly, and cooperative. Furthermore, a portable interferometer must be affordable to ensure commercial success.

4.3.1 Robust

The interferometer must be robust against environmental demands. Its conception and construction must be designed to coexist with some degree of mechanical vibrations, temperature variations, voltage fluctuations, dust, moisture, and daylight. Because it is generally impossible to prevent mechanical vibrations of the specimen, the interferometer design must be optimized to minimize the relative motion among its parts and between the interferometer and the specimen to be measured. The configuration and measurement principle should be (ideally) insensitive to temperature variations, or an efficient compensation strategy can be used. The electronic devices must be either resistant to voltage fluctuations or battery operated. If possible, the optical parts must be assembled in a sealed enclosure to avoid dust and droplet contamination and must be protected from daylight.

4.3.2 Flexible

The interferometer conception must be flexible enough to enable adjustment and installation in a variety of specimen geometries. Ideally, the interferometer should be installed without difficulty in flat or curved surfaces, as well as in magnetic or nonmagnetic materials. It should have proper alignment devices to allow for fast positioning and effective alignment between the interferometer and the specimen.

4.3.3 Compact

It is highly desirable that interferometers have a compact design. A compact size is not only important when placing the interferometer in small places; it is also a fundamental issue in order to achieve stiffness and mechanical robustness against shock and mechanical vibrations. A compact design is also an important feature for easy transportation to field measurements.

4.3.4 Stable

Long-term stability is desirable for any portable measurement device. Ideally, the system will remain reliable and traceable everywhere and at all times. No further calibration should be required. This condition can only be true if the response of the interferometer has no time or temperature dependency, thus maintaining stable metrological parameters.

4.3.5 User-friendly

The interferometer must be easy to use. It should be simple to transport, install, adjust, and operate. It is also highly desirable that it is able to present

on-demand, clear results. All of these qualities are important to save time during measurements and to keep the system ergonomic.

4.3.6 Organized

The interferometer should help the user organize the experimental task. The software should guide the user step-by-step to complete the measurement. It should collect and organize the experimental data in a clear and permanent way. The software may also document the test and produce a technical report.

4.4 Possible Solutions to Improve Robustness

There are some possible solutions to make interferometers work outside the laboratory. These solutions can be divided into three main groups: (a) isolation, (b) robustness, and (c) simultaneous isolation and robustness.

Isolating the interferometer from harsh agents is a natural solution. However, an alternative must be provided to make the interferometer capable of receiving a signal from the mesurand. The second group involves making the interferometer robust enough to successfully operate in harsh environments. The third group is a combination of both previous groups.

4.4.1 Isolation

There are several solutions for isolation already available in the market, some of which are discussed in the following subsections.

4.4.1.1 Environmental isolation

Encapsulation is a common in-field solution to isolate the instrument from atmospheric contamination produced by dust, rain, droplets, water sprays, and even the extreme case of underwater operation. The parts to be isolated are kept within a hermetic container, usually with a transparent and cleanable optical window. There is also the possibility of using a nonhermetic container with an open window. In this case, clean and dry air is continuously blown inside the container, resulting in a positive pressure, and producing a permanent air flow through the window from inside to outside, thus blowing away dust and particles. This solution is common for pharmaceutical applications.

4.4.1.2 Temperature isolation

In order to isolate an optical system from excessive surrounding temperature, it can be kept inside a container built with thermal insulating materials. Active cooling by air conditioning or chilled water circulation can be added in severe cases. Thermoelectric cooling, using the Peltier effect, is another attractive active-cooling possibility. Closed-loop temperature control might be needed for optical systems with strong temperature dependence.

4.4.1.3 Radiation isolation

Faraday cages are effective ways to isolate optical systems from strong electromagnetic fields. A Faraday cage or Faraday shield is an enclosure formed by a conducting material or a mesh of such material. Such an enclosure blocks external static-electric fields.

The interferometer can be isolated from ambient light by keeping the device inside a closed container, thus creating a darkroom. Although this solution is effective, a large darkroom is not practical for applications outside the laboratory. However, a compact interferometer can be packed inside a small and closed container, simultaneously producing isolation against ambient light, electromagnetic fields, and atmospheric effects.

Another possibility to strongly reduce the influence of the ambient light is the use of narrow-bandpass interference filters in front of the imaging system. This is particularly useful for interferometers based on laser light illumination. The interference filter is tuned to the laser wavelength. The amount of ambient light intensity in such a wavelength is usually negligible when compared with the intensity coming from the area illuminated with the laser light. In this case, no darkroom-like container is necessary.

4.4.1.4 Vibration isolation

Passive and active dumping elements are widely used for vibration isolation in laboratory environments. There is a large variety of optical tables equipped with pneumatic or elastomeric isolators. Passive damping is very effective for seismic vibration isolation (coming from the ground underneath the table), but it is affected by varying tabletop loads. Actively damped tables incorporate sensors and electronics to sense and actively damp tabletop vibrations, which is effective for isolation from both kinds of vibrations. These elements are usually not portable.

Active stabilization is another approach that can be used to reduce vibration effects in optical systems. It can make the system more complex and expensive, but it can provide a useful solution for portable devices. The main concept is presented in Fig. 4.8. The optical system is equipped with a sensor capable of detecting the presence of a disturbance that produces mechanical vibrations. The disturbance signal is sent to an appropriate controller that produces a reactive signal with a sign opposite that of the input signal. This signal is sent to an actuator and applied to the optical system. The disturbance-cancelation effect on the optical system is obtained by superimposing both signals.

There are several ways to capture the disturbance signal. Additional photodiodes, CMOS cameras with fast readings in small areas on the active sensor, and additional interferometers are some possibilities. The actuator can be formed by a piezoelectric-driven mirror, optical fibers stretched by a piezoelectric element, a different diode laser injection current, acoustic optical

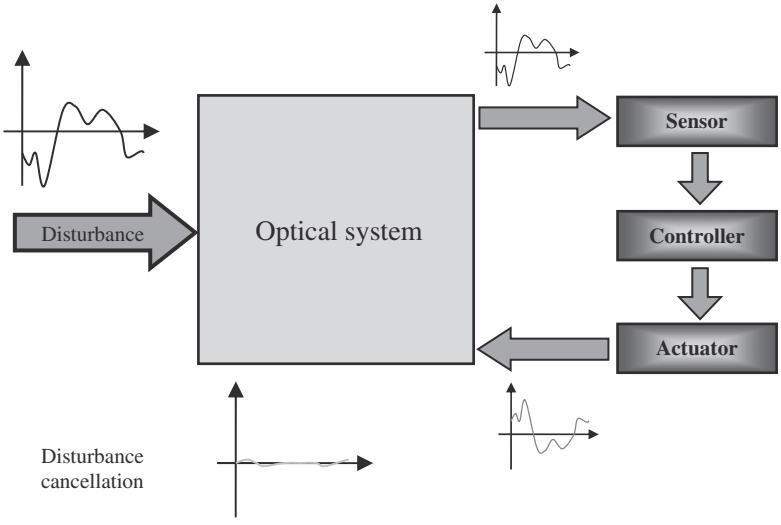

Figure 4.8 Principle of active stabilization.

modulators, etc.[4–6] Commercial fringe-stabilization systems can actively stabilize vibrations from 0–500 Hz, up to λ/20.

4.4.2 Robustness

The Oxford English Dictionary defines the adjective "robust" as (a) strong and healthy; vigorous; (b) sturdy in construction (of an object); (c) able to withstand or overcome adverse conditions (of a process, system, organization, etc.); and (d) uncompromising and forceful. Therefore, a robust interferometer should be able to reliably operate in adverse conditions.

The robustness of an interferometer can be defined by its (a) physical properties and (b) measurement strategies. Robustness in physical properties involves the following aspects:

- **Rigid/stiff construction:** A rigid/stiff mechanical design is very important to reduce relative motions between the interferometer's internal parts, thus increasing the ability of the interferometer to work under moderate vibration levels.
- **Stiff clamping:** An adequate and effective stiff-clamping system is also very important to minimize the relative motions between the interferometer and the specimen surface during the measurement.
- **Compactness:** Compact units are usually stiff and easy to firmly attach to the specimen surface.
- **Monolithic:** Another very attractive approach is achieved by using monolithic constructions. In this case, all active optical components are embedded and integrated in the same solid, transparent media (usually fused silica).[8,9]

The measurement strategies can strongly influence the success of an interferometer performance in nonideal and noncooperative environments. These strategies can be connected to a measurement principle and/or to the data-analysis approach.

- **Common or quasi-common path interferometer:** In these configurations, both interferometer arms are almost equal.[10] Atmospheric or vibration disturbances produce undesirable phase shifts in the interferometer arms by nearly the same amount. Therefore, the phase difference between the arms, which is usually related to the quantity of interest, is not practically affected by the disturbances. Lateral shearing interferometers are examples of quasi-common path interferometers.
- **Robust algorithm:** There are algorithms, capable of tolerating vibrations, that have been developed for phase-shifting calculation.[11–13] They may use sinusoidal phase-shifting algorithms and harmonic analysis,[11] or a combination of fast and slow image-acquisition hardware,[12] or pure mathematic compensation.[13]
- **Fast/one shot:** The most promising approach for interferometry in harsh environments is based on a single-shot measurement.[14–22] The main idea is to use an exposure time short enough to halt the effects of vibrations and atmosphere disturbances. Several approaches, involving the application of carrier fringes,[14,15] polarization and pixelated arrays,[16–20] or simultaneous acquisitions with two wavelengths,[21,22] have been reported. The vibrations effects are simply halted. The effects of convection currents are averaged by combining several repeated measurements.
- **Self-compensating:** It is desirable that the measurement principle, or working algorithm, be self-compensating for long-term temperature or wavelength fluctuations. Some possibilities use achromatic interferometers.[23]

The relationships between the physical properties and measurement strategies, along with their effectiveness against the primary harsh agents, are presented in Table 4.1. A positive signal (+) means a strong effect, and a

Table 4.1 Relationship between robust features and harsh agents.

Feature	Temperature	Environment	Vibration	Humidity	Radiation
Physical properties					
Rigidly stiff construction			+		
Stiff clamping			+		
Compact	−	−	+	−	
Monolithic	−	+	+	−	
Measurement strategy					
Common/quasi-common path	−	+	+	−	
Robust algorithms	−	−	+		
Fast/one shot	−	+	+		−
Self-compensating	+	−	−		−

negative signal (−) means a medium effect. Blank areas correspond to weak or nonexistant effects.

Self-compensating strategies are the most effective at addressing long-term temperature variations. Fast/one-shot measurement is excellent at stopping vibrations and atmosphere effects. When possible, common or quasi-common path configurations are suitable as simple solutions to automatically reduce vibration and atmosphere disturbances. From the perspective of the physical principle, monolithic constructions are very attractive when attempting to reduce vibrations and atmospheric disturbances. The chances of an interferometer successfully operating under vibration are higher if it is stiff, compact, and can be securely clamped on the specimen surface.

References

1. A. Albertazzi, Jr., "Interferometry in harsh environments," *Optical Imaging and Metrology*, W. Osten and N. Reingand, eds., Wiley-VCH, Weinheim, Germany (2012).
2. M. R. Viotti, A. Albertazzi, Jr., and W. Kapp, "Experimental comparison between a portable DSPI device with diffractive optical element and a hole drilling strain gage combined system," *Opt. Lasers Eng*. **46**, 835–841 (2008).
3. A. Albertazzi, Jr. and M. R. Viotti, "In-field loading analysis of pipelines using a radial digital speckle pattern interferometer combined with the hole drilling method," *OPTIMESS 2009: 4th International Conference on Optical Measurement Techniques for Structure & Systems*, Antwerp (2009).
4. M. R. Viotti and A. Albertazzi, Jr., "Industrial inspections by speckle interferometry: general requirements and a case study," *Proc. SPIE* **7389**, 73890G (2009) [doi: 10.1117/12.827585].
5. J. L. Santos, T. P. Newson, and D. A. Jackson, "Electronic speckle-pattern interferometry using single-mode fibers and active fringe stabilization" *Opt. Lett.* **15**, 573–575 (1990).
6. J. Liu, I. Yamaguchi, J. Kato, and T. Nakajima, "Real-time surface shape measurement by an active interferometer," *Opt. Rev*. **4**(1), A216–A220 (1997).
7. P. P. Young, P. S. Priambodo, T. A. Maldonado, and R. Magnusson, "Simple interferometric fringe stabilization by charge-coupled-device-based feedback control," *Appl. Opt.* **45**, 4563–4566 (2006).
8. A. M. Ledger, "Monolithic interferometric angle sensor," *App. Opt.* **14**, 3095–3101 (1975).
9. L. Salbut, "Waveguide grating (moiré) microinterferometer for inplane displacement/strain field investigation," *Opt. Eng.* **41**, 626–631 (2002) [doi: 10.1117/1.1431557].

10. D. Malacara, *Optical Shop Testing*, 3rd Ed., John Wiley & Sons, New York (2007).
11. P. de Groot, "Design of error-compensating algorithms for sinusoidal phase shifting interferometry," *App. Opt.* **48**, 6788–6796 (2009).
12. L. L. Deck, "Vibration-resistant phase-shifting interferometry," *App. Opt.* **35**, 6655–6662 (1996).
13. L. L. Deck, "Suppressing phase errors from vibration in phase-shifting interferometry," *App. Opt.* **48**, 3948–3960 (2009).
14. D. M. Sykora and P. de Groot, "Instantaneous Interferometry: Another View," *International Optical Design Conference (IODC)*, Jackson Hole, WY (2010).
15. J. L. McLaughlin and B. A. Horwitz, "Real-time snapshot interferometer," *Proc. SPIE* **680**, 35–43 (1987) [doi: 10.1117/12.939589].
16. B. Kimbrough, J. E. Millerd, J. Wyant, and J. Hayes, "Low coherence Vibration insensitive Fizeau interferometer," *Proc. SPIE* **6292**, 62920F (2006) [doi: 10.1117/12.682956].
17. J. E. Millerd, "Pixelated phase-mask dynamic interferometers," *Proc. Fringe 2005*, 640–647 (2005).
18. J. Hayes, "Dynamic interferometry handles vibration," *Laser Focus World*, 109–113 (March 2002).
19. K. Freischlad, R. Eng, and J. B. Hadaway, "Interferometer for testing in vibration environments," *Proc. SPIE* **4777**, 311–322 (2002) [doi: 10.1117/12.472245].
20. L. L. Deck, "Environmentally friendly interferometry," *Proc. SPIE* **5532**, 159–169 (2004) [doi: 10.1117/12.559722].
21. J. Kühn, F. Charrière, T. Colomb, E. Cuche, F. Montfort, Y. Emery, P. Marquet, and C. Depeursinge, "Axial sub-nanometer accuracy in digital holographic microscopy," *Meas. Sci. Technol.* **19**, 074007 (2008).
22. J. Kühn, T. Colomb, F. Montfort, F. Charrière, Y. Emery, E. Cuche, P. Marquet, and C. Depeursinge, "Real-time dual-wavelength digital holographic microscopy with a single hologram acquisition," *Opt. Exp.* **15**, 7231–7242 (2007).
23. M. R. Viotti, W. Kapp, and A. Albertazzi, Jr., "Achromatic digital speckle pattern interferometer with constant radial in-plane sensitivity by using a diffractive optical element," *App. Opt.* **48**, 2275–2281 (2009).

Chapter 5
Quantitative Evaluation of Stresses and Strains

5.1 Mechanical Stress and Strain Fields

The usual way to evaluate the integrity of structural parts of machines, buildings, vehicles, aircraft, etc., is based on strength-of-material calculations. This methodology is efficient provided that the component loads are known qualitatively and quantitatively. As explained in Chapter 1, problems occur when loads are unknown or when they are estimated from a determined model. Previously, the risk of overloading was outlined by using safety coefficients, thus generating oversized parts in most cases. However, the aeronautical industry demands light parts, and thus safety margins are stretched considerably. Industry generally uses design strategies that demand saving material for economical reasons (lower costs) and for weighting. In order to satisfy safety requirements and provide adequate service life for the mechanical component, the material stresses must be correctly known. Consequently, the accurate measurement of service stresses is necessary under operational conditions.

The quantity used to evaluate structural parts is the mechanical stress present in the material. Mechanical stresses are virtually impossible to determine under operational conditions.[1] However, a practical method based on a discovery by Robert Hooke can be used for the experimental determination of material stresses. Hooke's discovery found a relationship between stresses and their resulting deformations.[2,3] These deformations, called strains, also occur on the surface of the object, making them accessible for measurement and allowing for assessment of their associated mechanical stress field.

In order to simplify the understanding of the following topics, a short introduction including some definitions about stresses and strains will be presented. In general, when a body is affected by a system of forces, individual points will move. This movement of an arbitrary point is a vectoral magnitude known as displacement or deformation. This vector can be represented by

three components along the Cartesian directions x, y, and z, which are denoted as u, v, and w, respectively.

The motion of a body can be considered as the sum of two parts:[1] (a) a translation and/or rotation of the body as a whole and (b) the movement of points of the body relative to each other. The former is known as "rigid-body motion," and it is applicable to either an idealized rigid body or a real deformable body. The latter is known as "deformation." Rigid-body motions can be small or large, whereas deformations are typically small, except in special mechanical structures or rubber-like materials.

The geometric quantity associated with deformations is called "strain." There are two types of strains: normal strain and shearing strain. For example, Fig. 5.1 shows a bar with an initial length l_o (left image), which is under a compressive force (middle image) and a tensile force (right image). The ratio between the length change (Δl) and the length (l_o) is the strain ε:

$$\varepsilon = \frac{\Delta l}{l_o}, \tag{5.1}$$

where $\Delta l = l_f - l_o$. Therefore, Δl is negative for compressive forces and positive for tensile ones.

Equations relating strain and displacements frequently encountered in the literature have the following reduced forms:[4,5]

$$\begin{aligned} \varepsilon_x &= \frac{\partial u}{\partial x}, & \varepsilon_y &= \frac{\partial v}{\partial y}, & \varepsilon_z &= \frac{\partial w}{\partial z}, \\ \gamma_{xy} &= \frac{\partial u}{\partial y} + \frac{\partial v}{\partial x}, & \gamma_{yz} &= \frac{\partial v}{\partial z} + \frac{\partial w}{\partial y}, & \gamma_{zx} &= \frac{\partial u}{\partial z} + \frac{\partial w}{\partial x}, \end{aligned} \tag{5.2}$$

where ε indicates the normal strains, and γ represents the shear strains.

Figure 5.2(a) shows a body in equilibrium under a set of external loads $F_1 \ldots F_n$ that generates internal forces between the parts of the body. For the section a-a, this body is divided into two parts—A and B—in order to study the internal forces at the point O.

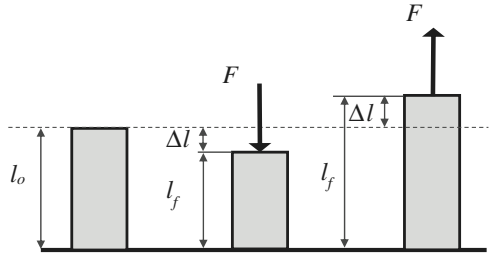

Figure 5.1 Normal strain in a bar: initial length (left), compressive strain (middle), and tensile strain (right).

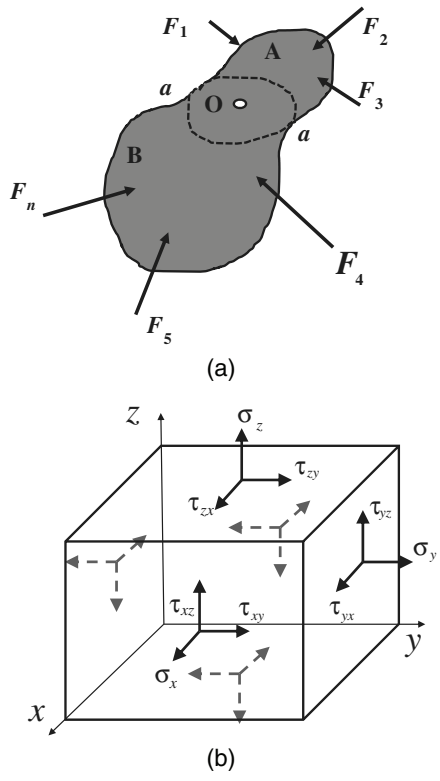

Figure 5.2 (a) Body in equilibrium with a set of external loads. (b) Cubic element at point O.

It can be seen that a part, such as A, is in equilibrium via the action of loads $F_1 \ldots F_n$ and the inner loads applied to section *a-a*, which represents the action of the material of part B on the material of part A. The inner forces are usually assumed to be uniformly distributed as a hydrostatic pressure distributed on the surface on which it acts. The magnitude of these forces is defined by their intensity (force per unit area of the surface where they are applied). These intensities are generally known as stresses in the literature. As before, stresses can be divided in two types: normal stresses, denoted as σ, and shearing stresses, represented by τ. If a very small cubic element is taken into account at point O, the stress field acting on it is represented by Fig. 5.2(b).

Thus, to describe the stress field acting in a cubic element, three symbols (σ_x, σ_y, σ_z) are necessary for normal stresses, and six symbols (τ_{xy}, τ_{yx}, τ_{xz}, τ_{zx}, τ_{yz}, τ_{zy}) for shearing stresses. Via a simple consideration of the equilibrium of the element, the six shearing stresses can be reduced to three. Thus,[5]

$$\tau_{xy} = \tau_{yx}; \quad \tau_{xz} = \tau_{zx}; \quad \tau_{yz} = \tau_{zy}\,. \tag{5.3}$$

By assuming a linear relationship between stresses and strains (Hooke's law), it is possible to write the general stress–strain expressions as

$$\begin{aligned}
\sigma_x &= K_{11}\varepsilon_x + K_{12}\varepsilon_y + K_{13}\varepsilon_z + K_{14}\gamma_{xy} + K_{15}\gamma_{yz} + K_{16}\gamma_{zx},\\
\sigma_y &= K_{21}\varepsilon_x + K_{22}\varepsilon_y + K_{23}\varepsilon_z + K_{24}\gamma_{xy} + K_{25}\gamma_{yz} + K_{26}\gamma_{zx},\\
\sigma_z &= K_{31}\varepsilon_x + K_{32}\varepsilon_y + K_{33}\varepsilon_z + K_{34}\gamma_{xy} + K_{35}\gamma_{yz} + K_{36}\gamma_{zx},\\
\tau_{xy} &= K_{41}\varepsilon_x + K_{42}\varepsilon_y + K_{43}\varepsilon_z + K_{44}\gamma_{xy} + K_{45}\gamma_{yz} + K_{46}\gamma_{zx},\\
\tau_{yz} &= K_{51}\varepsilon_x + K_{52}\varepsilon_y + K_{53}\varepsilon_z + K_{54}\gamma_{xy} + K_{55}\gamma_{yz} + K_{56}\gamma_{zx},\\
\tau_{zx} &= K_{61}\varepsilon_x + K_{62}\varepsilon_y + K_{63}\varepsilon_z + K_{64}\gamma_{xy} + K_{65}\gamma_{yz} + K_{66}\gamma_{zx},
\end{aligned} \tag{5.4}$$

where K_{11} to K_{66} are the coefficients of elasticity of the material.

These 36 coefficients can be reduced to 21 by using strain energy considerations and to 2 by considering the materials to be isotropic. In this latter case, these coefficients are called the modulus of elasticity E and the Poisson coefficient ν. Thus, expressions for normal strains in terms of normal stresses are[4,5]

$$\begin{aligned}
\varepsilon_x &= \frac{1}{E}[\sigma_x - \nu(\sigma_y + \sigma_z)],\\
\varepsilon_y &= \frac{1}{E}[\sigma_y - \nu(\sigma_x + \sigma_z)],\\
\varepsilon_z &= \frac{1}{E}[\sigma_z - \nu(\sigma_x + \sigma_y)].
\end{aligned} \tag{5.5}$$

For the shearing strains,

$$\gamma_{xy} = \frac{2(1+\nu)}{E}\tau_{xy}; \quad \gamma_{yz} = \frac{2(1+\nu)}{E}\tau_{yz}; \quad \gamma_{zx} = \frac{2(1+\nu)}{E}\tau_{zx}. \tag{5.6}$$

The notation $G_r = [2(1+\nu)] / E$ is used. This constant is called the modulus of elasticity in shear, or the modulus of rigidity.

In the same way, expressions for normal stresses as a function of normal strains are

$$\begin{aligned}
\sigma_x &= \frac{E}{(1+\nu)(1-2\nu)}[(1-\nu)\varepsilon_x + \nu(\varepsilon_y + \varepsilon_z)],\\
\sigma_y &= \frac{E}{(1+\nu)(1-2\nu)}[(1-\nu)\varepsilon_y + \nu(\varepsilon_x + \varepsilon_z)],\\
\sigma_z &= \frac{E}{(1+\nu)(1-2\nu)}[(1-\nu)\varepsilon_z + \nu(\varepsilon_x + \varepsilon_y)].
\end{aligned} \tag{5.7}$$

For the shearing stresses,

$$\tau_{xy} = \frac{E}{2(1+\nu)}\gamma_{xy}; \quad \tau_{yz} = \frac{E}{2(1+\nu)}\gamma_{yz}; \quad \tau_{zx} = \frac{E}{2(1+\nu)}\gamma_{zx}. \tag{5.8}$$

More detailed explanations about the theory of elasticity can be found in Dally and Riley[4] and Timoshenko and Goodier[5]. (Plasticity is outside the scope of this book.)

5.2 Experimental Measurement of Stress and Strain Fields

The previous section stated that superficial strains are related to stress fields present in an evaluated material according to equations that use the theory of elasticity. Thus, knowledge gained through the experimental measurement of strain magnitudes can lead to a correct understanding of the real magnitude of stresses acting on a material after loading.

The measurement of strains with strain gages assumes that the strain on the object under investigation is transferred without loss of signal to the strain gage. This requirement involves a close bond between the strain gage and the surface of the object. In most cases, only the external surface of the object is accessible for measurement. In special cases, such as composite materials, the strain gages are molded during the manufacturing of the part.

Several devices involving mechanical, electrical, acoustic, and optical principles were developed and used for strain measurements. Among them, electrical resistance strain gages are the most widely used sensors to monitor mechanical strain fields.[4,6]

For electrical-resistance strain gages, the strain transferred to the strain gage from the surface under measurement causes a change in the electrical resistance of the gage. In general, the resistance R of a uniform conductor with length L, cross-sectional area A, and specific resistance ρ is given by

$$R = \rho \frac{L}{A}. \tag{5.9}$$

By differentiating Eq. (5.9) and dividing by R,

$$\frac{dR}{R} = \left(\frac{d\rho}{\rho}\right) + \left(\frac{dL}{L}\right) - \left(\frac{dA}{A}\right). \tag{5.10}$$

The term dA represents the change in the area A due to the transverse strain, which is equal to $-\nu dL/L$. If the diameter of the conductor before the application of the strain is d_o, then the final diameter will be

$$d_f = d_o\left(1 - \nu\frac{dL}{L}\right), \tag{5.11}$$

and from Eq. (5.10) it is clear that

$$\frac{dA}{A} = -2\nu\frac{dL}{L} + \nu^2\left(\frac{dL}{L}\right)^2 \approx -2\nu\frac{dL}{L}. \tag{5.12}$$

By substituting Eq. (5.12) into Eq. (5.10),

$$\frac{dR}{R} = \frac{d\rho}{\rho} + \frac{dL}{L}(1 + 2\nu), \tag{5.13}$$

which can be rewritten as

$$S_A = \frac{dR/R}{\varepsilon} = 1 + 2\nu + \frac{d\rho/\rho}{\varepsilon}, \tag{5.14}$$

where S_A is the sensitivity of the metallic alloy used as a conductor, and it is defined as the resistance change per unit of initial resistance divided by the applied strain ε.

Equation (5.14) shows that the resistance change is generated partially by (a) the deformation of the electrical conductor used for the strain gage $(1 + 2\nu)$ and (b) the change in the resistivity ρ of the conductor as a result of the microstructural changes $[(d\rho/\rho) / \varepsilon]$.

Most electrical resistance strain gages are fabricated from a copper–nickel alloy called Advance or Constantan. This alloy is useful for the following reasons:[4]

- The value of the strain sensitivity S_A is linear over a wide range of strain. Thus, it can be applied for a wide range of loads, including plastic and elastic strains. Additionally, the hysteresis of bonded filaments is extremely small.
- The value of S_A does not significantly change when the material becomes plastic. Consequently, it has calibration constants that do not vary with the applied strain level. In other words, a single calibration constant is adequate for all levels of measured strains.
- The alloy has a specific resistance, allowing for the construction of small gages.
- The alloy has excellent thermal stability. This feature allows for application and mounting in common structural materials.
- Changes in resistance generated by temperature variations can be controlled by heat treatment or with trace impurities. Thus, temperature-compensating strain gages can be fabricated for several applications.

Finally, Fig. 5.3 shows a single-element strain gage. In order to measure along two directions, two-element gages are usually used whose configuration depends on the application and the manufacturer.

The strains to be measured with strain gages are generally very small; consequently, changes in the resistance of the conductor of the gage will be also very small (infeasible to measure with an ohmmeter). For this reason, the strain

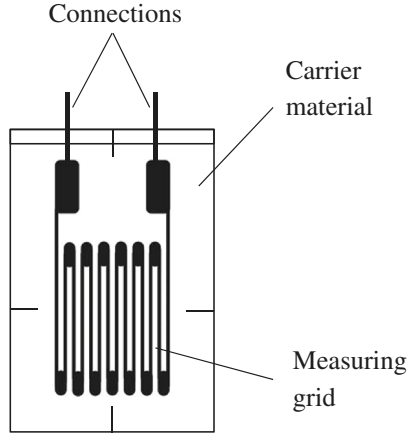

Figure 5.3 Single-element strain gage following a flat-grid construction.

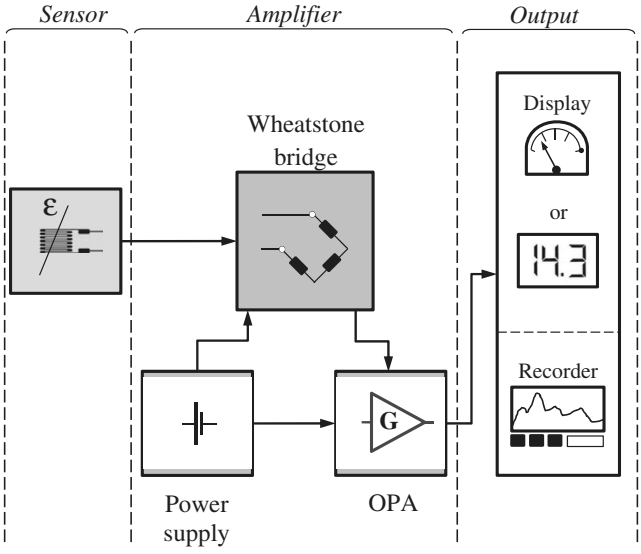

Figure 5.4 Measurement system for strain monitoring.

gage is included in a measurement system where the precise determination of the resistance change would be possible. Figure 5.4 shows a simple scheme of a measurement system for measuring strains with a strain gage.

The first component is formed by the sensor, which is the strain gage. In this case, the sensor transforms mechanical strain into an electrical resistance signal. The second element is the amplifier. This is formed by a Wheatstone bridge with the strain gage as one arm. The power source supplies the energy (constant voltage or constant current) to obtain a useful signal. When the resistance of the strain gage changes, the bridge circuit loses its symmetry and becomes unbalanced. Thus, an output voltage proportional to the bridge's unbalancing is generated. The operational amplifier (OPA) amplifies the output voltage to a level suitable to be shown in an output device (display). Depending on the measurement system, the display will show the output as a voltage value, as a current value, or directly as the applied strain. Additional elements, such as filters, scanners, transient recorders, etc., can be added to increase the versatility of the measurement system.

5.3 Interferometric Solutions to Measure Mechanical Stress and Strains

Despite the fact that the portability, robustness, accuracy, and range of measurement of strain gages have been firmly established, they have some drawbacks:

- The installation process takes a long time because the surface must be prepared to have an adequate roughness and flatness to correctly adhere to the electrical sensor.

- Installation requires the skills and aptitudes of a well-trained technician to avoid trouble during the cleaning and gluing process.
- Two elements, or two-element stacked rosettes, are used to monitor the 2D state of stresses.[4] A gage (or both gages in a rosette) can sometimes malfunction, thus necessitating removal and reinstallation of the rosette.[7]

In order to overcome strain-gage drawbacks, optical techniques can be used as alternative methods to evaluate displacement fields from generated fringe patterns, among which is moiré interferometry. The measurement of in-plane displacements and strains was investigated with this technique[8–10] by developing laboratory systems not suited for industrial applications. Conversely, a grating (moiré) interferometer adequate for outdoor measurements was also developed.[11,12] Despite the fact that grating (moiré) interferometry has high-quality interferograms (high interference contrast and low noise), wide strain range, and easy alignment and operation,[11] it requires additional modification of the object surface because a reflection phase grating is glued on it.

A traditional interferometer with in-plane sensitivity, similar to that shown in Fig. 3.4, can measure on the surface to be investigated. The main direction of the principal stresses is usually unknown in practical situations; therefore, the sensitivity direction will be close to or coincident with the principal direction of stresses in order to have a strong signal of displacements. As an alternative solution, three observations or three different illumination directions can be used to obtain the three unknown displacement components.[13–17] Additionally, an analysis has been carried out regarding the effect of illumination beam divergence on the sensitivity vector.[18–21] Martínez et al.[22] provide a possible layout used to measure displacements in three sensitivity directions; Fig. 5.5 shows the optical layout that they developed. Figures 5.5(a) and (b) have in-plane sensitivity, and Fig. 5.5(c) has out-of-plane sensitivity. In this case, the illumination setup is rotated by placing the switcher after the laser output. Thus, a set of three interferograms is acquired before and after the deformation of the object.

Figure 5.6 shows another possible layout presented by Martinez et al.[22] In this case, the laser light is split into two beams: one beam serves as the reference beam, and the other is used sequentially to illuminate the object along three different directions, thus obtaining three different sensitivities along the reference-beam direction.

When these setups are analyzed by using the list provided in Chapter 4, the "Robust" and "Compact" requirements are not completely fulfilled because these systems are usually bulky. Therefore, a large environmental-isolation structure should be developed for use outside the laboratory. Despite these drawbacks, the optical layouts shown in Figs. 5.5 and 5.6 is suitable for 3D displacement measurements because it can also evaluate out-of-plane displacements with a complete description of the deformation field that occurred on the surface of the material being evaluated.

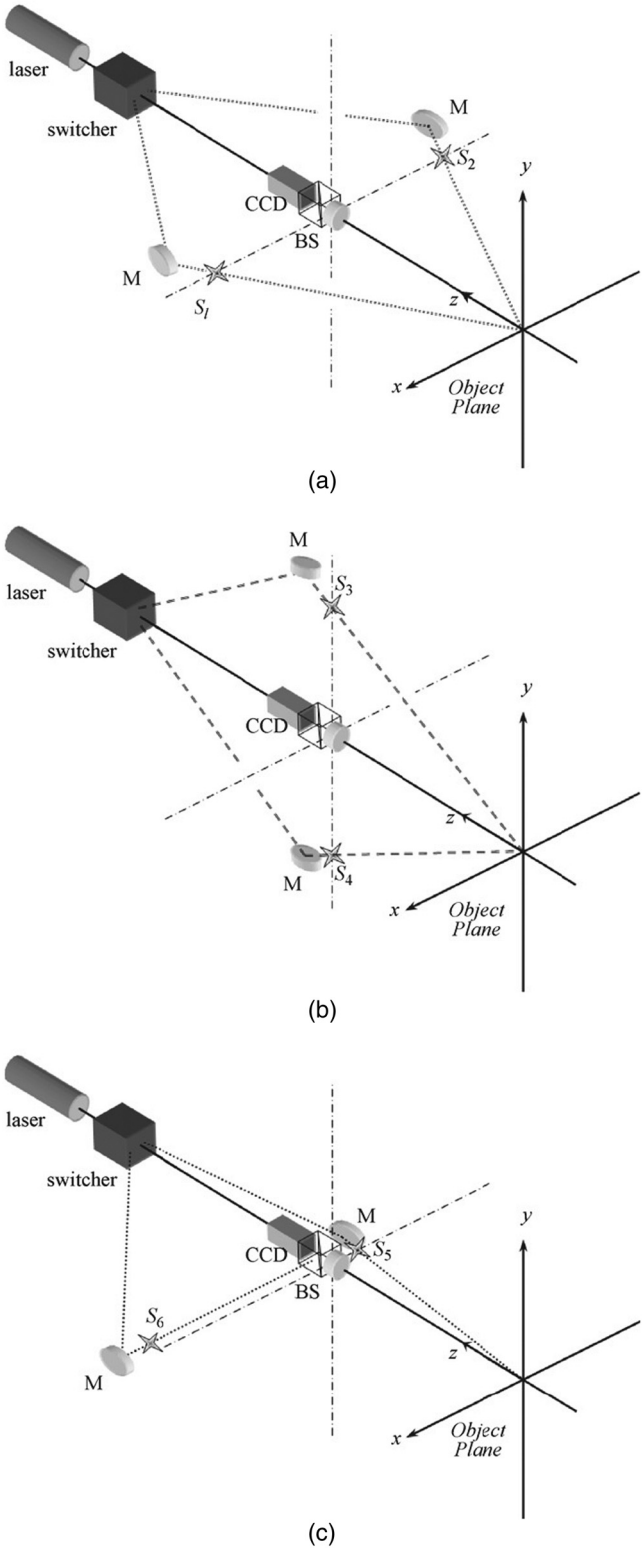

Figure 5.5 (a) Dual-beam optical setup with *x* sensitivity, (b) dual-illumination interferometer with *y* sensitivity, and (c) one-beam interferometer with *z* sensitivity (reprinted from Martinez et al.[22] with permission).

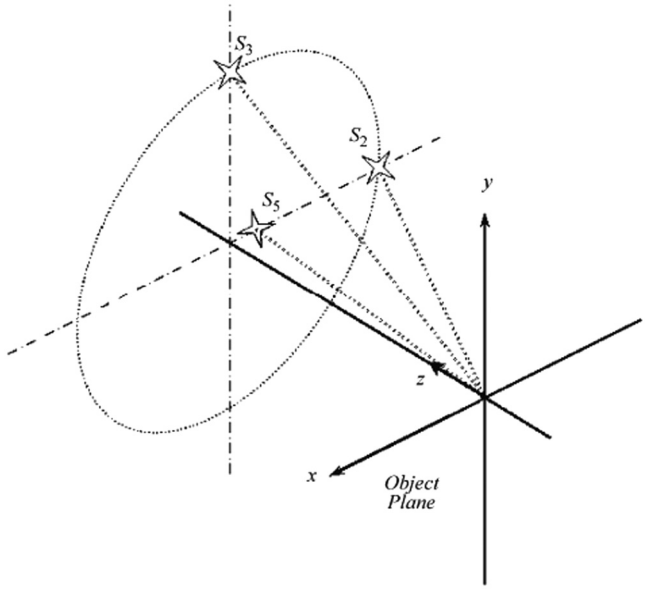

Figure 5.6 Scheme of the ESPI system with three illumination beams (reprinted from Martinez et al.[22] with permission).

In several applications, the local measurements of strains generated in the surface of the material (only in-plane movements of the surface) are enough to quantify and describe the stress field in this material. In these cases, out-of-plane displacements are considered negligible. Thus, the interferometer of Fig. 3.10 is a suitable tool to discover only the in-plane displacement fields. Because this interferometer measures displacements in polar coordinates, expressions relating measured radial displacements to applied stresses and strains should be developed in polar coordinates.

The polar radial-displacement field measured in a circular region provides sufficient information to characterize the mean level of rigid-body translations as well as strain or stresses that occur in that region. For uniform displacements and strain or stress fields, the full determination of the associated parameters is almost a straightforward process.[23,24]

If a uniform in-plane translation is applied on the specimen surface, the following radial displacement field is developed:

$$u_r(r, \theta) = u_t \cos(\theta - \alpha), \tag{5.15}$$

where u_r is the radial component of the in-plane displacement, u_t is the amount of uniform translation, α is the angle that defines the translation direction, and r and θ are polar coordinates. Readers can note that the displacement field does not depend on the radius r at all.

When a uniform stress field is applied to the measured region, the radial in-plane displacement field can be derived from the linear strain-displacement

or stress-displacement relations. Cartesian coordinates (x and y) are usually used to describe strain or stress states. Because the radial in-plane speckle interferometer measures polar coordinates, the strain and stress states are better described in terms of the principal axis 1 and 2, where the strains and stresses assume the maximum and minimum values, respectively. If η is the angle that the principal axis 1 forms with the x axis, the in-plane radial displacement field is related to the principal strain and stress components by the following equations:[24]

$$u_r(r,\theta) = \frac{r}{2}\left[(\varepsilon_1 + \varepsilon_2) + (\varepsilon_1 - \varepsilon_2)\cos(2\theta - 2\eta)\right], \tag{5.16}$$

$$u_r(r,\theta) = \frac{r}{2E}\left[(1-\nu)(\sigma_1 + \sigma_2) + (1+\nu)(\sigma_1 - \sigma_2)\cos(2\theta - 2\eta)\right], \tag{5.17}$$

where ε_1 and ε_2 are the principal strains, σ_1 and σ_2 are the principal stresses, E and ν are the material's Young modulus and Poisson ratio, respectively, and η is the principal angle.

Figure 5.7 shows two examples of interferograms obtained with a radial in-plane speckle interferometer. In this case, the phase difference fringes correspond to the radial displacement component. The left part of picture is related to a displacement pattern of pure translation ($u_t = \sim 1.5$ μm) in a direction $\alpha = 120$ deg with the horizontal axis. Note that the fringes due to pure translation are straight lines pointing to the polar origin. That behavior is predicted by Eq. (5.15) because the radial displacement component is independent of the polar coordinate r. The phase difference pattern on the right of Fig. 5.7 is due to a single stress state of ~40 MPa applied in a steel specimen in the vertical direction. Note that due to Poisson's effect, the

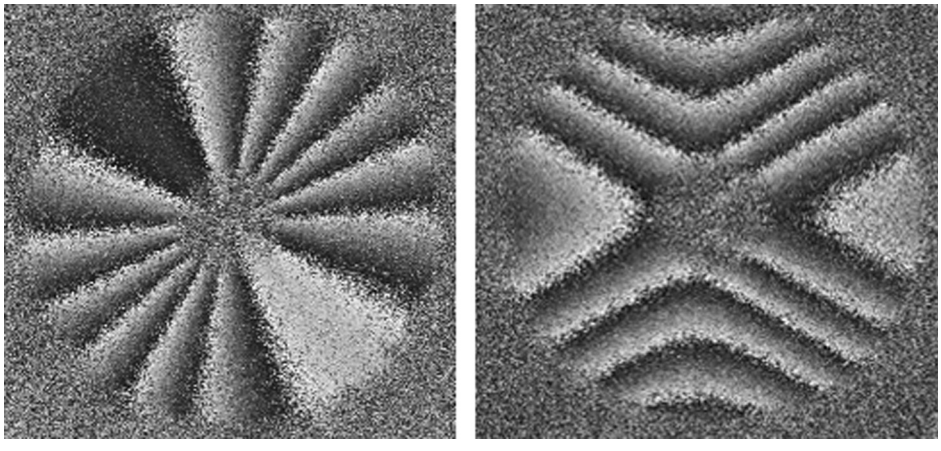

Figure 5.7 Two wrapped-phase maps obtained with the radial in-plane speckle interferometer. Left: pure translation. Right: a uniaxial stress field applied in the vertical direction.

number of fringes in the vertical axis is approximately three times larger than in the horizontal one.

In order to quantify the rigid-body translations or mechanical stress fields from the measured radial in-plane displacement field, two approaches can be used: (a) the Fourier approach or (b) the least-squares solution. The former uses data from a single sampling circle, concentric with the polar origin, and the latter uses the whole image.

For the Fourier approach, a finite number of regularly spaced sampling points can be extracted from the same circular line. From this dataset, the first three Fourier series coefficients are computed by Eqs. (5.18). To determine the amount of translation u_t, it is necessary to compute the sine and cosine components and the total magnitude of the first Fourier series coefficient by[24]

$$\begin{aligned} H_{nS}(r_s) &= \int_0^{2\pi} u_r(r_s,\theta)\sin(n\theta)d\theta, \\ H_{nC}(r_s) &= \int_0^{2\pi} u_r(r_s,\theta)\cos(n\theta)d\theta, \\ H_n(r_s) &= \sqrt{H_{nS}^2(r_s)+H_{nC}^2(r_s)}\,, \end{aligned} \tag{5.18}$$

where r_s is the sampling radius, $H_{nS}(r_s)$ and $H_{nC}(r_s)$ are respectively the sine and cosine component of the n^{th} Fourier series coefficient, and $H_{nS}(r_s)$ is the total magnitude of the n^{th} harmonic. As a singular case, note that if $n = 0$, components $H_{0S}(r_s) = 0$ and $H_{0C}(r_s) = H_0(r_s)$ will be equal to the mean value of $u_r(r_s, \theta)$ along the sampling radius r_s.

In order to compute the translation component u_t, Eq. (5.15) can be expanded to

$$u_r(r,\theta) = u_t\cos(\alpha)\cos(\theta) + u_t\sin(\alpha)\sin(\theta). \tag{5.19}$$

In this case, only the first harmonic is present. The translation amount u_t and its direction α can be computed from the first Fourier series coefficient by

$$\begin{aligned} u_t &= H_1(r_s), \\ \alpha &= \tan^{-1}\left(\frac{H_{1S}(r_s)}{H_{1C}(r_s)}\right). \end{aligned} \tag{5.20}$$

In the same way, the cosine term of Eq. (5.17) can be expanded:

$$\begin{aligned} u_r(r,\theta) = {} & \frac{r(1-\nu)}{2E}(\sigma_1+\sigma_2) + \frac{r(1+\nu)}{2E}(\sigma_1-\sigma_2)\cos2\theta\cos2\eta \\ & + \frac{r(1+\nu)}{2E}(\sigma_1-\sigma_2)\sin2\theta\sin2\eta. \end{aligned} \tag{5.21}$$

As before, it is possible to verify that the principal stresses and direction can be determined from the zero- and second-order Fourier coefficients by

$$\sigma_1 = \frac{E}{r_s}\left(\frac{H_0(r_s)}{1-\nu} + \frac{H_2(r_s)}{1+\nu}\right),$$

$$\sigma_2 = \frac{E}{r_s}\left(\frac{H_0(r_s)}{1-\nu} - \frac{H_2(r_s)}{1+\nu}\right),$$

$$\eta = \frac{1}{2}\tan^{-1}\left(\frac{H_{2S}(r_s)}{H_{2C}(r_s)}\right). \tag{3.22}$$

In practical situations, it is very usual that both stresses and rigid-body translations are mixed in the same interferogram. They can be measured simultaneously and computed independently because different Fourier series coefficients are involved and the terms of a Fourier series are mutually orthogonal.

The other approach is based on the least-squares method. In this approach, a set of experimental data is sampled from the measured displacement field. No particular sampling strategy is required, but it is a good practice to select sampling points regularly distributed over the whole measured region. The sampled data is fitted to a mathematical model by least squares. An appropriate mathematical model can be obtained by adding and rewriting Eqs. (5.19) and (5.21):

$$\begin{aligned} u_r(r,\theta) = {} & K_{0R}(1-\nu)r + K_{1C}\cos(\theta) + K_{1S}\sin(\theta) \\ & + K_{2C}(1+\nu)r\cos(2\theta) + K_{2S}(1+\nu)r\sin(2\theta) + K_0. \end{aligned} \tag{5.23}$$

Terms K_{0R}, K_{1C}, K_{1S}, K_{2C}, and K_{2S} are easily identified by comparison with Eqs. (5.19) and (5.21). K_0 is an additional term that was only introduced to account for a constant bias in the phase pattern that can be occasionally caused by a thermal drift.

At least six measured points are necessary to determine all six coefficients; tens of thousands of measured points are usually used, and the coefficients are computed by the least-squares method. Because the coefficients are all linear, the least squares can be conducted simply by using a multilinear fitting procedure. The displacement and stress components can be computed from the fitted coefficients by the following set of equations:

$$u_t = \sqrt{K_{1C}^2 + K_{1S}^2},$$

$$\alpha = \tan^{-1}\left(\frac{K_{1S}}{K_{1C}}\right),$$

$$\sigma_1 = E\left(K_{0R} + \sqrt{K_{2C}^2 + K_{2S}^2}\right),$$

$$\sigma_2 = E\left(K_{0R} - \sqrt{K_{2C}^2 + K_{2S}^2}\right),$$

$$\eta = \frac{1}{2}\tan^{-1}\left(\frac{K_{2S}}{K_{2C}}\right). \tag{5.24}$$

Two practical optical setups that use the DOE for radial in-plane measurements are shown in Figs. 5.8(a) and (b). (These setups were previously presented and discussed in Chapter 3, but a more-detailed explanation is provided here to complement the following example application.) In the setup shown in Fig. 5.8(a),[26,27] the light L emitted from a diode laser is expanded by the lens E. It then passes through the elliptical hole of mirror M_1, which forms a 45-deg angle with the axis of the DOE, impinges mirrors M_2 and M_3, and reflects back to mirror M_1. After that, the expanded light is directed to the collimating lens CL, thus obtaining an annular collimated beam. Finally, the light is diffracted by the DOE, primarily in the first diffraction order toward the center of the circular region on the specimen surface. The elliptical hole in mirror M_1 is very important to avoid triple illumination in the central circular measurement area and also to promote a viewing window for the imaging system located in the CCD camera. The diameter of the double-illuminated circular region is $\sim$10 mm.

In order to build a more robust and compact device used principally to measure mechanical stress fields, the DOE should be as small as possible. Consequently, the central hole of the 45-deg mirror M_1 should be smaller, and the manufacturing of the hole becomes a complex task because its diameter decreases considerably and two perpendicular milling steps are needed. To overcome this practical problem, an off-axis configuration in accordance with Fig. 5.8(b) was developed.[28] As before, the illumination beam emitted by the diode laser L is expanded by the lens E and passes through the central window of the first 45-deg plane mirror M_4. After that, the light reaches mirrors M_2 and M_3 and is reflected toward M_4, which reflects the light to the collimating lens CL. The central window of the mirror M_4 is actually an oblique hole that has two functions: (a) to allow the laser beam to reach mirrors M_2 and M_3 and

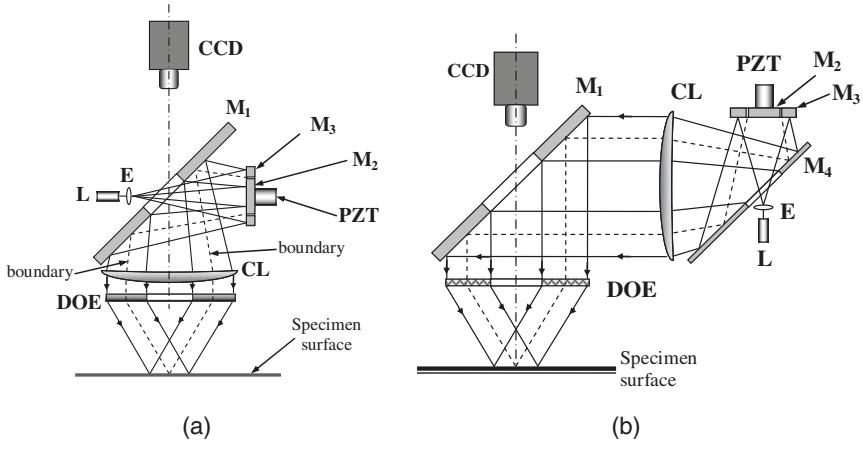

Figure 5.8 (a) Traditional optical arrangement of a radial in-plane interferometer with a DOE; (b) off-axis configuration.

(b) to avoid letting the central portion of the laser beam be reflected by these mirrors, instead directing it to the collimating lens CL. After coming out of the lens, the annular laser beam is collimated by being directed to the second 45-deg plane mirror M_1 and deflected to the DOE. Finally, the light is diffracted by the DOE primarily in the first diffraction order toward the specimen surface, thus obtaining an illuminated area of $\sim$5 mm in diameter. As previously indicated, residual nondiffracted light or light from higher diffraction orders cannot be considered a problem because it is not directed to the central measuring area on the specimen surface.[27]

In both cases, mirrors M_2 and M_3 are two special circular mirrors. The former is bound to a piezoelectric actuator PZT, and the later has a circular hole with a diameter slightly larger than the diameter of M_2. Because M_3 is fixed, a relative phase difference between the beam reflected by M_2 (central beam) and the one reflected by M_3 (annular beam) is introduced when the PZT moves the mirror M_2 along its axial direction. The boundary between both beams is indicated in Figs. 5.8(a) and (b) with dashed lines. According to these figures, readers can see that every point over the illuminated area receives one ray coming from M_2 and other one from M_3. Thus, the PZT enables the introduction of a uniform phase shift in all double-illuminated circular areas to calculate the optical phase distribution by means of phase-shifting algorithms.[29,30]

The intensity of the light is not constant over the whole circular illuminated area on the specimen surface, and it is particularly higher at the central point because it receives light contributions from all cross-sections. As a result, a very bright spot will be visible at the central part of the circular measurement region, and thus the fringe quality will be reduced. For this reason, the outlier diameter of mirror M_2 and the diameter of the central hole of M_3 are computed, obtaining a gap of $\sim$0.5 mm and blocking the light rays reflected to the center of the measurement area.

Finally, the illuminated area is imagined by a USB 2.0 digital video camera joined to a lens system. The camera has 1296×964 pixels and 8 bits (256 gray levels). Figure 5.9 shows a photograph of the sensor that shows the camera (at the top) as well as its compact construction and clamping system.

The universal base and the measurement module presented by Viotti et al.[26] have been successfully used as a strain sensor for residual-stress measurement using the blind hole-drilling method. In this case, the universal base is rigidly attached to the specimen surface by means of four adjustable and strong magnetic legs in combination with three rigid feet with sharp conical tips. The feet are located quite a way from each other. This kind of clamping system has managed to successfully reduce the relative out-of-plane and in-plane motion between the universal base and the specimen surface primarily for residual-stress measurements, where there is no relative motion among the legs. Chapter 6 explores this measurements system in greater detail.

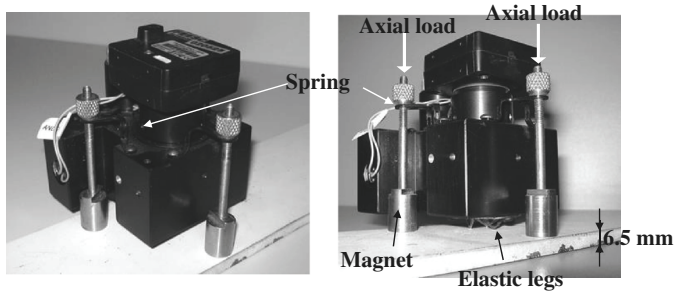

Figure 5.9 Photographs of the strain sensor. The steel bar on which it is placed has a thickness of ~6.5 mm.

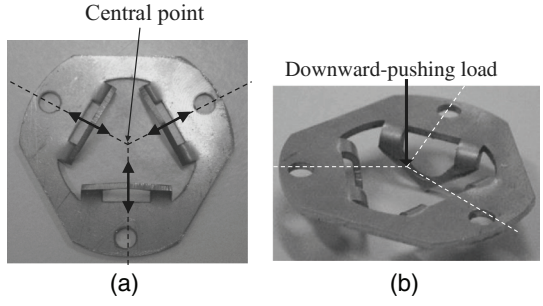

Figure 5.10 Photographs of elastic legs showing the stiffness principle.

Mechanical strains or stresses applied on a mechanical part have a different behavior. They will produce displacement fields over the whole surface where the device is clamped. For this reason, if the portable device in Viotti et al.[26] were used to monitor this kind of displacement, excessive unwanted relative motion would occur among the rigid clamping legs, which can produce excessive relative translations of the measured surface and degrade the fringe quality. Therefore, unhandled rigid clamping is not a good solution for measuring displacements where the whole specimen surface moves. A solution that uses elastic legs capable of absorbing relative motion would be a better option.

Figure 5.9(b) and Figs. 5.10(a) and (b) illustrate an elastic clamping system developed for the strain sensor. It consists of two parts: (a) a set of elastic legs and (b) a set of special springs and magnets. The former is composed of a steel plate with three legs. According to Fig. 5.10(a), each leg has a triangular shape and two main stiffness directions: a weak one (along the arrow's direction) and a strong one (orthogonal to the arrow). If an axial load is applied on the three legs [see Fig. 5.10(b)], they will be pressed and fixed on the specimen surface, and a displacement of the specimen surface will simultaneously deform the three legs primarily along their weak stiffness directions. Consequently, the central point [intersection of the dashed lines in

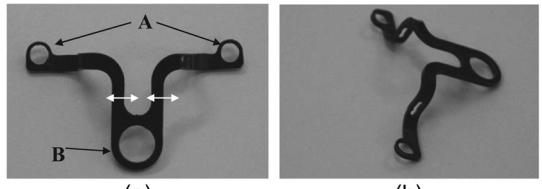

Figure 5.11 Special springs with different stiffness in two orthogonal directions.

Figs. 5.10(a)] will stay at nearly the same place, and the sensor will measure only displacements produced by mechanical stresses and not translations of the sensor structure (rigid-body displacements). The three legs are separated by a short distance, which helps to decrease their deformation and possibly increase the rigid-body translation.

Finally, the other important part of the clamping system involves three special springs and three associated magnets. Figure 5.11 shows two views of the springs. They are fixed to the body of the strain sensor by means of holes A and connected to the magnets by hole B. Through this hole, magnets apply an axial load that bends each spring, transmitting a downward load to the body of the strain sensor that is also applied to the elastic legs of Fig. 5.10. Because the magnets have a stiff contact with the specimen surface, they can move by surface displacements and transmit unwanted rigid-body displacements to the body of the sensor. In order to avoid this, springs are mounted on the body of the strain sensor in accordance with the position of the three elastic legs. Thus, the weak stiffness of the spring along the two white arrows in Fig. 5.11(a) is coincident in position with the strong stiffness of the elastic legs (see Fig. 5.12). This arrangement allows springs to produce the downward force without changing the stiffness of the elastic legs and without generating rigid-body translations because the springs open or close their arms [see Fig. 5.11(a)] according to the relative movement between holes A and B.

Figures 5.13(a) and (b) show two examples of interferograms, obtained with the measurement sensor shown in the previous section, for a compressive uniaxial stress state of $\sim$135 MPa. This load was applied on a steel specimen along the horizontal and vertical directions, respectively. These interferograms clearly show that radial in-plane sensitivity allows for the quick identification of principal stress directions with only one phase map.

Phase maps of Figs. 5.14 were processed by using Eqs. (5.19) and (5.21) to remove possible rigid-body translations generated during the measurement process. For example, Fig. 5.14(a) shows the original phase map mixing a small rigid-body displacements and a mechanical stress displacement field. Figure 5.14(b) shows the synthesized phase map obtained from the rigid body translation presented in Fig. 5.14(a). In this case, the rigid-body translation had a magnitude of $\sim$0.53 μm.

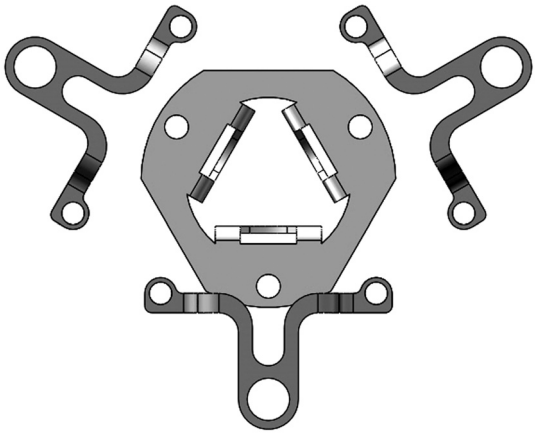

Figure 5.12 Mounting diagram of the elastic legs and the springs in order to avoid increasing the stiffness along the weak direction of the elastic legs.

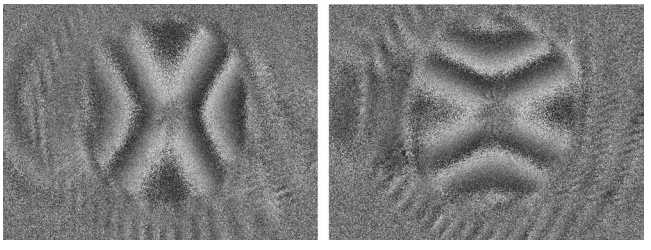

Figure 5.13 Radial in-plane component for a mechanical stress of ~135 MPa applied along the horizontal (left) and vertical (right) directions.

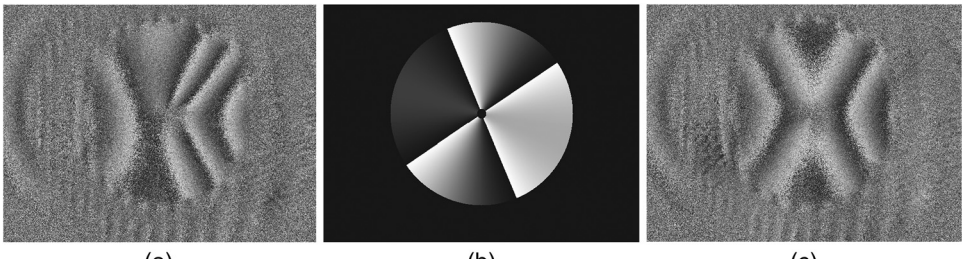

(a) (b) (c)

Figure 5.14 (a) Phase map mixing rigid-body and mechanical stress displacements; (b) synthesized phase map computed from the rigid-body displacement of Fig. 5.14(a); and (c) phase map obtained from subtracting Fig. 5.14(a) from 5.14(b), corresponding to pure mechanical stress displacements.

5.4 In-Field Applications

Figure 5.15 shows the experimental setup used to generate several levels of mechanical stresses corresponding to mechanical strains ranging from 50 μm/m

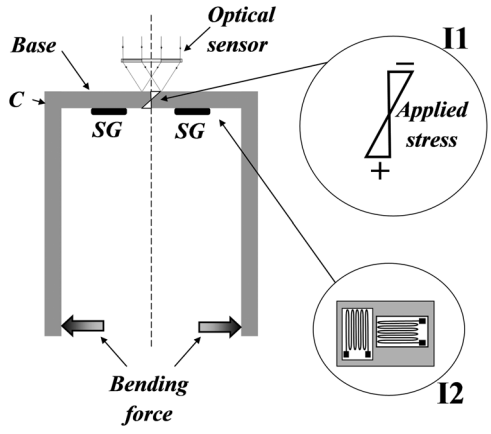

Figure 5.15 Four-point bending device showing where the sensors were placed.

to 800 μm/m. According to this scheme, a compressive load is applied to both arms of the U-body in order to open them. Consequently, a four-point bending configuration is obtained, thus producing a uniform bending moment over the base of the U-body (see stress distribution in the inset I1). Thus, a tensile stress is generated on the bottom surface that is monitored by a couple of two-element stacked rosettes symmetrically placed from the center of the U-body. In the same way, a compressive stress is produced on the top of the base and is simultaneously monitored by the optical strain sensor. Due to the four-point bending configuration, the optical strain sensor as well as the strain-gage rosettes measure the same strain value, which is uniform in the whole area covered by all sensors, but with the opposite sign. Strain gages are placed in the bottom part of the U-body to avoid problems while positioning the optical strain sensor.

In order to determine the applied strain and stress fields, the following experimental procedure is conducted. First, strain-gage rosettes are connected to a direct-reading strain indicator and zeroed. Two stacked rosettes (see inset I2 in Fig. 5.15) are used to measure two orthogonal strain directions coincident with the principal strain and stress directions. After that, the strain sensor is placed over the top face of the U-body and fixed by the clamping system. After the radial interferometer is positioned, a set of five phase-shifted speckle interferograms is acquired, and the reference phase distribution is calculated by the five-frame algorithm[30] and finally stored in a computer. The load is then applied, opening the arms of the U-body to reach a predefined reference strain value. The strain-gage values are then read, a second set of five phase-shifted speckle interferograms is acquired, and a new phase distribution is calculated and stored. Finally, the wrapped-phase difference map is evaluated, and the U-body is unloaded. This experimental procedure is repeated for several strains and their associated stress values, starting with a reference strain value of 50 μm/m and going to 800 μm/m with increments of 50 μm/m.

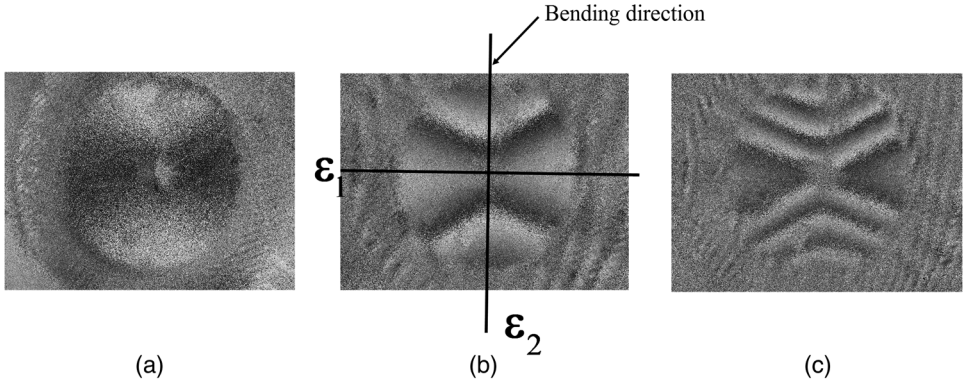

Figure 5.16 Wrapped-phase maps for a reference strain of (a) 50 μm/m, (b) 400 μm/m, and (c) 800 μm/m.

For example, Figs. 5.16(a)–(c) show phase maps corresponding to strain references of 50, 400, and 800 μm/m, respectively. The maximum mechanical strain direction ε_1, the minimum ε_2, and the bending direction are indicated in Fig. 5.16(b).

Figure 5.17(b) shows that relative deviations are larger for smaller reference strains values, namely, 50 μm/m and 100 μm/m are near 10%. For larger reference strain values, relative deviations range from 1.4% to 4.3%. Large deviation values for smaller strain magnitudes can be explained by observing their respective measured phase maps [e.g., Fig. 5.16(a)] and by noting that they have less than one fringe, which might be corrupted by speckle noise, thus considerably increasing the error. When the absolute deviation is evaluated and considered for the analysis (differences between strains measured by the strain-gage sensor and the optical sensor), it ranges from −3.71 μm/m to −23.05 μm/m for nearly all measured values.[31] Thus, agreement can be found between measurements realized with optical sensors and strain gages.

In the example presented here, relative deviations obtained for maximum strain magnitudes oscillated between −4.7% and 15.1% [see Fig. 5.17 (a)]. They were larger than deviations for minimum strains. However, when absolute deviations were analyzed, they ranged from −7.08 μm/m to −10.73 μm/m. Even though large values of relative deviations were assessed, reasonable agreement could be found between both sensors because they successfully found transversal strains with close values of magnitude and primarily the same sign.

Finally, Fig. 5.17(c) shows a plot of the measured stress field. According to this plot, readers can see that measured compressive stresses followed the increase of the reference strains. Moreover, because reference strain increments were performed in consecutive and incremental steps of 50 μm/m, measured stresses presented a linear behavior when they were related to

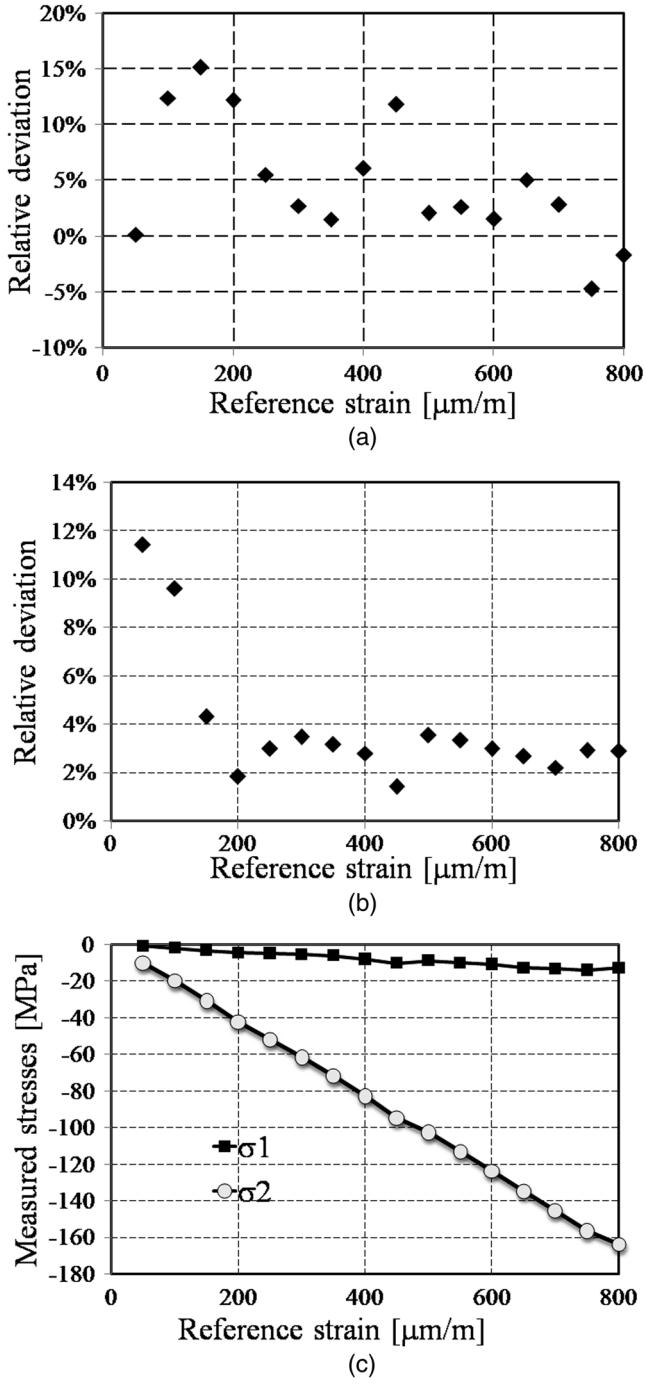

Figure 5.17 Plots of the relative deviations (a) for maximum and (b) minimum applied strains. (c) Plot of the measured stress field.

reference strains. Figure 5.17(c) shows that the linear behavior is primarily observed for the minimum measured stress σ_2. The maximum measured stress σ_1 also has a linear behavior, but some oscillations were found.

5.5 Final Remarks

The radial interferometer discussed in this chapter was developed to satisfy the requirements listed in Chapter 4. Its compact design and construction avoid the effects of atmospheric conditions, temperature, and humidity (see Fig. 4.2). For this interferometer, the laser is split after its reflection in mirrors M_2 and M_3. From this point, both interfering arms travel inside the main body of the interferometer, which also works as an enclosure. Moreover, they are below the effect of atmospheric conditions, temperature, and humidity; only a short length of $\sim$10 mm extends from the external face of the DOE to the surface of the object (see Figs. 5.8 and 5.9). Thus, the effect of these agents over the arms of the interferometer is low, permitting applications outside the laboratory or in laboratories without strict control of temperature and humidity. The clamping system works reasonably well with small shocks and vibrations; furthermore, it enables measurements without the influence of unwanted rigid-body motions.

Other very interesting solutions can be found elsewhere.[11,12] In these cases, the authors used moiré interferometry and a monolithic architecture to obtain a robust and compact strain sensor. Although the measurement principle is outside the scope of this book, the principles behind the construction of these sensors completely fulfill the requirements listed in Chapter 4. For this reason, these references are recommended for readers interested in further information about the development of robust optical sensors for NDT testing.

References

1. K. Hoffmann, *An Introduction to Measurements Using Strain Gauges*, Hottinger Baldwin Messtechnik GmbG, Darmstadt, Germany (1989).
2. R. Hooke, *De potentia restitutiva,* Lectures (1678).
3. N. E. Dowling, *Mechanical Behavior of Materials: Engineering Methods for Deformation, Fracture, and Fatigue*, 3rd Ed., Prentice-Hall, Upper Saddle River, NJ (2007).
4. J. W. Dally and W. F. Riley, *Experimental Stress Analysis*, 4th Ed., McGraw-Hill, New York (2005).
5. S. Timoshenko and J. N. Goodier, *Theory of Elasticity*, 3rd Ed., McGraw-Hill, New York (1970).
6. A. Albertazzi, Jr. and M. R. Viotti, "Radial speckle interferometry and applications," *Advances in Speckle Metrology and Related Techniques*, G. H. Kaufmann, ed., John Wiley & Sons, New York (2011).

7. D. V. Nelson and J. T. McCrickerd, "Residual-stress determination through combined use of holographic interferometry and blind-hole drilling," *Exp. Mech.* **26**, 371–378 (1986).
8. M. Kujawinska and L. Salbut, "Recent development in instrumentation of automated grating interferometry," *Opt. Appl.* **25**, 211–232 (1995).
9. L. Salbut and M. Kujawinska, "Grating interferometer for local in-plane displacement/strain field analysis," *Proc. SPIE* **3407**, 490–494 (1998) [doi: 10.1117/12.323361].
10. R. Czamek, "High sensitivity moiré interferomety with compact achromatic interferometer," *Opt. Lasers Eng.* **13**, 93–101 (1990).
11. M. Kujawinska and L. Salbut. "New generation of optical extensometers based on grating (moiré) interferometry," *Proc. SPIE* **4101**, 380–388 (2000) [doi: 10.1117/12.498404].
12. L. Salbut "Waveguide grating (moiré) microinterferometer for inplane displacement/strain field investigation," *Opt. Eng.* **41**(3), 626–631 (2002) [doi: 10.1117/1.1431557].
13. C. A. Sciammarella and J. A. Gilbert, "Strain analysis of a disk subject to diametral compression by means of holographic interferometry," *Appl. Opt.* **12**, 1951–1956 (1973).
14. E. Hack and R. Brönnimann, "Electronic speckle pattern interferometry deformation measurement on lightweight structures under thermal load," *Opt. Lasers Eng.* **31**, 213–222 (1999).
15. M. J. Huang, L. Zhao-Cheng, and J. Jhen-Huei, "Self-marking phase-stepping electronic speckle pattern interfometry (ESPI) for 3D displacement measurement on cathode ray tube (CRT)-panels," *Opt. Lasers Eng.* **38**, 245–260 (2002).
16. T. Matsumoto, K. Iwata, and R. Nagata, "Measuring accuracy of 3D displacements in holographic interferometry," *Appl. Opt.* **12**, 961–967 (1973).
17. S. Winther, "3D strain measurements using ESPI," *Opt. Lasers Eng.* **8**, 45–57 (1988).
18. D. Albrecht, "Estimation of the 2D measurement error introduced by in-plane and out-of-plane electronic speckle pattern interferometry instruments," *Opt. Lasers Eng.* **31**, 63–81 (1999).
19. W. S. W. Abdullah, J. N. Petzing, and J. R. Tyrer, "Wavefront divergence: a source of error in quantified speckle shearing data," *J. Modern Opt.* **48**, 757–772 (2001).
20. A. Martínez, R. Rodríguez-Vera, J. A. Rayas, and H. J. Puga, "Error in the measurement due to the divergence of the object illumination wavefront for in-plane interferometers," *Opt. Commun.* **223**, 239–246 (2003).

21. N. Sujatha, V. M. Murukeshan, and A. R. Ganesan, "Effect of illumination beam divergence in digital speckle pattern interferometry (DSPI) fringe formation," *J. Hologr. Speckle* **2**, 20–25 (2005).
22. A. Martínez, J. A. Rayas, R. Cordero, and K. Genovese, "Analysis of optical configurations for ESPI," *Opt. Lasers Eng*. **46**, 48–54 (2008).
23. A. Albertazzi, Jr., D. P. Willemann, and C. L. N. Veiga, "Preliminary evaluation of the optical rosette—a portable device for stresses measurement with ESPI," *Proc. 7th International Symposium on Laser Metrology Applied to Science, Industry, and Everyday Life*, 1073–1084 (2002).
24. A. Albertazzi, Jr., C. L. N. Veiga, and D. P. Willemann, "Evaluation of the optical rosette for translation, stresses, and stresses gradients measurement," *Proc. SPIE* **5144**, 533–544 (2003) [doi: 10.1117/12.503013].
25. G. H. Kaufmann and A. Albertazzi, Jr., "Speckle interferometry for the measurement of residual stresses," *New Directions in Holography and Speckle*, H. J. Caulfield and C. S. Vikram, eds., American Scientific Publishers, Stevenson Ranch, CA (2008).
26. M. R. Viotti, A. Albertazzi, Jr., and W. A. Kapp, "Experimental comparison between a portable DSPI device with diffractive optical element and a hole drilling strain gage combined system," *Opt. Lasers Eng.* **46**, 835–841 (2008).
27. M. R. Viotti, W. A. Kapp, and A. Albertazzi, Jr., "Achromatic digital speckle pattern interferometer with constant radial in-plane sensitivity by using a diffractive optical element," *App. Opt.* **48**, 2275–2281 (2009).
28. A. Albertazzi, Jr., M. R. Viotti, and W. A. Kapp, "Axis-symmetrical diffractive optical element, interferometer including this element and method for measurement of radial in-plane radial displacement fields on surfaces," (in Portuguese) Brazilian patent #PI 0803794-9 A2 (October 2008).
29. P. K. Rastogi, "Measurement of Static Surface Displacements, Derivatives of Displacements, and Three-Dimensional Surface Shapes-Examples of Applications to Non-destructive Testing," *Digital Speckle Pattern Interferometry and Related Techniques*, P. K. Rastogi, ed., John Wiley and Sons, Chichester, UK (2001).
30. J. M. Huntley, "Automated analysis of speckle interferograms," *Digital Speckle Pattern Interferometry and Related Techniques*, P. K. Rastogi, ed., John Wiley and Sons, Chichester, UK (2001).
31. M. R. Viotti, A. Albertazzi, Jr., and W. A. Kapp, "Mechanical stress measurement by an achromatic optical digital speckle pattern interferometry strain sensor with radial in-plane sensitivity: experimental comparison with electrical strain gages," *App. Opt.* **50**, 1014–1022 (2011).

Chapter 6
Quantitative Evaluation of Residual Stresses

6.1 Residual Stress Fields

The stress field that exists in the bulk of some materials without the application of external loads or other stress sources is known as "residual stress."[1,2] Many service failures of structural or mechanical components are caused by the combination of residual stress fields in the material and mechanical stresses produced by applied loads.

One of the most famous examples of the effect of residual stresses is the Liberty Bell in Philadelphia, Pennsylvania. The bell cracked some years after its manufacturing, probably due to residual stresses generated by the casting process.

Compressive stresses are sometimes introduced deliberately, e.g., the shot peening used to improve fatigue resistance. Furthermore, in natural or artificial multiphase materials, residual stresses can arise from differences in thermal expansion, yield stress, or stiffness.[3]

In the case of the Liberty Bell, manufacturers can avoid this kind of failure by understanding the casting process and its influence on the introduction of residual stresses in cast parts. Moreover, accurate knowledge of the levels of introduced compressive stresses is important to ensure the stress resistance of the material or the part. Consequently, accurate residual stress measurement becomes a valuable task not only when the structure integrity must be evaluated but also for the development of new materials or fabrication procedures or for the design of mechanical parts. Although recent advances in finite-element-based analyses have improved predictions about residual stress distributions, it is essential to accurately assess the history of the structure of the raw material from which the mechanical part is created, which can be done in a few experimental cases. For this reason, current experimental methods cannot be fully replaced to determine the magnitude and principal direction of residual stresses, not only in raw materials but also in components under operating conditions.

Residual stresses can be classified by (a) the cause that produces them (e.g., thermal differences in the material), (b) the scale or range in which they are self-equilibrated, or (c) the method by which they are measured. This chapter only addresses criterion (b).

According to this criterion, three types of residual stresses can be identified: macroscopic, microscopic, and submicroscopic residual stresses. Macroscopic residual stresses influence a large area, thus affecting several grains of the material. They are self-equilibrated, and any modification in the distribution produced, e.g., by a material remotion, will redistribute the stresses in order to achieve equilibrium again. The microscopic residual stresses influence only one grain or a part of it. This kind of residual stress occurs when the microstructure contains several phases or when phase transformations occur. The last type, submicroscopic residual stresses, typically includes stresses produced by coherency at interfaces and dislocation stress fields.

The connection between the three types of residual stresses can be observed when a plate is plastically deformed by the application of a uniaxial load. When the application of the load is stopped, a system of microstresses is generated by the inhomogeneous yielding of the material and by the hardening of the surface of the plate with respect to the center of the plate. A schematic plot of the stress distribution along the thickness of the plate is shown in Fig. 6.1.

The component of the stress with a high oscillation frequency belongs to the microscopic residual stresses (solid lines in Fig. 6.1). The dashed line with low frequency is the macroscopic residual stress. In this case, the stresses are compressive between points *a* and *b* and points *c* and *d*, and they are tensile between points *b* and *c*. The figure shows that the total stress is zero because residual stresses are self-equilibrated between points *a* and *d*.

The macroscopic residual stresses should be taken into account by design teams when designing a mechanical structure or part. The microscopic stresses should be analyzed when the behavior of the microstructural properties of the material are evaluated. Nondestructive testing usually involves evaluating the

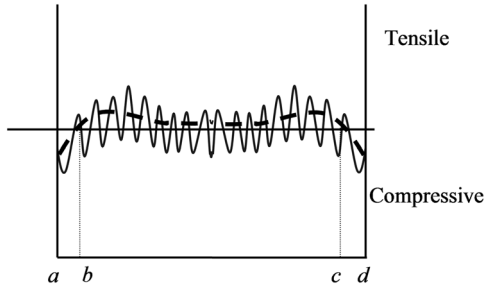

Figure 6.1 Stress distribution along the thickness of a plate plastically loaded by a uniaxial force.

former stresses; for this reason, subsequent sections only address methods suitable for macroscopic residual stresses.

6.2 Experimental Measurement of Residual Stresses

There are several methods that qualitatively and quantitatively characterize residual stresses in engineering materials. These methods are generally classified as destructive or nondestructive. The former are based on the local destruction equilibrium of the residual stresses; thus, the residual stress is quantified by measuring the effects generated by the local stress relief (deformations or displacements). These methods allow for the measurement of macroscopic residual stresses via the following steps:

a. Creation of a new local stress state due to the machining or remotion of a layer of the stressed material.
b. Detection of the local stress change by measuring deformation or displacement fields.
c. Computation of the residual stresses as a function of the deformation or the displacement by using the theory of elasticity.

The most important destructive methods are the hole-drilling method, the bending deflection method, and the sectioning method.[1,4] Among them, the hole-drilling technique is the most recent and widely used for industrial and laboratory applications.[5,6] This method involves measuring in-plane strains generated by relieved stresses when a small hole is drilled into the stressed material, either in a single pass or in multiple increments. Further information about the other two methods can be found elsewhere.[7–9]

The second group of techniques includes the nondestructive methods. They are based on measuring the variation of a material's physical or crystallographic parameters in order to evaluate the residual stress present in the material. The most-known techniques are the x-ray diffraction method, the neutron diffraction method, the ultrasonic method, and the magnetic method.[1,3,4]

The most widely used method for nondestructive measurement of residual stresses is x-ray diffraction. This method measures the deformations generated in the crystal lattice of a material by the residual stresses present in it. This method measures deformations produced in the surface of the material (a layer of $\sim$50 μm). In order to measure stress distributions inside the material, a layer of material is removed, enabling access to deeper parts. This version of the method is known as incremental x-ray diffraction. On the other hand, the neutron diffraction technique is capable of measuring residual stresses in the volume of the material without remotion of layers. Its main problem is that it uses a nuclear reactor, which is difficult to do outside a laboratory.[10–12] Diffraction techniques can be used to measure the three types of residual stresses analyzed in the previous section. Further information about the other nondestructive techniques can be found elsewhere.[9,13,14]

Among all of the techniques, the hole-drilling and x-ray diffraction methods are the most widely used internationally due to their high reliability. Both techniques have specific standards (ASTM and SAE, respectively) explaining their correct application. The hole-drilling method has the following advantages: it uses portable instrumentation, and it has a low cost. However, this method should only be applied for measurements where introducing a hole does not affect the working performance of the part being evaluated. Conversely, x-ray diffraction is recognized for its nondestructive nature, but its application is more limited due to its high cost and low portability. (Given the cited reasons and the feasible combination with speckle techniques, the following sections will only discuss the hole-drilling method.)

As previously mentioned, the hole-drilling method involves measuring in-plane strains generated by relieved stresses when a small hole is drilled into a stressed material. This measurement is usually performed by using strain-gage rosettes similar to the one shown in Fig. 6.2.

Traditionally, this method has been used to measure uniform stresses;[15] however, practical applications have shown that most cases of residual stress vary in depth from the surface. Several efforts have attempted to develop a method to compute nonuniform residual stresses by using the strains measured after each depth hole increment. These works solve the problem as an inverse problem by means of the integral method.[16–18]

The entire procedure to compute residual stress from the measured strain fields has been completely developed and explained.[6,18] For this reason, only a short overview of some equations of this procedure is provided here. The standard ASTM E837[6] directs users to perform consecutive hole increments to reach a hole with a depth of 1 mm or less. Consequently, up to 20 consecutive hole increments should be performed to discretize and assess the nonuniform stress profile. For example, Fig. 6.3 shows a smooth residual stress profile varying with the hole depth and a set of hole increments where the stress is

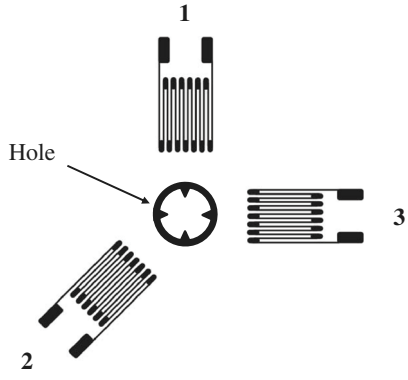

Figure 6.2 Strain gage rosette used to measure residual stresses in accordance with ASTM E837.

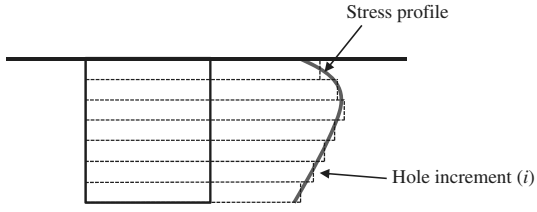

Figure 6.3 Residual stress profile varying with depth.

computed as uniform. The smooth profile is thus approximated by a stepped contour.

The combination variables between the strains ε_1, ε_2, and ε_3 read by gages 1, 2 and 3 (see Fig. 6.2) are defined as[6,18]

$$p = (\varepsilon_1 + \varepsilon_3)/2, \quad q = (\varepsilon_1 - \varepsilon_3)/2, \quad t = (\varepsilon_1 + \varepsilon_3 - 2\varepsilon_2)/2\,, \tag{6.1}$$

and

$$P = (\sigma_x + \sigma_y)/2, \quad \mathrm{Q} = (\sigma_x - \sigma_y)/2, \quad T = \tau_{xy}\,, \tag{6.2}$$

where P is the equal-biaxial stress, Q is the 45-deg shear stress, T is the shear stress, and the x direction corresponds to gage 1 (rosette Type A of the ASTM standard).

The relaxation strain measured after each hole increment i depends on stresses present in all hole increments up to that point in accordance with the following equations:[18]

$$p_i = \frac{1+\nu}{E}\sum_{j=1}^{i}\overline{a}_{ij}P_j, \quad q_i = \frac{1}{E}\sum_{j=1}^{i}\overline{b}_{ij}\mathrm{Q}_j, \quad t_i = \frac{1}{E}\sum_{j=1}^{i}\overline{b}_{ij}T_j\,. \tag{6.3}$$

According to Schajer,[18] $\overline{a}_{ij}$ and $\overline{b}_{ij}$ are matrices of calibration coefficients that relate the strain relief in a hole step i to a unit stress within step j. Because only stresses relieved within the hole depth contribute to strains, matrices $\overline{a}_{ij}$ and $\overline{b}_{ij}$ are lower triangular. E and ν are the modulus of elasticity and Poisson's coefficient of the material, respectively. In matrix-vector format, and considering the Tikhonov regularization, Eq. (6.3) becomes

$$\left(\overline{\mathbf{a}}^{\mathrm{T}}\overline{\mathbf{a}} + \alpha_P\mathbf{c}^{\mathrm{T}}\mathbf{c}\right)\mathbf{P} = \frac{E}{1+\nu}\overline{\mathbf{a}}^{\mathrm{T}}\mathbf{p}, \quad \left(\overline{\mathbf{b}}^{\mathrm{T}}\overline{\mathbf{b}} + \alpha_Q\mathbf{c}^{\mathrm{T}}\mathbf{c}\right)\mathbf{Q} = E\overline{\mathbf{b}}^{\mathrm{T}}\mathbf{q}, \quad \left(\overline{\mathbf{b}}^{\mathrm{T}}\overline{\mathbf{b}} + \alpha_T\mathbf{c}^{\mathrm{T}}\mathbf{c}\right)\mathbf{T} = E\overline{\mathbf{b}}^{\mathrm{T}}\mathbf{t}\,, \tag{6.4}$$

where boldface type indicates matrix and vector notation. Matrix $\mathbf{c}$ is an operator that acts over the curvature of the solution in order to avoid many sharp peaks and dips in the stress solution.

Factors α_P, α_Q, and α_T control the amount of regularization that is used in the solution. When they are zero, the solution is computed without regularization; otherwise, positive values produce regularization (smoothing) of the stress solution. As the factors increase, so does the smoothing. Large values of coefficients deform the solution due to excessive smoothing, and

small values retain a high noise level in the solution. It is clear that an optimal amount of regularization should be used to minimize distortions and remove noise. Optimal values of α_P, α_Q, and α_T are obtained by using an iterative method proposed in Schajer[18] that follows the Mozorov criterion.

6.3 Interferometric Solutions to Measure Residual Stresses

Although strains are usually monitored by specialized three-element strain gage rosettes, the combined hole-drilling strain gage method has some practical and economical drawbacks:

- the specimen surface must be flat and smooth to bond to the rosettes,
- the hole must be drilled exactly in the center of the rosette to avoid eccentricity errors, and
- the important time and cost associated with installing rosettes is high, usually exceeding one hour for each measurement.[5,19,20]

The difficulties of using strain gages can be overcome by using optical techniques.[21] Several techniques can be used to generate fringe patterns, from which the local displacements can be calculated. The use of moiré interferometry for residual stresses determination was investigated by McDonach et al.[22] The feasibility of using holographic interferometry was shown independently by Antonov,[23] Bass et al.,[24] and Nelson and McCrickerd.[25] Hung and Hovanesian[26] used shearography in conjunction with a small ball indentation instead of a hole. Pechersky et al.[27] used DSPI and local heat treatment to release the stress and determine residual stresses. Zhang[28] investigated the practicality of combining DSPI and hole drilling.

In all of the previous papers, fringe analysis was carried out by laborious manual reduction. More recently, Díaz et al.[29] developed a combined hole-drilling and DSPI technique that uses automated data analysis. The in-plane displacement field generated by the introduction of a small hole is determined by calculating the optical phase distribution with a phase-shifting method and a robust iterative phase-unwrapping algorithm. Viotti and Kaufmann[20] have evaluated the accuracy and sensitivity of this combined technique. In this case, they use an in-plane interferometer and a uniaxial reference stress state. The interferometer they used is shown in Fig. 6.4.

The output of a He–Ne laser LA, with a wavelength $\lambda = 632.8$ nm and a power of 10 mW, is divided into two symmetric beams by a beamsplitter BM. Each beam is then reflected by two mirrors M_1 and M_2 and expanded by two lenses L with a short focal distance. The angle formed between the direction of illumination and the normal to the specimen surface is approximately $\gamma = 31$ deg. Phase shifting is produced through the mirror M_1, which is joined to a piezoelectric transducer PZT. The linear displacement of the mirror is controlled by means of a control unit CU.

The specimen is imaged by a CCD camera whose output is digitized by a frame grabber located inside a personal computer PC, with a resolution

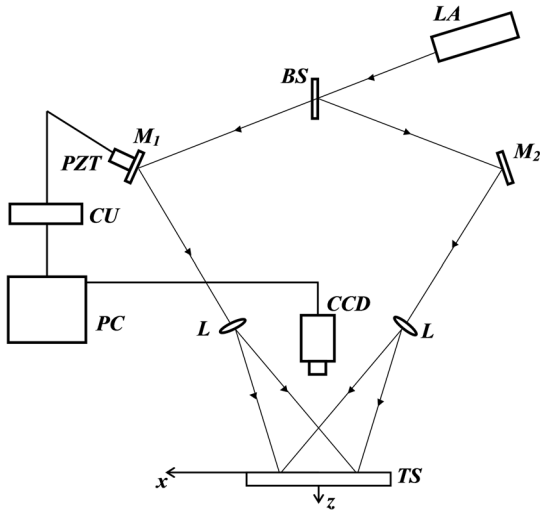

Figure 6.4 Experimental setup used by Viotti and Kaufmann.[20]

of 512 × 512 pixels and 256 grey levels (8 bits). This camera provides a field of view of 13 × 13 mm. The test specimen TS is a plate with a rectangular cross-section of 110 × 31.7 × 1 mm. It is made of an aluminum alloy with a Poisson's ratio $\nu = 0.34$ and a longitudinal elastic modulus $E = 35.9$ GPa. Before testing, the specimens are subjected to a normalization annealing at a temperature of 315 °C for 20 min. The longitudinal elastic modulus is determined by means of a tensile test after the annealing process.

For each test, the sample is localized in a loading system[29] that ensures a uniform, uniaxial tensile stress. This system incorporates an air turbine drill with a tungsten-carbide end mill 1.6 mm in diameter. This drill has a specified speed of 350,000 rpm and generates minimal residual stresses during operation.[30]

The experimental procedure is as follows: First, the sample is bolted into the jaws of the loading system. The load is then applied, and its value is measured using a loading cell. After the sample is loaded, the first set of four phase-shifted speckle interferograms is acquired. The hole is then drilled in the center of the image. After waiting several minutes to relax the measurement region, a second set of four phase-shifted speckle interferograms is recorded. Afterwards, the wrapped-phase distribution is determined, and the continuous-phase distribution is finally obtained by applying the iterative L^0-norm unwrapping algorithm. The last step evaluates $u(x, y)$ and $\sigma(x, y)$ at each pixel of the image. The displacement field is related along the axis $y = 0$ to the residual stress by[20]

$$u(x, y = 0) = \frac{(\nu + 1)\sigma r_0^2}{2E}\left[\left(\frac{\nu + 5}{\nu + 1}\right)\frac{1}{x} - \frac{r_0^2}{x^3}\right], \tag{6.5}$$

where r_0 is the radius of the hole.

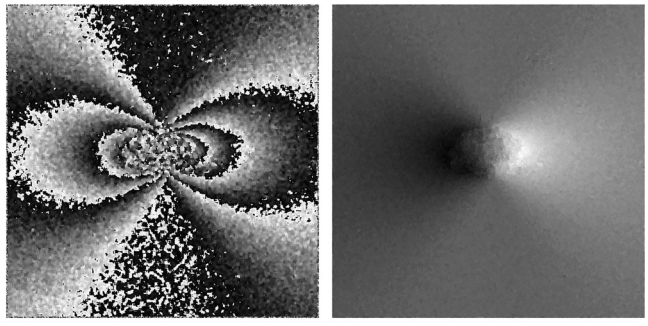

(a) (b)

Figure 6.5 Phase distributions obtained for 57% of the yielding stress: (a) wrapped and (b) unwrapped phase.

As a typical example, Figs. 6.5(a) and (b) show the wrapped and continuous-phase distributions, respectively, that were obtained for an applied stress of ~85 MPa, which is equivalent to 57% of the yield stress of the material. Conversely, Figs. 6.6(a) and (b) show the wrapped and the continuous-phase distributions generated by a specimen subjected to a tensile stress equal to 10% of the yield stress.

For the previous systems, the main residual stress direction should be known before starting measurement in order to adequately orient the in-plane illumination to have the large displacement values coincident with the sensitivity direction or close to it. Additionally, some experimental applications have showed that unwanted rigid-body displacements can be introduced when the hole is performed with the combined system of Viotti and Kaufmann.[20] For this reason, Dolinko and Kaufmann[32] have developed a least-squares method to cancel rigid-body motions by computing correction parameters determined from two evaluation lines located near the edge of the phase map.

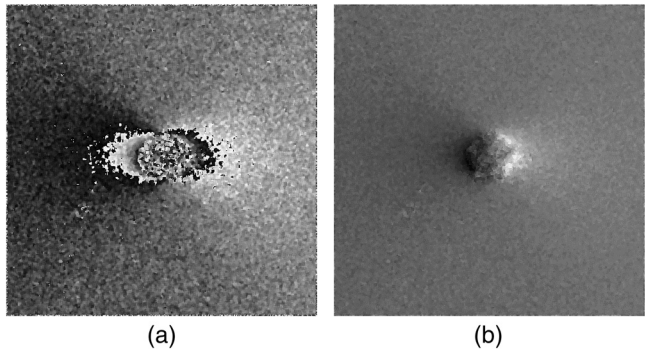

(a) (b)

Figure 6.6 Phase distributions obtained for 10% of the yielding stress: (a) wrapped phase and (b) unwrapped phase.

Other sources[31,33,34] use an interferometer commercially in a system called PRISM. Figure 6.7 shows the layout of this interferometer: the specimen is illuminated by the laser light, and the scattered light is imaged by the CCD camera. The reference beam passes through a piezoelectric actuator (for phase-shifting computation) and travels via a fiber link directly to the CCD sensor. The interference between both beams is produced by the CCD sensor. Readers can see that for this kind of interferometer, the sensitivity vector is oblique with respect to the surface of the specimen. Consequently, displacements that occurred in the out-of-plane direction as well as the in-plane direction are measured simultaneously. Schajer and Steinzig[34] illustrate a way to compute residual stress from this full displacement field. They also discuss the mathematical way to compute residual stresses without the influence of unwanted rigid-body motions.

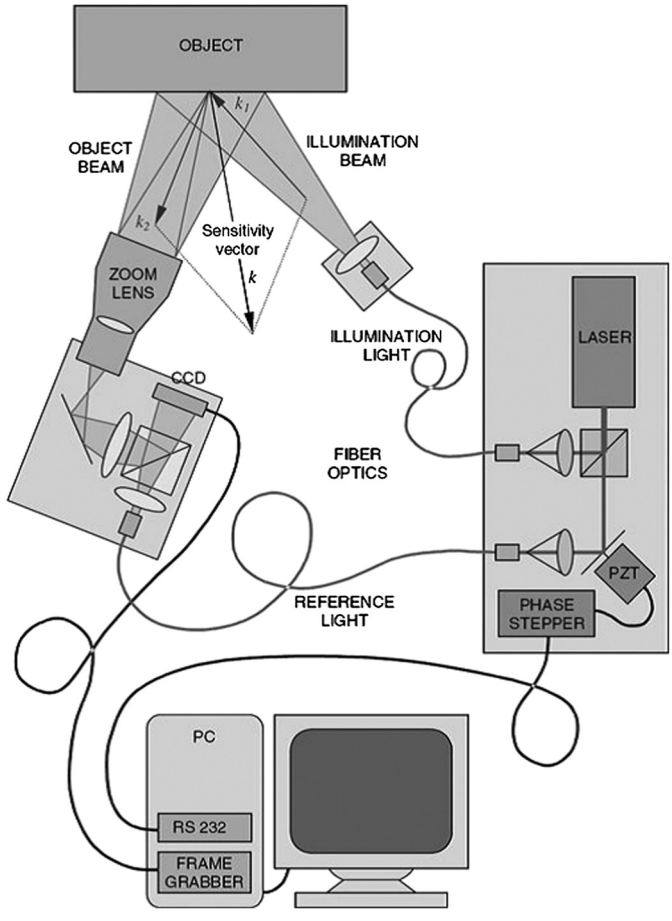

Figure 6.7 Experimental setup used for measurements (reprinted from Steinzig and Ponslet[33] with permission).

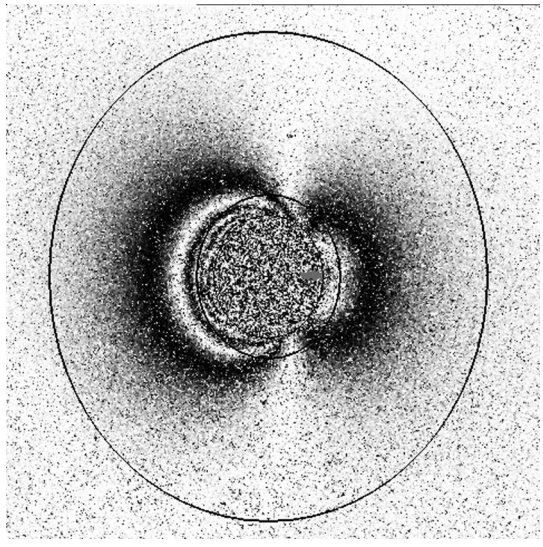

Figure 6.8 Measured fringe pattern for the twelfth hole step (reprinted with permission from G. S. Schajer).

Figure 6.8 shows the fringe pattern for the twelfth DSPI measurement referenced to the initial phase map obtained before the introduction of the hole measured with the interferometer.[31,33,34]

In order to measure residual stress fields where their principal direction is unknown, DSPI systems based on the optical layout presented in Chapter 3 (see Fig. 3.9) can be a possible solution to measure residual stress fields when combined with a hole-drilling device. Thus, a portable measurement device can be built as a modular configuration with three parts: a universal base (UB), a measurement module (MM), and a hole-drilling module (HM).[35] The universal base is rigidly clamped to the specimen surface by four adjustable and strong magnetic legs and three feet with sharp conical tips to reduce the relative motion between the base and the specimen surface.

The measurement module implements the radial in-plane interferometer shown in Fig. 3.9. A 50-mW diode laser with a wavelength $\lambda = 658$ nm is used as a light source. The angle between the directions of illumination and the normal to the specimen surface is chosen as 30 deg. The test specimen surface is actively monitored by a CCD camera whose output is digitized by a frame grabber with a resolution of 1280×1024 pixels and 256 gray levels (8 bits). This camera provides a field of view that includes an illuminated area of 10 mm in diameter over the specimen. The hole-drilling module is based on an air turbine with a tungsten end mill 1.6 mm in diameter, which is moved by a manual micrometric screw. The measurement and hole-drilling modules are fixed to the universal base by an interface that allows for fast and accurate reposition of the modules. The interface is shown in Fig. 6.9.

Both modules have three spheres (Sph) of steel positioned at 120 deg and a set of nine strong magnets (Mg2) rigidly fixed on them. The interface has three

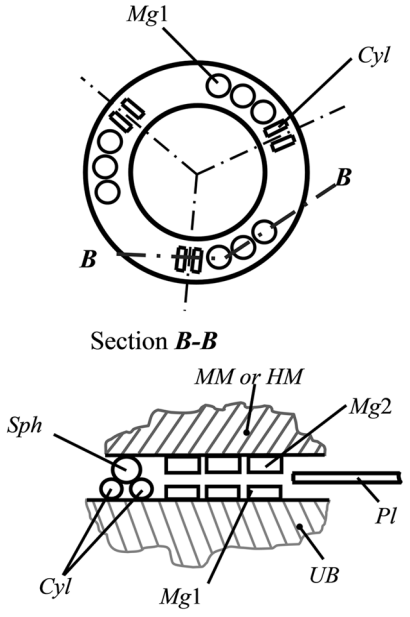

Figure 6.9 Scheme of the kinematic interface of the universal base.

pairs of cylindrical supports (Cyl) positioned at 120 deg, another similar set of nine magnets (Mg1) fixed rigidly to it, and a mobile steel plate (Pl). When either the measurement or the hole-drilling module is placed over the universal base, the three spheres are precisely positioned on each pair of cylindrical supports, thus forming a kinematic mounting. The magnet sets are aligned in such a way that a light repulsion force is presented between the movable module and the clamping base. That principle avoids mechanical shocks. After positioning the measurement or hole-drilling module on the base, the plate is laterally displaced so that it is located between both sets of magnets (Mg1 and Mg2). In this way, the light repulsion force is smoothly changed to a strong attraction force that keeps both modules rigidly fixed to the universal base. By using an unloaded specimen, it is shown that the measurement module can be repositioned in the universal base with an error much lower than $\lambda/4$. Figure 6.10 shows a photograph of the portable system. In this figure, UB is the universal base, HM is the hole-drilling module, and MM is the measuring module with the radial in-plane interferometer. Figure 6.11(a) shows the universal base; three pairs of cylinders are placed at a 120-deg angle as are the nine magnets labeled Mg1 in Fig. 6.9. In turn, Fig. 6.11(b) depicts the bottom of the hole-drilling module; the three spheres and the nine magnets Mg2 can be seen.

In order to perform measurements with the portable system, the following procedure is applied. First, the universal base is positioned over the surface to be measured, and the measurement module is fixed using the kinematic interface. A set of phase-shifted speckle interferograms is then acquired, and the reference phase distribution is computed and stored in the

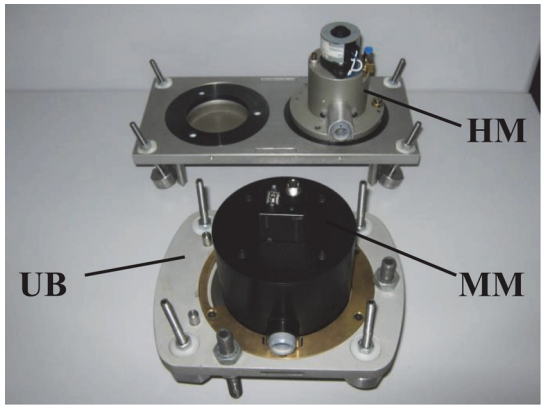

Figure 6.10 Portable device.

(a)

(b)

Figure 6.11 (a) Universal base with the kinematic system. (b) Bottom view of the hole-drilling module.

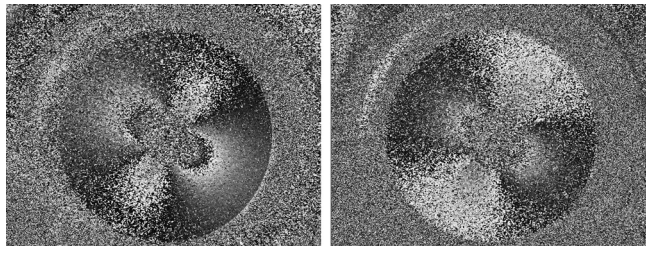

Figure 6.12 Wrapped-phase maps obtained by the radial in-plane speckle interferometer for a uniform residual stress field.

portable computer. The measurement module is removed from the universal base and replaced with the hole-drilling module. A blind hole is drilled to a depth of ~2 mm. After waiting some seconds to cool the measurement region, a second set of phase-shifted speckle interferograms is acquired, and a new phase distribution is calculated and stored. Finally, the wrapped-phase difference map is evaluated, and the continuous-phase distribution is obtained by applying a flood-fill phase-unwrapping algorithm.[36]

Figure 6.12 show two typical wrapped-phase difference patterns obtained for different stress magnitudes. The radial in-plane displacement field generated around the hole is calculated from the optical phase distribution. The last step involves computing the principal residual stresses and their direction, which is accomplished by using the numerical solution developed by Makino and Nelson[37] or the ASTM solution for uniform stresses[6] (both are obtained from the analytical Kirsch's solution[38]). Consequently, relieved residual stresses are computed with these solutions by considering that they have a uniform distribution along the whole depth of the hole.

As previously noted, most situations involve residual stress cases in which the stresses vary with the hole depth (called nonuniform residual stresses). Therefore, applying the standardized procedure with the modular system would involve interchanging both modules up to 20 times during the measurement, which becomes a difficult and unappealing process. To overcome these drawbacks, Fig. 6.13 shows a more-compact configuration

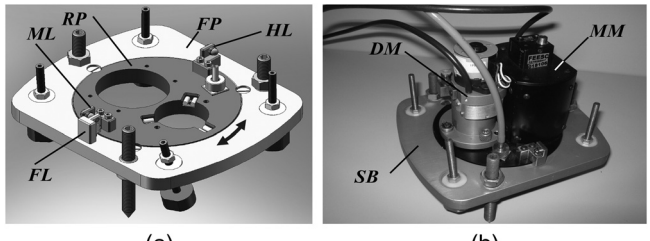

Figure 6.13 (a) Supporting base with labeled components. (b) Compact device with both modules.

that considers simplifying the measurement. As before, the compact device is primarily composed of a supporting base (SB) on which the measurement module (MM) is fixed by a set of screws. The hole-drilling module (DM) is placed near the MM. The DM is fixed and placed on the supporting base by means of two screws and three kinematic supports, respectively.[39,40]

The working principle of the interchanging module process can be understood by referring to Fig. 6.13(a). The main body of the supporting base (FP) is rigidly clamped to the specimen surface by four adjustable and strong magnetic legs and three feet with sharp conical tips to reduce the relative out-of-plane and, principally, the in-plane motion between the base and the specimen surface. The circular plate (RP) is a rotatory plate, and it is joined to the fixed body (FP) by means of a thin-section rigid ball bearing. The plate (RP) can be rotated in both directions (along gray arrows) in order to place the measurement or the drilling modules over the surface to be measured. The right positioning is performed by a kinematic device constituted by two spherical limits (HL and ML) and a conical fixed limit (FL). The combination of the rigid ball bearing and the kinematic device allows both the positioning of both modules with an error much lower than $\lambda/2$ and the interchanging of the module quickly and easily.

In order to perform a measurement, the supporting base is positioned on the specimen and clamped with the three legs and four magnets. When the measurement module is placed over the area to be measured, the limit (ML) is in contact with the FL. A set of phase-shifted speckle interferograms is acquired, and the reference phase distribution is computed and stored in the computer. The plate (RP) is then rotated toward the limit (HL) and contacts the FL. In this case, the hole-drilling module is positioned to drill a hole into the material, and then the RP is rotated back. At this moment, ML and FL are in contact, and the measurement module is once again placed over the measurement area. After waiting some seconds to cool the region around the hole, a second set of phase-shifted speckle interferograms is acquired, and a new phase distribution is calculated and stored. Finally, the wrapped-phase difference map for the first hole step is evaluated. This procedure is performed 20 times to assess the stress distribution along the depth. For example, Fig. 6.14 shows a set of difference phase maps measured for each hole increment.

6.4 Qualitative Evaluation of Residual Stresses by Indentation

Hole-drilling techniques involve introducing a small hole into the material. As previously explained, most applications can accept a hole without losing the part being evaluated. In other cases, the presence of the hole becomes a stress concentrator that can cause the part to fail. It is clear that for these cases the measurement of residual stresses with the hole-drilling technique is prohibitive.

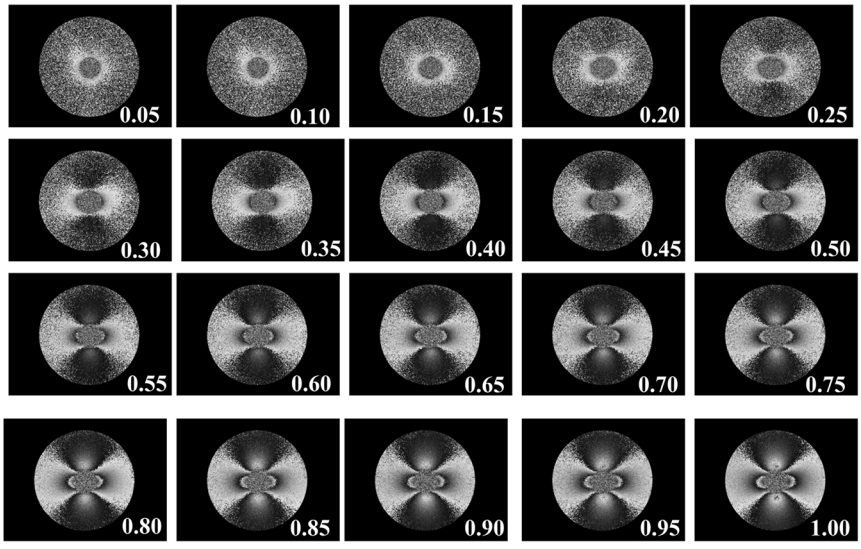

Figure 6.14 Difference phase maps measured for each hole increment. Numbers indicate hole depths in millimeters.

Several works[41–43] use indentation as an experimental technique to determine the curve relating the indentation force to its depth. These works present applications to measure the following:

- Mechanical properties of the material (Young modulus, fracture resistance),
- Residual stress amplitude (by comparison to another material free of residual stresses), and
- Gradients in elastic properties and yield point evaluation.

The main limitations for these applications: the clear interpretation of results is affected by the material plastic properties,[41] and the true contact area is used in the computations and is very difficult to evaluate reliably.

An alternative possibility combining indentation with DSPI was explored and evaluated by Suterio et al.[44] The measurement principle involves the application of a controlled indentation print to the surface of the specimen by using a conical or spherical tip. Consequently, local yielding is produced, and the material on the surface of the specimen moves away from the indentation print. In contrast to the hole-drilling method, the indentation does not release stresses but instead adds more stresses, creating a local plastic zone. Furthermore, it introduces a compressive stress field and affects a small region of the material because its depth is $\sim$0.3 mm, which is smaller than the hole depth obtained in a hole-drilling measurement.

The following experimental procedure is applied in Suterio et al.[44] to evaluate residual stresses with a radial in-plane interferometer. First, a reference set of images of the specimen surface is acquired and the correspondent phase

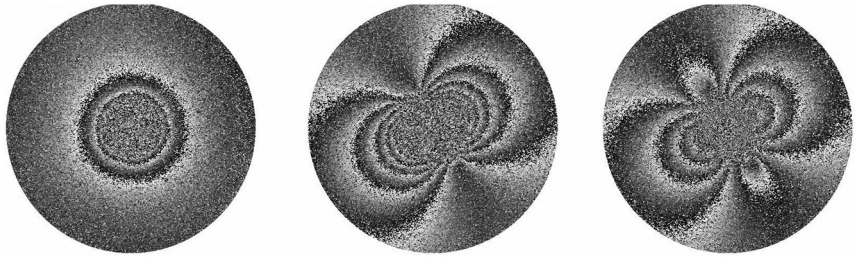

Figure 6.15 Difference phase maps obtained after indentation: (a) stress-free material and (b) with a residual stress of 200 MPa. (c) Difference between (a) and (b) (reprinted with permission from Suterio et al.[44]).

map is computed. The stress state in the material is then modified by the introduction of the indentation. After that, a second set of images of the same region is acquired, and the phase is computed again. Finally, the phase difference with information about the radial in-plane displacement field around the indentation print is obtained. A permanent displacement field is always generated around the indentation tip due to the local yielding of the material.

Figure 6.15(a) shows the difference phase map measured in a stress-free steel plate. This displacement field is axisymmetric and repeatable if the indentation tip geometry, the indentation loading, and the material properties are kept constant.[44] If residual stresses are present in the material prior to the indentation, the permanent displacement field is affected in a way that depends on the residual stress level. Figure 6.15(b) shows the radial in-plane displacement in a material with a uniaxial stresses field (200 MPa) aligned $\sim$30 deg from the horizontal axis. Note that there are clear differences between both maps, illustrated in Fig. 6.15(c). This phase map was obtained by subtracting Fig. 6.15(b) from 6.15(a). In this case, Fig 6.15(c) would show the displacement field generated only by the residual stresses.

The amount of the radial displacement component that is around the indentation print is influenced by the level and direction of residual stresses acting on the specimen. For example, Fig. 6.16 shows several difference phase maps obtained for different residual stress magnitudes. It demonstrates that the combined technique can be used to qualitatively evaluate the presence of residual stresses. Suterio et al.[44] present a mathematical model that is suitable for a type of material and for uniaxial stresses. Further investigations should be performed in order to obtain a suitable model for biaxial stresses on several materials.

6.5 In-Field Applications

Previous sections presented the hole-drilling technique as a method to measure residual stress fields. However, there are several cases where hole drilling is used to evaluate the integrity of mechanical components under a severe and unknown load. In this case, the measurement quantifies not only the residual

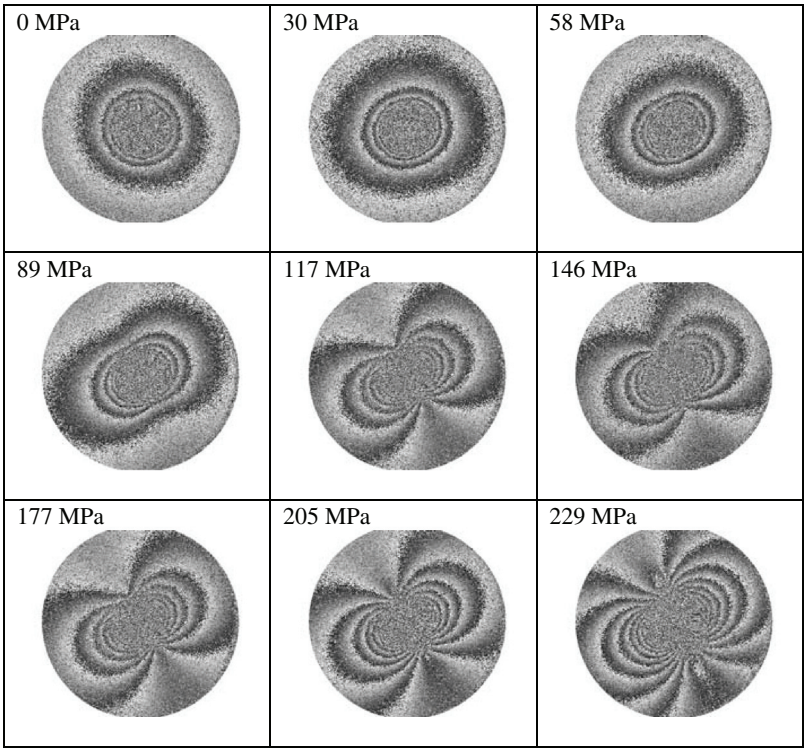

Figure 6.16 Difference phase maps with spherical indentation in different levels of induced residual stresses (reprinted with permission from Suterio et al.[44]).

stresses in the part but also all other stresses applied, such as thermal stresses, mechanical stresses, etc. These stresses are called "combined stresses," and they provide valuable information about the amount of solicitation under which a part is submitted. This principle is frequently used to evaluate the integrity of pipelines with severe in-field loads, and this section discusses it as an application.

6.5.1 Determining the external loading of a pipeline

A pipe transmission line is obtained by joining several individual pipes by welding. As a result, mounting stresses will be present in the material. Moreover, these stresses will also be influenced by movements of the pipeline, the geometry and regularity of the ditch, and the soil in which the pipeline will be placed. Because these movements and mounting operations are very different and vary for each case, it is difficult to exactly predict the magnitude of the mounting stresses for simple calculations or through complex numerical simulations. The presence of strange elements in the soil, such as stones, can dramatically alter the local magnitude of this stress. After the ditch is closed, mounting stresses will remain stable over time.

Stresses generated by the interaction between the pipeline and the soil are primarily produced by the movement of the soil in which the pipe is placed. They can be caused by natural factors, such as heavy rain, or by human activity, namely, excavation activities, road construction, and heavy vehicles passing through the area where the pipe is buried. These components of strains can grow over time, developing very high magnitudes of stress. They can even cause the pipeline to fail if they are not carefully evaluated.

Thermal stresses originate from differences in temperature between the pipeline and soil. Daily variations in temperature of the soil and changes in the temperature of the fluid being transported will induce thermal stresses due to differences in thermal expansion between the pipeline and the soil. These stresses are not constant, and they directly change with temperature variations.

Finally, residual stresses are produced by the tube-manufacturing process; e.g., seam-welded pipes are fabricated from hot-rolled steel plates in three cold-forming steps. In Step 1, a U-shape is generated. In Step 2, the O-shape is formed. The seam-weld joining of the O-shape is produced by submerged arc welding (SAW). Finally, in Step 3, the diameter of the pipe is E-expanded to its final dimension (UOE–SAW process).[45] According to this description, readers can see that pipes are exposed to a severe yielding process of mechanical shaping and welding that pushes the material beyond its yielding stress. Consequently, nonuniform distributions of stresses in the pipe wall will be found that remain stable during the whole life of the tube.

By accounting for all previously described stresses, the loading state that acts on the wall of a pipe is the result of the combination. Some of these stresses remain stable over time, and others are variable. In order to continuously monitor the loading state of the combined stresses at a critical point of the pipeline, it is necessary to combine a monitoring method with a reference version. The reference method is used to determine the state of combined stress present in the assessed point of the pipeline, which is adopted as the starting value for continuous monitoring.

According to the principles of classical elasticity, an isotropic beam subjected to pure bending presents a linear distribution of stresses along its cross-section. The bending moment is proportional to the applied load, and, for each point of the cross-section of the beam, it is proportional to its distance from the neutral line, as shown in Fig. 6.17.

The bending stress is then calculated by

$$\sigma_B = \frac{My}{I_{ner}}, \tag{6.6}$$

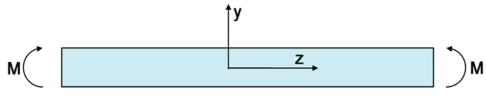

Figure 6.17 Pure bending applied to a beam.

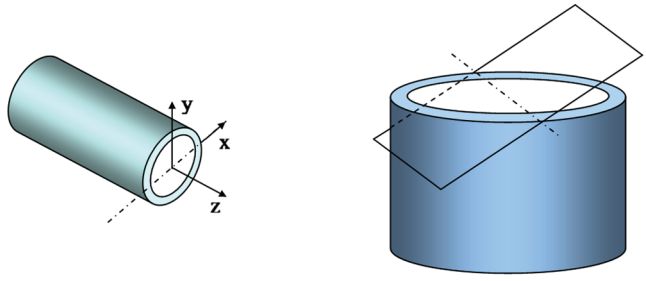

Figure 6.18 Bending stress distribution along a cross section of the pipe.

where M is the bending moment applied to the beam, and y is the distance from the neutral line. In this case, the neutral line is placed at the coordinate $y = 0$, and I_{ner} is the moment of inertia of the section. For a circular hollow cross-section, $I_{ner} = (\pi/4)(R_{ex}{}^4 - r_{in}{}^4)$, where R_{ex} and r_{in} are the external and internal radius of the pipe, respectively.

The bending stress σ_B acts in the longitudinal direction, which is coincident with the z axis (see Fig. 6.18). Note that the signal of the bending stress changes when it is above or below $y = 0$. If the magnitude of the bending stress is represented in the direction of the z axis, Eq. (6.6) is the equation of a line inclined at zy plane. If the x dimension is also considered, Eq. (6.6) becomes the equation of an inclined plane containing the x axis. Thus, its slope does not depend on the x dimension. The line whose stress value is zero is called the neutral line, which in this case corresponds to the x axis.

When a pipe is subjected to a state of pure bending due to a bending moment applied around the x axis (zy plane), Eq. (6.6) can be used. In this case, the x axis corresponds to the neutral line. If the bending moment is applied around the y axis, the neutral line corresponds to the y axis. For bending moments applied in other directions, the neutral line is located in other directions. However, the bending stress will always be represented by an inclined plane, as illustrated in Fig. 6.18.

The bending stress state can be caused by the load produced by the interaction between the pipeline and the soil. Nevertheless, pure bending will rarely be found in a buried pipeline, depending on thermal stresses and other stress components. In the absence of a load caused by internal pressure, the presence of an axial load is expected, which adds longitudinal tensile or compressive stresses to the stresses caused by bending. This combination does not change the slope of the bending plane, but it changes its average value as well as the position of the neutral line (displacement c). This effect is illustrated in Fig. 6.19.

The longitudinal stress component (along the z axis in Fig. 6.18) measured by the hole-drilling method can be used to determine (a) the magnitude of the bending stresses and bending moment applied on the pipeline, (b) the orientation of the neutral line, and (c) the average longitudinal stress. This computation assumes that the residual stresses are approximately invariable in several angular positions of

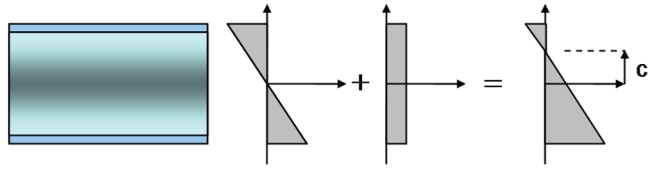

Figure 6.19 Displacement of the neutral line generated by axial loading.

the same section, except for the welding seam. This hypothesis seems reasonable for validating the determination of the external bending load but not for the external axial load. When a reference method is used to evaluate the stress state of a pipeline, note that the average stress measured on the external surface of the pipe cannot be directly associated with an external axial load because the pipe-manufacturing process usually produces longitudinal compressive residual stresses on the external surface of their walls; these stresses are added to stresses produced by an axial external load, masking the real value.

In order to determine the external loads applied in the pipeline, the following actions should be performed:

1. Measuring the combined stresses by using the hole-drilling method in at least three different angular positions of the same cross-section of the pipeline and the determination of the longitudinal stress components. Interrogated points should be regularly distributed along the perimeter. It is extremely important when placing these points to avoid the welding seam, defects, or irregularities observed in the external surface of the pipeline.
2. Applying the least-squares method to find the best equation of the plane that fits to the values of the longitudinal stresses already obtained in Step 1. With the equation of the plane, other parameters can be calculated.

   The plane equation is given by

$$\sigma_L(x, y) = K_0 + K_x x + K_y y, \tag{6.7}$$

where $\sigma_L(x, y)$ is the longitudinal stress component measured in each angular point, and K_0, K_x, and K_y are constant fitting values of the plane. x and y are the Cartesian coordinates that describe the position of each point along the perimeter of the cross-section of the pipe. The origin of the coordinate's system coincides with the center of the circular cross-section. The x axis is horizontal, and the y axis is vertical. With these constants and the external (r_{ex}) and internal (r_{in}) radius of the pipe, a set of parameters that represents the loading state of the pipeline in service can be computed:

- Average longitudinal stress: $\sigma_{Lm} = K_0$.
- Angular position of the maximum stress axis: $\delta_{\sigma\max} = \tan^{-1}(K_x/K_y)$
- Angle of the neutral line $\delta_{NL} = \delta_{\sigma\max} + 90$ deg
- Bending stress: $\sigma_B = K_x r_{ex}\sin(\delta_{\sigma\max}) + K_y r_{ex}\cos(\delta_{\sigma\max})$
- Minimum stress: $\sigma_{\min} = \sigma_{Lm} - \sigma_B$

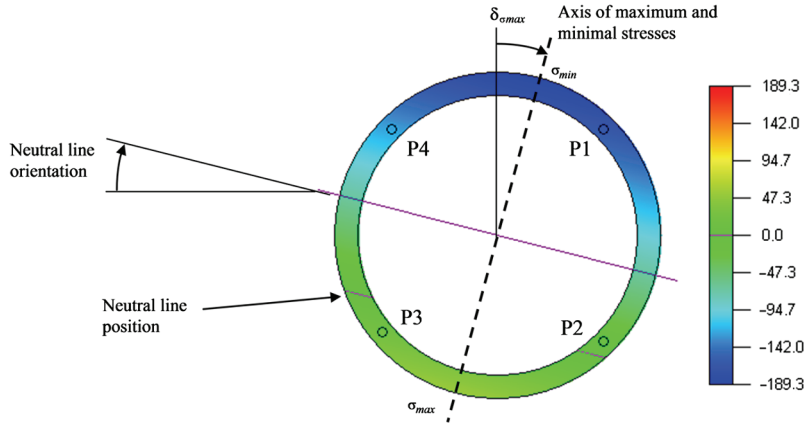

Figure 6.20 Result obtained after evaluating a cross-section of a pipeline.

- Maximum stress: $\sigma_{\max} = \sigma_{Lm} + \sigma_B$
- External bending moment: $M = \frac{\pi\sigma_B({r_{ex}}^4 - r_{in}^4)}{4r_{ex}}$
- External axial load: $C_{Ax} = \pi\sigma_{Lm}(r_{ex}^2 - r_{in}^2)$

Figure 6.20 shows a suitable graphical way to represent the results of a measured cross-section at four points. Points where the longitudinal stresses were measured are labeled as P1, P2, P3, and P4. The color scale represents the values of the longitudinal stress at each point of the section so far. The green color corresponds to the zero longitudinal stress. Blue colors are related to negative stresses (compressive), and the yellow, orange, and red colors represent positive stresses (tensile). The points of maximum and minimum longitudinal strains are also represented, as well as the axis of maximum stress, represented by a dashed line. The orientation of the neutral line is given by the violet line. In the presence of axial loads, the neutral line moves away from the center of the section.

6.5.2 Measurement of combined stresses in a gas pipeline in service

As a practical example, the radial in-plane interferometer shown in the previous sections was used outside the laboratory to measure combined stresses in a working gas pipeline. This pipeline was placed in a risk area near a river slope where soil moves constantly. A contention structure was projected and built to minimize soil movement and interaction between it and the pipeline. The interferometer measurements were used to investigate the effectiveness of the repair.

The measurements were made in five cross-sections in different places on the river slope, and four points were measured for each cross-section. The measured points were positioned away from the seam weld. Figure 6.21 shows some photographs of the measurement conditions.

Measured values of combined stresses were obtained at each point. By using Mohr's circle, the stresses were calculated along the longitudinal (σ_L)

Figure 6.21 Measurement of combined stresses in two cross-sections of the gas pipeline.

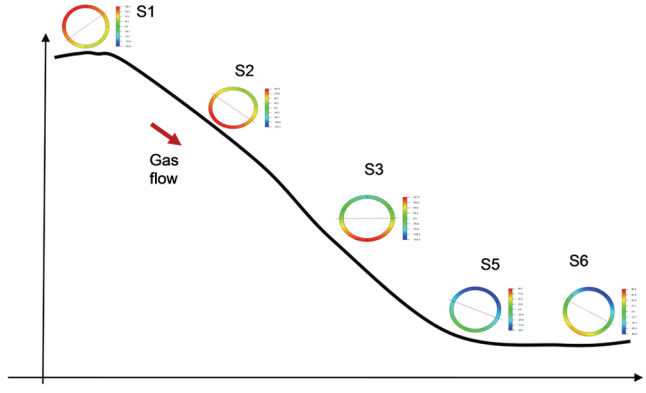

Figure 6.22 Location of cross-sections along the river slope.

and circumferential (σ_C) directions. Several levels of axial load were found, as well as bending moments in the five different cross-sections. (The actual values could not be presented here due to confidentiality agreements.)

Figure 6.22 shows the estimated profile of the pipeline along the river slope and the approximated location of each evaluated cross-section. It is possible to find a presence of strong traction in sections S1 and S2, which are places at the top of the river slope that are being pulled down. On the other hand, sections S5 and S6, located in the valley of the river slope, are under compression because of the downward-moving slope.

6.6 Final Remarks

In order to make the portable DSPI system "cooperative," some elements are incorporated in its operating software. For *in situ* applications, working conditions are frequently much more hostile than in a quiet and controlled laboratory environment. For cases similar to that shown in Fig. 6.21, users are frequently under time limitations because they must perform the measurement as fast as possible and in a short time period. Additionally, they work under

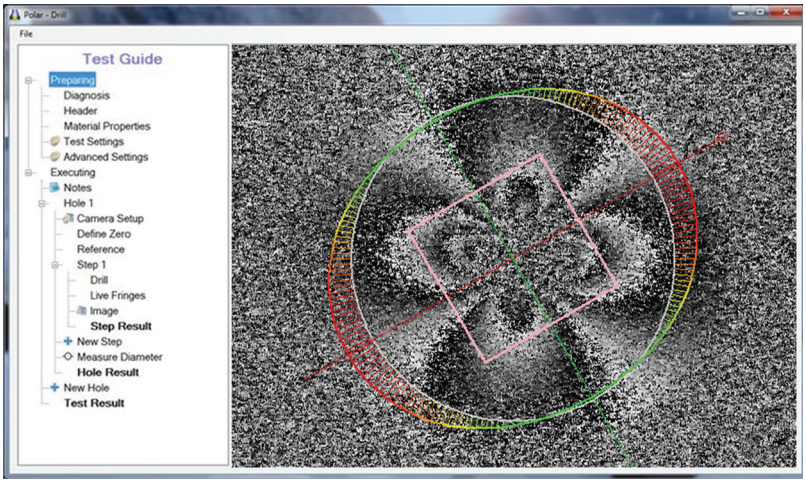

Figure 6.23 Main interface of the test-oriented software.

uncomfortable conditions, such as insects, sunburns, rain, etc. The probability of forgetting an important step or mixing data increases under such conditions. In order to simplify the measurement process, test-oriented software was designed.

The main idea is to guide the user through all measurement steps in a logical way and to keep the acquired data organized. The solution is displayed in Fig. 6.23. On the left is an "action tree" with branches and leaves. The branches are associated with high-level stages. Each leaf represents an action that must be completed under each branch. Some actions must be followed sequentially; others are more flexible. The action tree, which is either previously configured from a file or configured locally, guides users through a predefined test. However, in accordance with users' needs, the test tree can be dynamically modified during the experiment. Annotation fields can be used to keep notes and records of exceptional facts that occurred during the measurement.

Data management is done automatically. The software creates a directory to accommodate all acquired data. The results are calculated and promptly displayed as soon as they are available. Adjustment tools—such as system leveling and positioning, laser power adjustment, and camera shutter speed optimization—are available. Diagnostic tools help check the hardware integrity. At the end of the measurement, a technical report is produced and exported to word-processing software when the "Test Result" leaf is clicked.

References

1. J. Lu, *Handbook of Measurement of Residual Stresses*, The Fairmont Press, Lilburn, GA. (1996).

2. J. Lu, *Handbook on residual stress*, Vol. 1, 2nd Ed., Society of Experimental Mechanics, Inc., Bethel, CT (2005).
3. P. J. Withers and H. K. D. H. Bhadeshia, "Residual stress Part 1—Measurement techniques," *Mat. Sci. Technol.* **17**, 355–365 (2001).
4. R. E. Rowlands, "Residual Stresses," *Handbook on Experimental Mechanics*, A. S. Kobayashi, ed., 785–828, Prentice-Hall, New York (1987).
5. N. J. Rendler and I. Vigness, "Hole-drilling strain-gage method of measuring residual stresses," *Exp. Mech.* **6**, 577–586 (1966).
6. American Society for Testing and Materials, "Standard test method for determining residual stresses by the hole-drilling strain-gage method," ASTM E837-08e1, Annual Book of ASTM Standards, Vol. 03.01 (2008).
7. M. Larsson, P. Hedenqvist, and S. Hogmark, "Deflection measurements as a method to determine residual stress in thin hard coatings on tool materials," *Surface Eng.* **12**, 43–48 (1996).
8. A. J. Perry, J. A. Sue, and P. J. Martin, "Practical measurement of the residual stress in coatings," *Surface Coatings Technol.* **81**, 17–28 (1996).
9. G. S. Schajer, *Practical Residual Stress Measurement Methods*, John Wiley & Sons, New York (2013).
10. A. Allen, M. T. Hutchings, and C. G. Windsor, "Neutron diffraction methods for the study of residual stress fields," *Adv. Phys.* **34**, 445–473 (1985).
11. I. C. Noyan and R. B. Cohen, *Residual Stress Measurement by Diffraction and Interpretation*, Springer-Verlag, Berlin (1987).
12. J. Lu and D. Retraint, "A review of recent developments and applications in the field of X-ray diffraction for residual stress studies," *J. Strain Anal.* **33**, 127–136 (1998).
13. D. E. Bray, N. Pathak, and M. Srinivasan, "Residual stress distributions in the rim of a steam turbine disk using the L(CR) ultrasonic technique," *Mat. Sci. Forum* **210**, 317–324 (1997).
14. H. Hognestad and A. Honne, "Determination of stress in ferromagnetic steel by potential drop measurements," *Mater. Sci. Technol.* **14**, 1109–1114 (1998).
15. G. S. Schajer, "Application of finite element calculations to residual stress measurements," *J. Eng. Mater. Technol.* **103**, 157–163 (1981).
16. G. S. Schajer, "Measurement of non-uniform residual stresses using the hole-drilling method. Part I: stress calculation procedures," *J. Eng. Mater. Technol.* **110**, 338–342 (1988).
17. G. S. Schajer, "Measurement of non-uniform residual stresses using the hole-drilling method. Part II: practical application of the integral method," *J. Eng. Mater. Technol.* **110**, 344–349 (1988).
18. G. S. Schajer, "Hole-drilling residual stress profiling with automated smoothing," *J. Eng. Mater. Technol.* **129**, 440–445 (2007).

19. H. P. Wang, "The alignment error of the hole-drilling method," *Exp. Mech.* **19**, 23–27 (1979).
20. M. R. Viotti and G. H. Kaufmann, "Accuracy and sensitivity of a hole drilling and digital speckle pattern interferometry combined technique to measure residual stresses," *Opt. Lasers Eng.* **41**, 297–305 (2004).
21. F. M. Furgiuele, L. Pagnotta, and A. Poggialini, "Measuring residual stresses by hole drilling and coherent optics techniques: a numerical calibration," *J. Eng. Mat. Technol.* **113**, 41–50 (1991).
22. A. McDonach, J. McKelvie, P. M. MacKenzie, and C. A. Walker, "Improved moiré interferometry and applications in fracture mechanics, residual stresses and damage composites," *Exp. Technol.* **7**, 20–24 (1983).
23. A. A. Antonov, "Inspecting the level of residual stresses in welded joints by laser interferometry," *Weld. Prod.* **30**, 29–31 (1983).
24. J. D. Bass, D. Schmitt, and T. J. Ahrens, "Holographic in situ stress measurements," *Geophys. J. R. Astron. Soc.* **85**, 13–41 (1986).
25. D. V. Nelson and T. T. McCrickerd, "Residual stress determination through combined use of holographic interferometry and blind hole drilling," *Exp. Mech.* **26**, 371–378 (1986).
26. Y. Y. Hung and J. D. Hovanesian, "Fast detection of residual stress in an industrial environment by thermoplastic-based shearography," *Proc. SEM Spring Conference on Experimental Mechanics*, 769–775, Albuquerque, NM (1990).
27. M. J. Pechersky, R. F. Miller, and C. S. Vikram, "Residual stress measurements with laser speckle correlation interferometry and local heat treating," *Opt. Eng.* **34**, 2964–2971 (1995) [doi: 10.1117/12.210762].
28. J. Zhang, "Two-dimensional in-plane electronic speckle pattern interferometer and its application to residual stress determination," *Opt. Eng.* **37**, 2402–2409 (1998) [doi: 10.1117/1.602007].
29. F. V. Díaz, G. H. Kaufmann, and G. E. Galizzi, "Determination of residual stresses using hole drilling and digital speckle pattern interferometry with automated data analysis," *Opt. Lasers Eng.* **33**, 39–48 (2000).
30. M. Kabiri, "Toward more accurate residual-stress measurement by the hole-drilling method: analysis of relieved-strain coefficients," *Exp. Mech.* **26**, 14–24 (1986).
31. G. S. Schajer and T. J. Rickert, "Incremental computation technique for residual stress calculations using the integral method," *Exp. Mech.* **51**, 1217–1222 (2011).
32. A. E. Dolinko and G. H. Kaufmann, "A least-squares method to cancel rigid body displacements in a hole drilling and DSPI system for measuring residual stresses," *Opt. Lasers Eng.* **44**, 1336–1347 (2006).

33. M. Steinzig and E. Ponslet, "Residual stress measurement using the hole drilling method and laser speckle interferometry: part I," *Exp. Tech.* **27**, 43–46 (2003).

34. G. S. Schajer and M. Steinzig, "Full-field calculation of hole drilling residual stresses from electronic speckle pattern interferometry data," *Exp. Mech.* **45**, 526–532 (2005).

35. R. Sutério, A. Albertazzi, Jr., and M. A. M. Cavaco, "Preliminary evaluation: the indentation method combined with a radial interferometer for residual stress measurement," SEM Annual Conference and Exposition on Experimental and Applied Mechanics, Society of Experimental Mechanics, Inc., Bethel, CT (2003).

36. A. Asundi and Z. Wenzen, "Fast phase–unwrapping algorithm based on a gray–scale mask and flood fill," *App. Opt.* **37**, 5416–5420 (1998).

37. A. Makino and D. Nelson, "Residual–stress determination by single–axis holographic interferometry and hole drilling – Part I: theory," *Exp. Mech.* **34**, 66–78 (1994).

38. J. Mathar. "Determination of initial stresses by measuring the deformations around drilled holes," *Trans. ASME* **56**, 249–254 (1934).

39. M. R. Viotti and A. Albertazzi, Jr., "Compact sensor combining DSPI and the hole-drilling technique to measure non-uniform residual stress fields," *Proc. SPIE* **8413**, 841310 (2012) [doi: 10.1117/12.978183].

40. M. R. Viotti and A. Albertazzi, Jr., "Compact sensor combining DSPI and the hole-drilling technique to measure nonuniform residual stress fields," *Opt. Eng.* **52**, 101905 (2013) [doi: 10.1117/1.OE.52.10.101905].

41. A. E. Giannakopoulos and S. Suresh, "Determination of Elastoplastic Properties by Instrumented Sharp Indentation," *Scripta Materialia* **40**, 1191–1198 (1999).

42. A. E. Giannakopoulos and S. Suresh, "Indentation of Solids with Gradients in Elastic Properties. Part I: Point Force," *J. Sol. Struct.* **34**, 2357–2392 (1997).

43. A. E. Giannakopoulos and S. Suresh, "Theory of Indentation of Piezoelectric Materials," *Acta Materialia* **47**, 2153–2164 (1997).

44. R. Suterio, A. Albertazzi, Jr., F. K. Amaral, and A. Pacheco, "Performance evaluation of a residual stress measurement device using indentation and a radial in-plane ESPI interferometer," *Proc. SPIE* **5856**, 763–774 (2005) [doi: 10.1117/12.612615].

45. L. D. Rodrigues, J. L. F. Freire, and R. D. Vieira, "Measurement of residual stresses in UOE–SAW line pipes," *Exp. Tech.* **32**, 58–62 (2008).

Chapter 7
Qualitative Fault Detection and Evaluation

7.1 Traditional Nondestructive Methods to Detect Defects

As explained in Chapter 1, the application of nondestructive techniques for NDT is intended for the early detection and characterization of anomalies in the material being evaluated. Because these defects have a negative influence on the mechanical performance of the mechanical part,[1] NDT is an essential tool for quality assurance when manufacturing the part and maintaining it after the start of its service life.[2,3]

There are several nondestructive techniques based on various physical principles. Usually the iteration between anomalies present in the material under study and the detecting medium (e.g., sound waves, electromagnetic radiation, etc.) is used to compare nondestructively measured or derived physical parameters with quantitative information generated by an anomaly present in the material. One such technique, based on eddy-current phenomena, involves measuring the change of the material impedance, which is affected by anomalies such as changes in the microstructure or cracks.

7.1.1 Visual inspection

Visual inspection is the most widely used nondestructive technique for evaluating the structural integrity of mechanical parts. This technique works well for external defects (such as cracks, etc.) that appear on the surface. However, it is inadequate for subsurface or internal discontinuity evaluation. Current developments in optics and image processing enhance the sensitivity of this technique, as well as its reliability, because it becomes independent of the user's ability to identify defects.

7.1.2 Radiographic techniques

Radiographic techniques use a beam of x rays, gamma rays, or atomic particles (neutrons, protons, or electrons). When the beam passes through the

part being analyzed, some portion of the energy is absorbed, which reduces the final energy of the beam. The absorption is proportional to the density of the material; for this reason internal defects produce variations in the beam intensity. These variations are recorded in a digital medium, allowing digital processing. X-ray computed tomography is an alternative approach that is very useful in the automotive industry.[4]

7.1.3 Magnetic techniques

Magnetic methods are among the oldest and most used nondestructive methods due to the importance and broad application of steel and ferromagnetic materials.[1] When a magnetic material is magnetized, the magnetic flux lines are uniformly distributed inside it. The presence of cracks or other internal defects affects the distribution of these lines, causing local magnetic flux leakage fields. These fields are identified on the surface of the analyzed material by using powders or sensors. Thus, the discontinuity that causes the leakage is found.[5] Magnetic methods can be classified as magnetic particle inspection, magnetic leakage flux, and magnetic Barkhausen noise. These methods are used to evaluate microstructural degradation.

7.1.4 Ultrasonic techniques

Ultrasonic testing uses sound waves that travel through the material and lose energy when they encounter a defect. This energy loss is indicated by a loss in the pulse amplitude and a change in its form. Ultrasonic methods are widely used to detect and characterize defects in welding.[6] Phase arrays methods have been developed that enable detailed, 3D searches for defects.[7,8]

Objects with a high temperature or complex shape cannot be measured with conventional ultrasonic techniques. These limitations can be overcome with the use of laser ultrasound.[9] This technique provides absolute measurement values without contact, and it allows remote detection.[10] (See other publications[11–13] for more information.)

7.1.5 Liquid-penetrant inspection

Liquid-penetrant inspection is another widely used nondestructive technique for the detection of discontinuities exposed on a material's surface. This technique uses the natural accumulation of a fluid (penetrant) around a discontinuity. A developer helps users quickly identify cracks on the surface.

7.1.6 Eddy-current methods

Eddy-current methods use the principle of electromagnetic induction. Thus, they are adequate for inspection of electricity-conducting materials. The presence of a defect disturbs the eddy-current flow, generating a perturbation in the signal. These methods are adequate for assessing microstructural degradations of components, as well as corrosion in materials.

Table 7.1 Overview of the applicability and capability of NDT techniques. The + symbol indicates that a technique is capable, the × symbol indicates that it is not capable, and the − symbol indicates that it is application-dependent.

		Detection			Evaluation				
Technique	Material	Surface	Sub-surface	Internal	Stress	Defect	Micro-structure	Inspect inaccessible regions	Online auto-mation
Visual	All	+	×	×	×	+	×	+	+
Radiographic	All	+	+	×	+	+	−	×	+
Magnetic	Magnetic	+	+	−	+	+	×	−	+
Ultrasonic	All	+	+	+	+	+	+	+	+
Liquid penetrant	All	+	×	×	×	+	×	−	−
Eddy current	Conductive	+	+	+	−	+	+	−	+
Thermography	All	+	+	−	×	+	×	×	+

7.1.7 Thermography

Thermography is a technique based on scanning the temperature profiles of the surface of an object. This method uses a special camera with an infrared sensor. Temperature variations on the surface of the object are displayed as shades of grayscale or pseudo-color images. Defects can produce alterations in the thermal flow of the material that are revealed by the camera. Of course, an external excitation should provide the energy capable to show the internal defect.

Most NDT techniques have a wide range of application and capabilities. Selecting the right technique for a determined application depends on several factors, such as the minimum size of the defect to be detected, the confidence level of detection, etc. It will also depend on factors such as applicability, accessibility, and suitability. Sometimes only one technique is adequate for a specific application; otherwise, the combination of two or more techniques in a complementary way will provide a more-reliable and complete inspection. Information about the material composition, properties, and microstructure will enable the identification of probable kinds of defects. This information helps users select the correct combination or individual application.

Table 7.1 presents an overview of the previously listed NDT techniques. Note that the capability of the eddy-current techniques to detect internal defects has a maximum depth of $\sim$6 mm.

7.2 Shearography as a NDT Inspection Tool

7.2.1 Optical configurations suitable for field applications

Chapter 3 explained how digital speckle shearing interferometry (shearography) is a useful tool to measure derivatives of the surface displacements generated in an object under deformation. A shearing device is introduced in the imaging system to produce two superimposed images of the object on the

CCD of the camera. In other words, either the object is duplicated or a point of the object is displaced a determined lateral shift, which is called shear.

The most common optical layout used for shearography is shown in Fig. 7.1. It comprises two mirrors and a beamsplitter cube in a traditional Michelson configuration,[14–16] and it is based on the layout proposed by Leendertz and Butters.[14] The object is illuminated by a collimated light with an incidence angle of γ. The scattered light is partially deflected by the beamsplitter illuminating a flat mirror M_1 (rays represented by solid lines). The light is then reflected by this mirror to the imaging system and focused on the CCD sensor at point P. Light rays passing through the beamsplitter (represented with dashed lines) illuminate the flat mirror M_2. These rays are reflected back from this mirror, and after being reflected into the beamsplitter, they are imaged at point P″ on the CCD sensor. By tilting mirror M_2, point P″ is laterally shifted from P′ by δx. The amount of tilt to mirror M_2 controls the magnitude of lateral shear of the image and the distance between points P′ and P″. The tilt show in Fig. 7.1 produces a vertical shear. A horizontal shift of these points is achieved by rotating mirror M_2 around a vertical axis.

The configuration shown in Fig. 7.1 is very convenient to introduce the phase shift between both interfering beams. Mirror M_1 can be slightly moved up and down in a parallel way, changing by a small amount the relative phase difference between the interfering light rays. This effect can easily be achieved by attaching the upper flat mirror to a microtranslator, such as a piezoelectric translator.

Wu et al.[17] show that the angle of view of the optical setup shown in Fig. 7.1 is limited by the Michelson configuration to an approximate angle of 28 deg. To overcome this limitation, Wu et al. modify the Michelson interferometer in Fig. 7.1 by introducing a 4*f* system. Figure 7.2 shows the modified layout.

In Fig 7.2, two lenses L_1 and L_2 with the same focal length are introduced into the optical layout. In this case, the Michelson interferometer is placed between them. The imaging lens and the CCD of the camera are "separated"

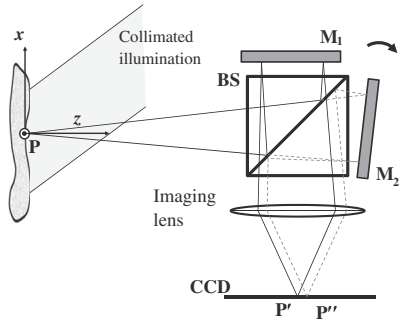

Figure 7.1 Production of variable shearing effect by tilting a flat mirror (formation of a laterally shifted image).

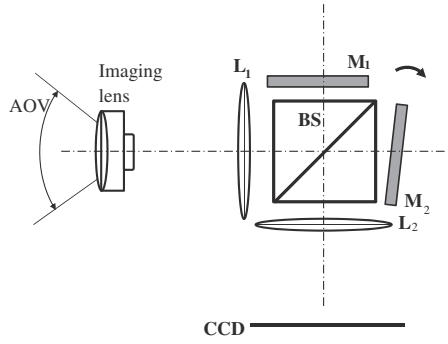

Figure 7.2 Optical arrangement for the 4*f*-modified Michelson interferometer.

because between them is the arrangement of the lenses L_1 and L_2 and the Michelson interferometer. This configuration has some advantages:

a. The Michelson interferometer no longer limits the angle of view (AOV). According to Wu et al.,[17] an AOV of 57 deg in the horizontal direction and 44 deg in the vertical direction can be obtained with a 2/3 CCD camera and an imaging lens with an 8-mm focal length. Moreover, the AOV can be increased by exchanging the imaging lens for one with a shorter focal length. This feature makes the device more versatile because several fields of view can be reached in accordance with measurement needs.
b. The focus and zoom are more easily controlled because the imaging lens is placed in the front of the Michelson arrangement.
c. It is possible to use a small beamsplitter and mirrors to produce a lighter measurement sensor, which simplifies its application outside the laboratory, where vibration is a common problem for heavy systems.

The main disadvantage of the 4*f* system is its influence on the obtained image because it changes the image direction; it affects the image quality and changes the image intensity distribution.[17] These problems can be corrected, as well: the image-direction problem by image processing, and the image-quality problem by using high-quality Fourier lenses in the 4*f* system. Finally, the nonuniform intensity can be compensated for with the correct choice of optical components.[17]

An alternative optical setup for shearography has been presented.[18–20] The authors of these works exchanged the cube beamsplitter for a diffractive grating that worked as a diffractive optical beamsplitter. The high diffraction efficiency makes this alternative very attractive when compared with a traditional Michelson setup for applications with low-intensity scattered light. In this kind of interferometer, phase shifting is generated by in-plane translation of the grating. The shearing principle is presented in Fig. 7.3, and the interferometer used by Gundlach et al.[20] is shown in Fig. 7.4.

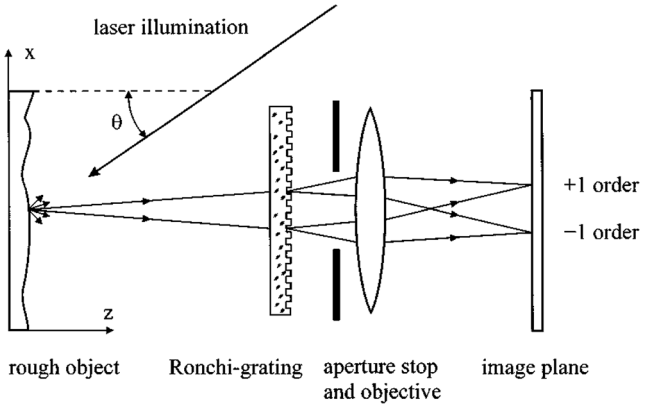

Figure 7.3 Schematic geometry of the shearing principle with a diffraction grating (reprinted from Gundlach et al.[20] with permission).

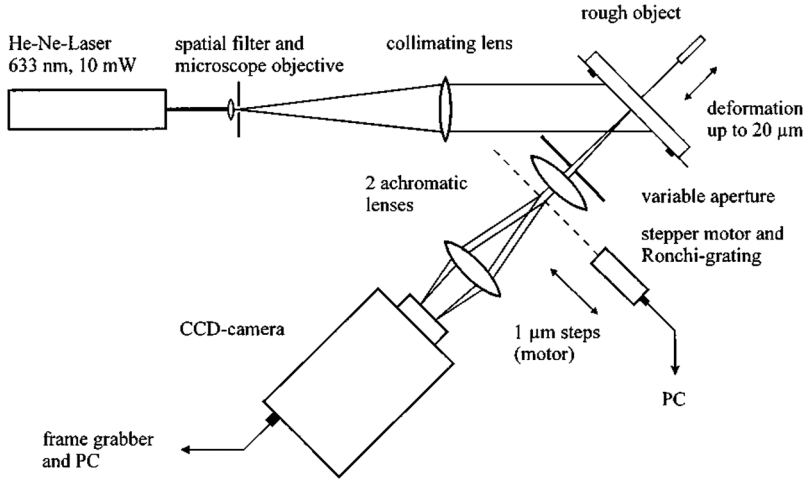

Figure 7.4 Optical setup of a speckle shearing interferometer (reprinted from Gundlach et al.[20] with permission).

The incident light illuminates the object, and it is imaged onto the CCD sensor. The grating is placed in front of the objective lens, producing two laterally sheared images of the object (see Fig. 7.3). In this case, the amount of shear is fixed by the grating period. In Gundlach et al.,[19,20] the interference beams are the $+1$ and -1 diffraction orders, which confers a high fringe contrast because both interfering beams have the same intensity. When the 0 and $+1$ orders interfere, the contrast is worse due to the different intensities.

Finally, for measurements outside the laboratory, optical setups that use diffraction gratings confer to the interferometer a high degree of compactness. These kinds of interferometers also have an in-line optical configuration that improves the stability of the interferometer. Thus, they are more suitable for *in situ* measurements in places with space restrictions and vibration.

Different authors have used other shearing devices: glass wedges,[21,22] Fresnel's biprisms,[23] Wollaston prisms,[24,25] and glass plates with parallel faces.[26]

7.2.2 The importance of shearography as a NDT inspection tool

Current industrial trends include reducing production costs, downsizing products (e.g., cars and engines), and simplifying the production process.[28] For these reasons, new fabrication techniques and lighter-weight materials, such as aluminum space-frame structures or carbon-fiber-reinforced polymers (CFRP), are replacing the traditional material: steel.

Adhesive bonding is widely used to join composite parts. However, this technique is prone to quality variations due to lack of adhesive, contamination, and inclusion of foreign materials.[28] The presence of moisture also reduces the bonding quality. Consequently, a suitable nondestructive technique or set of techniques is necessary for in-line inspection. Among the several NDT methods discussed in Section 7.1, the ultrasonic and x-ray diffraction approaches are the most suitable. However, for real-time applications, these methods present several practical limitations during in-mass inspection. For example, ultrasonic methods require point-by-point scanning and subsequent data analysis. In this case, the control process is too low when compared with the production process.

Shearography is a noncontact optical technique with full-field capability. As a result, it can scan a large area (depending on the AOV of the interferometer) in one camera shot. Thus, it is a fast technique suitable for in-line inspection as well as for the measurement of large structures, such as planes and tanks. Shearography also has several advantages when compared with holographic or other speckle techniques:[29]

(a) A reference beam is not required. For this reason, lasers with a large coherence length as well as vibration controls are not necessary for most cases.
(b) Surface strains are measured directly, and, depending on the optical layout, the whole strain field can be measured.[30]

For these reasons, shearography is a practical measurement tool that has been widely accepted by industry for NDT. The following sections describe applications in the automotive and aeronautical industry. Additionally, several examples in the oil and gas industry for tanks and pipelines are presented.

Other applications of shearography include measurement of strains, material properties, residual stresses, 3D shapes, and vibrations, as well as leakage detection. (A detailed description of shearography and its applications is given by Hung and Ho.[31])

7.3 Excitation Methods Used for Flaw Detection

When an object containing internal defects is loaded, strains are concentrated around the defect. If the defect is near the surface of the object, the strain

concentration will produce anomalies in the strain distribution generated on the surface. When the surface is illuminated by laser light and then imaged by a shearing interferometer (independent of the optical setups shown in the previous section), anomalies in the strain distributions will appear as fringe anomalies in the specklegram. Thus, an external load must be applied to the material in order to transmit the required energy to the internal defect so that it becomes "visible" to the interferometer.

Four kinds of excitations are normally used: thermal, vacuum, mechanical loading, and vibration. Thermal loading is easily applied to a composite surface by turning on a heat source, such as a high-power lamp, or blowing hot air on the area of interest. The thermal expansion of the composite material produces a relatively homogenous strain field in the absence of any defect. Defects within the composite material layers, e.g., a local disbonding or delamination, will expand and produce local deformation gradients that will generate discontinuities in the fringe pattern and reveal the presence of this defect. The amount of heating can be very small (on the order of $\sim$2 °C) to moderate (on the order of 20 °C), depending on the properties of the material, its thickness, and the kind of defect.

Figure 7.5 illustrates a scheme combining thermal loading with shearography. In this case, the correct bonding between both materials is being evaluated. Additionally, this figure shows that the location of the flaw will suffer an out-of-plane deformation due to the concentration of heating. This out-of-plane deformation will be identified by the interferometer.

Vacuum loading is applied by placing the area to be inspected inside a vacuum chamber. A first exposure is taken at normal pressure. While the pressure is reduced, the local region with the disbonding will expand and produce local deformation gradients. The second exposure is taken, and the difference between both exposures will reveal fringe patterns with a fringe concentration or anomalies in the flaw area. The shearography device can be completely inside the vacuum chamber or outside. In the latter case, a local vacuum chamber with a glass window should be placed around the area to be inspected. (The

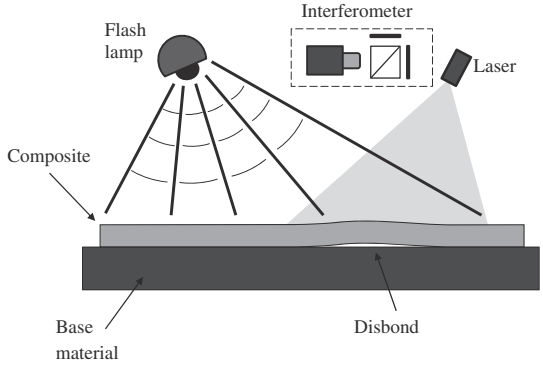

Figure 7.5 Thermal loading used to identify disbonding between two materials.

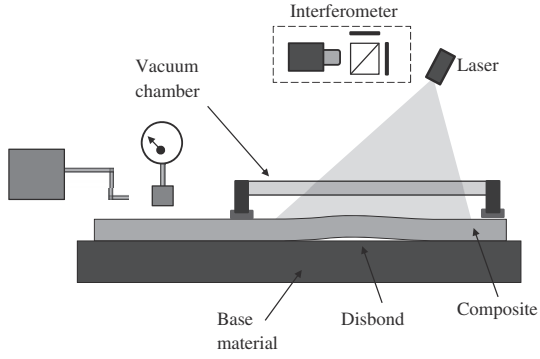

Figure 7.6 Vacuum loading used to identify disbonding between two materials.

illumination and observation of the composite surface will be conducted through the window.) The amount of vacuum to be applied will not be very intense: it will range from 100–600 mbar. Figure 7.6 shows this loading case combined with shearography; note that the vacuum chamber has a glass window.

Mechanical loading can also be applied to reveal flaws in composite materials. Pipes and pressure vessels can be loaded by changing the internal pressure by a known amount. Other mechanical structures can be loaded by bending, traction, or torsion. A fairly homogeneous deformation field is expected in the areas without flaws, producing smooth fringe patterns. The deformation gradients near flaw areas are very intense and produce recognizable anomalies in the fringe patterns. Figure 7.7 shows this kind of loading combined with shearography.

Flaws can also be detected by vibration excitation. The idea is to harmonically excite the composite material to be tested with a piezoelectric actuator or a loudspeaker. By changing the excitation frequency, different resonance modes can be obtained. A flaw area locally changes the stiffness of the composite material, which modifies the resonance frequency around that area. By using time-average or stroboscopic shearography, fringe patterns related to the vibration amplitude become clearly visible. By continuously

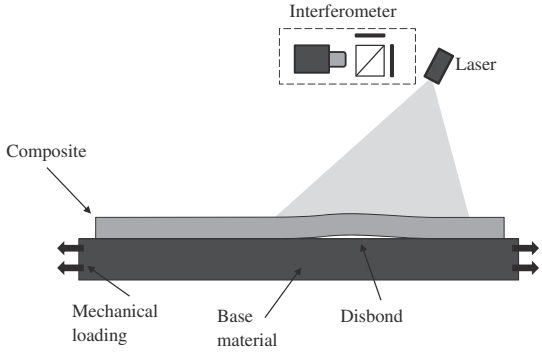

Figure 7.7 Mechanical loading to identify disbonding between two materials.

sweeping the excitation frequency, fringe patterns for different resonance modes appear and disappear. When the resonance frequency of the flaw area is reached, it starts to locally vibrate with a high amplitude, which produces localized fringe patterns that reveal the defect area. The resonance frequency of a flaw typically ranges from a few tens of hertz to 100 kHz. Figure 7.8 shows this kind of loading.

Figure 7.9 shows three fringe patterns for the same defect excited three different ways. The defect is a local disbanding in the interface between a steel pipe with a 500-mm diameter and a 4-mm-thick composite glove that was applied for corrosion protection. The defect was artificially introduced and has a rectangular shape. Figure 7.9(a) was produced by thermal loading with a 500-W lamp that increased the local temperature ~2 °C. The edges of the defect are clearly visible. Figure 7.9(b) shows fringes produced by vacuum loading. The flaw area is very easily distinguished from the remaining area. Finally, Fig. 7.9(c) was produced by mechanical loading applied by a hydraulic jack placed inside the pipe (simulating an internal pressure variation). The fringe shape and its number are different in these three loading cases, but they clearly reveal the presence and extension of the flaw.

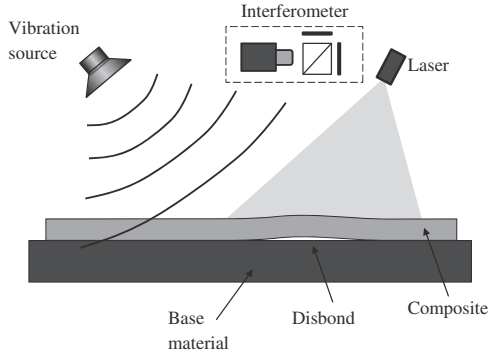

Figure 7.8 Mechanical loading used to identify disbonding between two materials.

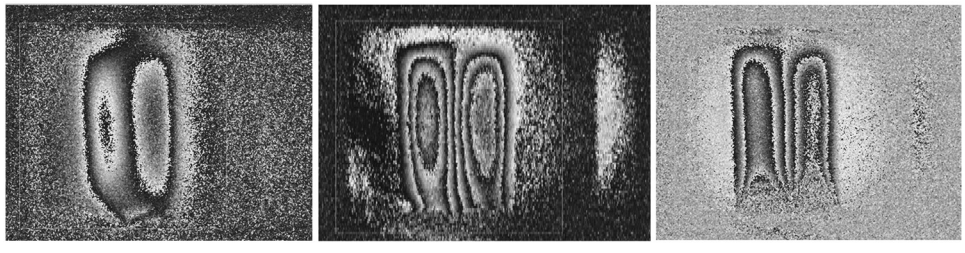

Figure 7.9 Different phase maps obtained for (a) mechanical, (b) thermal, and (c) vacuum loading.

7.4 Requirements for *in situ* Applications

As previously stated, one of most important applications of shearography is the NDT of composite materials. These materials are currently used in

- airplanes (e.g., vertical and horizontal stabilizer, airbrakes, and spoiler),[32]
- petroleum platforms (transmission of water in pipelines of composite materials),
- vehicles (to reduce weight of several parts), and
- tanks (in petroleum industry and in gas tanks for cars).

On the other hand, adhesive bonding is used in numerous industries to replace traditional mechanical fasteners, such as bolts, screws, and welding. Consequently, shearography deals with a wide variety of applications and materials with different textures. Thus, several requirements should be met for successful use.

7.4.1 Uncooperative surfaces

Materials such as CRFP, shining aluminum, and coatings can be considered uncooperative materials. "Uncooperative" means that the iteration between the laser light and the surface of the object under testing is not constructive.[33] These materials then generate regions with specular reflections close to regions with drastic intensity losses. The interferometer should be capable of managing these difficulties. Possible solutions include active intensity control by beam shaping,[34] polarization control, and image processing. Without these solutions, interferograms will have weak contrast areas and low sensitivity.[33]

7.4.2 Large inspection areas

Several cases have large areas to be inspected, e.g., aircraft components, naval parts, and petroleum storage tanks. The main problem for the illumination of large areas is the Gaussian distribution of the laser beam used as a light source, which leads to low fringe contrast in the margins of the image.[32] One possible solution uses an acousto-optical modulator (AOM) to divide the single laser light into several mutually incoherent parts.[32] This technique is known as multiple-beam shearography. Another method uses several independent light sources, e.g., a battery of laser diodes.[35]

Additionally, for the inspection of a large area using a single shearography interferometer, the ideal approach uses a modular device that is compact, mobile, flexible, and easy to handle, allowing for application in several kinds of structures. It should also have a lightweight construction that is user-friendly and reliable.

7.4.3 Quality control for in-line production

Manufacturing lines are usually dedicated to the constant production of the same product without changes. The main objective is generally to create the

product with good quality and with a low production time (to reduce costs). For this reason, an in-process inspection should be capable of adapting to the process in order to control the parts at the same speed of the production line. Thus, the inspection will not delay the production; in other words, the operator will not need to wait for the inspection procedure results, which keeps the production rate constant. Additionally, the inspection will avoid the consecutive production of a large number of parts with defects, thus decreasing the total scrap.

Considering the previous conditions, it is clear that full-field techniques are more suitable than their point-by-point counterparts. Moreover, automated processing should be used to meet requirements for high throughput in mass-inspection applications.

7.4.4 Loading adjustment

One of the most important components in a NDT experiment with shearography is the loading module. The correct application of loading will successfully detect defects. The response of the object to loading excitation depends on the following factors:[33] the material, the size and location of the flaw, the stiffness of the construction, and the type of loading. This list shows that for a specific measurement, the user can adjust only the loading in order to obtain a suitable detection. Thus, the kind of loading and its amount should be selected carefully. Special specimens are usually used as a reference to perform empirical investigations. Because these specimens have internal defects that were intentionally introduced, and because they represent real conditions of application for a specific situation (e.g., material, kind of flaw, etc.), investigations will typically lead to the best loading performance for NDT with shearography for the evaluated application.

7.5 Optical Setups for Inspection

The following sections present different shearography applications in which the previously listed requirements are accomplished by the shearographic systems.

7.5.1 Pipeline inspection

Transmission tubes made of composite materials have been used in various industrial segments, including the oil and gas industry. The union between adjacent composite tubes is often accomplished by adhesives. Thus, the inspection for flaws in adhesive-bonded joints becomes crucial. Figures 7.10 (a)–(c) show a general view of an experiment[36] wherein tubes and elbows made of epoxy resin reinforced with glass fiber were assembled with adhesive, forming loops (spools). During the assembly of these loops, artificial defects (areas without adhesive or disbondings) were inserted inside the joints to evaluate the capability of detecting failures by shearography.[36] Willemann et al. applied the traditional Michelson interferometer shown in Fig. 7.1.

(a) (b) (c)

Figure 7.10 (a) General view of the assembly; (b) detail of the flange and manometer; and (c) end of the specimen attached to the wall (reprinted from Willemann et al.[36] with permission).

Several tests using thermal loading applied to the composite joint inspections were carried out.[36] However, no satisfactory result was obtained, demonstrating that this kind of loading is inadequate for this particular application. To overcome this difficulty, a new setup was assembled to apply hydrostatic loading to the specimens. Thus, the correct selection of loading type will lead to the success of the experiment. In other words, it will or will not allow for the possible identification of defects.

For example, Figs. 7.11(a) and (b) show a uniform fringe pattern that resulted from shearographic inspection in a healthy area. Conversely, Figs. 7.12(a) and (b) show a part of the joint where an artificial flaw is present. The (a) figures are related to a horizontal shear of 10 mm, and the (b) figures are related to a vertical shear of 10 mm. The amount of shear was also determined after experiments designed to find the best sensitivity. A comparison of Figs. 7.11 and 7.12 reveals a

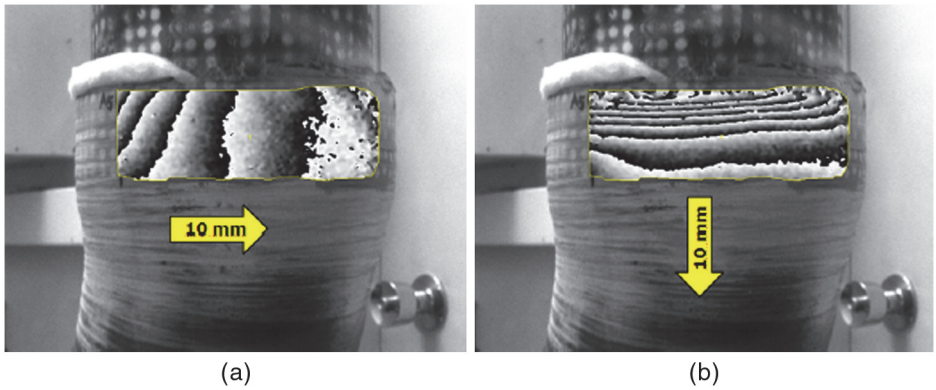

(a) (b)

Figure 7.11 Adhesive-bonded joint with no flaws: (a) transversal fringe pattern, (b) axial fringe pattern (reprinted from Willemann et al.[36] with permission).

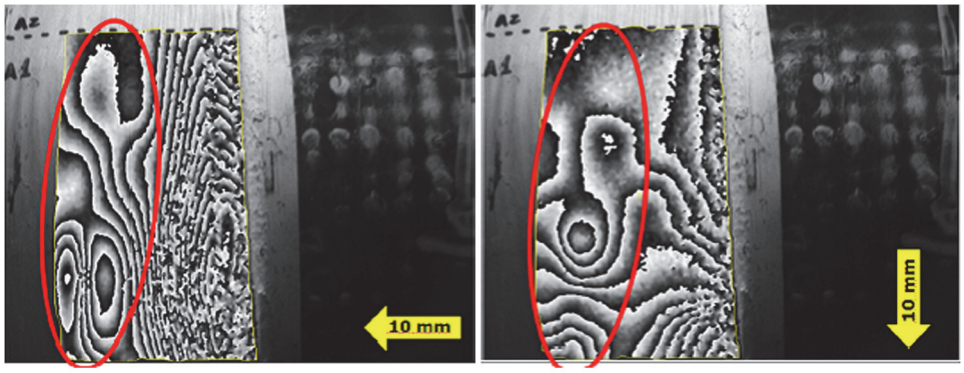

(a) (b)

Figure 7.12 Adhesive-bonded joint with artificial flaws: (a) transversal fringe pattern, (b) axial fringe pattern (reprinted from Willemann et al.[36] with permission).

set of discontinuities in the measured fringe patterns of Figs. 7.12. Depending on the shear direction, flaws will cause different variations in the fringe patterns. This means that the same flaw analyzed by different shear directions will present different fringe patterns. For example, the "butterfly" pattern[36] found in Fig. 7.12(a) has a different fringe pattern than Fig. 7.12(b) despite having the same flaw.

After a long time of operation, pipelines may present internal or external metal loss caused by corrosion and erosion. A segment of a pipeline with metal loss defects can return to the maximum operating pressure after the replacement of the entire damaged segment or after the application of local repairs. The repair of corroded pipelines with fiber-reinforced composite materials is a well-developed practice in the oil and gas transportation industry.[37]

Because these repairs are usually applied *in situ*, operational conditions for correct adhesion between the composite material and the metallic wall of the pipe are not completely fulfilled. For example, adequate cleaning of the surface, before application of the adhesive, might be nearly impossible. Consequently, some regions without complete gluing between both materials will occur. This case is an unwanted condition because places with disbondings will have a poorer mechanical behavior (e.g., fatigue loading) when compared with healthy areas. Additionally, these regions will be subject to continuous corrosion due to the presence of air between the materials. This last fact is highly problematic because visual inspection (e.g., looking for corrosion areas) cannot be achieved because the metallic surface of the pipe is completely covered by the composite repair. Shearography can be used to determine possible disbondings between the repair and the pipe, as well as within layers of the repair.

Figure 7.13 shows a photograph of two pipe samples covered by a fiber-reinforced layer. These samples have simulated disbondings introduced between the composite material and the steel wall. Figure 7.9 shows the fringe patterns measured in these pipes for three kinds of loadings. The figures show that thermal loading generates more fringes than mechanical and

Figure 7.13 Pipe samples with composite repairs (reprinted from Willemann et al.[36] with permission).

vacuum loadings. Due to its simple implementation, thermal loading was selected for evaluating this type of problem.

As an example, Fig. 7.14(a) shows a practical measurement on an oil platform. The measured pipe was placed near sea level and was protected with a composite material to avoid extreme corrosion. Figure 7.14(b) shows that small defects in the composite material caused incorrect adhesion.

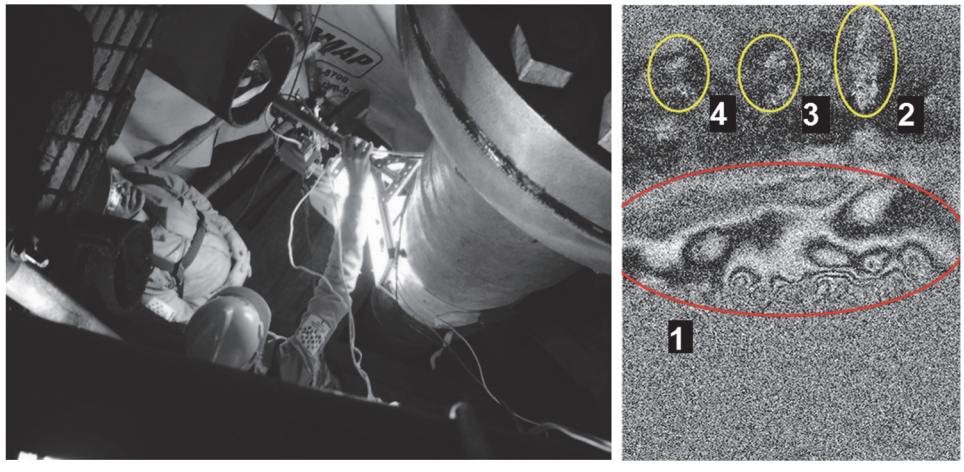

(a) (b)

Figure 7.14 Integrity evaluation of pipelines repaired with composite materials (reprinted from Willemann et al.[39] with permission).

A different application of shearography is provided by Wang and Chiang.[40] The authors performed nondestructive inspection of a composite hollow cylinder by combining a Michelson interferometer and a conical mirror. Thus, the conical mirror optically transforms the cylindrical surface to a plane surface that is measured with a traditional shearography setup.

7.5.2 Tank inspection

Tanks are used in the oil and gas industry for the storage of petroleum and its refined products, such as gasoline, fuel, gas oil, etc. They are built from steel, and they are internally protected against corrosion by fiber-reinforced composite layers. Corrosion usually strongly affects the lower part of the tank walls as well as its floor because salt water mixed with petroleum is stored at the bottom due to its higher density when compared with pure petroleum. Thus, correct adhesion between the composite layer and the steel surface will guarantee corrosion-free effects under the composite layer. Figure 7.15(a) is a photograph of the external view of a storage tank for petroleum; Fig. 7.15(b) shows its internal view. The composite layer on the metallic surface can be clearly seen.

Figure 7.16 shows two photographs of a shearography interferometer based on a Michelson arrangement. A high-power diode-pumped solid state (DPSS) laser is expanded, obtaining an illuminated area $\sim$1 m in diameter. The interferometer is mounted on a tripod fixed to the tank floor by means of vacuum (suction cups). A rigid clamping is achieved in a nonmagnetic alternative to the magnetic solutions shown in Chapters 5 and 6.

Finally, Fig. 7.17 shows four fringe phase maps measured on four consecutive areas located at the floor of the tank. Small anomalies appear inside the uniform fringes, generated by the uniform displacement of the composite layer. The inset image amplifies area A2, and two disbonded regions are highlighted with black circles. Thermal loading was applied during these measurements. The main drawback observed in this application is the

(a) (b)

Figure 7.15 (a) External and (b) internal view of a petroleum storage tank (reprinted from Martins de Souza[41] with permission).

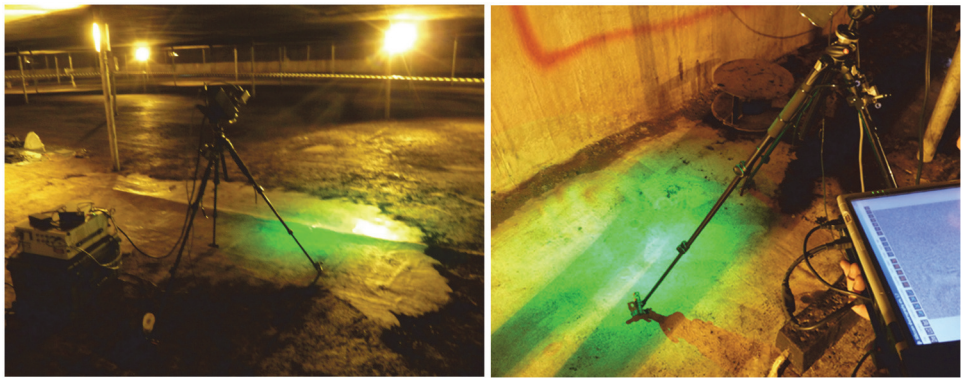

Figure 7.16 Shearography interferometer measuring the floor of a tank (reprinted from Martins de Souza[41] with permission).

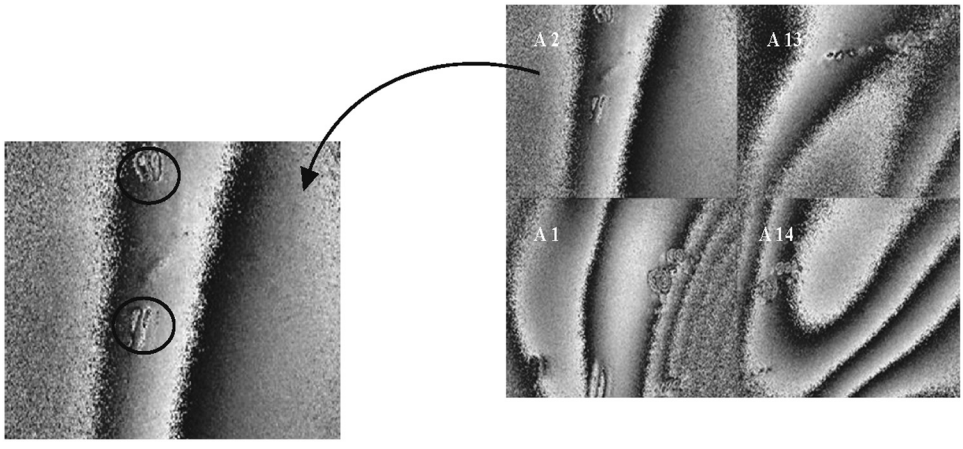

Figure 7.17 Four consecutive measured areas. Left inset: amplified area with highlighted defects (reprinted from Martins de Souza[41] with permission).

large amount of time required to completely inspect the tank, which has a diameter of ~80 m. A robotic, automated system is a possible solution to handle the large dimensions of petroleum tanks.

7.5.3 Aeronautical inspection

Carbon-reinforced fiber and GLARE (glass-reinforced aluminum laminate) have been used in the aeronautical industry for the construction of airplane parts and structures. These materials have extraordinary mechanical performance and light weight when compared with traditional materials, e.g., steel. For these reasons, they are highly suitable for aircraft fabrication. However, these sophisticated materials need a quality-assurance system in order to recognize possible damages or defects, thus ensuring safe operation.[42]

Kalms[42] has developed a mobile shearographic setup capable of performing NDT inspections in aircraft parts as well as in different aircraft materials. Figure 7.18(a) shows a photograph of the vacuum window used by the system as a source of loading excitation. In order to generate thermal loading, several high-power infrared radiator bars are used as IR sources. They are combined with the shearography sensor in a portable cabinet. Pneumatic suction cups are used to fix the device to the structure under analysis. These cups are flexible in all directions to facilitate working with spherical surface areas.

As an example, Fig. 7.19 shows the mobile shearographic device measuring an aircraft wing by using thermal loading. Figures 7.20(a) and (b) show two

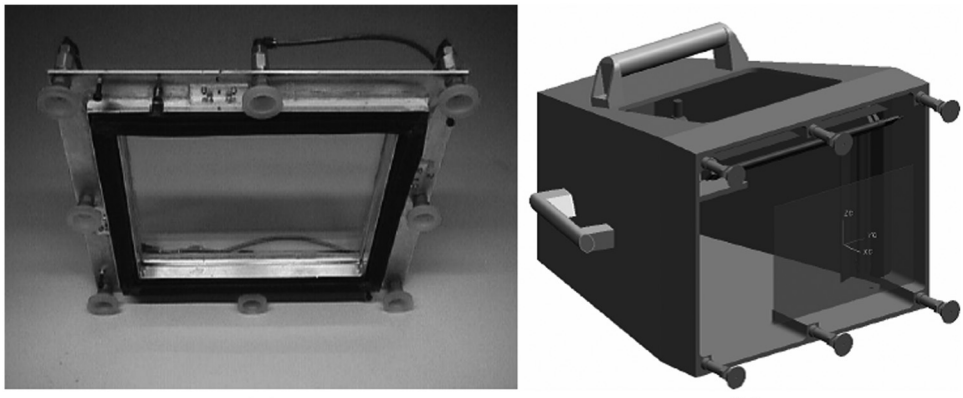

Figure 7.18 (a) Vacuum loading device. (b) Portable shearographic cabinet (reprinted from Kalms[42] with permission).

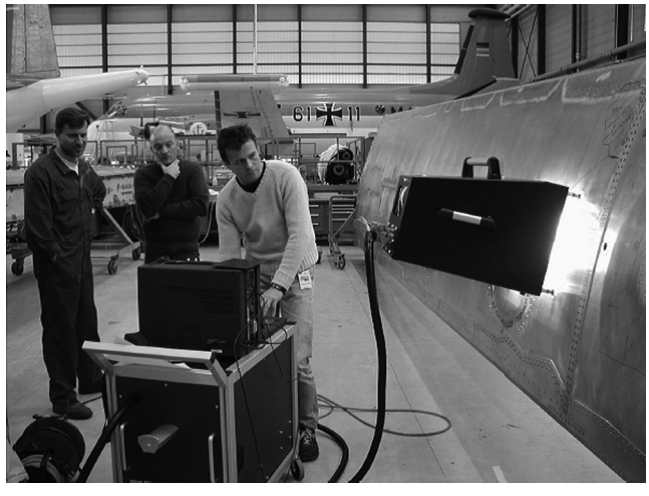

Figure 7.19 Wing inspection using the mobile shearographic system (reprinted from Kalms[42] with permission).

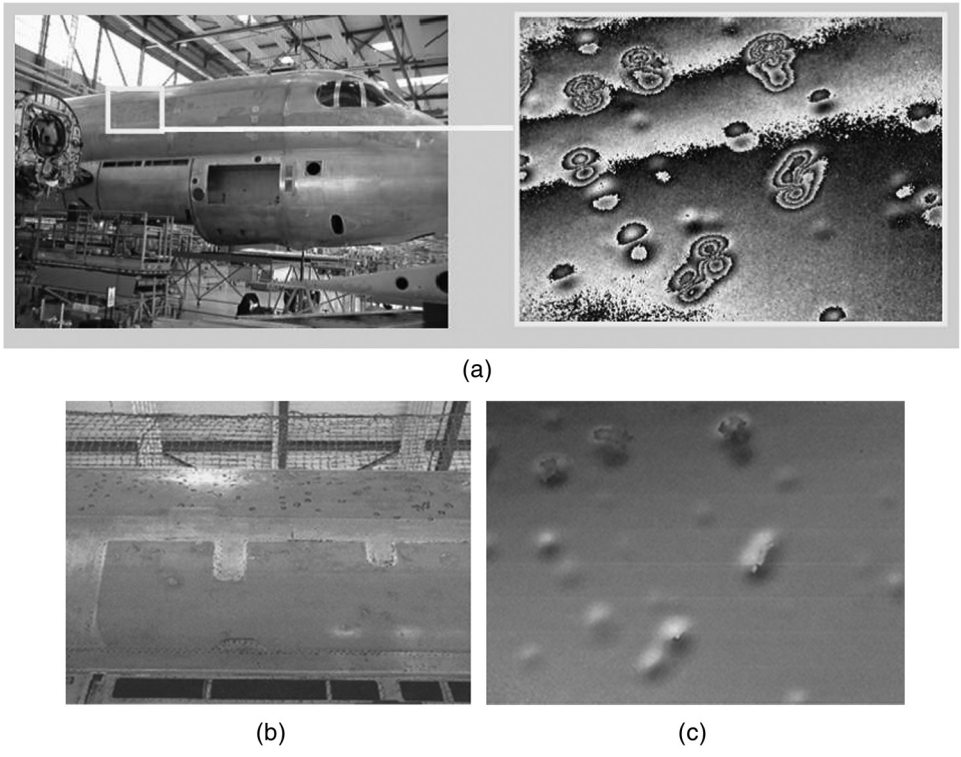

Figure 7.20 (a) Airplane under testing with a measured phase map; (b) hailstone marks on the top of the fuselage; and (c) measured optical phase distribution (reprinted from Osten et al.[33] with permission).

photographs of a plane fuselage that was subjected to a heavy hailstorm. The amplified image in Fig. 7.20(a) shows many detected hailstone impacts. Figure 7.20(c) represents the continuous optical phase distribution obtained from the difference phase map measured in Fig. 7.20(a). The images show good-quality test results achieved under the unfavorable working conditions of a maintenance facility.[33]

Finally, Findeis et al.[43] compare thermography and shearography for the detection of induced defects in composite helicopter rotor blades and a wing section of an aerospace vehicle. The measured results of the rotor blade identify a relation between the defect depth and the number of fringes.

7.6 Image Processing Tools for Fast Defect Identification

Shearography images usually have fringe patterns with a butterfly shape that clearly identify the presence of a defect inside the matrix of the composite material under testing. However, when the surface to be inspected has a complex geometry, the resulting phase image can contain a complex fringe pattern that can completely hide defect indications.[41]

Chapter 1 listed several requirements for optical systems performing in-field measurements. Among them, the "user-friendly" requirement refers to not only the easy operation of the interferometer but also the presentation of results. Consequently, a processing tool used to improve flaw detection for complex shearographic images can also be used to obtain a robust measurement system. Evaluation does not depend on the user's ability because the processing program directly provides the result.

In this way, Fantin et al.[44] introduce a processing method whose main goal is to highlight "butterfly" fringes typically found in shearography maps. The method calculates a sum of local radial variations of phase. This kind of variation is especially significant when the region is composed of irregular fringes, and it is inexpressive for regular fringes patterns, such as parallel fringes.

Consider an 8-bit synthetic phase image, where values range from 0 to 255 gray levels. Consider also a pixel of the image and a set of neighboring pixels symmetrically distributed over a region of interest (ROI) defined by two concentric circles, as shown in Fig. 7.21. The radial phase variation around a pixel can be calculated through the sum of phase differences between two pixels located in the same angular position, each one belonging to one circle:[43]

$$V_r = \sum_i (\phi_i{}^E - \phi_i{}^I) \tag{7.1}$$

where $\phi_i{}^E$ is the phase value for the i^{th} pixel on the external circle, and $\phi_i{}^I$ is the phase value of i^{th} pixel on the internal circle.

In the Fig. 7.21, only ten points are used to illustrate the pixel distribution on the ROI, but in practice, a larger number of points should be used for the calculation. The maximum number of pixels used is limited by the smaller circle perimeter.

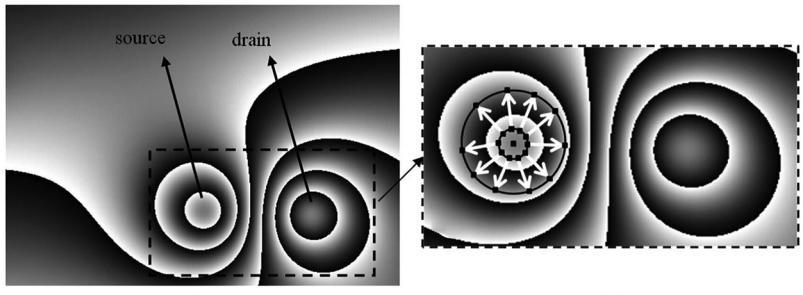

Figure 7.21 (a) Synthetic phase image with a butterfly pattern. (b) Pixel in the image, and a set of neighboring pixels symmetrically distributed over a ROI defined by two concentric circles. The arrows show the correspondence between two pixels in the same angular position in the ROI.

The phase pattern in the region with defects has a source and a drain, analogous to the electric-field divergence, where the common convention states that a charge "flows out of" a positive charge and "flows into" a negative charge (Gauss's law). Similarly, the presence of flaws is detected by the local divergence of the phase variation. The radial phase variations are positive in the source region of phase map, whereas the changes are negative in the drain region. As phase variations are computed closer to the source or drain, larger values are found. Thus, positive phase changes result in a peak, and negative phase changes result in a valley, as shown in Fig. 7.22. A color map of the results is an alternative that might produce better representation. Finally, Fig. 7.23 shows a practical application in a complex fringe map obtained in a composite joint similar to that shown in Fig. 7.12. In this case, the processing method clearly highlights the defect in the joint [Fig. 7.23(b)], which is not the case in the single analysis of Fig. 7.23(a).

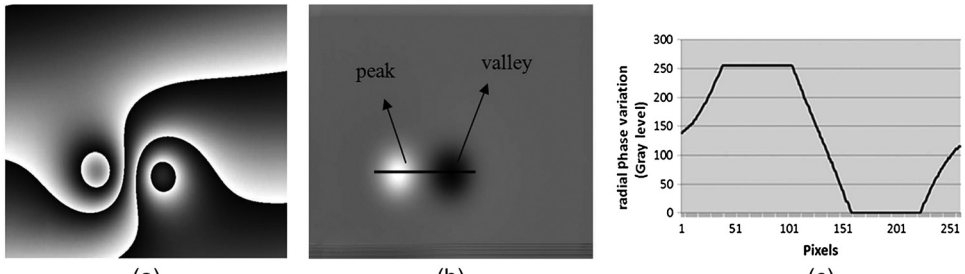

Figure 7.22 (a) Simulated phase map for a defect, (b) graymap of radial phase variation, and (c) phase profile of the defect region.

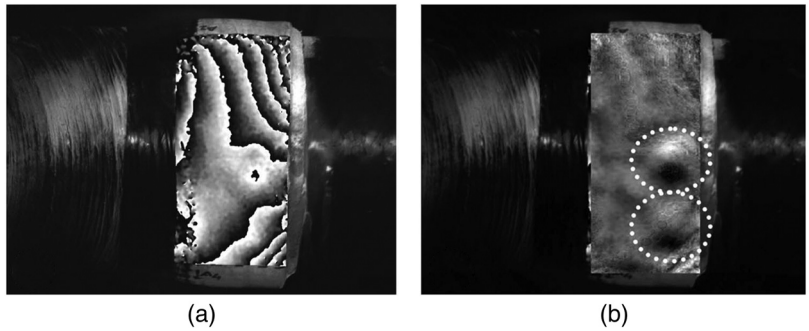

Figure 7.23 (a) Common map acquired with shearography in a bell-and-spigot composite pipe joint. (b) Map obtained with the proposed method.

7.7 Commercial Systems

There are a number of companies that commercialize shearography systems intended for the aeronautical, aerospace, and automotive industries. One of the worldwide leading suppliers of measurement systems is Dantec Dynamics. It manufactures, among other optical systems, the Q-800 portable shearography system for NDT, shown in Fig. 7.24(a), as well as a portable version called the Q-810 [Fig. 7.24 (b)].

In the same way, Steinbichler has also commercialized portable shearographic devices. The ISISmobile 3000 from Steinbichler is shown in Fig. 7.25. According to the company website, some of the main features of the measurement system are (a) flexibility for use on various tasks, (b) easy adjustability, (c) one-man operation, (d) customer-specific user interface, (e) real-time data display, and (f) data export in common file formats as well as network capability. This list nicely matches the requirements stated in Chapter 1.

The SNT 4045 from Optonor AS in Norway is a compact shearography system combined with dynamic excitation (using vibrational excitation) for NDT. The SNT 4040 is a system with very high resolution that uses vacuum and static excitation.

(a)

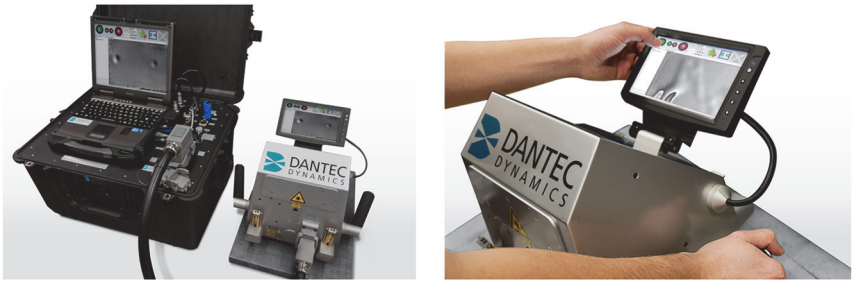

(b)

Figure 7.24 (a) Q-800 portable shearography system for NDT. (b) Portable version Q-810 (reprinted with permission, © Dantec Dynamics AS).

Figure 7.25 ISISmobile 3000 (reprinted with permission © Steinbichler).

Another well-known company is isi-sys GmbH, which also commercializes optical devices for NDT and strain measurements. Shearography systems developed by isi-sys employ vibrational excitation for object loading through a piezoshaker that is placed on the surface to be measured.

Shearography can also be applied to the preservation of artwork. In this case, it is used to evaluate surface and subsurface defects, allowing for posterior repair, e.g., paintings. Francis et al.[45] provide an extensive review of several applications of shearography.

References

1. R. Baldev, T. Jayakumar, and B. P. C. Rao, "Non-destructive testing and evaluation for structural integrity," *Sadhana* **20**, 5–38 (1995).
2. P. O. Moore, *Nondestructive Testing Handbook*, 3rd Ed., Vols. 1–10, American Society for Nondetructive Testing, Columbus, OH (1998–2010).
3. R. B. Bergmann and P. Huke, "Advanced methods for optical nondestructive testing," *Optical Imaging and Metrology*, W. Osten and N. Reingand, eds., Wiley-VCH, Weinheim, Germany (2012).
4. R. B. Bergmann, F. T. Bessler, and W. Bauer, "Non-Destructive Testing in the Automotive Supply Industry - Requirements, Trends and Examples Using X-ray CT," Ninth Conference on NDT (2006) (available online at http://www.ndt.net).
5. P. E. Mix, *Introduction to Non-Destructive Testing: A Training Guide*, John Wiley and Sons, New York (1980).
6. J. P. Pelseneer and G. Louis, "Ultrasonic testing of austenitic steel castings and welds," *Br. J. Non-Destructive Test*. **16**, 107–113 (1974).

7. M. Kröning, J. G. H. Ribeiro, and A. Vidal, "Progress in NDT system engineering through sensor physics and integrated efficient computing," 17th World Conference on Non-Destructive Testing, Shanghai (2008).
8. W. L. Schmerr and S. J. Song, *Ultrasonic Nondestructive Evaluation Systems: Models and Measurements*, Springer, New York (2007).
9. J. P. Monchalin, P. Bouchard, C. Padioleau, R. Heon, M. Choquet, J.-D. Aussel, G. Durou, and J. A. Nilson, "Laser-ultrasonics: from the laboratory to the shop floor," *Adv. Perform. Mater.* **5**(1–2), 7–23 (1998).
10. J. P. Monchalin, "Optical and laser NDT: a rising star," 16th World Conference on Non-Destructive Testing, Montreal (2004).
11. M. Kalms, O. Focke, and C. V. Kopylow, "Applications of laser ultrasound NDT methods on composite structures in aerospace industry," *Proc. SPIE* **7155**, 71550E (2008) [doi: 10.1117/12.814512].
12. M. Kalms and R. B. Bergmann, "Applications of laser ultrasound NDT methods in aircraft industry," 13th Asia-Pacific Conference on Non-Destructive Testing, Yokohama, Japan (2009).
13. M. Kalms, C. Peters, and R. Wierbos, "Assessment of carbon fiber-reinforced polyphenylene sulfide by means of laser ultrasound," *Proc. SPIE* **7983**, 79830B (2011) [doi: 10.1117/12.877223].
14. J. A. Leendertz and J. N. Butters, "An image-shearing speckle pattern interferometer for measuring bending moments," *J. Phys. E. Sci. Instrum.* **6**, 1107–1110 (1973).
15. Y. Y. Hung and C. E. Taylor, "Speckle-shearing interferometric camera – a tool for measurement of derivatives of surface displacements," *Proc. SPIE* **41**, 169–175 (1973) [doi: 10.1117/12.953850].
16. Y. Y. Hung, "Shearography: a novel and practical approach to nondestructive testing," *J. Nondestruct. Eval.* **8**, 55–68 (1989).
17. S. Wu, X. He, and L. Yang, "Enlarging the angle of view in Michelson-interferometer-based shearography by embedding a 4*f* system," *App. Opt.* **50**, 3789–3794 (2011).
18. H. Rabal, R. Henao, and R. Torroba, "Digital speckle pattern shearing interferometry using diffraction gratings," *Opt. Commun.* **126**, 191–196 (1996).
19. A. Gundlach, B. Manske, and J. Schwider, "Speckle shearing interferometry using a phase Ronchi-grating," *Lehrstuhl für Optik*: *Annual Report*, p. 44 (1995).
20. A. Gundlach, J. M. Huntley, B. Manske, and J. Schwider, "Speckle shearing interferometry using a diffractive optical beamsplitter," *Opt. Eng.* **36**(5), 1488–1493 (1997) [doi: 10.1117/1.601351].
21. Y. Y. Hung and C. Y. Liang, "Image-shearing camera for direct measurement of surface strains," *Appl. Opt.* **18**, 1046–1051 (1979).

22. B. Bhaduri, M. P. Kothiyal, and N. K. Mohan, "Curvature measurement using three-aperture digital shearography and fast Fourier transform," *Opt. Lasers Eng*. **45**, 1001–1004 (2007).
23. N. A. Ochoa and A. A. Silva-Moreno, "Fringe demodulation in time-averaged digital shearography using genetic algorithms," *Opt. Commun.* **260**, 434–437 (2006).
24. S. Kim, "Polarization phase-shifting technique in shearographic system with a wollaston prism," *J. Opt. Soc. Korea* **8**, 122–126 (2004).
25. Y. Y. Hung, Y. H. Huang, L. Liu, S. P. Ng, and Y. S. Chen, "Computerized tomography technique for reconstruction of obstructed phase data in shearography," *Appl. Opt.* **47**, 3158–3167 (2008).
26. E. Mihaylova, M. Whelan, and V. Toal, "Simple phase-shifting lateral shearing interferometer," *Opt. Lett.* **29**, 1264–1266 (2004).
27. C. Falldorf, E. Kolenovic, and W. Osten, "Speckle shearography using a multiband light source," *Opt. Lasers Eng.* **40**, 43–52 (2003).
28. Y. Y. Hung, Y. S. Chen, S. P. Ng, S. M. Shepard, Y. Hou, and J. R. Lhota, "Review and comparison of shearography and pulsed thermography for adhesive bond evaluation," *Opt. Eng.* **46**(5), 051007 (2007) [doi: 10.1117/1.2741277].
29. Y. Y. Hung, "Role of shearography in nondestructive testing," *Proc. SPIE* **4537**, 1–8 (2002) [doi: 10.1117/12.468755].
30. S. Waldner and S. Brem, "Compact shearography system for the measurement of 3D deformation," *Proc. SPIE* **3745**, 141–148 (1999) [doi: 10.1117/12.357771].
31. Y. Y. Hung and H. P. Ho, "Shearography: an optical measurement technique and applications," *Mater. Sci. Eng.* **49**, 61–87 (2005).
32. M. K. Kalms, W. Osten, W. P. O. Jüptner, W. Bisle, D. Scherling, and G. Tober, "NDT on wide-scale aircraft structures with digital speckle shearography," *Proc. SPIE* **3824**, 280–286 (1999) [doi: 10.1117/12.364280].
33. W. Osten, M. K. Kalms, W. P. O. Jüptner, G. Tober; W. Bisle, and D. Scherling, "A shearography system for the testing of large-scale aircraft components taking into account non-cooperative surfaces, " *Proc. SPIE* **4101**, 432–438 (2000) [doi: 10.1117/12.498440].
34. W. Osten, M. K. Kalms, W. P. O. Jüptner, "Some ways to improve the recognition of imperfections in large scale components using shearography" *Proc. SPIE* **3745**, 244–256 (1999) [doi: 10.1117/12.357785].
35. W. Setinchen and L. Yang, *Digital Shearography: Theory and Application of Digital Speckle Pattern Shearing Interferometry*, SPIE Press, Bellingham, WA (2003).

36. D. P. Willemann, A. V. Fantin, and A. Albertazzi, Jr., "Defect assessment of bonded joints of composite tubes using shearography," *Proc. SPIE* **7387**, 73870J (2010) [doi: 10.1117/12.870680].

37. J. L. F. Freire, R. D. Vieira, J. L. C. Diniz, and L. C. Meniconi, "Part 7: effectiveness of composite repairs applied to damaged pipeline," *Exp. Tech.* **31**, 59–66 (2007).

38. A. Albertazzi, Jr., C. L. Meniconi, D. P. Willemann, R. V. Bepler, P. B. Sfredo, R. P. Ferreira, E. Devegili, M. R. Viotti and D. Hofmann, "Detecção de falhas de adesão entre mantas poliméricas e dutos Detecção de falhas de adesão entre mantas poliméricas e dutos usando interferometria de deslocamento lateral," XXIV Congresso Nacional de Ensaios Não Destrutivos e Inspeção (2006).

39. D. P. Willemann, A. Albertazzi, Jr., and C. L. Meniconi, "Um sistema prático para identificação e localização de defeitos em revestimentos de materiais compósitos utilizando shearografia," 9ª COTEQ-Conferência Internacional sobre Tecnologia de Equipamentos (2007).

40. W. C. Wang and C. S. Chiang, "Nondestructive Inspection of Defects in Pressure Vessels," XI International Congress & Exposition on Experimental & Applied Mechanics, Society for Experimental Mechanics, Orlando, FL (2008).

41. J. P. Martins de Souza, "Inspeção de defeitos em revestimentos de materiais compósitos aplicados em tanques metálicos utilizando shearografia," Master's thesis, Federal University of Santa Catarina, Brazil (2013).

42. M. Kalms, "Mobile shearography in applications," *Proc. SPIE* **6762**, 67620K (2007) [doi: 10.1117/12.735483].

43. D. Findeis, J. Gryzagoridis, and V. Musonda, "NDT detection and quantification of induced defects on composite helicopter rotor blade and UAV wing sections," *Proc. SPIE* **7155**, 71551N (2008) [doi: 10.1117/12.814560].

44. A. V. Fantin, D. P. Willemann, M. R. Viotti, and A. Albertazzi, Jr., "Radial phase variation computing: a tool to improve flaw detection in optical diagnosis by shearographic images," *App. Opt.* **52**, 5460–5468 (2013).

45. D. Francis, R. P. Tatam, and R. M. Groves, "Shearography technology and applications: a review," *Meas. Sci. Technol.* **21**, 102001 (2010).

Chapter 8
Digital Image Correlation for Structural Monitoring

8.1 Noninterferometric Methods for Monitoring

Previous chapters presented several applications of speckle metrology that used a full-field and noncontact technique to measure displacements on the surface of an object. Other interferometric techniques include holography interferometry and moiré interferometry, both of which are outside the scope of this book.

Interferometric techniques usually require a coherent light source. Furthermore, measurements are normally performed in laboratories with isolated-vibration tables.[1] Previous chapters provide solutions and improvements that bring these techniques outside the laboratory. The measurement procedure used in these techniques can generally be summarized by the following steps:

1. Recording a reference phase map;
2. Introducing the perturbation (phenomena to be measured);
3. Recording the deformed phase map;
4. Computing the difference phase map (fringe pattern);
5. Finally, phase processing is used to recover information about the deformation field.

On the other hand, noninterferometric techniques are also used to measure displacement fields and their associated loading fields, e.g., stresses and strains. Two such techniques are the grid method[2,3] and digital image correlation (DIC).[4]

By definition, DIC refers to noncontact techniques that acquire images of an object before and after the deformation.[4] The full-field deformation or motion of the object is extracted by comparing changes between images through image analysis. Digital image registration has been performed with many types of patterns: lines, dots, grids, and random arrays. Random arrays

are most commonly used; they compare subregions in the image to obtain full-field information about the measurement. The patterns can occur in solid surfaces or a collection of particles in a fluid medium.

One of the earliest methods using DIC was developed by a group of researchers at the University of South Carolina in the 1980s.[5–9] These authors digitally recorded a full-field pattern by subjecting an object to ultrasonic waves before (reference image) and after (deformed image) loading. Peters and Ranson developed a method that analyzes the full-field recorded images comparing various small regions (called subsets) in the images before and after the deformation. The authors used fundamental continuum-mechanics principles governing the deformation of small areas as part of the matching process.[4]

Since its inception, DIC has been extensively investigated, improved, and used as a powerful and flexible tool to measure deformations on the surface of objects. Sutton et al.[4] give an extensive and complete review of DIC developments over time, including a list of works published from 1985. It is clear that the fast growth of DIC applications was significantly helped by progress in digital image technology as well as in methods for digitally recording images. DIC has received several names in the numerous publications: texture correlation,[10] computer-aided speckle interferometry (CASI),[11,12] electronic speckle photography,[13–16] and digital speckle correlation method (DSCM).[17,18]

8.2 Fundamentals of Image-Matching Methods

As previously explained, DIC computes the motion of each image point by comparing digital images of the surface of the object before and after the deformation. However, there are several cases in which a unique correspondence between features present in the images cannot be achieved.[4]

In order to solve the correspondence problem as well as the aperture problem shown in Sutton et al.,[4] the ideal surface texture should be isotropic (i.e., without a preferred direction limiting the determination of motion vectors). Furthermore, the texture should be nonperiodic to avoid misregistration problems. The speckle pattern can be the natural texture of the surface of the object or it can be artificially made by applying white and/or black paint. These patterns usually adhere to the surface and deform with it in order to avoid correlation losses under large translations and deformations. One of the most interesting features is that the speckles carry a rich and plentiful amount of information. Moreover, because the whole measured surface is textured, the information for matching is available for each point of the surface, allowing the application of small apertures for matching, called subsets.

It is relatively simple for the human eye to identify a motion in successive images; however, for mathematical models, it is not a straightforward process. A simple method based on optical flow is known as the differential method.[4] In this case, two assumptions should be made: (a) the motion should be sufficiently small for the applied first-order Taylor series expansion to be valid, and (b) the

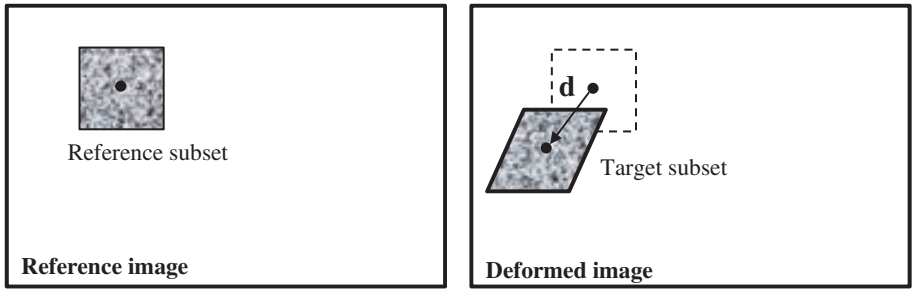

Figure 8.1 Schematic representation of a square subset before and after deformation.

motion should be constant for the neighbor used for estimation. An alternative matching method is the well-known Lucas–Kanade tracker algorithm.[4] It is equivalent to the differential method, but it is an iterative method that minimizes the gray value difference between a small subset from one image (template) and a displaced copy of the subset in the other image.

The Lucas–Kanade method is not restricted to small motions, and large motions can be found and computed.[4] This method is an iterative method that minimizes the squared difference in gray values, known as the sum of squares deviation (SSD), over a neighborhood:

$$\mathbf{d}_{opt} = \arg\min \sum \left| G(\mathbf{x} + \mathbf{d}) - F(\mathbf{x}) \right|^2 \tag{8.1}$$

where G is the image after the displacement, F is the reference image, $\mathbf{d}$ is the displacement vector, and $\mathbf{d}_{opt}$ is the optimal displacement vector.

Previous matching algorithms are limited to extract information from square subsets between two images. The main reason for using square subsets rather than individual pixels is that a subset has a wider variation of gray levels that will distinguish it from the other subset. Thus, identifying the subset will be more unique in the deformed image.

For real cases, the specimen under investigation will undergo elongations, compressions, shear, or rotations; Fig. 8.1 illustrates this case. The reference subset is square, and then it is transformed into a considerably distorted shape (e.g., a parallelogram).

8.3 Subset Shape Functions

Iterative methods used to determine pure translation can be extended to deformation computation.[4] This is accomplished by introducing a subset function $\zeta(\mathbf{x}, \mathbf{p})$, where $\mathbf{x}$ is the position, and $\mathbf{p}$ is the parameter vector of the shape function. Thus, the cost function is written as

$$\chi^2(\mathbf{p}) = \sum \left[G(\zeta(\mathbf{x}, \mathbf{p})) - F(\mathbf{x}) \right]^2. \tag{8.2}$$

In this case, the minimization of the SSD requires the computation of derivatives of the cost function with respect to all parameters of $\mathbf{p}$.

Polynomials in the subset coordinates are suitable as a simple solution for shape functions. This family includes pure displacements (zero-order polynomial) and affine transformation (first-order polynomial). Quadratic or higher-order polynomial functions can be used. (See Sutton et al.[4] and Schreier and Sutton[21] for a more detailed discussion about polynomial shape functions and associated systematic errors.)

In summary, the analysis of shape functions shows that subset shape functions act as low-pass filters applied to the displacement field encoded in the images. For this reason, these references state that a better expression of the cost function of Eq. (8.2) is obtained when a weighting function $w(\mathbf{x})$ is introduced, as follows:

$$\chi^2(\mathbf{p}) = \sum w(\mathbf{x})[G(\zeta(\mathbf{x}, \mathbf{p})) - F(\mathbf{x})]^2. \tag{8.3}$$

For the weighting function, the Gaussian distribution is a good choice because it gives the best compromise between spatial and displacement resolution.[4]

8.4 Optimization Criteria for Pattern Merging

In an ideal world with perfect conditions, images recorded at different times would have different light intensities. In reality, these problems are amplified, thus complicating the matching process. Reasons for changes in the intensity of the images are

- changes in the illumination source,
- changes in the reflectivity of the specimen generated by its deformation, and
- changes in the orientation of the specimen.

These changes usually occur in localized areas of the image and do not affect the whole image. The matching process is increasingly laborious, and thus it is important to have matching algorithms capable of dealing with these issues.

In order to process images in which lighting changes by an offset, the zero-mean sum of square difference (ZSSD) criterion can be used:

$$\chi^2_{ZSSD} = \sum \left((G_i - \overline{G}) - (F_i - \overline{F}) \right)^2, \tag{8.4}$$

where $\overline{F} = \sum F/n$ and $\overline{G} = \sum G/n$ are medium values for the subset. In the same way, the so-called normalized sum of square difference (NSSD) criterion can be used for images scaled in lighting:

$$\chi^2_{NSSD} = \sum \left(\frac{\sum F_i G_i}{\sum {G_i}^2} G_i - F_i \right)^2. \tag{8.5}$$

By combining both previous criteria, an optimization criterion can be obtained to deal with images that feature changes in lighting in offset as well as in scale:

$$\chi^2_{ZNSSD} = \sum \left[\left(\frac{\sum \overline{F}_i \overline{G_i}}{\sum \overline{G_i}^2} G_i - \overline{G} \frac{\sum \overline{F}_i \overline{G_i}}{\sum \overline{G_i}^2} \right) - F + \overline{F} \right]^2, \qquad (8.6)$$

which is called the zero-mean normalized sum of square difference. (Cross-correlation criteria can be found in the literature.[1,22–24])

To obtain pixel accuracy, the cost function should be evaluated at noninteger locations. Consequently, gray levels should be interpolated between pixels. In the literature, several interpolation schemes are used, including bilinear interpolation, bicubic bi-spline interpolation, bicubic interpolation, biquintic B-spline interpolation, and bicubic spline interpolation.[1] (Further information about these algorithms can be found in Press et al.[25]. High-order interpolation is strongly recommended by Schreier et al.[26] and Knauss et al.[27] because it provides better convergence character of the algorithm and higher registration accuracy.)

8.5 Optical Configurations Used in DIC

8.5.1 In-plane measurements using 2D DIC

Figure 8.2 shows a traditional optical setup used for 2D DIC. The specimen surface is illuminated by white-light sources; thus, the specimen has a random gray intensity distribution that deforms together with the surface. The CCD camera obtains the images of the object in different loading states. The camera is placed with its optical axis normal to the specimen surface.

2D DIC is restricted to planar surfaces that experience in-plane deformations. In addition, the camera should be placed normal to the surface. However, out-of-plane motions are common in practice; for example, in a

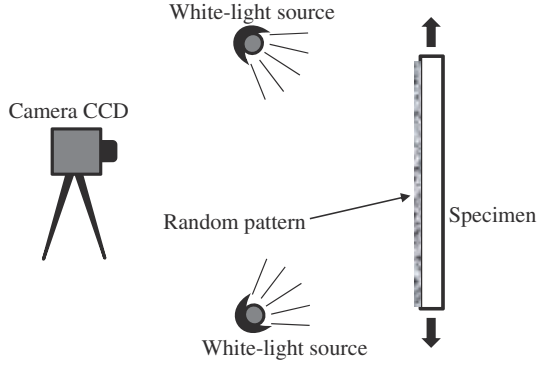

Figure 8.2 Optical layout used in 2D DIC.

tensile test, out-of plane motions are generated by[28] (a) local necking along the loading process, (b) Poisson's effect, (c) deviation from planarity, (d) small bending of the specimen, and (e) deviation from ideal grip constraints. Out-of-plane motions will introduce image plane displacement gradients that can corrupt the in-plane displacement measurements if they are large enough. This influence can make it difficult or impossible to separate true deformations from pseudo image deformation produced by out-of-plane motions. Sutton et al.[28] show that out-of-plane motions decrease image magnification and introduce a negative normal strain in all directions. The same reference shows that for a telecentric lens system, the effect of out-of-plane motions is reduced if the light passing through the entrance pupil is nearly parallel to the object axis.

Although subject to the previously mentioned limitations, 2D DIC is currently used to characterize the mechanical response of homogeneous and heterogeneous materials under planar deformations.[29–33] Commercial software is also available to simplify the image analysis.[34]

8.5.2 Three-dimensional measurements using DIC

Three-dimensional DIC is based on stereovision principles.[4,35] Thus, two cameras are used simultaneously to capture 2D images of the same area of the object. These cameras are placed at different angles to recover the 3D information.

When a unique camera is used to image the surface of an object [as seen in Fig. 8.3(a)], the third dimension is irreversibly removed from the 2D image. Thus, the two 3D points Q and R are imaged at the same point p lying in the same projecting ray (C_1, p). Consequently, infinite 3D points will correspond to the image point p.

It is possible to recover the 3D position of the true object points by using two cameras simultaneously [see Fig. 8.3(b)] at setup that will capture image points of the same object. Thus, two image points p and q' are uniquely related to the 3D point Q. If the corresponding points are p and r', then the 3D point will be R, in this case.

For a stereovision system, the transformation from the image coordinate system to the world coordinate system is the most important step. The coordinate transformation is performed by using a 4×4 matrix, which is related to rotation, translation, affine transformation, and homographies.[36] Figure 8.4 shows the transformations accomplished between the cameras and the world coordinate system. Thus, R_1 and R_2 rotate the world system and align it to cameras 1 and 2, respectively. In the same way, T_1 and T_2 translate the world system to the origin of both cameras.

Consider that the point Q of Fig. 8.3(b) has (x_w, y_w, z_w, 1) homogeneous coordinates in the world coordinate system. In the same way, (x_{c1}, y_{c1}, z_{c1}, 1) and (x_{c2}, y_{c2}, z_{c2}, 1) represent the homogeneous coordinates corresponding to Q in camera 1 and camera 2, respectively. Finally, (u_1, v_1, 1) and (u_2, v_2, 1)

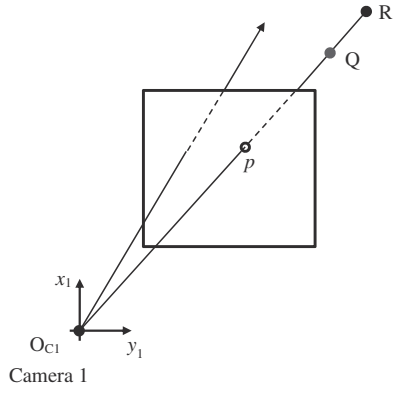

(a)

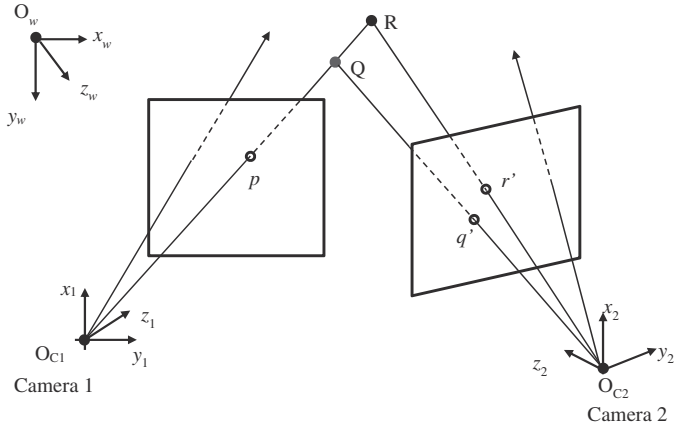

(b)

Figure 8.3 (a) Pinhole camera configuration. (b) Two cameras set up for 3D recovery.

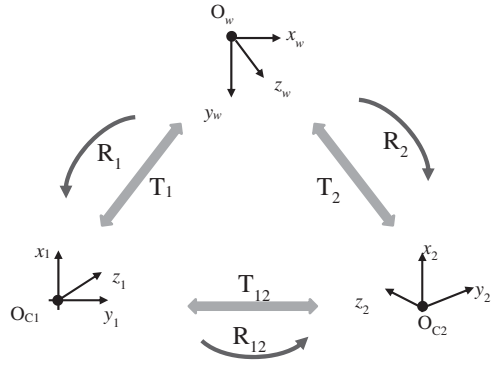

Figure 8.4 Transformations between cameras in a stereovision system.

represent the image coordinates for both cameras, respectively. Sutton et al.[4] and Chen et al.[36] have shown that the transformation equation is

$$s\begin{bmatrix} u \\ v \\ 1 \end{bmatrix} = A_i \begin{bmatrix} R_i & T_i \\ 0 & 1 \end{bmatrix} \begin{bmatrix} x_w \\ y_w \\ z_w \\ 1 \end{bmatrix} \quad i = 1, 2, \tag{8.7}$$

where s is a scale factor, $\mathbf{A}_i$ is the camera calibration matrix, $\mathbf{R}_i$ is the rotation matrix, and $\mathbf{T}_i$ is the translation vector. Thus, by solving Eq. (8.7), the space coordinates of the object can be evaluated in order to obtain the 3D morphology.

Finally, to determine the displacement of any subset, it is necessary to match a region of the reference image to a region of the deformed image and to match the same region between the left and right cameras. This can be accomplished by using the subset-matching processes discussed in the previous section for 2D DIC.

However, for 3D DIC systems, stereovision matching aims to match two speckle patterns on the same specimen surface recorded by both cameras from different angles before and after the deformation.

Figure 8.5 shows the various steps to take a measurement using the 3D DIC method. After the system is calibrated, the reconstruction can be

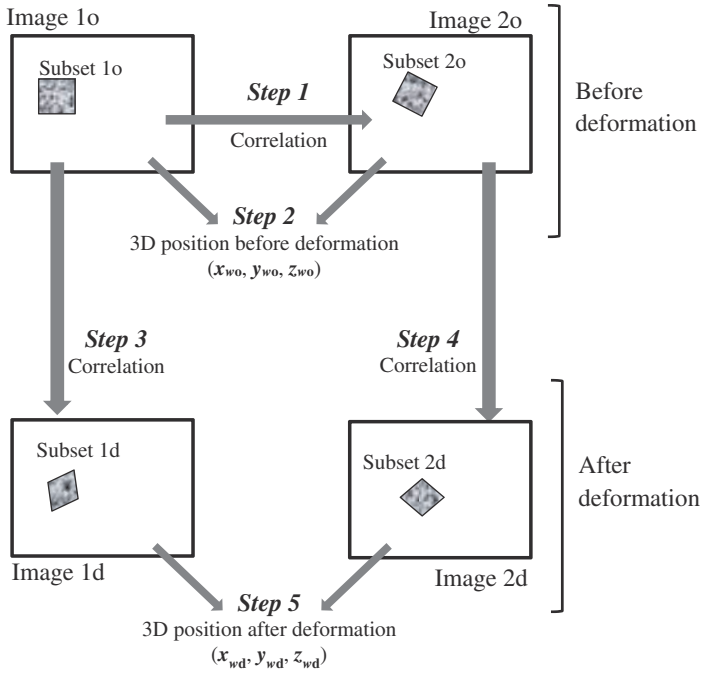

Figure 8.5 Processing steps for 3D DIC measurements.

accomplished by triangulation. The triangulation process requires that the image points be matched in the images acquired by both cameras. By using the calibration parameters, the 3D position of all of the matched image points is computed. 3D DIC has some limitations:[36]

- The distance between cameras and the object must be adjusted or lenses must be changed when the size of the object is beyond the field of view of the cameras.
- The mutual occlusion or the complex curvature of the object may produce blind visual spots that cannot be covered by cameras.

To overcome these practical limitations, Chen et al.[36] proposed a multicamera system consisting of four cameras. For this system, each pair of cameras can be considered as an independent stereovision system that can measure a determined area of the object.

Figure 8.6 shows an adaptation of the schematic setup presented by Chen et al.[36] with multiple cameras. The pair of cameras 1 and 2 scans the left part of the object, and the pair of cameras 3 and 4 images the right part. There is an overlapping area that corresponds to both parts.

Finally, Sutton et al.[4] have presented the principles for volumetric digital image correlation (VDIC) in order to produce volumetric information of the deformation of the object. (Further information as well as the mathematical computation can be found in Sutton et al.[4])

This section has shown that 2D and 3D setups use DIC as a robust technique for measurements of displacement fields in objects outside the laboratory via optical setups that are very easy to apply to practical situations. The following section will show some applications of DIC in order to illustrate its potential as an experimental technique related to NDT testing.

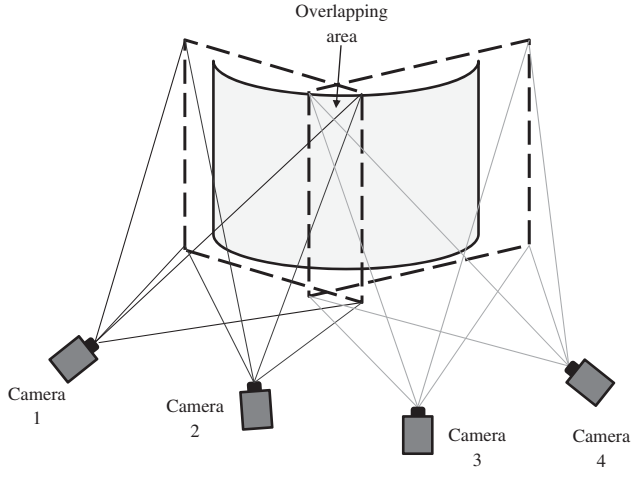

Figure 8.6 Measurement setup using multiple cameras.

8.6 Application Examples

During the 1990s, a wide range of experimental methods were developed to monitor aerospace structures. Examples of these techniques include eddy-current probes and ultrasonic devices that are used to identify cracks near rivet holes.[37] In the same way, thermography was used to recognize disbonding areas in lap joints, and shape measurements were applied to find bulges in regions of extensive corrosion, However, these methods are not capable of providing quantitative full-field 3D measurements, which are important to validate computational structural predictions.

For this reason, Helm et al.[37] used a 3D DIC system that acquires stereovision images and analyzes them in order to obtain the 3D deformations in large panels and correct the effects of perspective distortions.[38,39] This stereovision system was successfully used to characterize crack growth in aluminum panels subject to tension torsion loadings.[40,41] During loading, these panels experience large out-of-plane displacements and large in-plane strains. The DIC system was capable of dealing with them.

Helm et al.[37] used the same 3D DIC system to evaluate the response of wide M(T) center-notched tensile specimens under tensile tests [M(T) signifies middle-crack tension]. Figure 8.7 shows a schematic of the middle-flawed tension M(T) specimen geometry used in this reference. Specimens were loaded in a tensile machine. Figure 8.8 shows a photograph of the specimen under loading and the stereovision system mounted on a frame on the right.

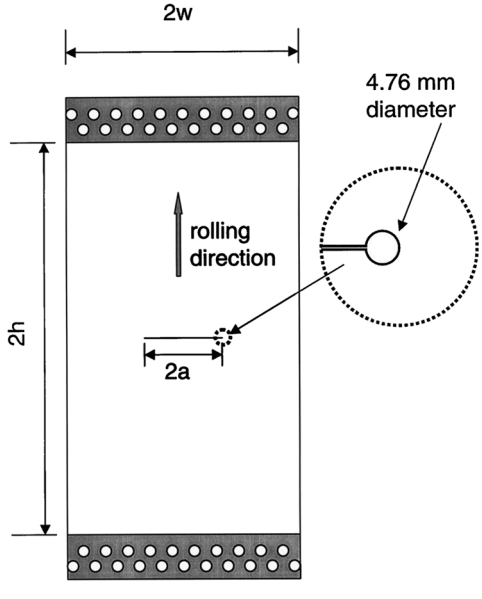

Figure 8.7 Specimen geometry (reprinted from Helm et al.[37] with permission).

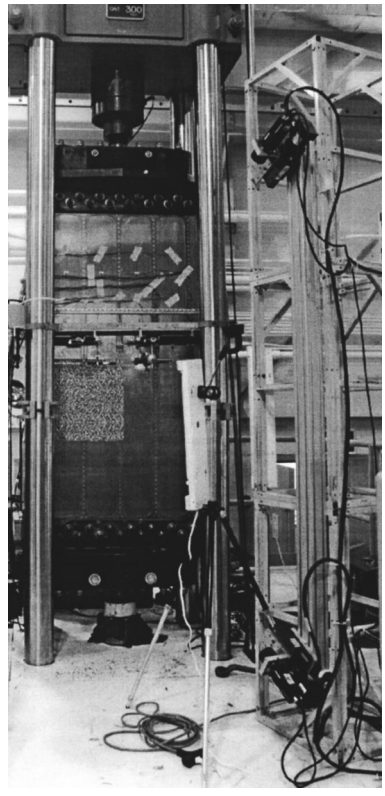

Figure 8.8 Stereovision system for global image acquisition (visible at right, mounted vertically on frame) with a 1.3-MN-tension loading frame and a 1016-mm panel specimen (reprinted from Helm et al.[37] with permission).

In order to measure concentrated strains that occurred around the hole and the notched area, a local imaging system was used and mounted on a translation stage, which enables movement to track the location of the hole and the notch after loading. Thus, a flexible DIC mounting uses two stereovision systems:[37] one for measuring deformations for a large portion of the specimen, and one for measuring deformations in a small area of interest. Figure 8.9 shows the stereovision system used for local image acquisition.

Surface displacements were determined by correlating images acquired by the cameras before and after the deformation. Via image correlation and knowledge of the camera calibration parameters, the system was capable of measuring the initial shape of the object (profiling) and the true-full-field 3D displacements of the objects. Figure 8.10 shows the initial profiles measured for three panels with a 305-mm, 610-mm, and 1016-mm width and evaluated by Helm et al.[37]

The data show that (a) the 305-mm panel has a saddle shape, (b) the 610-mm panel has a rounded shape with the same sign in curvature in both the

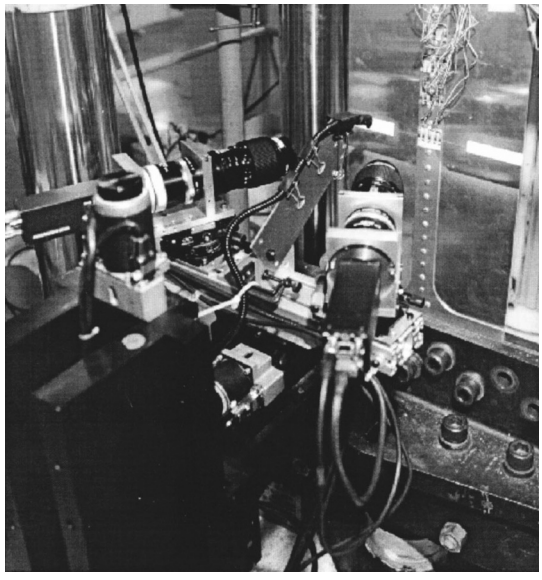

Figure 8.9 Stereovision system for local image acquisition (reprinted from Helm et al.[37] with permission).

x and y directions, and (c) the 1016-mm panel has a significant local gradient near the centerline of the notch.[37]

Figure 8.11 clearly shows that a 3D measurement system is capable of measuring true, 3D structural deformations, both in regions with large out-of-plane displacements (23 mm $< w <$ 19 mm in a 1016-mm panel) and in regions where the in-plane deformations are dominant. Furthermore, in regions with a rapid change in one or more of the displacement components, the experimental data demonstrated that the measurement system is capable of resolving the large displacement gradients while simultaneously determining the remaining displacement components.[37] Figure 8.12 shows the local strain at the maximum load for the larger panel. (Further information and results are discussed by Helm et al.[37])

Fractures in ductile thin-sheet structures, such as fuselage or automobile panels, often occur under complex loading conditions.[43] The experimental characterization employed for thin-sheet plates exposed to mixed-mode I/III loading is very cumbersome and sophisticated. Additionally, a cracked structure is subjected to a combination of in-plane stresses and large out-of-plane tearing deformations. For this reasons, Sutton[43] uses 3D DIC to acquire the full-field deformation field during the loading and stable tearing processes in aluminum specimens. Measurement results were used to characterize the stable crack extension behavior of specimens under quasi-static and dynamic mixed-mode I/III loading. Results confirm that 3D DIC is a robust and efficient tool to measure 3D deformations in the presence of large out-of-plane deflections and motions.

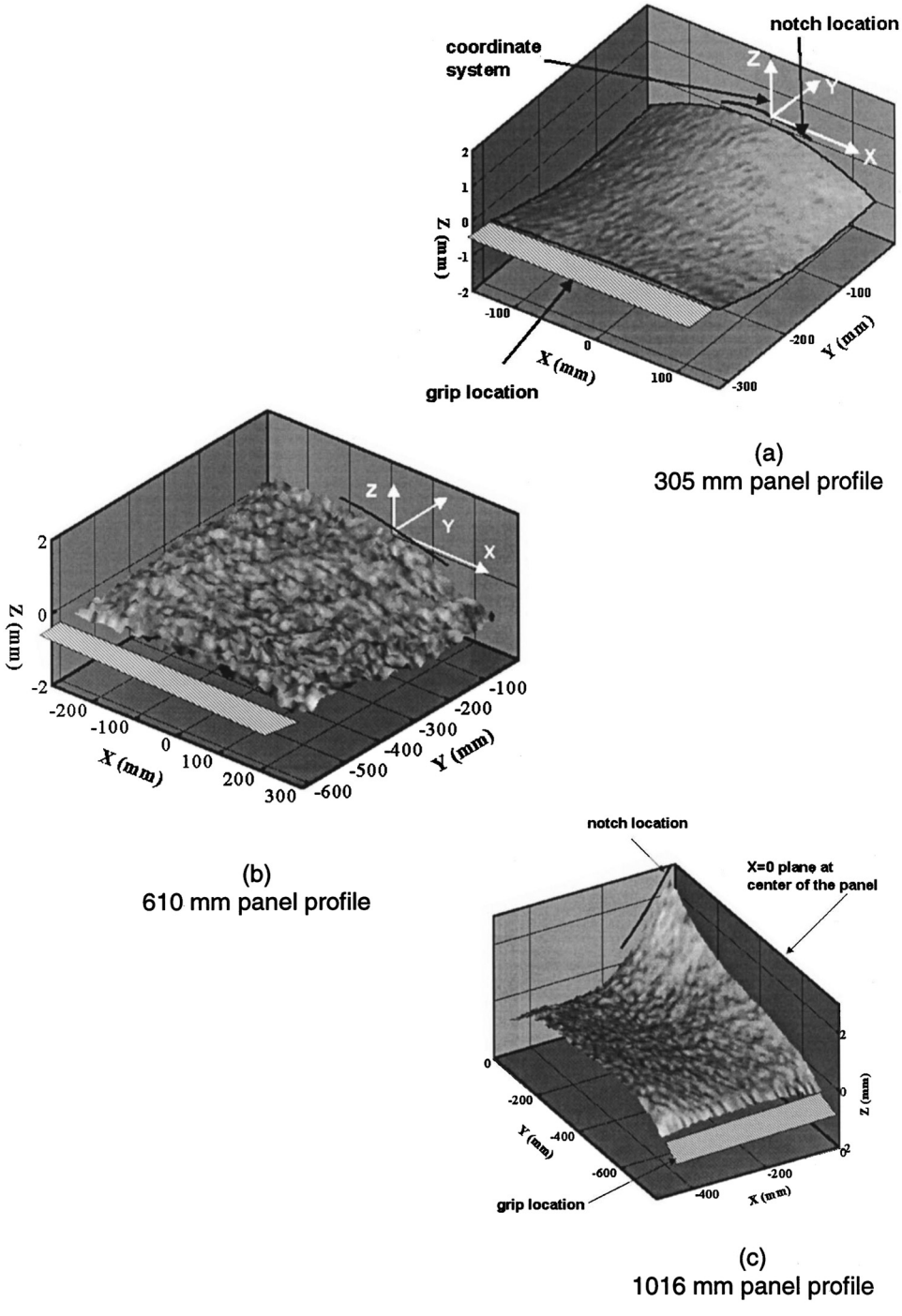

Figure 8.10 Initial profiles for panels (reprinted from Helm et al.[37] with permission).

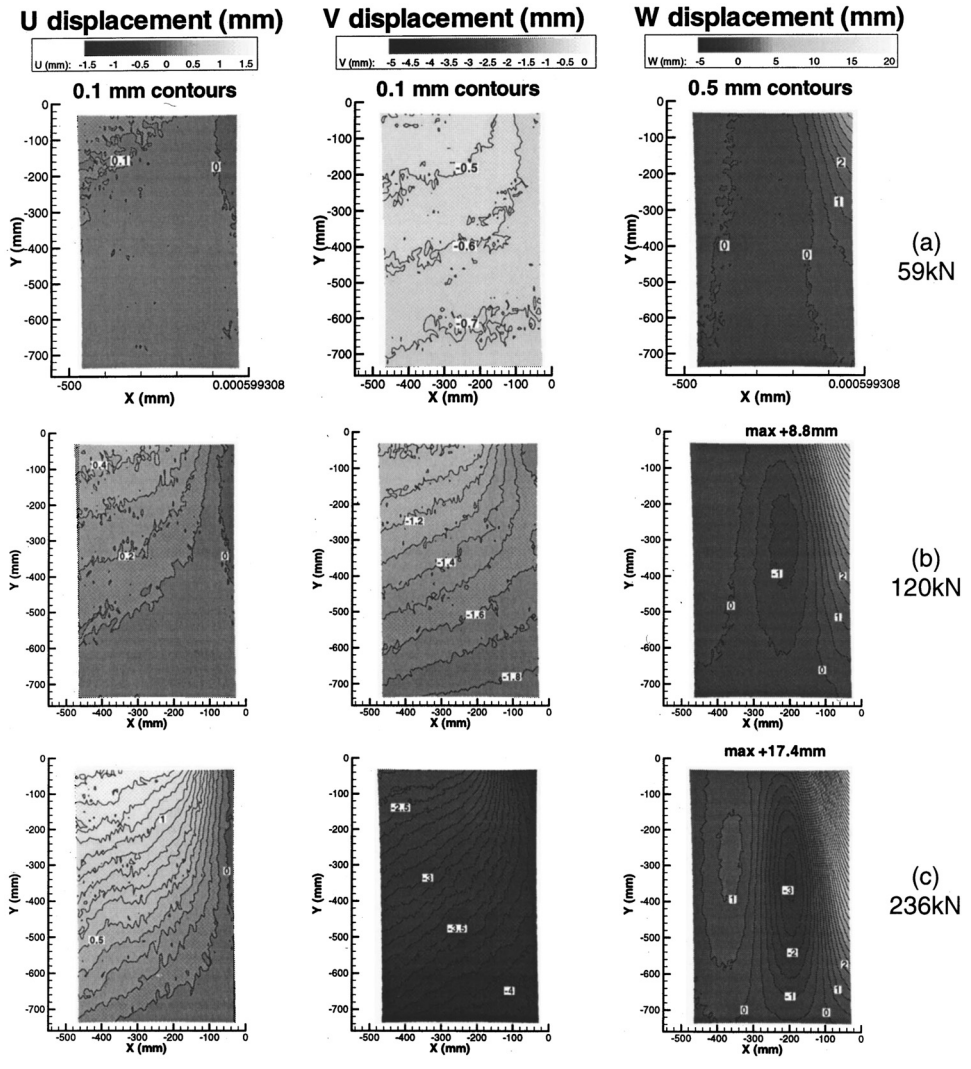

Figure 8.11 3D displacement data for a 1016-mm panel (reprinted from Helm et al.[37] with permission).

Figure 8.13(a) shows a photograph of the aluminum specimen used by the authors during experiments; the specimen is mounted in the loading fixer device. Figure 8.13(b) shows the specimen's dimensions; the random structure painted on the surface of the specimen can be clearly seen.

Figure 8.14(a) shows the 3D DIC setup used for quasi-static loading. Figure 8.14(b) shows the optical setup developed for impact loading. For the latter case, two high-speed cameras are used to capture images.[44] Due to safety requirements, the cameras are located outside the steel protective barrier surrounding the specimen by using special camera lenses. Additionally, a rigid

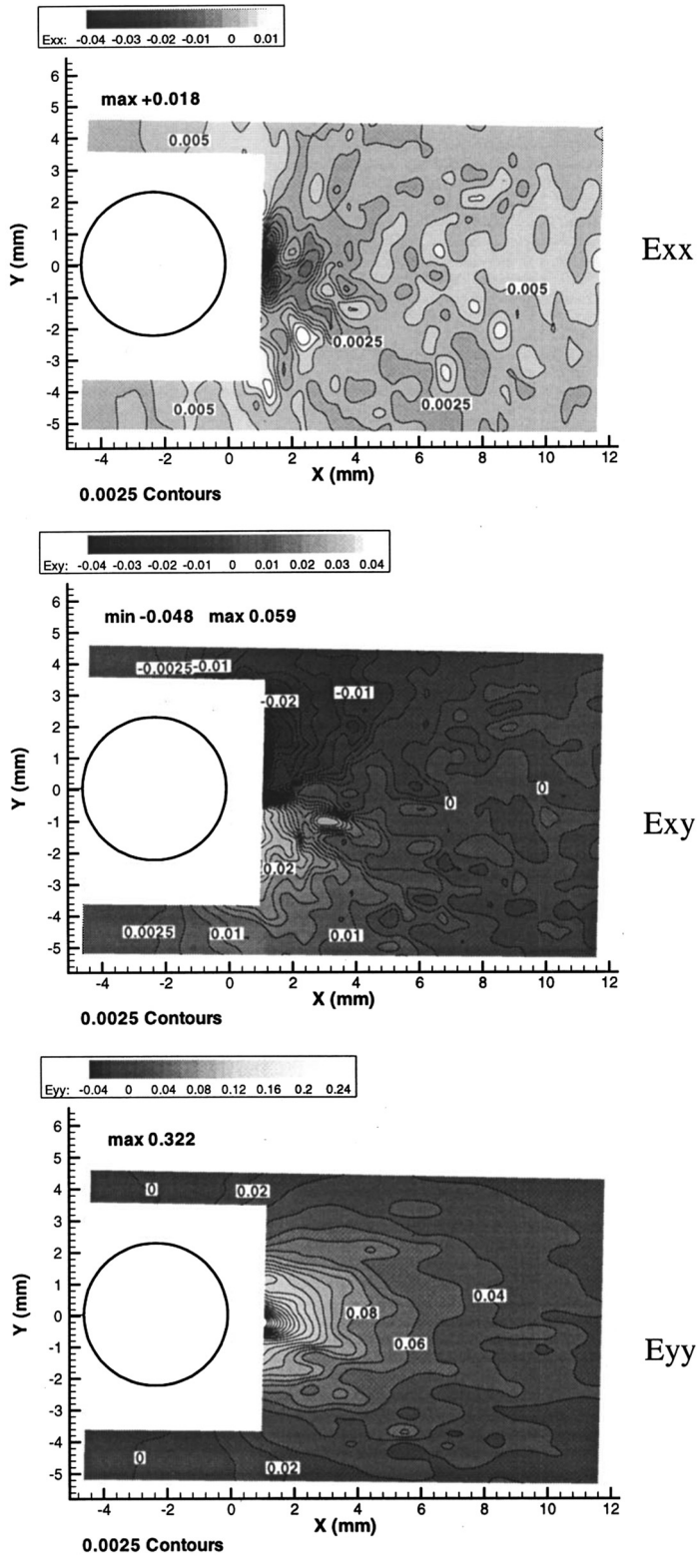

Figure 8.12 Local strains at maximum load for a 1016-mm panel (reprinted from Helm et al.[37] with permission).

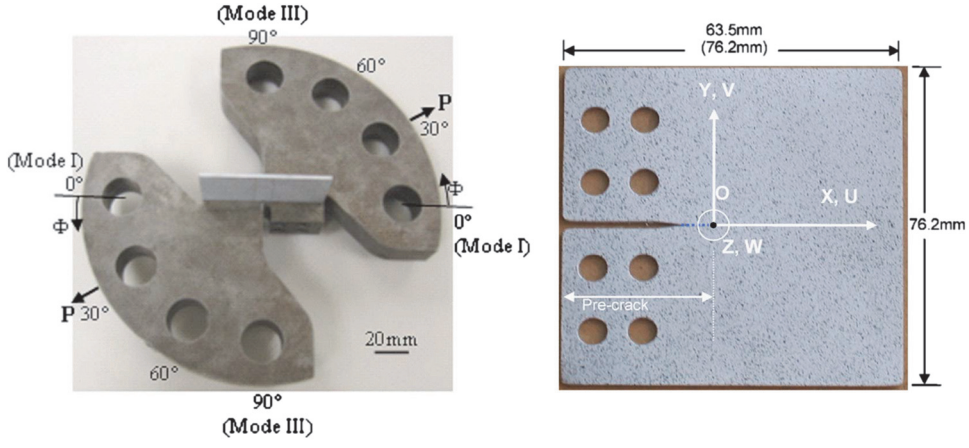

(a) (b)

Figure 8.13 (a) Loading fixture with specimen and loading angle. (b) In-plane dimensions of specimen and global coordinate system for mixed I/III mode experiments. Origin O is at the fatigue precrack tip, and the thickness is 2 mm (reprinted from Sutton[42] with permission).

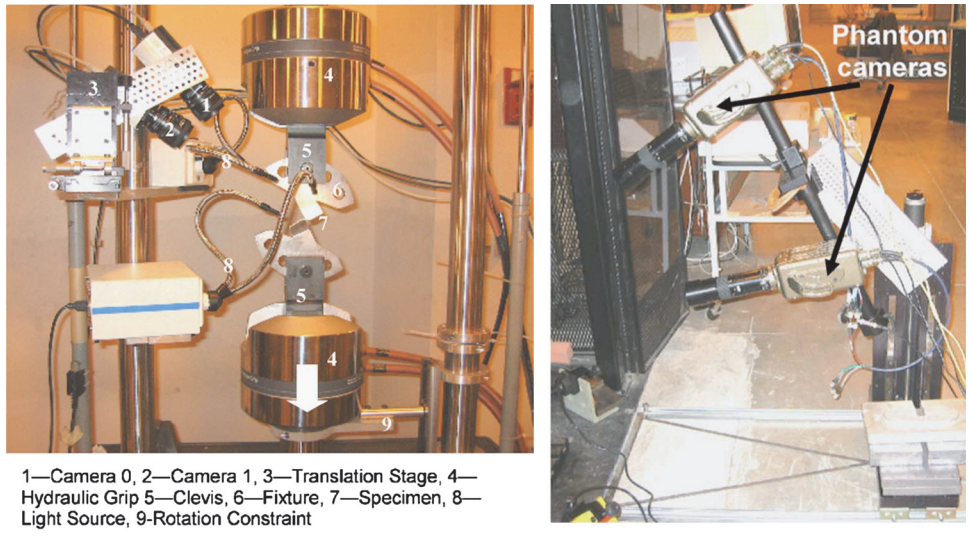

(a) (b)

Figure 8.14 Close-up view of the 3D displacement measurement system used for quasi-static mixed I/III mode experiments. (b) Phantom camera stereo rig for viewing the impact process (reprinted from Sutton[42] with permission).

cross-member is used to minimize relative motions between cameras during experiments.

Current bridge-health monitoring is usually performed by visual inspection. This procedure is not completely reliable because the accuracy directly depends on the experience and training of the inspector. For this reason, instruments

Figure 8.15 Experimental setup for projected pattern measurement to quantify spalling on a bridge in Lowell, MA (reprinted from Nonis et al.[46] with permission).

such as strain gages, fiber optic sensors, and displacement transducers are becoming common instruments in structural health monitoring.[44,45] However, these sensors perform local measurements, making detection of damage difficult if the sensor is not placed in the immediate vicinity of the crack or deformation. A full-field technique is more suitable for this kind of evaluation. For this reason, Nonis et al.[46] shows, as a final example, the application of DIC for structural health monitoring of bridges.

Nonis et al.[46] illustrate the application of a DIC system to locate nonvisible cracks in concrete, to quantify spalling, and to measure bridge deformations. The main idea is to use DIC to periodically monitor a bridge and compute deformations from images recorded at different dates or operating conditions.

Figure 8.15 shows the experimental setup used for spalling quantification. In this case, a high-power projector is used to project the random pattern onto the surface being analyzed. Figure 8.16 shows two areas with obvious and active spalling that were selected by the authors. For these figures, the surface geometries were measured at two different times: the initial measurement was performed on November 20th, 2012, and the subsequent measurement was on February 5th, 2013. They were then aligned, and the deviation between the surfaces was computed to quantify the spalling.

Sutton[4] states that it is currently possible to find more than 400 publications related to DIC developments and applications. For this reason, in the literature, several applications can be found, ranging from material testing, passing through NDT of structures, and reaching art structure investigations.[47] In the same way, there are applications in the literature that involve large structures as well as microscopic measurements by combining DIC with high-spatial-resolution devices, such as SEM (scanning electron microscopy) and AFM (atomic force microscopy). All of these publications and available examples show DIC as a reliable, valuable, and robust tool for experimental measurements in and outside the laboratory.

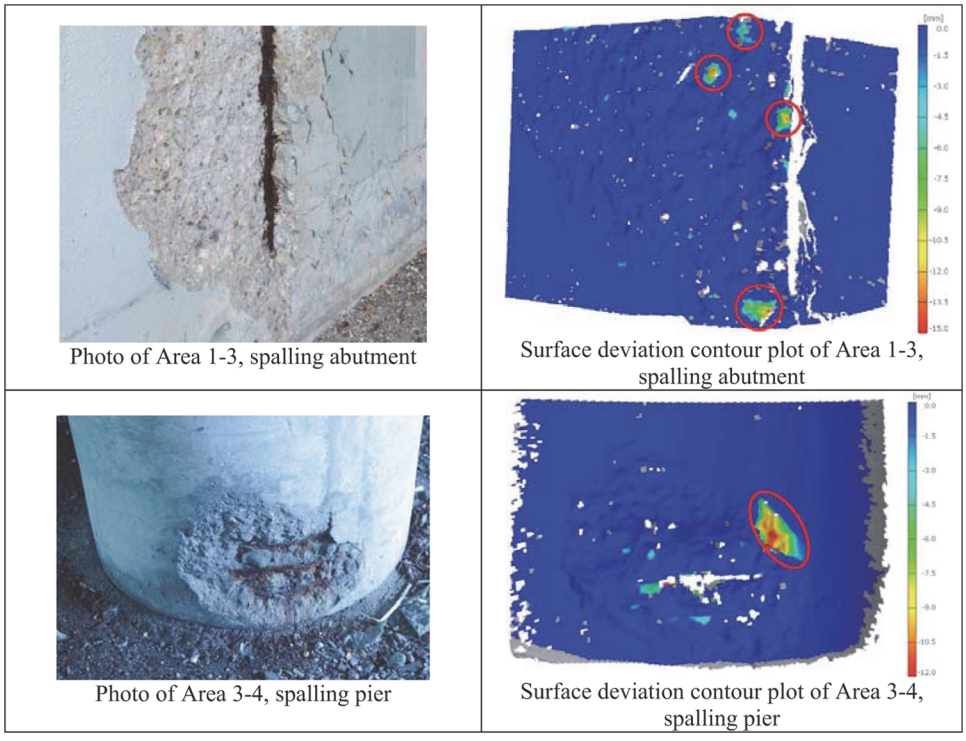

Figure 8.16 Photographs (left) and corresponding surface deviation contour plots (right) of spalling test areas. The largest areas of spalling are indicated by the red ovals (reprinted from Nonis et al.[46] with permission).

In conclusion, DIC has advantages and disadvantages when compared with interferometric techniques. Its advantages include the following: (a) it uses a simple experimental setup, (b) it needs a simple preparation of the specimen's surface, (c) it has low requirements in the measurement environment, and (d) it has a wide range of measurement and sensitivity. However, 2D DIC, for example, has some disadvantages: (a) the surface of the object must have a random gray intensity distribution, (b) measurements are dependent on the quality of the imaging system, and (c) the strain measurement accuracy is lower than that of the interferometric techniques. Consequently, noninterferometric and interferometric techniques are not exclusive methods; rather, they are complementary tools for experimental NDT.

References

1. B. Pan, K. Qian, H. Xie, and A. Asundi, "Two-dimensional digital image correlation for in-plane displacement and strain measurement: a review," *Meas. Sci. Technol.* **20**, 062001 (2009).

2. J. S. Sirkis and T. J. Lim, "Displacement and strain-measurement with automated grid methods," *Exp. Mech.* **31**, 382–388 (1991).
3. H. T. Goldrein, S. J. P. Palmer, and J. M. Huntley, "Automated fine grid technique for measurement of large-strain deformation maps," *Opt. Lasers Eng.* **23**, 305–318 (1995).
4. M. A. Sutton, J. J. Orteu, and H. W. Schreier, *Image Correlation for Shape, Motion and Deformation Measurements*, Springer, New York (2009).
5. W. H. Peters and W. F. Ranson, "Digital imaging techniques in experimental stress analysis," *Opt. Eng.* **21**(3), 213427 (1981) [doi: 10.1117/12.7972925].
6. T. C. Chu, W. F. Ranson, and M. A. Sutton, "Applications of digital-image-correlation techniques to experimental mechanics," *Exp. Mech.* **25**, 232–244 (1985).
7. M. A. Sutton, C. Mingqi, W. H. Peters, Y. J. Chao, and S. R. McNeill, "Application of an optimized digital correlation method to planar deformation analysis," *Image Vis. Comput.* **4**, 143–150 (1986).
8. W. H. Peters, W. F. Ranson, M. A. Sutton, T. C. Chu, and J. Anderson, "Application of digital correlation methods to rigid body mechanics," *Opt. Eng.* **22**(6), 226738 (1983) [doi: 10.1117/12.7973231].
9. M. A. Sutton, S. R. McNeill, J. D. Helm, and Y. J. Chao, "Advances in two-dimensional and three-dimensional computer vision," *Topics Appl. Phys.* **77**, 323–372 (2000).
10. B. K. Bay, "Texture correlation-a method for the measurement of detailed strain distributions within trabecular bone," *J. Orthop. Res.* **13**, 258–267 (1995).
11. D. J. Chen, F. P. Chiang, Y. S. Tan, and H. S. Don, "Digital speckle-displacement measurement using a complex spectrum method," *Appl. Opt.* **32**, 1839–1849 (1993).
12. G. R. Gaudette, J. Todaro, I. B. Krukenkamp, and F. P. Chiang, "Computer aided speckle interferometry: a technique for measuring deformation of the surface of the heart," *Ann. Biomed. Eng.* **29**, 775–780 (2001).
13. M. Sjodahl and L. R. Benckert "Electronic speckle photography: analysis of an algorithm giving the displacement with subpixel accuracy," *Appl. Opt.* **32**, 2278–2284 (1993).
14. M. Sjodahl and L. R. Benckert, "Systematic and random errors in electronics speckle photography," *Appl. Opt.* **33**, 7461–7471 (1994).
15. M. Sjodahl, "Electronic speckle photography-increased accuracy by nonintegral pixel shifting," *Appl. Opt.* **33**, 6667–6673 (1994).
16. M. Sjodahl, "Accuracy in electronic speckle photography," *Appl. Opt.* **36**, 2875–2885 (1997).

17. D. Zhang, X. Zhang, and G. Cheng, "Compression strain measurement by digital speckle correction," *Exp. Mech.* **39**, 62–65 (1999).
18. P. Zhou and K. E. Goodson, "Subpixel displacement and deformation gradient measurement using digital image/speckle correlation," *Opt. Eng.* **40**(8), 1613–1620 (2001) [doi: 10.1117/1.1387992].
19. I. Yamaguchi, "Speckle displacement and deformation in the diffraction and image fields for small object deformation," *Opt. Acta* **28**, 1359–1376 (1981).
20. J. Brillaud and F. Lagattu, "Limits and possibilities of laser speckle and white-light image-correlation methods: theory and experiments," *Appl. Opt.* **41**, 6603–6613 (2002).
21. H. W. Schreier and M. A. Sutton, "Systematic errors in digital image correlation due to under-matched subset shape functions," *Exp. Mech.* **42**, 303–310 (2002).
22. A. Giachetti, "Matching techniques to compute image motion," *Image Vis. Comput.* **18**, 247–260 (2000).
23. W. Tong, "An evaluation of digital image correlation criteria for strain mapping applications," *Strain* **41**, 167–175 (2005).
24. B. Pan, H. M. Xie, Z. Q. Guo and T. Hua, "Full-field strain measurement using a two-dimensional Savitzky-Golay digital differentiator in digital image correlation," *Opt. Eng.* **46**(3), 033601 (2007) [doi: 10.1117/1.2714926].
25. W. H. Press et al., *Numerical Recipes in C++*, 2nd Ed., Cambridge University Press, Cambridge (2002).
26. H. W. Schreier, J. R. Braasch, and M. A. Sutton, "Systematic errors in digital image correlation caused by intensity interpolation," *Opt. Eng.* **39**(11), 2915–2921 (1999) [doi: 10.1117/1.1314593].
27. W. G. Knauss, I. Chasiotis, and Y. Huang, "Mechanical measurements at the micron and nanometer scales," *Mech. Mater.* **35**, 217–231 (2003).
28. M. A. Sutton, J. H. Yan, V. Tiwari, H. W Schreier, and J. J. Orteu, "The effect of out-of-plane motion in 2D and 3D digital image correlation measurements," *Opt. Lasers Eng.* **46**, 746–757 (2008).
29. F. Lagattu, J. Brillaud, and M. C. Lafarie-Frenot, "High strain gradient measurements by using digital image correlation technique," *Mater. Charact.* **53**, 17–28 (2004).
30. W. D. Lockwood, B. Tomaz, A. P. Reynolds, "Mechanical response of friction stir welded AA2024: experiment and modeling," *Mater. Sci. Eng.* **A323**, 348–353 (2002).
31. A. P. Reynolds and F. Duvall, "Digital image correlation for determination of weld and base metal constitutive behavior," *Welding J.* **78**, 355s–360s (1999).

32. W. D. Lockwood and A. P. Reynolds, "Simulation of the global response of a friction stir weld using local constitutive behavior," *Mater. Sci. Eng.* **A339**, 35–42 (2003).
33. J. Yan, M. A. Sutton, A. P. Reynolds, A. Samer, and D. Horsley, "Characterization of heterogeneous response of pipeline steel weld using digital image correlation," *Proc. 2006 SEM Annual Conference and Exposition on Experimental and Applied Mechanics*, 90–96 (2006).
34. VIC2D and VIC3D, Correlated Solutions Incorporated, Columbia, SC, USA, http://www.correlatedsolutions.com.
35. J. J. Orteu, F. Bugarin, and J. Harvent, "Multiple-camera instrumentation of a single point incremental forming process pilot for shape and 3D displacement measurements: methodology and results," *Exp. Mech.* **51**, 625–639 (2011).
36. F. Chen, X. Chen, X. Xie, X. Feng, and L. Yang, "Full-field 3D measurement using multi-camera digital image correlation system," *Opt. Lasers Eng.* **51**, 1044–1052 (2013).
37. J. D. Helm, M. A. Sutton, and S. R. McNeill, "Deformations in wide, center-notched, thin panels, part I: three-dimensional shape and deformation measurements by computer vision," *Opt. Eng.* **42**(5), 1293–1305 (2003) [doi: 10.1117/1.1566001].
38. R. Y. Tsai, "An efficient and accurate camera calibration technique for 3-D machine vision," *Proc. IEEE Intl. Conf. Comp. Vision Pattern Recognition*, 364–374 (1986).
39. J. Weng, P. Cohen, and M. Herniou, "Camera calibration with distortion models and accuracy evaluation," *IEEE Trans. Pattern Anal. Mach. Intell.* **14**(10), 965–980 (1992).
40. J. D. Helm, M. A. Sutton, and M. L. Boone, "Characterizing crack growth in thin aluminum panels under tension-torsion loading using three-dimensional digital image correlation," *ASTM Spec. Tech. Publ.* **1323**, 3–14 (2001).
41. M. A. Sutton, J. D. Helm, and M. L. Boone, "Experimental study of crack growth in thin sheet 2024-T3 aluminum under tension-torsion loadings," *Int. J. Fract.* **109**, 285–301 (2001).
42. M. A. Sutton, J. Yan, X. Deng, C. Cheng, and P. Zavattieri, "Three-dimensional digital image correlation to quantify deformation and crack-opening displacement in ductile aluminum under mixed-mode I/III loading," *Opt. Eng.* **46**(5), 051003 (2007) [doi: 10.1117/1.2741279].
43. M. A. Sutton, "Digital Image Correlation," *Springer Handbook of Experimental Solid Mechanics*, W. N. Sharpe, ed., Springer, Boston (2008).
44. H. Sohn, C. R. Farrar, F. M. Hemez, D. D. Shunk, D. W. Stinemates, B. R. Nadler, and J. J. Czarnecki, "A review of structural health monitoring

literature: 1996–2001," *Los Alamos National Laboratory Report, LA-13976-MS* (2004) [http://library.lanl.gov/cgi-bin/getfile?00796820.pdf].

45. S. W. Doebling, C. R. Farrar, M. B. Prime, and D. W. Shevitz, "Damage identification and health monitoring of structural and mechanical systems from changes in their vibration characteristics: a literature review," *Los Alamos National Laboratory Report, LA-13070-MS* (1996) [http://institute.lanl.gov/ei/shm/pubs/lit_review.pdf].
46. C. Nonis, C. Niezrecki, T. Yu, S. Ahmed, C. Su, and T. Schmidt, "Structural health monitoring of bridges using digital image correlation," *Proc. SPIE* **8695,** 869507 (2013) [doi: 10.1117/12.2009647].
47. M. Kujawinska, M. Malesa, K. Malowany, A. Piekarczuk, L. Tymińska-Widmer, and P. Targowski, "Digital image correlation method: a versatile tool for engineering and art structures investigations," *Proc. SPIE* **8011**, 80119R (2011) [doi: 10.1117/12.915566].

Chapter 9
Closing Remarks

Civil structures (such as bridges and buildings) and mechanical parts (for cars, planes, trains, etc.) exist to solve problems and simplify life. The final part must be functional, safe, reliable, competitive, usable, manufacturable, and marketable.

As explained throughout the book, designed components are exposed to specified and unspecified loads. The main task of the design team is to develop the component to mechanically withstand this set of loads during the service life. Nevertheless, unpredictable loads, external agents (generating corrosion), and known service loads produce fatigue or wear and necessitate inspection to ensure the integrity and safe functioning of the component.

Visual inspection was the first way to evaluate health integrity of a mechanical or civil structure, and it remains an important, valuable, and widely used nondestructive method to assess discontinuities exposed to the surface of the material. Advances in optics, digital image storage, and digital image processing have expanded the applications of visual inspection. In this case, optical methods can be considered as an extension of this technique because they are used to "monitor" the surface of a material under test and to identify possible anomalies not only on the surface but also below it.

Optical techniques are very attractive for NDT due to their noncontact nature and its relatively high speed of inspection. The application of digital techniques allows automatic processing. Consequently, a fast inspection procedure is obtained, enabling the evaluation of large areas (e.g., aircraft wings, ship sides, etc.) or a large number of parts, such as automotive components. Thermography, reflectometry, laser ultrasound (LUS), computed tomography (CT), and speckle techniques are notable optical techniques applied to NDT of materials.

The speckle effect is a consequence of the interaction between the coherent light of a laser source and the microgeometry of rough surfaces. By using interferometric or noninterferometric approaches, speckle properties can be deterministically related to displacement fields produced on the surface of the specimen under investigation.

Speckle techniques have the advantages cited for optical methods, such as high inspection velocity, digital processing, automation of data analysis process, and noncontact nature. Furthermore, they are adequate for evaluating real components without further preparation of the surface and without dedicating a lot of time to analysis. Consequently, speckle techniques are very suitable for NDT in industrial applications.

This book shows that noninterferometric techniques are primarily used to measure displacement fields and their associated loading fields, e.g., stresses and strains. Among them, DIC is notable as an experimental technique used worldwide in the laboratory and in the field. There are several optical setups used in DIC that are very simple and easy to apply in industrial applications. For these reasons, DIC is an excellent tool for full-field measurements involving test materials, as well as NDT; however, the strain measurement accuracy of DIC is lower than that of interferometric techniques.

For this reason, interferometric techniques are used as alternative measurement tools. Interferometric speckle setups should be built in portable devices for application outside the laboratory with the same efficiency as noninterferometric techniques. To accomplish this, the interferometer should be:

- robust,
- flexible,
- compact,
- stable,
- user-friendly, and
- organized.

Accounting for the preceding list, miniaturized and/or monolithic optical measurement systems (OMSs) are good choices to achieve robustness against shock and mechanical vibration. Special optical configurations can be designed to be achromatic, i.e., wavelength-independent. Temperature-insensitive and self-calibrating OMSs have a good chance to succeed in harsh environments. Specimen-embedded OMSs are also excellent candidates for operation in an unfavorable environment.

The use of diffractive optical elements can bring new conceptual designs and properties to robust OMSs for a variety of applications. Intensive use of general-purpose computing on graphics processing units (GPGPUs) opens new possibilities for very fast image processing. (Ideally, an open-source scientific image processing library using CGCGU platforms would be used.) Underwater optical metrology and remote passive optical sensors would be ideal for demanding applications in the near future.

Optical noninterferometric and interferometric techniques based on the speckle phenomena have grown since the invention of the laser. They are being increasingly used for industrial applications as control tools for quality tests, replacing traditional NDT techniques, such as ultrasound and x-ray diffraction.

Mechanical, computational, and optical solutions, shown throughout the book and used to bring robustness to optical systems, are among the main reasons for the constant expansion of the techniques outside the scientific field. Finally, several companies around the world are commercializing not only image processing software but also specific interferometric hardware that are used for NDT (primarily in the aeronautical industry).

To conclude, a short list with possible applications is presented. This list is intended to help readers select the best technique for a determined application or identify a possible measurement solution or a combination of them.

a. To measure displacements that occur in the same plane as the surface, an in-plane interferometer and 2D DIC are adequate solutions.
b. If in-plane displacements are large in magnitude and if out-of-plane displacements are also present, DIC would be more suitable than interferometric in-plane systems. In this case, interferometric sensors would experience loss of correlation between images due to the presence of out-of-plane displacements.
c. For high strain-measurement accuracy, interferometric techniques are suitable. In this case, radial in-plane interferometers are the best solution because the principal directions of the strain and stress fields are unknown in advance.
d. To simultaneously measure out-of-plane and in-plane displacement fields, 3D DIC systems are the most appropriate solution.
e. To indentify internal defects, shearography is the most adequate technique. Correct selection of the loading methodology will ensure the correct detection of defects and the success of the measurement. In this case, the measurement is qualitative, not quantitative.

Index

Matias R. Viotti is an Associate Researcher in the Mechanical Engineering Department of the National University of Santa Catarina, Brazil. He works at the Metrology and Automatization Laboratory (Labmetro), which is linked to the university. He is a senior member of SPIE and a member of OSA. He has co-authored more than 50 papers published in international journals and conference proceedings, and one book chapter.

Armando Albertazzi, Jr. is a Professor of Mechanical Engineering at the National University of Santa Catarina, Brazil. He is the head of the Metrology and Automatization Laboratory (Labmetro), which is linked to the university. He is a fellow of SPIE and a member of OSA and SEM. Prof. Albertazzi has co-authored more than 150 papers published in international journals and conference proceedings, and several book chapters.

ROBUST SPECKLE METROLOGY: TECHNIQUES FOR STRESS ANALYSIS AND NDT

Matias R. Viotti
Armando Albertazzi, Jr.

Optical techniques are usually applied inside laboratories equipped with temperature, humidity and vibration control. These techniques are very suitable for fast measurements due to their noncontact nature and their capability to measure on surfaces without special, time-consuming preparation. Among them, optical methods based on the speckle phenomenon have developed substantially over the last two decades due to the development of digital image processing, digital cameras, computers, lasers, and optical components.

However, applying speckle methods outside of the laboratory becomes a challenging task. This book presents techniques and tools that will enable the development of robust measurement instruments to be used outside the laboratory for nondestructive structural-integrity-evaluation devices. Additionally, several technical solutions that combine mechanical systems to solve industrial measurement demands are described.

SPIE.
P.O. Box 10
Bellingham, WA 98227-0010

ISBN: 9781628413182
SPIE Vol. No.: PM251